

## INFORMATION TO USERS

This manuscript has been reproduced from the microfilm master. UMI films the text directly from the original or copy submitted. Thus, some thesis and dissertation copies are in typewriter face, while others may be from any type of computer printer.

**The quality of this reproduction is dependent upon the quality of the copy submitted.** Broken or indistinct print, colored or poor quality illustrations and photographs, print bleedthrough, substandard margins, and improper alignment can adversely affect reproduction.

In the unlikely event that the author did not send UMI a complete manuscript and there are missing pages, these will be noted. Also, if unauthorized copyright material had to be removed, a note will indicate the deletion.

Oversize materials (e.g., maps, drawings, charts) are reproduced by sectioning the original, beginning at the upper left-hand corner and continuing from left to right in equal sections with small overlaps. Each original is also photographed in one exposure and is included in reduced form at the back of the book.

Photographs included in the original manuscript have been reproduced xerographically in this copy. Higher quality 6" x 9" black and white photographic prints are available for any photographs or illustrations appearing in this copy for an additional charge. Contact UMI directly to order.

# U·M·I

University Microfilms International  
A Bell & Howell Information Company  
300 North Zeeb Road, Ann Arbor, MI 48106-1346 USA  
313/761-4700 800/521-0600



**Order Number 9322437**

**Study of surface properties produced by magneto-plasma ion  
nitriding for improving wear resistance**

**Shih, I-Tsung, Ph.D.**

**New Jersey Institute of Technology, 1993**

**Copyright ©1993 by Shih, I-Tsung. All rights reserved.**

**U·M·I**  
300 N. Zeeb Rd.  
Ann Arbor, MI 48106



**STUDY OF SURFACE PROPERTIES  
PRODUCED BY MAGNETO-PLASMA ION NITRIDING  
FOR IMPROVING WEAR RESISTANCE**

by  
**I-Tsung Shih**

A Dissertation  
Submitted to the Faculty of  
New Jersey Institute of Technology  
in Partial Fulfillment of the Requirements for the Degree of  
Doctor of Philosophy

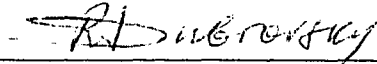
Department of Mechanical and Industrial Engineering

January 1993

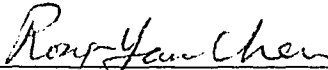
# APPROVAL PAGE

## Study of Surface Properties Produced by Magneto-Plasma Ion Nitriding for Improving Wear Resistance

by  
I-Tsung Shih

 11/20/92

Dr. Roman Dubrovsky, Dissertation Adviser  
Associate Professor of Mechanical Engineering  
Department of Mechanical and Industrial Engineering  
New Jersey Institute of Technology

 11/20/92


Dr. Rong-Yaw Chen, Committee Member  
Professor of Mechanical Engineering  
Department of Mechanical and Industrial Engineering  
New Jersey Institute of Technology

 11/20/92

Dr. John V. Droughton, Committee Member  
Professor of Mechanical Engineering  
Department of Mechanical and Industrial Engineering  
New Jersey Institute of Technology

 Nov. 20, 92

Dr. Nouri Levy, Committee Member  
Associate Professor of Mechanical Engineering  
Department of Mechanical and Industrial Engineering  
New Jersey Institute of Technology

 11-20-92

Dr. Lawrence Suchow, Committee Member  
Professor Emeritus of Chemistry  
Department of Chemical Engineering, Chemistry, and Environmental Science  
New Jersey Institute of Technology

Copyright © 1993 by I-Tsung Shih  
**ALL RIGHTS RESERVED**

## **ABSTRACT**

### **Study of Surface Properties Produced by Magneto-Plasma Ion Nitriding for Improving Wear Resistance**

**by  
I-Tsung Shih**

In this work a newly developed surface treatment process, Magneto-Plasma Ion Nitriding process, was developed and studied. This process was developed to increase durability and wear resistance of operational surfaces of different machine components.

In this study, orthogonal experimental analysis was used to develop, optimize, and select the process parameters. Coating layers were characterized and studied by using scanning electron microscopy(SEM), Auger electron spectroscopy(AES), and image analysis system. The influence of different process treatment parameters, such as temperature, nitrogen concentration, and magnetization, on the layers properties was studied. The mechanism of layer formation and bonding was proposed and a mathematical model was derived. To perform the wear resistance test, the wear testing methodology and a computer-controlled wear testing machine were designed, manufactured, and assembled.

Selected process parameters permitted developing different types of compound layers, such as  $\epsilon$ ,  $\gamma'$ ,  $\alpha$  phases, or their combination. Microstructure and microhardness investigations were performed with respect to deposited layers.

Differently applied magnetic treatments to the surface provided improvement in diffusion bonding of deposited compound layers to substrate. The mechanism of this bonding was introduced and explained in this work.

As a result of the developed magneto-plasma ion nitriding surface treating process, it was found that durability and wear resistance of operational surfaces of machine components made from different steels have been significantly improved.



## BIOGRAPHICAL SKETCH

**Author:** I-Tsung Shih

**Degree:** Doctor of Philosophy in Mechanical Engineering

**Date:** January, 1993

**Date of Birth:** August 14, 1961

**Place of Birth:** Taipei, Taiwan, Republic of China

### **Undergraduate and Graduate Education:**

- Doctor of Philosophy in Mechanical Engineering,  
New Jersey Institute of Technology, Newark, NJ, U.S.A., 1993
- Master of Science in Mechanical Engineering,  
New Jersey Institute of Technology, Newark, NJ, U.S.A., 1988
- Bachelor of Science in Mechanical Engineering,  
Chung-Yuang University, Tao-Yuang, Taiwan, R.O.C., 1983

**Major:** Mechanical Engineering

### **Presentations and Publications:**

Shih, I-Tsung and R. Dubrovsky. "Development of The Computer Controlled Seizure Testing Methodology." *MRS*. 140s (1988).

Shih, I-Tsung, R. Dubrovsky, and Y. Kin. "Development of the Computer Controlled Wear Testing Methodology." *Proc. of The International Applied Mechanical Systems Design Conference(IAMSDC-1)*. 1 (1989): 57.1-4.

Shih, I-Tsung. "Magnetic Treatment for Plasma Ion Nitriding." *ASME Graduate Student Conference*, NJIT, 1991.

This thesis is dedicated to my beloved parents  
Pi-Yung Wang Shih and Chao-Shang Shih

## ACKNOWLEDGMENT

The author wishes to express his sincere gratitude to his advisor, Dr. Roman Dubrovsky, for his guidance, friendship, and moral support throughout this research.

Special thanks to Dr. Rong-Yaw Chen, John V. Droughton, Nouri Levy, and Lawrence Suchow for serving as members of the committee.

The author would like to thank the people who have been of assistance to him in the preparation of this dissertation. The author appreciates the timely help and suggestions from Mr. Don Rosand, Karl Ulatowski, Joe Glaz, and Dave Singh. The author also thanks to formal and present members of Surface Engineering Laboratory for their help and suggestions, including: Mr. W. L. Yao, Wenger Yang, Tian-zhong Xu, and Miss Ning Lee.

The author wishes to thank his parents for their support and encouragement throughout the period of his studying aboard. Finally, the author would like to express his appreciation to his wife, Yu-Hwa Kao, for typewriting the manuscript and for her patience, understanding, and taking care our new born baby during this study.

## TABLE OF CONTENTS

Chapter	Page
<b>1 INTRODUCTION</b> .....	<b>1</b>
<b>2 BACKGROUND</b> .....	<b>3</b>
2.1 Surface Engineering .....	3
2.2 Role of Plasma Ion Nitriding in Surface Engineering .....	6
2.2.1 Nitriding and Plasma Ion Nitriding .....	6
2.2.2 Plasma Ion Nitriding Process .....	9
2.2.2.1 Plasma Ion Nitriding System .....	9
2.2.2.2 Plasma Nitriding Mechanism .....	11
2.2.2.3 Phase Diagram .....	13
2.2.3 Advantages and Disadvantages .....	15
2.3 Magnetic Behavior of Materials .....	16
2.3.1 Introduction .....	16
2.3.2 Kinds of Magnetism .....	17
2.3.3 Free Energies of Ferromagnetism .....	21
2.3.4 Magnetic Domain and Domain Wall Motion .....	24
<b>3 GOAL AND OBJECTIVES</b> .....	<b>27</b>
<b>4 MECHANISM OF PULSED MAGNETIC TREATMENT</b> .....	<b>29</b>
4.1 Mechanism of Magnetization Process .....	29
4.2 Irreversible Magnetization Process .....	31
4.3 Hindrances of Domain Wall Motion .....	32
4.3.1 Inclusion .....	33
4.3.2 Residual Microstresses .....	34
4.4 The Interaction of Dislocations and Domain Wall Motion .....	35
4.5 Pulsed Magnetic Treatment .....	37
4.6 The Mechanism of Pulsed Magnetic Treatment .....	39

<b>Chapter</b>	<b>Page</b>
4.6.1 Effects of Domain Wall Motion .....	40
4.6.2 Effect of Domain Rotation .....	41
<b>5 MODEL FOR MAGNETO-PLASMA ION NITRIDING .....</b>	<b>43</b>
5.1 Magneto-Plasma Ion Nitriding .....	43
5.2 Fick's Laws for Diffusion Processes .....	45
5.2.1 Fick's First Law .....	45
5.2.2 Fick's Second Law .....	45
5.3 Nail Effect .....	47
5.4 Diffusion Through Dislocations .....	48
5.5 Nail Model For Nail Effect .....	51
<b>6 METHODOLOGY .....</b>	<b>61</b>
6.1 Materials Selection and Specimens Preparation .....	61
6.2 Design of Magneto-Plasma Nitriding Process Parameters .....	63
6.2.1 The Optimization of PIN Process Parameters .....	63
6.2.2 The Design of Magneto-Plasma Nitriding Parameters .....	66
6.2.3 Devices and Procedures .....	67
6.3 Characterization of Nitrided Layers .....	68
6.3.1 Auger Electron Spectroscopy(AES) .....	68
6.3.1.1 Principle .....	68
6.3.1.2 Equipment and Procedures .....	71
6.3.2 Microscope Analysis .....	73
6.3.3 Microhardness Measurement .....	73
6.4 Wear Testing Process .....	74
6.4.1 Wear Testing Methodology .....	74
6.4.2 Wear Testing Machine .....	77
6.4.3 Process Control and Procedure .....	79

<b>Chapter</b>	<b>Page</b>
6.4.4 Surface Measurement .....	80
<b>7 RESULTS AND DISCUSSION .....</b>	<b>81</b>
7.1 Selection of Control Parameters for PIN Process .....	81
7.2 Nitrided Layer Characterization .....	84
7.3 The Effect of Gas Composition and Temperature on PIN process .....	91
7.3.1 Temperature .....	91
7.3.2 Gas Composition .....	99
7.4 Role of Magnetic Field in Magneto-Plasma Ion Nitriding .....	99
7.4.1 Cycle Effect of Applied Magnetic Field .....	99
7.4.2 Pre-magnetized and Post-magnetized PIN Approach .....	104
7.5 Nail Model for Magneto-Plasma Ion Nitriding .....	111
7.6 Wear Evaluation .....	121
7.6.1 Friction Coefficient for Wear Testing Process .....	121
7.6.2 Wear Rate .....	125
<b>8 CONCLUSIONS .....</b>	<b>133</b>
APPENDIX A Layer Formation at Different Temperature .....	137
APPENDIX B Layer Formation at Different Nitrogen Concentration .....	144
APPENDIX C Properties of Pre-magnetized and Post-magnetized Specimens .....	148
APPENDIX D Program for Nail Model .....	167
REFERENCES .....	173

## LIST OF TABLES

<b>Table</b>	<b>Page</b>
2.1 Industrial application of plasma ion nitriding process . . . . .	8
6.1 Material compositions . . . . .	61
6.2 Etching solutions for tested materials . . . . .	63
6.3 The value of PIN process control parameters . . . . .	65
6.4 Parameters for orthogonal testing. . . . .	65
6.5 Magneto-plasma ion nitriding testing parameters and specimen symbols . . . . .	66
7.1 Orthogonal analysis of maximum hardness for AISI D2 tool steel. . . . .	82
7.2 Orthogonal analysis of case depth for AISI D2 tool steel . . . . .	83
7.3 Orthogonal analysis of weight gain for AISI D2 tool steel . . . . .	83
7.4 The results of orthogonal analysis . . . . .	84
7.5 Influence of pre-post magnetization on surface treatment . . . . .	100
7.6 Influence of PIN treatment on surface properties of AISI D2 tool steel . . . . .	105
7.7 Influence of PIN treatment on surface properties of AISI H13 tool steel . . . . .	107
7.8 Influence of PIN treatment on surface properties of AISI 420 stainless steel. . . . .	109
7.9 Testing parameters and specimen symbols for group1 . . . . .	125

## LIST OF FIGURES

Figure	Page
2.1 Plasma assisted surface modification techniques . . . . .	4
2.2 Plasma ion nitriding system . . . . .	9
2.3 Surface reaction during PIN process . . . . .	12
2.4 Nitrided layers . . . . .	13
2.5 Fe-N phase diagram . . . . .	14
2.6 Diamagnetism . . . . .	18
2.7 Paramagnetism . . . . .	19
2.8 Antiferromagnetism . . . . .	19
2.9 Ferrimagnetism . . . . .	20
2.10 Ferromagnetism . . . . .	21
2.11 Domain and domain boundary in the material . . . . .	24
2.12 Domain wall motion and domain rotation : (a) - (c) domain motion; (c) - (d) domain rotation . . . . .	26
4.1 Magnetization curve and hysteresis . . . . .	30
4.2 Irreversible domain wall process : (a) domain wall energy with respect to distance; (b) gradient of domain wall energy . . . . .	32
4.3 Passage of a domain wall through an inclusion . . . . .	33
4.4 Structure deformation due to magnetostriction . . . . .	39
4.5 The elimination of dislocation due to shear force . . . . .	42
5.1 Distribution of dislocations in material : (a) before magnetization; (b) after magnetization . . . . .	47
5.2 Nail Effect . . . . .	48
5.3 Nail model for "Nail Effect" . . . . .	49
5.4 Integral contour . . . . .	57
6.1 Shoe for wear testing . . . . .	62



<b>Figure</b>	<b>Page</b>
6.2 Specimen arrangement for metallurgical analysis . . . . .	62
6.3 The effect of gas composition on the formation of layers . . . . .	64
6.4 Energy level diagram of (a) photoelectron and (b) Auger electron excitation .	68
6.5 Auger electron spectrum for AISI H13 tool steel . . . . .	69
6.6 Auger electron spectrum for $d(N(E))/N(E)$ with respect to $N(E)$ . . . . .	70
6.7 Schematic representation of the PHI model 550 ESCA/SCM system . . . . .	71
6.8 The process of Auger indentation. . . . .	72
6.9 The method to perform microhardness indentation. . . . .	74
6.10 Schematic of the suspended motor . . . . .	75
6.11 Wear testing machine and system. . . . .	78
7.1 Microhardness profile along the hardened case.(AISI H13 tool steel; 6 hours, 600°C, 4 torr, 55 % N <sub>2</sub> PIN process parameters). . . . .	85
7.2 Nitrided layer microstructure of AISI D2 tool steel. . . . .	85
7.3 Nitrided layer microstructure of AISI H13 tool steel . . . . .	87
7.4 Nitrided layer microstructure of AISI 420 stainless steel. . . . .	87
7.5 Layers characterization by microstructure, microhardness distribution, and AES analysis for AISI H13 tool steel . . . . .	89
7.6 Layers characterization by microstructure, microhardness distribution, and AES analysis for AISI 420 stainless steel . . . . .	90
7.7 Variation in the microstructure and microhardness of the nitrided layer at different temperature for AISI D2 tool steel (65% N <sub>2</sub> , 6 hours, 3 torr): (a) 650°C; (b) 550°C . . . . .	92
7.8 Variation in the microstructure and microhardness of the nitrided layer at different temperature for AISI H13 tool steel (65% N <sub>2</sub> , 6 hours, 3 torr): (a) 650°C; (b) 550°C. . . . .	93
7.9 Variation in the microstructure and microhardness of the nitrided layer at different temperature for AISI 420 stainless steel (65% N <sub>2</sub> , 6 hours, 3 torr): (a) 650°C; (b) 550°C. . . . .	94

<b>Figure</b>	<b>Page</b>
7.10 Variation in the microhardness and microstructure of the nitrided layer at different nitrogen concentration for AISI D2 tool steel : (a) 65% N <sub>2</sub> ; (b) 25% N <sub>2</sub> ; (c) 5% N <sub>2</sub> .....	96
7.11 Variation in the microhardness and microstructure of the nitrided layer at different nitrogen concentration for AISI H13 tool steel (650°C, 6 hours, 3torr): (a) 65% N <sub>2</sub> ; (b) 25% N <sub>2</sub> ; (c) 5% N <sub>2</sub> .....	97
7.12 Variation in the microhardness and microstructure of the nitrided layer at different nitrogen concentration for AISI 420 stainless steel (650°C, 6 hours, 3torr): (a) 65% N <sub>2</sub> ; (b) 25% N <sub>2</sub> ; (c) 5% N <sub>2</sub> .....	98
7.13 Microhardness profile for post-magnetized AISI H13 tool steel .....	101
7.14 Microhardness profile for pre-magnetized AISI H13 tool steel .....	101
7.15 The definition of case depth and layer distribution .....	103
7.16 The variation of concentration along depth( $\eta$ ) .....	113
7.17 The variation of concentration along radial distance( $\rho$ ). .....	113
7.18 The concentration distribution along the radial distance when depth $\eta = 5a$ ..	114
7.19 Three dimensional concentration distribution along depth and radial distance ..	114
7.20 Isoconcentration line in depth and radial directions. ....	115
7.21 A profile for "nail" in 3 dimensional view for mean concentration $\langle c \rangle = 0.001$ .....	115
7.22 Mean concentration distribution along depth( $\eta$ ) for Nail model and Le Claire model at dislocation density $d = 1000$ .....	117
7.23 Mean concentration distribution along depth( $\eta$ ) for Nail model and Le Claire model at dislocation density $d = 100$ .....	117
7.24 Mean concentration distribution along depth( $\eta$ ) for Nail model and Le Claire model at dislocation density $d = 10$ .....	118
7.25 Mean concentration distribution along depth( $\eta$ ) for Nail model and Le Claire model at dislocation density $d = 1$ .....	118
7.26 Mean concentration distribution along depth( $\eta$ ) for Nail model and Le Claire model at dislocation density $d = 0.1$ .....	119

<b>Figure</b>	<b>Page</b>
7.27 Mean concentration distribution along depth( $\eta$ ) for Nail model and Le Claire model at dislocation density $d = 0.01$ . . . . .	119
7.28 Mean concentration distribution along depth( $\eta$ ) for Nail model and Le Claire model at dislocation density $d = 0.001$ . . . . .	120
7.29 Mean concentration distribution for (a) high dislocation density, (b) low dislocation density . . . . .	120
7.30 Calibration chart for friction coefficient versus strain readings . . . . .	122
7.31 Calibration chart for friction force and motor moments versus strain readings.	122
7.32 Friction forces versus sliding time for different treated AISI H13 tool steel : (a). nitrided; (b). nitrided + 20 cycles pre-magnetization; (c). nitrided + 40 cycles pre-magnetization; (d). nitrided + 60 cycles pre-magnetization . . . . .	123
7.33 Wear rate of nitrided and non-nitrided AISI D2 tool steel. . . . .	126
7.34 Wear rate of nitrided and non-nitrided AISI H13 tool steel. . . . .	126
7.35 Wear rate for pre-magnetized and nitrided AISI H13 tool steel . . . . .	127
7.36 Wear rate for post-magnetized and nitrided AISI H13 tool steel. . . . .	127
7.37 Wear rate for different nitrogen composition of AISI H13 tool steel. . . . .	130
7.38 Wear rate for 65% nitrogen composition of AISI H13 tool steel. . . . .	130
7.39 Wear rate for 25% nitrogen composition of AISI H13 tool steel. . . . .	131
7.40 Wear rate for 5% nitrogen composition of AISI H13 tool steel . . . . .	131

## LIST OF SYMBOLS

<b>Symbol</b>	<b>Meaning</b>
<b>A</b>	Ampere
<b>a</b>	Dislocation radius
<b>B</b>	Magnetic flux density
<b>b</b>	Burger vector
<b>b<sub>m</sub></b>	Burger vector for mixed dislocations
<b>b<sub>s</sub></b>	Burger vector for screw dislocation
<b>C</b>	Concentration of nitride gas
<b>c</b>	Concentration of diffusants
<b>c<sub>d</sub></b>	Concentration of diffusants in dislocation
<b>c<sub>g</sub></b>	Concentration of diffusants in grain
<b>c<sub>g1</sub></b>	Concentration of diffusants in grain from volume diffusion
<b>c<sub>g2</sub></b>	Concentration of diffusants in grain from dislocation diffusion
<b>&lt;c&gt;</b>	Mean concentration
<b>D</b>	Diffusivity
<b><math>\bar{D}</math></b>	Effective diffusivity
<b><math>\bar{D}'</math></b>	Effective diffusivity after magnetization
<b>D<sub>d</sub></b>	Diffusivity of dislocation
<b>D'<sub>d</sub></b>	Diffusivity of dislocation after magnetization
<b>D<sub>e</sub></b>	Diffusivity coefficient independent of temperature
<b>D<sub>g</sub></b>	Diffusivity of grain
<b>D'<sub>g</sub></b>	Diffusivity of grain after magnetization
<b>d</b>	Dislocation density
<b>d<sub>c</sub></b>	Distance from motor axis to calibration load
<b>d<sub>m</sub></b>	Distance from motor axis to reaction force W <sub>r</sub>

<b>dl</b>	Line element of dislocation
<b>ds</b>	Surface element
<b>E</b>	Young's modulus
<b>E<sub>γ</sub></b>	Energy required to move dislocation from one site to next site
<b>e</b>	Efficiency of wear testing system
<b>erfc</b>	Complementary error function
<b>F</b>	Reaction force on the rotor
<b>F<sub>f</sub></b>	Friction force
<b>f</b>	Friction coefficient
<b><math>\bar{f}</math></b>	Area ratio for dislocation to grain
<b>G</b>	Shear modulus
<b>H</b>	Applied magnetic field
<b>H<sub>0</sub></b>	Demagnetized field of the specimen
<b>H<sub>n</sub></b>	Actually magnetic field acting on the magnetized body
<b>H<sub>c</sub></b>	Coercivity
<b>H<sub>z</sub></b>	Hertz
<b>I</b>	Intensity of magnetization
<b>I<sub>d</sub></b>	Magnetic moment of a dislocation
<b>I<sub>r</sub></b>	Remanance
<b>I<sub>s</sub></b>	Spontaneous magnetization; induced intensity of magnetization
<b>J</b>	Exchange integral
<b>kn</b>	Knoop microhardness
<b>k<sub>n</sub></b>	Constant for anisotropy energy
<b>l</b>	Dislocation length
<b>l<sub>t</sub></b>	Distance which dislocation travel
<b>M</b>	Amount of diffusant at t=0 for instance source
<b>M<sub>f</sub></b>	Friction moment

$M_m$	Moment of motor's stator
$N$	Speed of rotor
$N_r$	Speed of roller
$P$	Pressure
$P_f$	Power generated by friction force at load and slide contact area
$P_t$	Total power spend to compensate the loss in the system
$p^w$	Force exerted on domain wall by dislocation
$Q_a$	Activation energy
$R$	Gas constant
$r$	Radial coordinate
$r_R$	Radius of rotor
$r_r$	Radius of roller
$r_l$	Radial distance from dislocation
$S$	Total spin momentum per atom
$T$	Temperature
$T_c$	Curie temperature
$T_N$	Ne'el temperature
$t$	Time
$V$	Voltage
$W$	Normal load
$W_{ex}$	Exchange energy
$W_K$	Anisotropy energy
$W_r$	Reaction force on roller
$W_c$	Calibration load
$W_\lambda$	Magnetoelastic energy
$W_\gamma$	Domain wall energy
$W_m$	Magnetostatic energy

$\alpha$	$= \frac{a}{\sqrt{D_g t}}$
$\alpha_1, \alpha_2, \alpha_3$	Direction cosines of intrinsic magnetization relative to crystal axes
$\beta$	$= (\Delta - 1) \alpha$
$\beta_s$	Structure factor for dislocation
$\sigma$	Stress
$\sigma^M$	A tensor of stress
$\tau$	Shear stress
$\nu$	Poisson ratio
$\epsilon$	$\text{Fe}_{2,3}\text{N}$
$\gamma'$	$\text{Fe}_4\text{N}$
$\mu$	Permeability
$\mu_0$	Permeability of vacuum
$\bar{\mu}$	Relative permeability
$\chi$	Magnetic susceptibility
$\bar{\chi}$	Relative susceptibility
$\gamma_i$	Direction cosines of the stress related to crystal axes; $i=1, 2, 3$
$\lambda_{100}, \lambda_{111}$	Magnetostrictions along [100] and [111] directions
$\lambda_{si}$	Saturated magnetostriction
$\bar{\theta}$	Angle between the magnetization vector and easy direction
$\bar{\phi}_{ij}$	Angle between the directions of the spin vectors of atom $i$ and $j$
$\Delta$	$= D_d / D_g$
$\nabla^2$	Laplacian operator

# CHAPTER 1

## INTRODUCTION

Surface modification technologies for the purpose of improving performance of machine components have been practiced since the beginning of civilization. It has been only in the past few decades that attention has been paid to the scientific and engineering aspects of surface modification. It is due to more and more engineers and designers realizing that the significantly improved performance can be achieved by applying modification techniques to the surface of machine components.

Among the advanced surface modification techniques, plasma ion nitriding (PIN) treatment is a currently established and extensively used surface treatment process in the industry. This process changes the surface of material into nitrogen-containing compound layers and a nitrogen diffusion zone. The main feature of this process is that a low-friction surface can be obtained by forming the compound layers.

Magnetic treatment is a treatment which uses a pulsed magnetic field to modify the properties of the metals non-thermally. This treatment was not brought to commercial application until recently but has been reported to be effective in increasing tool life. It is characterized by relieving the internal stresses of materials.

Although both mentioned treatments have their advantages, there are still some concerns and unknowns for both processes. Because of wide applications of the PIN process, the demands and requirements of the nitrided components are becoming critical. The residual stresses, layer formation, and interface-bonding of nitrided materials are concerned in PIN treatment. For magnetic treatment, the mechanism which is responsible for observed improvement in tool life is still not known.

During this study, a new surface treatment process, magneto-plasma ion nitriding treatment, was introduced and developed. This treatment process is the combination of the above-mentioned treatments: plasma ion nitriding and magnetic treatment. To help



understand the efficiency of the newly developed surface treatment process, the deposited layers on the surface were investigated.

## CHAPTER 2

### BACKGROUND

#### 2.1 Surface Engineering

Surface engineering is a new term that has come into use in the last decade. It includes multidiscipline activities which concentrate on the properties of functional surfaces of machine components to improve their durability, fatigue, wear, and corrosion resistance. Surface engineering is a broad field which involves physics, chemistry, metallurgy, mechanics, and manufacturing background. These background can be involved in the work which finds the coatings to protect surfaces from damage during operation, or finds the ways to alter the properties of surfaces.

In order to meet the requirements for better functional surfaces, various techniques have been developed to improve surface and near-surface properties. Among these techniques, the plasma-assisted surface treatment process is one of the most promising processes in today's surface engineering. The plasma-assisted process offers great flexibility to produce surfaces with desired properties. According to the energy required in the plasma-assisted process, the process can be classified into three categories.[1] They are plasma coatings, plasma beam technology and plasma thermochemical processes, Figure 2.1.

Plasma coating is a thin film or coating growth process which involves the deposition in a vacuum environment of physically generated atoms or molecules onto a substrate. There are two main techniques for applying plasma coating processes: sputtering and ion plating.[2] Sputtering is a process by which highly energetic ions or neutral atoms strike the surface of a solid substrate causing ejection of one or more atoms or molecules by the momentum transfer.[3] Because of the nature of sputtering, this process can coat compounds and alloys, and deposit nonconductive materials on nonconductive or conductive materials. Cleaning surfaces by sputtering also enhances

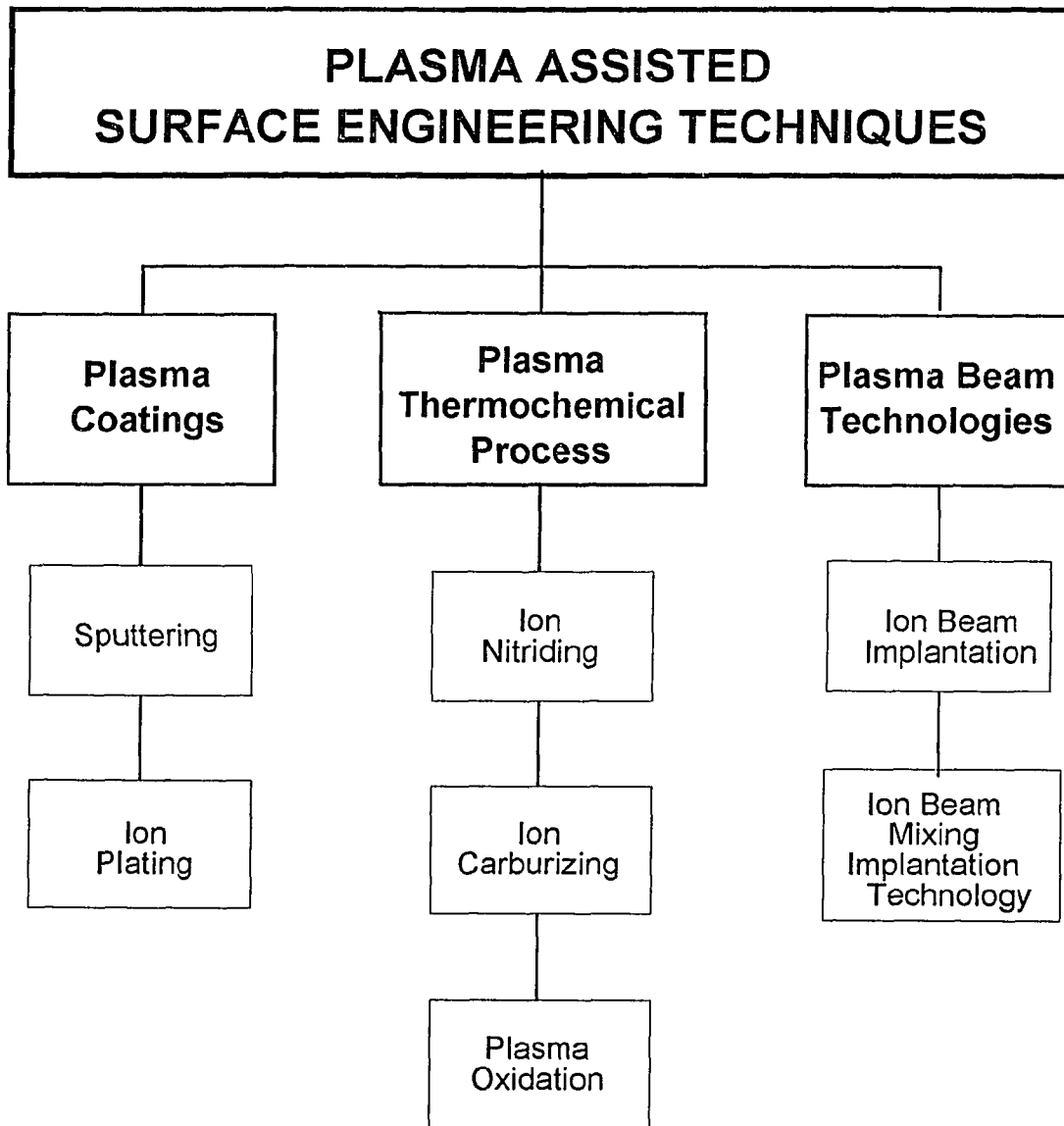


**Figure 2.1** Plasma assisted surface modification techniques.

coating bonds. Ion plating is a process which can deposit highly adherent metal, alloy, and ceramic coatings onto virtually any substrate at relatively low temperature.[4] This process provides a better coating bond, better coverage, and higher deposit rate than sputtering. However, both techniques have to be concerned with the substrate heating and complex process control problems. The mechanical properties of thin films or coating, such as tensile, compressive, and fatigue strength, are poor.

The plasma beam technique is a process which consists of bombarding the surface of a material in a vacuum chamber by an electrostatically accelerated ion beam.[5] When ions embed in the surface and come to rest, they dissipate their kinetic energy in displacing target atoms (ions) from their normal lattice sites and by ionizing target atoms. The nature of the process allows one to introduce any element into the near-surface region of any solid without equilibrium constraints. Since the process is nonequilibrium in nature, it can attain compositions and structures which conventional methods can not produce. Ion implantation is a typical technique of this process. Ion-beam mixing implantation is a variation process from the ion implantation process. It attempts to use the deposit energy to enhance the interface region between the film and the substrate. There are two undesirable effects of plasma beam techniques. One is sputtering, and the other is the heating of the substrate. Sputtering is undesirable because it removes the implanted surface itself. Like the plasma coating process, this process needs a cooling system to prevent substrate heating. High energy consumption and expensive facilities of the plasma beam technology are two reasons that this process is seldom used in industry.

Plasma thermochemical treatment is a plasma-activated thermochemical process.[6] It involves the formation of compound layers and diffusion of interstitial elements to the substrate material at elevated temperature. The most common plasma thermochemical treatments involve the introduction of nitrogen and/or carbon into ferrous substrates using processes such as ion nitriding, ion carbonitriding, or ion carbonitriding. The term "plasma thermochemical treatment" is used to describe treatments which are carried out in the presence of a glow discharge. A glow discharge system operates in a vacuum where the workpiece constitutes the cathode and the chamber wall is the anode. The introduction of a gas into the vacuum chamber at a given pressure, and applying voltage across the chamber create the glow discharge. The term glow discharge is due to the luminous appearance of a bright-glow region which results from low energy collisions of electrons with gas molecules. These processes can produce a high level surface cleaning,

a uniform surface treatment and an increased surface reaction rate. This process has lower energy consumption than plasma ion beam treatment and has stronger bonding between the interface of the coating than the plasma coating process. A more important factor is that this process is a distortion free process. It also means that there is no substrate heating problem. That is the main reason that the plasma thermochemical process is popular and accepted in today's surface engineering.

Plasma ion carburizing is a high temperature treatment which increases the surface hardness of low alloy steels. By introducing carbon, followed by a rapid cooling operation, this process can produce a hard martensitic surface layer. This also generates compressive residual stresses in the case. Fatigue and wear property improvements are thus obtained. It is applied where a deep case is required and some distortion can be tolerated. Except for the use of different gas species, the differences between ion carburizing and ion nitriding are that plasma ion nitriding is a low temperature treatment and can be applied to general ferrous materials. Most significant in this process is that low-friction surfaces are formed by the nitride compounds. Ion nitriding process are now gaining more and more attention and popularity in industry. Although the carbonitriding process uses both nitrogen and carbon as gas species, this process still has more limitations than the ion nitriding process.

## **2.2 Role of Plasma Ion Nitriding In Surface Engineering**

### **2.2.1 Nitriding and Plasma Ion Nitriding (PIN)**

Conventional nitriding processes commonly used are gas nitriding and salt-bath nitriding.[7] Both techniques require that the container be filled with the nitriding agent ammonia,  $\text{NH}_3$ , and parts to be treated are immersed into the container. The ammonia gas dissociates to nitrogen and hydrogen when it contacts heated parts at a temperature range of about  $900^\circ - 1100^\circ \text{ F}$  ( $480^\circ$  to  $590^\circ \text{ C}$ ). To ensure dissociated nitrogen stays in the container, a perfectly sealed container is required.

Salt-bath nitriding is performed in baths preheated to the temperature range of about 950° to 1150°F (510° to 620°C). The bath consists of a mixture of sodium cyanide (NaCN), sodium cyanate (NaCNO), potassium cyanide (KCN), and some other salts. The active nitriding agent is the cyanate,  $CNO^-$

There are economic and pollution considerations for both gas and salt-bath nitriding. Both techniques need large amounts of nitriding agents to fill the containers. Gas nitriding has part-size and time-consuming limitations. The salt-bath nitriding process has environmental problems in handling and disposal of the cyanate and bath solutions. Because the efficiency and environmental concerns have become more and more important, the conventional nitriding processes are being replaced by the advanced plasma ion nitriding technique.

Plasma ion nitriding (PIN) is a plasma-assisted ion-treatment process. This process became popular in industry in the mid 80's. Employing advances in electronic power components and vacuum technique, the plasma ion nitriding process has overcome the traditional nitriding problems. It does not require the use of ammonia or toxic nitriding agents. It only uses a small amount of process gases. PIN can be carried out over a wider range of temperature. It has become an accepted alternative to the nitriding process.

Plasma ion nitriding is now extensively applied in various fields of manufacturing and machining industries. In Table 2.1, some fields of industrial application are shown as examples. The acceptance of this technique is increasing in many other fields of manufacturing.

**Table 2.1** Industrial application of plasma ion nitriding process.

<p><b>1. General Machinery</b></p> <ul style="list-style-type: none"> <li>Pump and Compressor Parts               <ul style="list-style-type: none"> <li>- Pump Casing</li> <li>- Pump Torcholdes</li> <li>- Feed Screw and Piston</li> </ul> </li>   <li>Gearing               <ul style="list-style-type: none"> <li>- Synchronizer Gear</li> <li>- Differential Gear</li> <li>- Worm Gear</li> <li>- Rack</li> <li>- Pinion</li> <li>- Auger</li> <li>- Shift Fork</li> </ul> </li>   <li>Plastic Moulding and Manufacturing Machine               <ul style="list-style-type: none"> <li>- Screw for Die Casting Machine</li> <li>- Cylinder for Die Casting Machine</li> <li>- Head Plate for Double Screw Cylinder</li> <li>- Die Cast Form</li> <li>- Injector Plate</li> <li>- Torque Lever Bolt</li> <li>- Die Guide</li> </ul> </li> </ul>	<p><b>4. Rolling</b></p> <ul style="list-style-type: none"> <li>- Roll</li> <li>- Drive Shaft</li> <li>- Spline Shaft</li> </ul> <p><b>5. Hydraulic Machine</b></p> <ul style="list-style-type: none"> <li>- Piston</li> <li>- Rod</li> <li>- Cylinder</li> </ul> <p><b>6. Die Casting Machine</b></p> <ul style="list-style-type: none"> <li>- Die</li> <li>- Rod</li> <li>- Cylinder</li> </ul> <p><b>7. Tools for Cold Work</b></p> <ul style="list-style-type: none"> <li>- Mandrel and Drawing Tool</li> <li>- Sheet Forming Forge</li> <li>- Press Punch</li> </ul> <p><b>8. Tools for Hot Working/Forge</b></p> <ul style="list-style-type: none"> <li>- Forging Dies</li> <li>- Connecting Rod</li> <li>- Tools for Pressure Die Casing</li> <li>- Tools for Continuous Casting</li> </ul>
<p><b>2. Machine Tool</b></p> <ul style="list-style-type: none"> <li>- Punch</li> <li>- Twist Drill</li> <li>- Rimer</li> <li>- Threading Machine</li> <li>- Milling Cutter</li> <li>- Hob</li> <li>- Rack</li> <li>- Pinion</li> <li>- Main Shaft</li> </ul>	<p><b>9. Engine/Automotive Industry</b></p> <ul style="list-style-type: none"> <li>- Intermediate Plate for Rotary Engine</li> <li>- Slide Housing</li> <li>- Crank Shaft</li> <li>- Cam Shaft</li> <li>- Valve Shaft</li> <li>- Cam Disc, Tappet</li> <li>- Diesel Motor Cylinder</li> <li>- Clutch for Railway Wagon</li> </ul>
<p><b>3. Tools</b></p> <ul style="list-style-type: none"> <li>- Die</li> <li>- Punch</li> <li>- Cutting Tool</li> </ul>	<p><b>10. Precision Instruments</b></p> <ul style="list-style-type: none"> <li>- Ball Pens</li> <li>- Inner Surface of the Bearing for Precision Instrument</li> </ul>

## 2.2.2 Plasma Ion Nitriding Process

**2.2.2.1 Plasma Ion Nitriding System :** The basic plasma ion nitriding system is shown in Figure 2.2. The system consists of plasma ion nitriding furnaces - (1), gas distribution unit - (2), power unit - (3), electrical control unit - (4), vacuum system - (5).[8]

The components to be ion nitrided are placed on a support structure - (6) inside the furnace. The furnace is a double-walled, water-cooled vacuum chamber. Vacuum and gas supply systems enable the furnace to be evacuated to the required vacuum and be filled with the appropriate treatment gas.

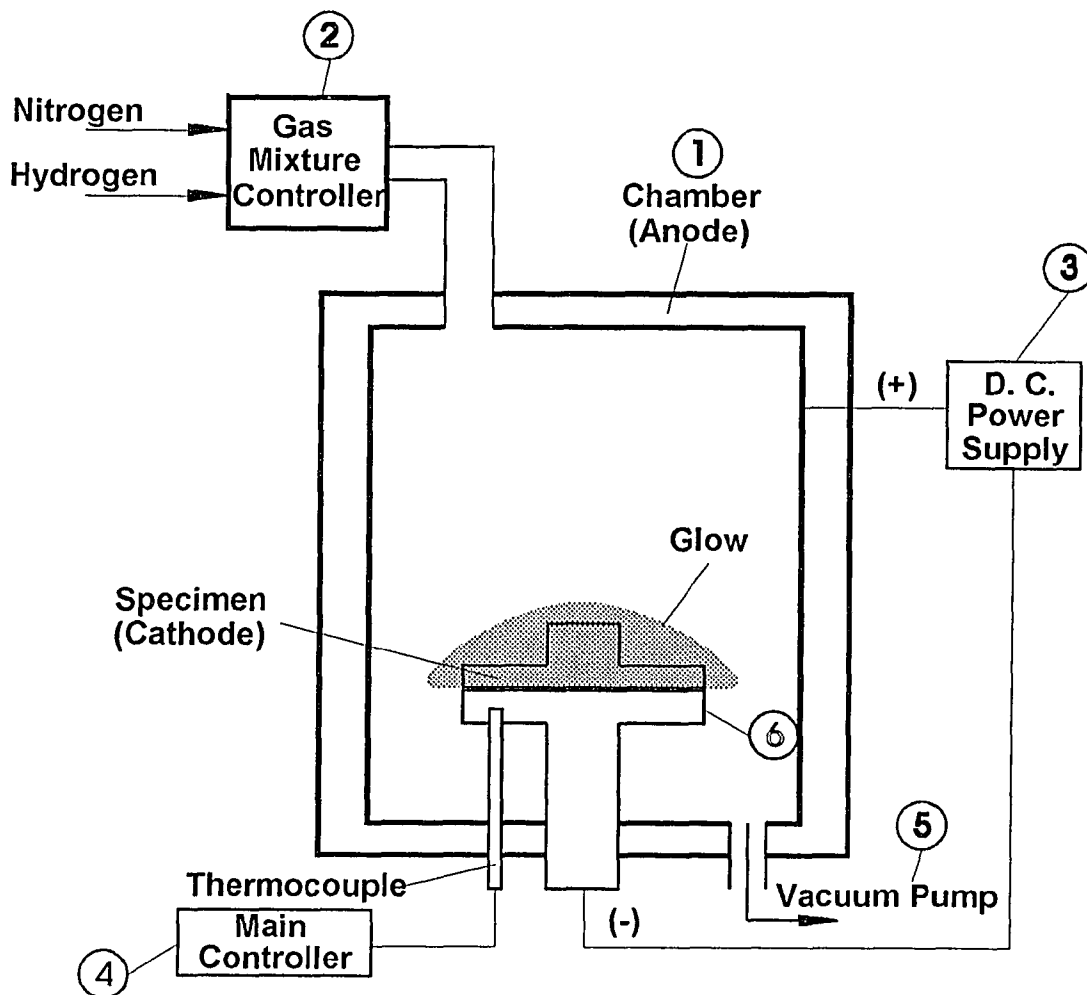


Figure 2.2 Plasma ion nitriding system.



The support plate is connected to a high current ( $> 40\text{A}$ ), high voltage ( $<1000\text{V}$ ), dc-pulsed power supply. The support plate is held at a negative potential (cathode) and the vacuum chamber acts as the positively charged anode. When voltage is applied under proper gas pressure conditions, a glow discharge is produced. The glow discharge is simply an electric current passing through an ionized gas mixture and behaves as a function of applied voltage.

When the chamber is in operation, the space between the wall of the nitriding chamber and the work piece is filled with a gas mixture selected for the process. Glow discharge occurs when the gas molecules are ionized by colliding with electrons. The electrons travel from the work piece (cathode) to the chamber wall (anode) under the influence of the applied electrical voltage. Ionization of the partial pressure gas mixture permits a sustained electrical current, i.e., a negative electron flow from the work piece to the chamber wall, and a positive ion flow from the ionized gas mixture to the work surface being treated.

Energy is dissipated while gas ions strike the surfaces of components. The energy appears as heat and acts to heat the components mounted to the cathode. The nitrogen ions which are near the cathode will then be thermally diffused into the surface of the components. Auxiliary heaters are often used to provide an additional heat source to minimize cycle times and provide better temperature uniformity on the surfaces of the components. Thermocouples are used to sense component temperature and provide accurate process control.

In order to provide a uniform ion nitrided case layer, an electrical control unit is essential in the plasma ion nitriding process. The electric field uniformity at the surfaces of the parts being nitrided is determined by the geometry of the surface. Electric flux concentrations will be different on flat surfaces, edges, borders, and holes. Adjustments in gas pressures, operating voltage, and current densities during the ion nitriding cycle can guarantee uniform nitrided case layer characteristics.

**2.2.2.2 Plasma Nitriding Mechanism :** Because of the complexity of the PIN process compared to conventional surface heat treatment, it is difficult to present a unique picture of the mechanism of PIN. A number of models have been proposed of what occurs at the plasma-surface interface and in bulk material during plasma nitriding. According to Tibbets[9], the adsorption of neutral atoms, not of ions on the metal surface, is the primary nitriding mechanism. Other authors[10] suggest that a "back-sputtering" process is responsible for nitriding. Bell[11] had reported that in order to produce good nitride case-depths, sufficient hydrogen and nitriding gas mixtures are essential. Hudis[12] concluded his work that  $\text{NH}^+$  and /or  $\text{NH}_2^+$  molecular ion species are primarily responsible for nitriding, and no nitriding occurs unless  $\text{H}_2$  is present. Xu and Zhang[13] claimed that in plasma ion nitriding the migration of nitrogen atoms from the gas phase to a solid surface is realized mainly through the penetration into the work-piece of active nitrogen atoms produced by collision dissociation. Positive ions of high energy dissociate  $\text{N}_2$  or  $\text{NH}_3$  to produce active N atoms by inelastic collision.

To summarize those proposed mechanisms, we can derive some basic contributing factors in the PIN process :

- (1). Sputtering
- (2). Ion-excited atom implantation
- (3). Adsorption
- (4). Condensation/deposition

In Figure 2.3 a suggested surface reaction during PIN is given. The detailed description is as follows:

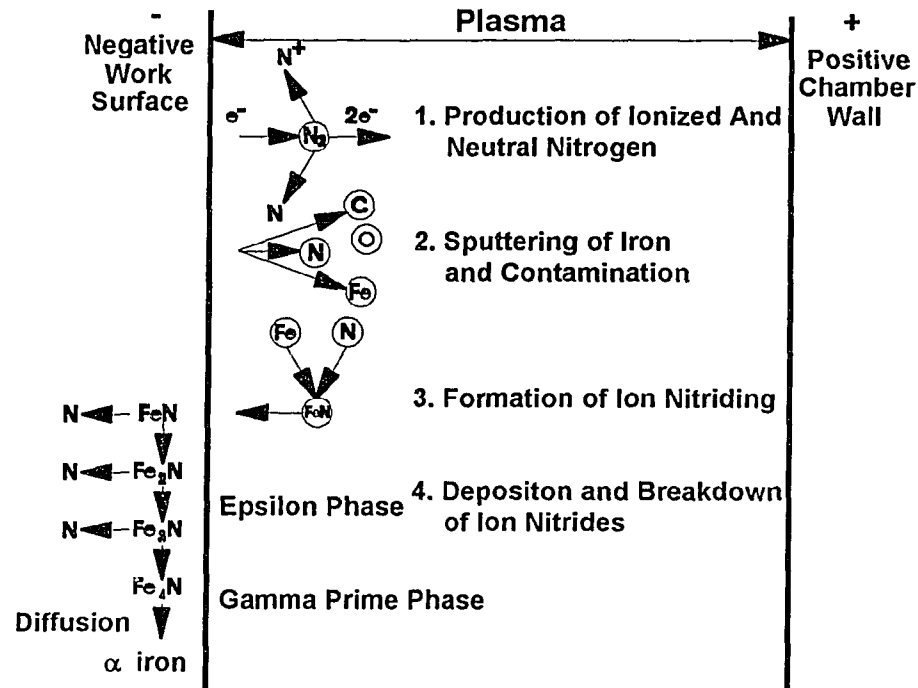
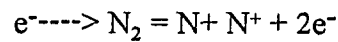
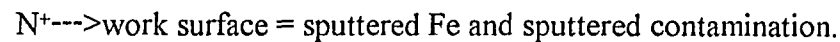


Figure 2.3 Surface reaction during PIN process.

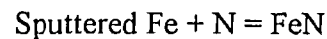
- (1). Production of ionized and neutral nitrogen atoms by energetic electrons



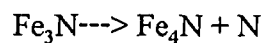
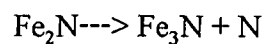
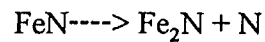
- (2). Sputtering of Fe and contaminants from the work surface by these ionized nitrogen atoms.



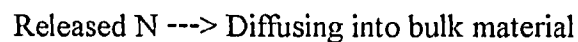
- (3). Formation of iron nitrides by the sputtered iron atoms and neutral nitrogen atoms.



- (4). Deposition and breakdown of FeN on the work surface.



- (5). Diffusion of nitrogen atoms into bulk materials.



After this series of surface reactions, we get a nitrided surface. Possible surface layers formed are given in Figure 2.4 . They are  $\epsilon$  ( $\text{Fe}_{2,3}\text{N}$ ) layer,  $\gamma'$  ( $\text{Fe}_4\text{N}$ ) layer , and a diffusion zone. The outer layer is  $\epsilon$  ( $\text{Fe}_{2,3}\text{N}$ ) layer, then the  $\gamma'$  ( $\text{Fe}_4\text{N}$ ) layer, and the deepest layer is a diffusion zone.

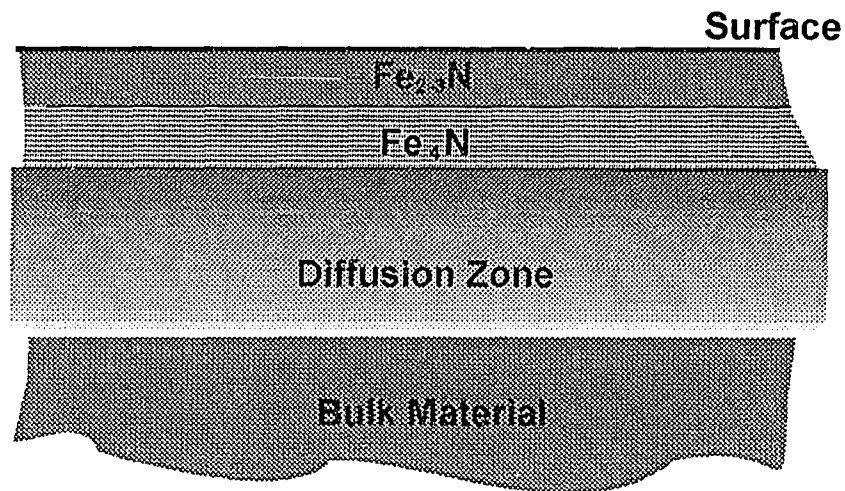


**Figure 2.4** Nitrided layers.

**2.2.2.3 Plasma Ion Nitriding Phase Diagram :** For ferrous materials, the compound layers are composed of nitrides and the diffusion zone. The nitrides are mainly  $\gamma'$  phase ( $\text{Fe}_4\text{N}$ ) and  $\epsilon$  phase ( $\text{Fe}_{2,3}\text{N}$ ).

The compound layer can vary from a  $\gamma'$  only layer,  $\gamma'+\epsilon$  layers, and an  $\epsilon$  only layer. The specific layer or layer thickness can be achieved by adjusting the plasma nitriding process parameters according to the iron-nitrogen phase diagram, Figure 2.5.[14]

In the phase diagram,  $\text{Fe}_4\text{N}(\gamma')$  mono-phase occurs between 5.6-6.0% weight nitrogen concentration and the temperature range of  $400^\circ\text{-}700^\circ\text{C}$ . The  $\gamma'$  is a face centered cubic structure and is very stable. Higher nitrogen concentration and temperatures of  $450^\circ\text{-}700^\circ\text{C}$  lead to the  $\epsilon\text{-}\gamma'$  multi-phase. The  $\epsilon$  phase ( $\text{Fe}_{2,3}\text{N}$ ) appears after the nitrogen concentration is over 6%. The main nitrogen concentration range to produce  $\epsilon$  phase only is 8 to 12 weight percent and the temperature range is  $400^\circ\text{-}800^\circ\text{C}$ .

The  $\epsilon$  phase is a hexagonal close-packed structure. Iron atoms occupy a hexagonal close-packed structure, while nitrogen atoms are in its octahedral interstices. If the nitrogen concentration is lower than 5.5 percent and the temperature is  $400^{\circ}\text{C}$ - $600^{\circ}\text{C}$ , a ferrite-nitrogen solid solution is obtained.

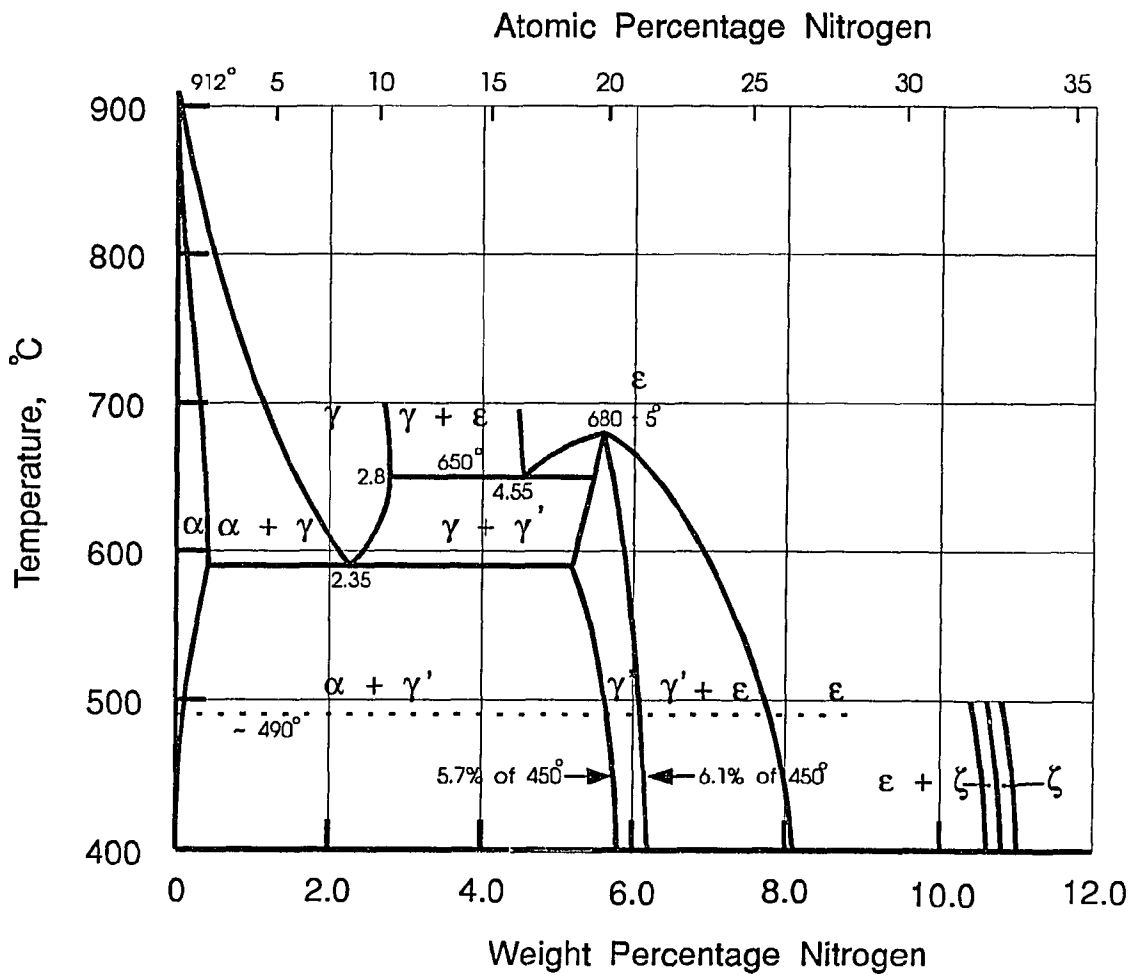


Figure 2.5 Fe - N phase diagram.[14]

### 2.2.3 Advantages and Disadvantages

The advantages of the plasma ion nitriding process over conventional surface heat treatment techniques are as follows:

- Controllable microstructure and properties of nitride layers.

Specific microstructure and properties can be produced to meet the demands of industry. The ratio between compound layers and diffusion zone thickness can be varied by controlling process parameters. Many results show that the process is controllable.[15, 16]

- Low treatment temperature.

The treatment temperature depends on diffusivity of the elements within the substrate which is governed by the diffusion law. It also relies on the supply of the diffusible elements to the solid surface.

In contrast to gaseous thermochemical processing, it is possible to create a large number of charged particles and excited, energetic neutral species at low temperatures, thus allowing the plasma ion nitriding to occur at relatively low temperature.[17]

- Reduced treatment time.

The treatment time can be reduced by the rapid saturation of the surface with diffusible elements. This is again due to the increased number of ions and energetic atoms in the plasma, while the molecules in a gaseous environment are only capable of dissociating at the metal surface.

Sputtering of the surface also enhances the plasma ion nitriding process. A clean surface is generated by sputtering. This reduces the retarding effect of oxide layers on the diffusion kinetics. Also sputtering induces a high-density defect concentration on the surface and leads to an accelerated diffusion of the elements.[18]

The enhancement of the overall mass transfer and accelerated diffusion into the substrate are responsible for the reduced treatment time for the plasma ion nitriding process compared to the conventional surface heat treatment process.

- Less energy and gas consumption.

The energy consumption can be reduced due to the enhanced mass transfer and accelerated diffusion. The reduction of energy consumption can be achieved by employing modern heating units.

The gas consumption ( $N_2$ ,  $NH_3$ ) for the PIN process is much less than for conventional surface heat treatment.

- Less environmental problems.

For the PIN process, no toxic products or fumes are produced. The problems of waste disposal inherent to the salt bath treatment can also be avoided.

While the PIN process has a wide range of technical and economic advantages, there are, nevertheless, some concerns about the PIN process. These include :

- The effect of materials' residual stresses on the nitriding result.
- The formation of residual micro stresses after the PIN process.
- The influence of diffusion rate on interface bonding.
- The difficulty in selecting process control parameters to obtain desired nitrided layers.

## 2.3 Magnetic Behavior of Materials

### 2.3.1 Introduction

Substances which are magnetized, more or less, by a magnetic field are called magnetic substances. There are various kinds of magnetism, and each is characterized by its own magnetic structure.

The magnetic moment of a magnetic substance is called the intensity of magnetization and is denoted by the vector  $I$ . [19] The magnetic induction or magnetic

flux density  $B$  is also commonly used in engineering applications to describe the magnetization. The relationship between  $B$  and  $I$  is given by the following equation:

$$B = I + \mu_0 H \quad (2.1)$$

where  $H$  is applied magnetic field; and  $\mu_0$  is the permeability of vacuum.

The relation between the intensity of magnetization  $I$  and the magnetic field  $H$  can be expressed by

$$I = \chi H \quad (2.2)$$

where  $\chi$  is the magnetic susceptibility. The unit of  $\chi$  is the same as  $\mu_0$ ; hence it is possible to measure  $\chi$  in units of  $\mu_0$ . The susceptibility thus measured is called a relative susceptibility and is usually denoted by  $\bar{\chi}$ , which is

$$\bar{\chi} = \chi / \mu_0 \quad (2.3)$$

Substituting for  $I$  of Equation (2.2) the expression Equation (2.1), we have

$$B = (\chi + \mu_0)H = \mu H \quad (2.4)$$

where  $\mu$  is the permeability. Usually we use a relative permeability, which is

$$\bar{\mu} = \frac{\mu}{\mu_0} = \bar{\chi} + 1 \quad (2.5)$$

The observed value of relative susceptibility ranges from  $10^{-5}$  for very weak magnetism to  $10^6$  for very strong magnetism. In some cases it has a negative value. Because  $\bar{\chi}$  depends on the intensity of the magnetic field, it is normally used to represent different magnetic structures of the material.

### 2.3.2 Kinds of Magnetism

From this point of view, we can classify the various kinds of magnetism as follows:

Diamagnetism

Paramagnetism

Ferromagnetism

Antiferromagnetism



### Ferrimagnetism

There are two atomic origins of magnetism which lead to the magnetization of magnetic substances. They are orbital motion and spin of electrons. An atom which has a magnetic moment caused by spin, by orbital motion of electrons or by both is generally called a magnetic atom.[20]

### Diamagnetism

Diamagnetism is a weak magnetism in which a magnetization is exhibited opposite to the direction of the applied field. Figure 2.6 The susceptibility is negative and the order of magnitude of  $\bar{\chi}$  is about  $10^{-5}$ . The origin of this magnetism is an orbital rotation of electrons about the nuclei induced by the application of an external field. This magnetism is so weak that the diamagnetic substances are used as a magnetic insulator. Diamagnetic elements include copper, silver, gold, rare gases, and other compounds.

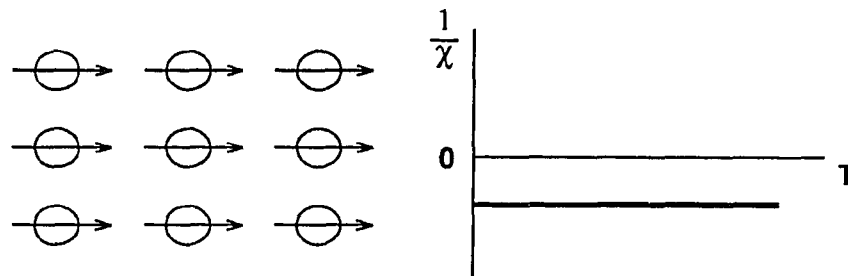


Figure 2.6 Diamagnetism.

### Paramagnetism

In paramagnetism, the magnetism  $I$  is proportional to the magnetic field  $H$ . Figure 2.7 The order of magnitude of  $\bar{\chi}$  is  $10^{-3}$  to  $10^{-5}$ . In most cases, paramagnetic substances contain magnetic atoms or ions whose spins are isolated from their magnetic environment. At finite temperatures, the spins are thermally agitated and take random orientations. Upon application of a magnetic field, the average orientations of the spins are slightly changed so as to produce a weak induced magnetization parallel to the applied magnetic field. The susceptibility in this case is inversely proportional to the temperature.

Paramagnetic materials include salts of transition elements, salts and oxides of rare-earth elements, and some metals.

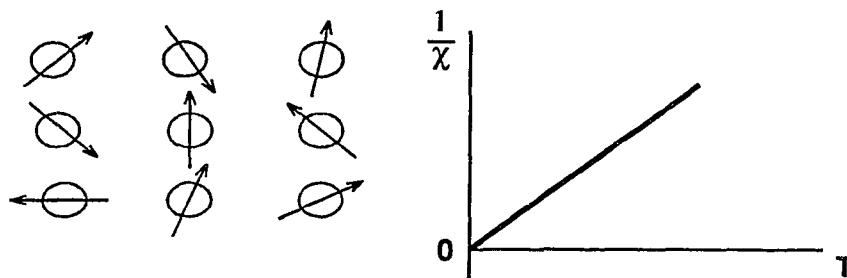


Figure 2.7 Paramagnetism.

### Antiferromagnetism

Antiferromagnetism is a weak magnetism which is similar to paramagnetism in the sense of exhibiting a small positive susceptibility. The susceptibility of this magnetism is temperature dependent as can be seen from the  $\chi - T$  curve in Figure 2.8. Below the temperature  $T_N$ , Ne'el temperature, an antiparallel spin arrangement is established in which positive and negative magnetic moments completely cancel each other. In such an arrangement the tendency to be magnetized by the external field is opposed by a strong negative interaction acting between positive and negative moments. So the susceptibility decreases with a decrease in temperature, which is contrary to the usual paramagnetic behavior. When temperature is above the Ne'el point, the magnetic moment arrangement becomes random. The susceptibility now decreases with an increase of temperature.

Antiferromagnetic substances include manganese, chrome alloys, and  $\text{Cr}_2\text{O}_3$ .

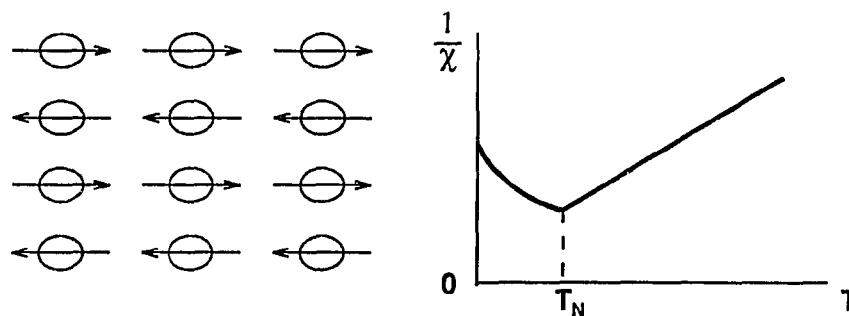


Figure 2.8 Antiferromagnetism.

### Ferrimagnetism

Ferrimagnetism is the term proposed by Ne'el to describe the magnetism of oxidic ferrites, like  $\text{Fe}_3\text{O}_4$ ,  $\text{NiFe}_2\text{O}_4$ ,  $\text{MnFe}_2\text{O}_4$ . In these substances, there are two kinds of atoms involved. The directions of the magnetic moments are opposite to each other. Since the number of magnetic atoms and the magnitude of moments of individual atoms are different, such an ordered arrangement of moments gives rise to a resultant magnetization. This kind of magnetization is called spontaneous magnetization.

As the temperature increases, the arrangement of the moments is disturbed by thermal agitation, which is accompanied by a decrease of spontaneous magnetization.

At the Curie Temperature,  $T_C$ , the arrangement of the moments becomes completely random, and the spontaneous magnetization vanishes. The temperature dependence for this magnetism is shown in Figure 2.9. Above the Curie point, the substance exhibits paramagnetism. The susceptibility decreases with increase of temperature.

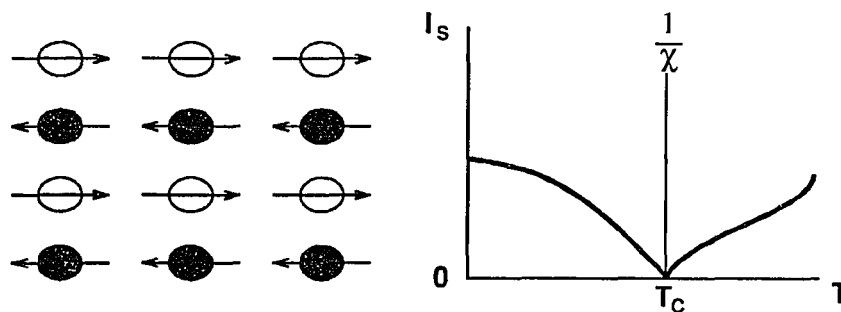


Figure 2.9 Ferrimagnetism.

### Ferromagnetism

In the case of ferromagnetism, the magnetic moments are aligned parallel to one another as a result of a strong positive interaction between the neighboring moments (Figure 2.10). As the temperature increases, the arrangement of the moments is disturbed by thermal agitation. This results in a temperature dependence of spontaneous magnetization. When the temperature reaches the Curie point the substance becomes

paramagnetic and the susceptibility obeys the Curie-Weiss law, which states that  $1/\chi$  rises from zero at the Curie point and increases linearly with temperature.

Ferromagnetism is exhibited mostly by metals and alloys, such as iron, cobalt, nickel, steel, gadolinium, and  $\text{CdCr}_2\text{Se}_4$ .

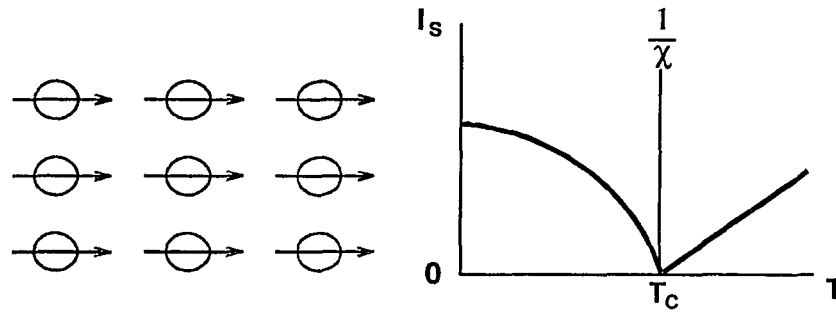


Figure 2.10 Ferromagnetism.

### 2.3.3 Free Energies of Ferromagnetism

In this study, we are more concerned with the magnetic properties of steel and iron, which are ferromagnetic. The magnetic phenomena of ferromagnetic material is of interest in our research because a large amount of materials now can be grouped under the ferromagnetic category.

The basic feature of the magnetic behavior of ferromagnetic materials is described in the above section. Now we will deal with some structure-sensitive properties to help understand the magnetization process.[21]

#### Exchange Energy

It is now believed that all of the magnetic moment of ferromagnetic substances arises from electron spin motion, rather than from orbital motion of the electron around a nucleus, except Gd. There are exchange interactions which occur in a crystal lattice between nearest neighbors, if the spin directions of the neighbors are different. The energy of the exchange interactions is called exchange energy. It can be expressed as

$$W_{\text{ex}} = -2 J S^2 \sum \cos\bar{\phi}_{ij} \quad (2.6)$$

where  $S$  is the total spin momentum per atom,  $\bar{\phi}_{ij}$  is the angle between the directions of the spin vectors of atoms  $i$  and  $j$ , and  $J$  is the exchange integral.

### **Anisotropy Energy**

In ferromagnetic crystals the magnetization is affected by the direction of the applied field relative to the crystal axes. It is found that in some directions the applied field which is required to induce a given magnetization is smaller than other directions. These directions are called directions of easy magnetization. The directions along which it is most difficult to magnetize the crystal are hard directions. More energy is required to magnetize a crystal to saturation in a hard direction than in an easy direction. The excess energy required in the hard direction is the anisotropy energy.

The anisotropy energy can be represented by a series expansion of the form

$$W_k = \sum_n k_n \sin^{2n} \bar{\theta} \quad (2.7)$$

where  $k_n$  are constants which are independent of  $\bar{\theta}$ , and  $\bar{\theta}$  is the angle between the magnetization vector and easy direction.

### **Magnetostriction and Magnetoelastic Energy**

Magnetostriction is the deformation that accompanies a change in the magnetization of a crystal. It occurs because the total free energy of the crystal depends upon its state of strain and the crystal therefore spontaneously deforms in order to minimize this energy. The magnetoelastic energy is part of the crystal energy and arises from the interaction between the magnetization and the strain of the lattice. Magnetoelastic energy is defined to be zero for an unstrained lattice.

The crystal anisotropy energy and exchange energy are found to depend on the atomic spacing of the structure. Any change in the atomic spacing gives rise to a further energy contribution to the free energy of a magnetic crystal. Anything involving interaction between the magnetization and the state of strain of the lattice are known as the magnetostrictive effects.

A ferromagnetic crystal generally changes its dimensions and creates strain in the crystal when a magnetic field is applied.

Considering the energy term, we may expect that if a magnetic crystal is strained by an external force, this additional strain will alter the direction of the intrinsic magnetization. In this way the preferred directions of domain magnetization may be controlled not only by the magnetocrystalline anisotropy but also by the presence of strained regions within the material. The effect of strain on a crystal then is to change the directions of the anisotropy energy with respect to the lattice.

The magnetoelastic energy of a cubic crystal is in the form of

$$W_{\lambda} = -3/2 \lambda_{100} \sigma (\alpha_1^2 \gamma_1^2 + \alpha_2^2 \gamma_2^2 + \alpha_3^2 \gamma_3^2) - 3 \lambda_{111} \sigma (\alpha_1 \alpha_2 \gamma_1 \gamma_2 + \alpha_2 \alpha_3 \gamma_2 \gamma_3 + \alpha_3 \alpha_1 \gamma_1 \gamma_3) \quad (2.8)$$

where  $\alpha_1, \alpha_2, \alpha_3$  are the direction cosines of intrinsic magnetization relative to the crystal axes, and  $\gamma_1, \gamma_2, \gamma_3$  are the direction cosines of the stress  $\sigma$  relative to the crystal axes.  $\lambda_{100}$  and  $\lambda_{111}$  are the magnetostrictions along the [100] and [111] directions respectively.

### Magnetostatic Energy

If an applied magnetic field  $H$  has an angle  $\theta$  with the induced intensity  $I_s$ , there is a couple equal to  $I_s H_a \sin\theta$  which tends to rotate the magnetization into the field direction. The contribution of the free energy of the system is therefore

$$W_m = -I_s H_a \cos\theta \quad (2.9)$$

where  $H_a$  is the field actually acting on the magnetized body. Because of the effect of the demagnetizing field of the specimen, the field  $H_a$  is considerably different from the applied field  $H$ .

When no external field is applied a magnetized body has a certain magnetostatic energy, equal to

$$W_m = -\frac{1}{2} I_s H_0 \cos\theta \quad (2.10)$$

where  $H_0$  is the demagnetizing field of the specimen itself.

### 2.3.4 Magnetic Domains and Domain Wall Motion

The presence of the ferromagnetic domain structure was first predicted by P. Weiss [22] in 1907. He hypothesized that in a ferromagnetic substance there existed microscopic regions called domains ( $10^{-6}$  to  $10^{-5}$  cm<sup>3</sup>) within which the magnetic moments of all atoms are parallel to each other. In unmagnetized iron, the domains are arranged so that the net magnetic moment of the specimen is zero, as shown in Figure 2.11 .

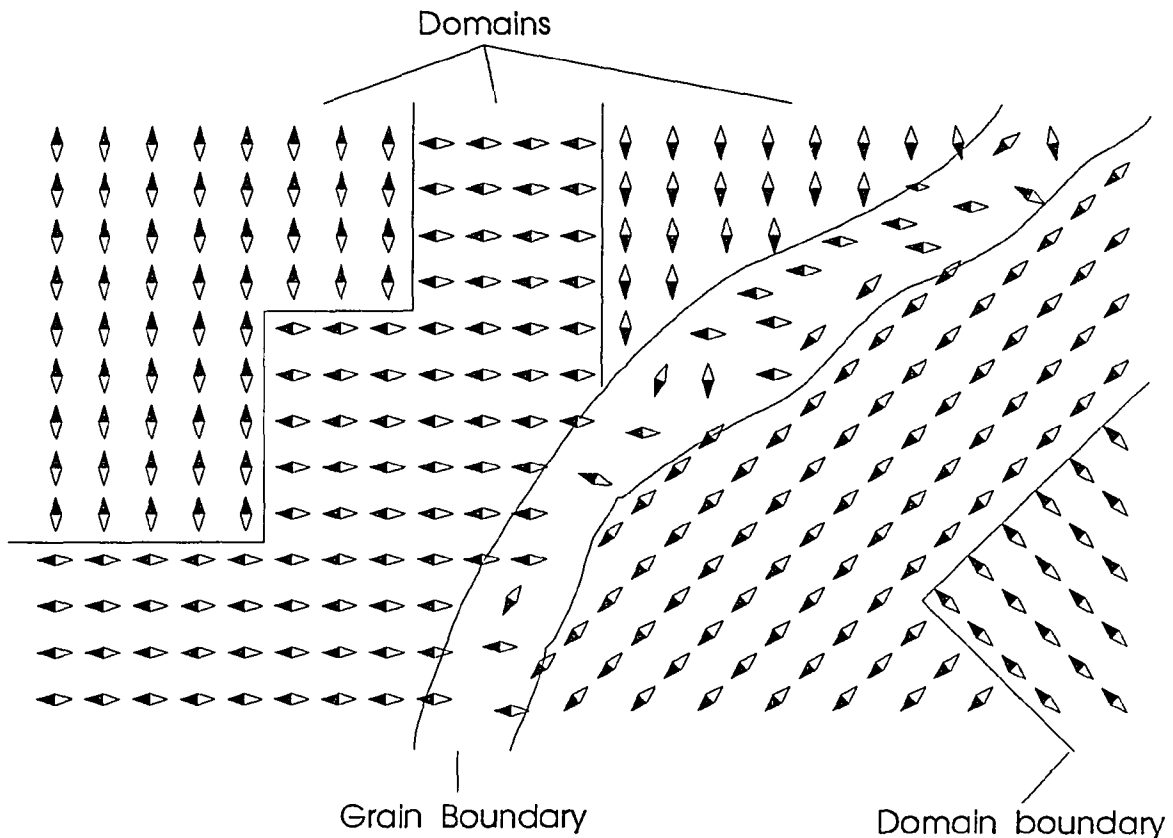


**Figure 2.11** Domain and domain boundary in the material.

In 1932 Bloch [23] showed that the boundary between two domains which are oriented in different directions is not sharp on the atomic scale. The boundary is spread over a certain thickness where the direction of spins changes gradually from one domain

to the next. This layer is usually called a domain wall and sometimes referred to as a Bloch wall. The structure of the domain wall is illustrated in Figure 2.12 (a).

As a magnetic field is applied to a ferromagnetic substance, the domain structure changes in such a way as to increase the favorably oriented domains and decrease the unfavorably oriented domains with respect to the field. This process is usually called magnetization.

The domain walls play an important role in the magnetization. Inside the domain wall the spins rotate gradually from one domain to the next when the external field is applied parallel to the spins of both domains. The spins inside both domains will not experience any torque resulting from the field because the directions of the spins are either parallel or antiparallel to the field. Since the spins inside the wall have some angle with the field direction, they start to rotate toward the field direction under the action of torque. As a result of the rotation of the spins inside the wall, the wall should be displaced as shown in Figure 2.12 (a)-(c). This will result in an increase in the volume of the domain which has the spins in the same direction as the applied field. Once the whole volume of the specimen is in one domain, the material is said to be in a saturation state.

If there are two kinds of domains whose spin directions are closest to the field direction in a specimen, these kinds of domains will increase their volume and finally cover the whole volume of the specimen. If the field is increased further, the spins in each domain will rotate from the easy direction to the field direction. This is called domain rotation. Figure 2.12 (c)-(d)



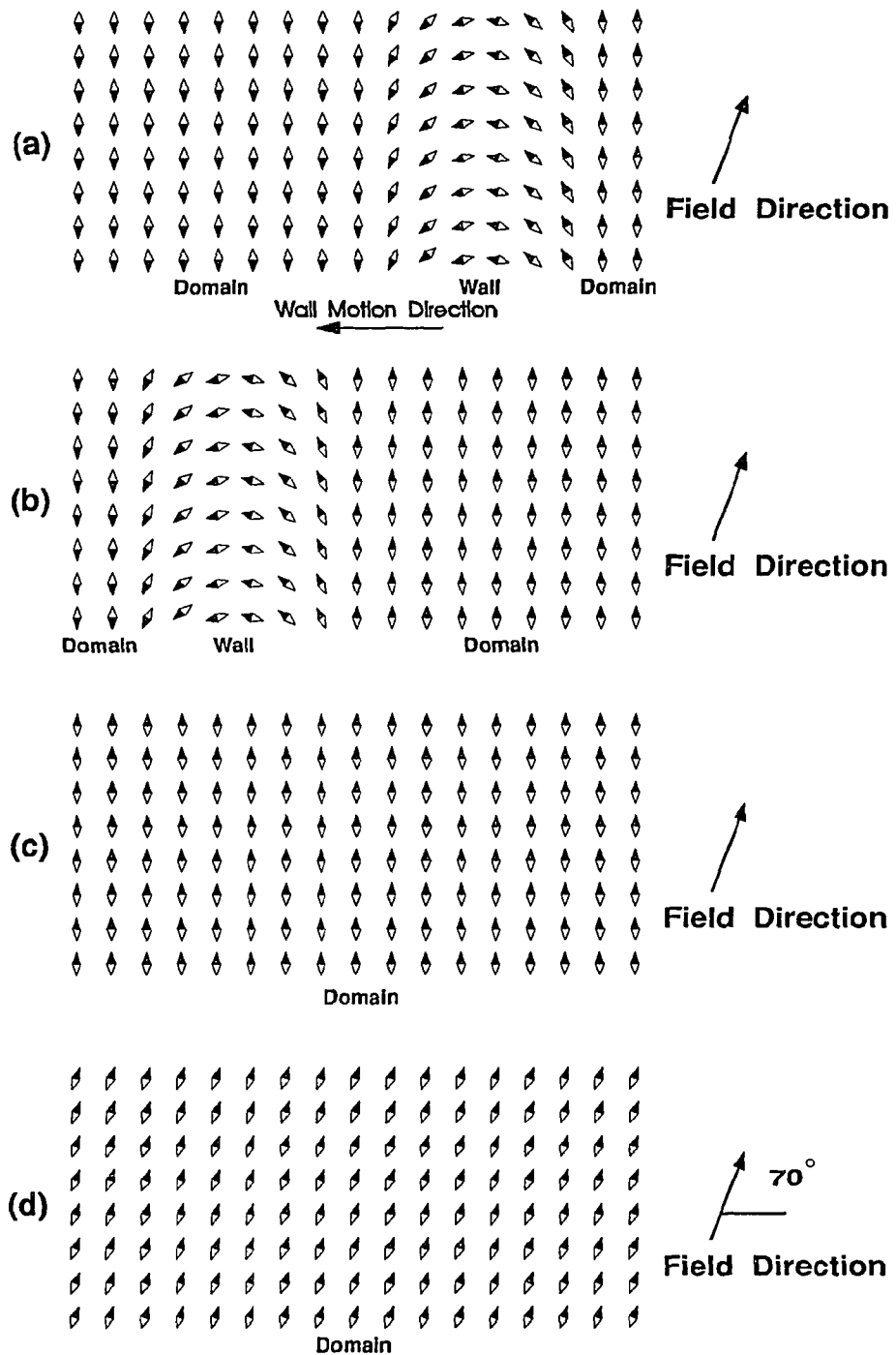


**Figure 2.12** Domain wall motion and domain rotation : (a)-(c) domain motion; (c)-(d) domain rotation.

## CHAPTER 3

### GOAL AND OBJECTIVES

The main goal of this study is to increase durability and wear resistance of different machine components by developing new surface treatment process. The conventional surface treatment processes, such as nitriding and carburizing can not sufficiently meet the requirement of today's industry. It is predicted that the traditional surface hardening processes are going to be replaced by more sophisticated and advanced processes. In advanced surface treatment processes, the plasma ion nitriding process(PIN) is the most widely applied process to improve surface properties of machine components. This process can form better low-friction surfaces than other surface treatments to increase surface wear resistance. However, there are some problems for the PIN process when it is applied to different machine components. They are residual stresses, layer formation and interface bonding.

Pulsed magnetic treatment is a new surface treatment approach. According to Joseph[24], this process is characterized by relieving the internal stresses of materials. Most of the known stress relief technologies involve heating processes which result in dimensional change, such as distortion or buckling. Additional machining processes are required for these techniques. Different from these technologies, the pulsed magnetic treatment process is a low temperature, fast, easy, and relatively inexpensive process. But due to the difficulty in detecting the change during magnetic treatment, the mechanism of this process has not been clearly defined yet.

In this study a new surface treatment process which involves a combination of PIN and pulsed magnetic treatment processes is developed. To implement and understand the presented new process, a few objectives have been achieved.

1. In order to develop new magneto-plasma surface treatment process, the combined PIN and pulsed magnetization process was designed.

2. Various process parameters of this treatment were selected and tested to optimize the treatment results.
3. Mechanism of the magneto-plasma treatment was investigated.
4. Wear testing methodology[25] and a computer controlled wear testing machine[26] were designed, manufactured, and implemented.
5. The physical metallurgy methods, such as Scanning Electron Microscope(SEM) and Auger Electron Spectrum(AES), were used to examine the treated and worn surfaces.

## CHAPTER 4

### MECHANISM OF PULSED MAGNETIC TREATMENT

#### 4.1 Mechanism of Magnetization Process

Magnetization processes occur when a ferromagnetic substance is put into an increasing magnetic field and reaches a so-called saturation point. The magnetization curve is the curve representing the history of magnetization,  $I$ , changed due to the applied field,  $H$ . If the alternative field is applied to perform demagnetization, the magnetization and demagnetization curves are similar to the hysteresis loop. Figure 4.1 By using this approach, we can describe the magnetization mechanism.

Starting from the demagnetized state ( $I = 0$  at  $H = 0$ ), there is a narrow range of magnetization where the magnetization changes reversibly. It is called the initial reversible range. In this range, magnetizations in every domain rotate reversibly from the stable directions. At the same time domain walls are displaced reversibly from their stable position. However, many studies and experiments [27, 28, 29] show that the reversible magnetization in this range is accomplished mainly by the reversible displacement of domain walls.

If the magnetic field is increased beyond the initial reversible range, the intensity of magnetization increases much drastically. Because the process is irreversible, this range is called the irreversible magnetization range. This range is attained mainly by irreversible displacement of domain walls from one stable position to another. In some material the irreversible rotation of domains is also expected because of the inclusions and precipitates. Barkhausen noise can be heard in this range. This results from the discontinuous changes in magnetization which are induced by irreversible domain rotation and domain wall displacement.

When the applied field is increased further, the magnetization curve becomes less steep and its process becomes reversible again. In this range the displacements of domain

walls have already been completed and the magnetization takes place by rotating magnetization. We call this range the rotation magnetization range.

Beyond the rotation magnetization range, the magnetization gradually approaches the saturation magnetization. The magnetization increases gradually in proportion to the intensity of the magnetic field when it approaches the saturation value. This effect results from increasing the perfection of spin alignment. This range is called the approaching saturation range. At this time, if the applied field is removed, the magnetization,  $I$ , would not return to its initial value. The magnetization will be  $I_r$  at  $H=0$ .  $I_r$  is called remanence. The value of  $I_r$  is depend on the amount of irreversible domain wall motion. A high value of  $I_r$  indicates that large amount of irreversible wall motion took place.

In the hysteresis loop the mechanism of magnetization from saturation point to remanence is the rotation of domain magnetization. From remanence to midway of the ascendant hysteresis curve the irreversible magnetization occurs. The rotation magnetization occurs again from the midpoint to the opposite saturation point.

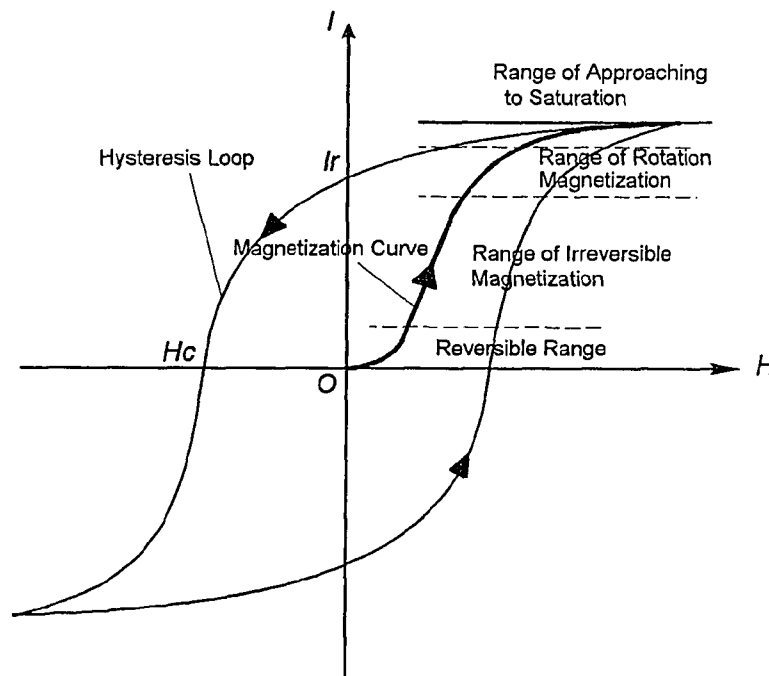


**Figure 4.1** Magnetization curve and hysteresis.

## 4.2 Irreversible Magnetization Process

In the previous discussion we know that there are two main mechanisms involved in the magnetization process. They are domain wall displacement and rotation of magnetization. For a ferromagnetic substance, the irreversible magnetization takes place most of the time along the magnetization curve. The main reason for the irreversible magnetization is the irreversible displacement of the domain wall. Hysteresis in ferromagnetic substance results from the irreversible displacement of the domain wall. The direct indication of this is the coercivity,  $H_c$ , in the hysteresis loop.

$H_c$  is the extra magnetic field required to bring the magnetization to its original direction while the applied magnetic field is removed from the material. If the magnetization process were reversible, then the coercivity would be zero. But in reality, there exists a finite coercivity for most materials. This indicates that irreversible domain wall motion always happens in the magnetization process. This also suggests that there are some imperfections in the materials. The major part of the hysteresis in ferromagnetic materials happens to be in the region of the magnetization curve where domain wall motion is taking place, and the irreversible component which causes hysteresis is therefore generally attributed to some impedance to domain wall motion.

The irreversible discrete changes in magnetization can be discussed in terms of the variation of the domain wall energy  $W_\gamma$  with wall position  $x$ . [29] We assume that  $W_\gamma$  varies with  $c$  as in Figure 4.2(a). The gradient of the energy is shown in Figure 4.2(b). The line  $Hc$  in (b) represents the pressure of the field on the wall. (The value of the constant  $c$  depends on the kind of wall and the orientation of the field.) At  $H = 0$ , the wall sits at position 1 where has the minimum energy. As  $H$  is increased from zero, the wall moves reversibly to 2. If the field were removed in this range, the wall would return to 1. Point 2 is a point of maximum energy gradient. If the field is sufficient to move the wall to 2, it is sufficient to make it take an irreversible jump to 3. This is a Barkhausen jump. If the field is then reduced to zero, the wall will go back, not to the point 1, but to point 4.

Point 4 is the nearest minimum energy. This exhibits the phenomena of hysteresis and remanence. A reverse field will drive the wall reversibly from 4 to 5 and by another Barkhausen jump from 5 to 6.

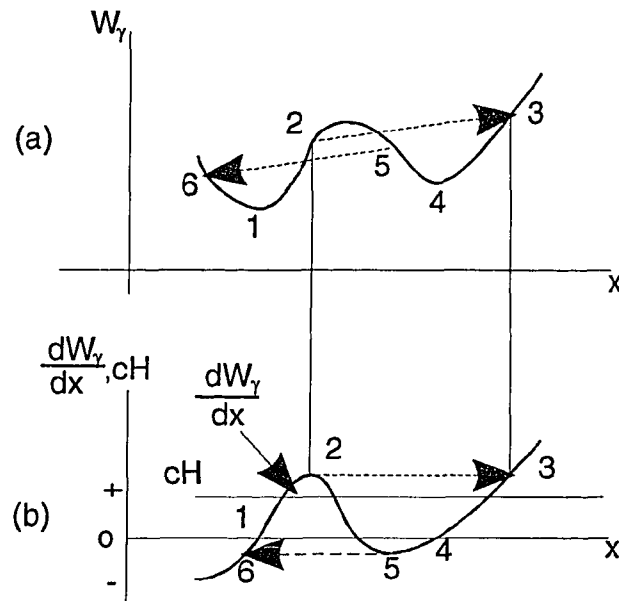


**Figure 4.2** Irreversible domain wall process : (a) domain wall energy with respect to distance; (b) gradient of domain wall energy.

### 4.3 Hindrances of Domain Wall Motion

Since irreversible domain wall motion plays the main role in the magnetization process for ferromagnetic materials, we may ask what gives rise to the irreversible domain wall motion? At zero applied field, a domain wall tries to be in a position which minimizes the energy of the system. The system, here, means the wall itself and/or the adjoining domains. According to Ne'el [30], a domain wall would always be located on the pinning sites. If a small field is applied, the wall will move, but it moves against a force tending to restore it to its original position. This restoring force results from the imperfections of the crystal. In general, most materials contain more or less crystal imperfections which hinder the easy motion of the domain wall. Some of special materials require less field to move

the wall, but the others may need more to do the job. These hindrances of domain wall motion can be classified into inclusion and residual microstresses.

#### 4.3.1 Inclusion

Inclusions may take many forms. They may be particles of a second phase in a binary alloy because the solubility limit has been exceeded. They may be oxide or sulfide particles which exist as impurities in a metal or alloy. They may simply holes or cracks. From a magnetic point of view, an "inclusion" in a domain is a region which has a different spontaneous magnetization from the surrounding material.

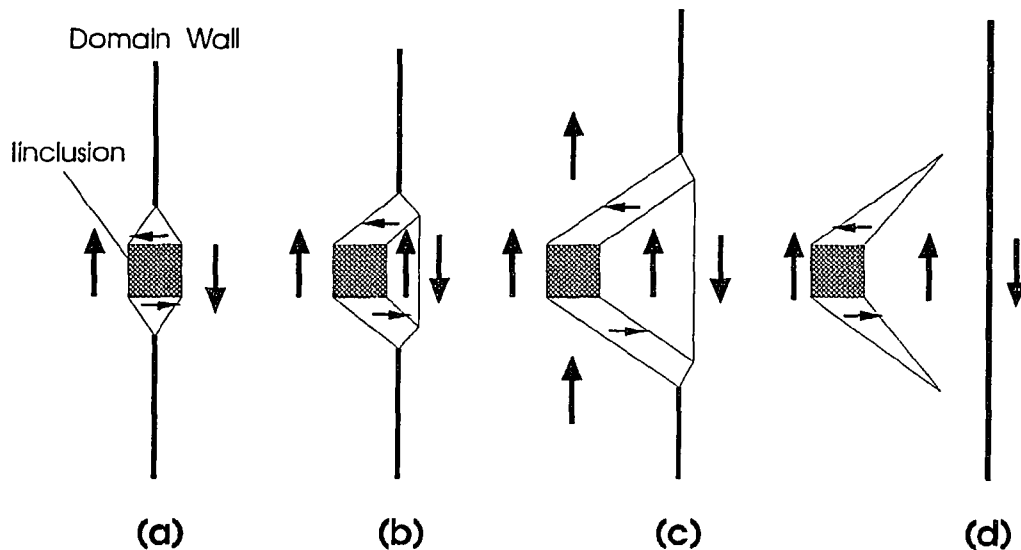


**Figure 4.3** Passage of a domain wall through an inclusion.

From the observation of moving domain walls in a crystal[31], it has been shown that wall motion is impeded by the interaction of the moving wall with spike domains rather than the inclusions themselves. A typical sequence is shown in Figure 4.3. A spike domain is a closure domain form as shown in Figure 4.3(a). It is due to magnetostatic energy being reduced to zero when a wall bisects an inclusion.



In response to an upward applied field, as shown in Figure 4.3, the wall in (a) moves to the right, as in (b). This drags out the closure domains into the form of tubes and creates a new domain just to the right of the inclusion. Further motion of the main wall lengthens the tabular domains, as in (c). The change from (a) to (b) and to (c) is reversible. The domain arrangement of (a) can be regained if the field is reduced. But if the field is continually increased, the tabular domains do not continue to lengthen. This is because their increasing surface area adds too much wall energy to the system. The wall will displace to a point where it suddenly breaks off the tabular domains and jumps a distance to the right. This will leave two spike domains attached to the inclusion, as in (d). If the field is removed, the domain wall will not return from (d) to (a). Also, if a reverse field is applied and strong enough, the wall will be driven to the left. The spike domains will then point to the left.

#### **4.3.2 Residual Microstresses**

The second kind of hindrance to domain wall motion is residual microstresses. Before examining the magnetic effects of such stresses, we have to get a clear understanding of what is meant by microstresses.

Stresses can be divided into applied stresses and residual stresses. Applied stresses are the stresses in a body due to external forces. Residual stresses are the stresses existing in a body after all external forces have been removed. Depending on the scale, residual stresses may be divided into macro and micro stresses.

Residual macrostress will not change its value with the position. The magnitude of the residual macrostrain is many times of the grain size in metals. Residual microstress varies its value and sign rapidly over the position. The magnitude of residual microstrain is equal to or smaller than the grain size. Residual macrostresses are of most concern to engineers because of their effects on fatigue and fracture. But this kind of stress can be almost removed by annealing. Residual microstresses always come from crystal

imperfections of various kinds, particularly dislocations. Although they may be reduced to quite low levels by annealing, they never entirely disappear from the material. Moreover, the improper heating process of annealing and other popular stress-relieving processes sometimes result in the deformation of components. Additional residual stresses can be generated.

Since the existence of microstresses in metal is not preventable, we now consider where the microstress comes from.

**Dislocations[32]:** All materials contain a number of dislocations. Dislocations can come from crystal imperfections during the cooling processes or machining processes at manufacturing. Dislocations in the surface are mainly generated by the latter one. Because the dislocation distorts the surrounding material, each dislocation has a stress field associated with it. These stresses are quite high near the dislocation and decrease as the reciprocal of the distance away from it. In a material, dislocation lines run in different directions. They form a complex network and a very irregular distribution of microstresses.

**Magnetostriction[33]:** When a ferromagnetic material is cooled below the Curie point, spontaneous magnetostriction tries to distort different domains in different directions. Because domains are not free to deform independently, microstresses are build up. The same argument shows that the stresses inside a domain wall differs from the stresses in the adjoining domains. Stresses of magnetostrictive origin are rather small. They are of the order of  $\lambda_s E$ , where  $E$  is Young's modulus. However, they are large enough to cause interactions between domain or domain wall and crystal imperfections.

#### 4.4 The Interaction of Dislocations and Domain Wall Motion

Dislocations are line defects. They act as sources of internal stresses. These internal stresses decrease in value along the distance  $r_1$  away from the dislocation line. They move in the material by gliding. Due to this gliding, the dislocation density can be increased and

decreased. The increase of dislocation density causes work hardening. The decrease of dislocation density can result in structure relaxation of the materials. In the magnetizing process, the dislocations are the main obstacles to the domain wall motion. The resistive force from the dislocations and wall motion may lead to the change of dislocation density.

The interaction of magnetization and dislocations is usually described in terms of the magnetoelastic energy[34]. By using Vicena's[35] approaches, we can calculate the interaction potential between the domain wall and dislocations. It has the same meaning as calculating the force of the domain wall on dislocations. As shown in [36], the force  $p^w$  exerted by dislocation on the domain wall is

$$p^w = \int_s (ds \times \Delta) \times \sigma^M \bullet b \quad (4.1)$$

or (by applying Stokes' theorem)

$$p^w = \int_l dl \times (\sigma^M \bullet b) \quad (4.2)$$

where  $ds$  is a surface element;  $dl$  is a line element of the dislocation; and  $\sigma^M$  is a tensor of stresses which are associated with the magnetostrictive strain due to the change of the direction of magnetization within the domain wall. In Equation (4.1) one has to integrate over the surface which is enclosed by the dislocation, and in Equation (4.2) the integral must be taken over the entire length of the dislocation line.

A domain wall is said to be of the first or second kind depending on whether  $\sigma^M$  has a zero value in the adjacent domains or not. For the second kind of domain wall, the projections of the magnetization vector in the two adjacent domains onto the wall must be parallel or antiparallel. This can be said to be the 180° walls. Equation (4.1) shows that for such a wall the interaction with dislocations is confined to those lying inside the wall. For the first kind of walls, such as 90° walls in iron or 71° and 109° wall in nickel, it is found that they have less mobility than 180° walls. Another important distinction between the two kinds of walls arises from the resultant force exerted by a dislocation threading a

wall. This force vanishes for a wall of the second kind, whereas for a wall of the first kind, it is in general different from zero.

Consider as an example for the application of Equation (4.2), a dislocation line parallel to a  $180^\circ$  wall ( $l_1, l_2$  are dislocation lengths in the  $x, y$  direction).

The force on the wall is [37]

$$p_z^w = l_1 b_2 \sigma_{22}^M - l_2 b_1 \sigma_{11}^M + \sigma_{12}^M (l_1 b_1 - l_2 b_2) \quad (4.3)$$

for a  $180^\circ$  wall in nickel crystal.

$$\sigma_{11}^M = \left[ \frac{2G}{(1-\nu)} \right] \left[ \frac{\nu}{4} (5\lambda_{111} + \lambda_{100}) \sin^2 \varphi - \frac{3}{2} \lambda_{111} \sin^2 \varphi \right] \quad (4.4)$$

$$\sigma_{22}^M = \left[ \frac{2G}{(1-\nu)} \right] \left[ \frac{1}{4} (5\lambda_{111} + \lambda_{100}) \sin^2 \varphi - \frac{3}{2} \nu \lambda_{111} \sin^2 \varphi \right] \quad (4.5)$$

$$\sigma_{22}^M = G(2\lambda_{100} + \lambda_{111}) \sin 2\varphi \quad (4.6)$$

Here  $\lambda_{100}$  and  $\lambda_{111}$  are magnetostrictive constants;  $\varphi$  is the angle between the local magnetization and the  $x$  direction;  $G$  is shear modulus of elasticity;  $\nu$  is Poisson's ratio.

The force exerted on such a wall by dislocations of length  $l$  parallel to  $[\bar{1}10]$  is

$$p_s^w = -Gb_s l (2\lambda_{100} + \lambda_{111}) \sin^2 \varphi \quad (4.7)$$

for a screw dislocation with Burger vector  $b_s$ , and

$$p_m^w = Gb_m l \left\{ \frac{2}{3} \cdot 6^{\frac{1}{2}} \cdot \left[ \frac{\sin^2 \varphi}{(\nu-1)} \right] \cdot \left[ 3\nu\lambda_{111} - \frac{1}{2}(5\lambda_{111} + \lambda_{100}) \right] - \sin 2\varphi (2\lambda_{100} + \lambda_{111}) \right\} \quad (4.8)$$

for a mixed dislocation with Burger vector  $b_m$  parallel to  $[0\bar{1}\bar{1}]$ .

#### 4.5 Pulsed Magnetic Treatment

Pulsed magnetic treatment is a surface treating process which uses varying magnetic field (field direction changes from one direction to the opposite direction) to modify the surface properties. This process is also characterized as a stress relieving process.

Stress relieving is a very important process during the manufacturing of materials and components. But most of the stress relieving techniques involve heating and cooling steps which again limits their range of applications. These techniques must be closely controlled in temperature, otherwise they will result in distortion or buckling of treated elements and even accumulating undesired residual stresses. Pulsed magnetic treatment is a nonthermal stress relieving process because this process uses an induced electromagnetic field as an energy input to the material. The stress relaxation is achieved through the vibration inside materials caused by the varying magnetic field. There is less heat generated during the process and are no dimensional changes of the treated components.

The principle behind pulsed magnetic treatment is magnetostriction.[38,39] Ferromagnetic materials (like iron, tool steel, stainless steel) deform elastically when they are placed in a magnetic field. Magnetostriction causes material to change its physical dimension in the magnetic field. In a grain, there are several domains. Once the magnetic field is applied to the grain, the domain will grow or shrink in the favorable magnetization direction. Due to the domain wall movement, the crystal structure experiences expansion and contraction.

However, when a magnetic field is applied to the materials, magnetization does not change uniformly throughout the substance. The magnetization duration does not give domain wall movement enough time to align the domain. The magnetization starts at the surface and occurs somewhat later inside the substance. The lag's duration is influenced by specimen shape, material conductivity, the frequency at which the magnetic field fluctuates and material permeability.

During this initial period of magnetization, the surface experiences the full magnetic field, but its interior does not. Consequently, the specimen surface grows or shrinks, but the core remains stable. At the end of a pulsed period, the magnetic field saturates the specimen if the correct magnetostrictive cycle has been selected.

Because the specimen's core and surface respond at different rates to a magnetic field, magnetostriction induces shear force into surface structure, Figure 4.4. As shown in the figure, the outer layer of the atoms expands longer than the lower layer. The rearrangement of atoms in the structure can be completed by eliminating the structure imperfection, such as point defects or dislocations.

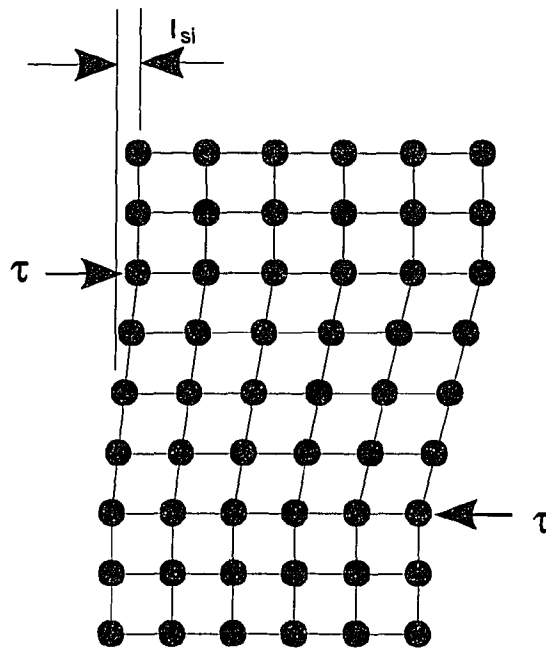


Figure 4.4 Structure deformation due to magnetostriction.

#### 4.6 The Mechanism of Pulsed Magnetic Treatment

In this study, the dislocations in the materials are assumed to be the mechanism of stress relieving by pulsed magnetic treatment. It is known that the main resource of internal stress or residual stress is from the deformation and imperfection of the crystal structure. Dislocations are line defects in the crystal. The internal stresses caused by those line defects are larger than the internal stresses caused by point defects. By effectively reducing the dislocation density the stress relief of materials can be expected.

Along the magnetization process, we can find that dislocations have strong interactions with the mechanisms of magnetization which are the domain wall motion and

the domain rotation. In section 4.3, we have discussed the force applied on the dislocation when the domain wall moves. If the applied force is large enough, the dislocations may be shifted; if not, it is expected that the free energy of the dislocations would not be the same when the domain wall crosses them. If we reach the range of domain rotation, the magnetostriction will be found. Because of the lag of magnetization on the surface, there are different levels of magnetization. The shear force is generated between the surface which has saturated magnetostriction and the inside layer which has less or no magnetostriction. A slip plane in the crystal could be generated along the shear force. Again dislocations can be relocated along the slip plane. In our process, the magnetization and demagnetization processes are applied to the components. The crystal structure experiences a shaking effect from the change of field directions. The crystal structure can be relaxed by the movement, redistribution, and annihilation of dislocations.

#### **4.6.1 Effects of Domain Wall Motion**

In the demagnetized state, the domain walls in the material are always located on the pinning site which has lower system free energy. The system free energy is the result of minimizing the exchange magnetoelastic, and magnetostatic energy. If an external field is applied to the material, the domain walls move in such a way that favorably aligned domains grow at the expense of unfavorably aligned domains. The whole system free energy is then changed. The varied system free energy depends on the process of domain wall motion and the final position of the domain wall.

During domain wall movements, if there are any impedances, more energy is required to overcome those impedances for domain wall motion. As a major impedance of domain wall movement, dislocations exert forces,  $p^w$ , on the domain wall. The consequences of these applied forces on dislocations are the displacement of dislocations and increasing free energy of dislocation.

Let the energy required to move dislocations from one site to the next site be  $E_\gamma$ .  $E_\gamma$  can be expressed as

$$E_\gamma = p^w \times l_t \quad (4.9)$$

where  $l_t$  is the distance which the dislocations travel. However,  $p^w$  is related to the free energy of dislocations, because dislocations possessing higher free energy will be the easiest one to start moving. The interactive force,  $p^w$ , is then small for high free energy dislocations.

Applying a magnetic field on the material, additional magnetic energy is added to each dislocation. According to Pavlov[40], the amount of free energy added to dislocations is  $\beta I_d H$ .  $\beta$  is the structure factor.  $I_d$  is the magnetic moment of a dislocation, and  $H$  is the external magnetic field strength. A dislocation possessing this additional magnetic energy has a greater probability to overcome the Peierls barrier[41] and can move to the next position. But not all dislocations can overcome the Peierls barrier. For those dislocations that do not move, they have at least increased their free energy. Later on, if there are any external force applied to the material, the possibility of the dislocations motion is then increased.

#### 4.6.2 Effect of Domain Rotation

Domain rotation takes place when the magnetizations in each domain are all aligned and try to rotate to the external field direction. Along with this process, the dimensional change of structure can usually be found. It is known as the magnetostriction. If the external field strength is strong enough, the maximum magnetostriction can be reached. This is the saturated magnetostriction,  $\lambda_{sj}$ , and it can be found from Equation. (2.8).

However, the induced magnetic field in the material is a function of depth and time. This is known as the skin-effect[38]. When we apply a constant magnetic field over a material the induced magnetic field is exponentially distributed along the thickness of the specimen. It takes a while to reach same magnetization level everywhere in the specimen.



But in an alternating magnetic field, the applied field does not remain constant and will not last long enough to let the whole specimen have the same induced magnetization. In a short time, the surface and the substrate experience different magnetizations. It is possible that the surface has saturated magnetization and the substrate does not. This then generates deformation of the structure because of different magnetostriction as shown in Figure 4.4. The deformation of the structure can be recognized as the result of applying shear forces on the surface layer.

Due to this shear force, a slip-plane is generated. Along the slip plane, forces are exerted on the dislocations. At this time, the mobility of the dislocations is increased. Also the dislocation motion under the deformation in the magnetic field is consistent with the field direction. This reduces the dislocation interactions with each other and leads to the decrease in the probability of dislocation net formation.

As the result of these interactions, the dislocation density on the surface can be reduced, especially for the situation in Figure 4.5. This also tends to reconstruct the crystal structure and attain a better structure. The internal stresses are then reduced.

Since we apply an alternating magnetic field on the specimen, the magnetizing and demagnetizing processes act just like applying vibration into the crystal structure. The structure vibrates with the field direction. This give dislocations opportunity to shift in both directions. The probability of relocation and delimitation of dislocations is increased. The structure relaxation can be enhanced.

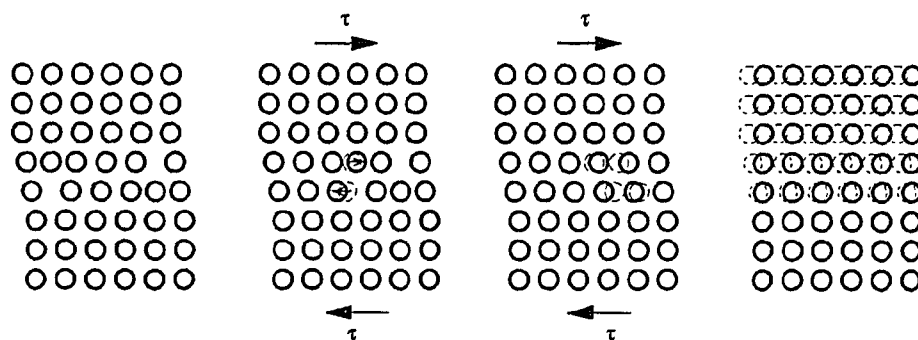


**Figure 4.5** The elimination of dislocation due to the shear force.

## CHAPTER 5

### MODEL FOR MAGNETO-PLASMA ION NITRIDING

#### 5.1 Magneto-Plasma Ion Nitriding

As mentioned before, the magneto-plasma ion nitriding process is defined as a surface modification technique which combines the pulsed magnetic treatment and plasma ion nitriding process. This new approach is designed to improve surface durability of materials. There are two reasons why these two processes are combined in this study.

First, residual stresses are one of important factors which affect the nitriding results in the plasma ion nitriding process. They influence the nitriding layer formation and subsequently the nitrided surface performance under service conditions. In plasma nitriding, the residual stresses come from the machining processes and the layer formation. The residual stresses affect the depth of layer formation. During the nitriding processes, a nitrided zone or a compound layer and a diffusion zone are developed. Residual stresses are generated due to the microstructural difference between compound layers and the diffusion zone. They can control the components' performance. They can not be removed by applying conventional stress relieving techniques. The low operating temperature and distortion-free stress-relieving treatment, pulse magnetic treatment, is thus applied to the plasma ion nitriding process to improve the nitriding result. It should be a distortion-free stress-relieving approach.

Second, the plasma ion nitriding process is characterized as a diffusion process. In the solid state, the diffusion process is accomplished by bulk diffusion, the diffusion through dislocations and grain boundaries. The diffusion rate is then controlled by the diffusivity. However, since the grain boundary is nothing else but aggregated dislocations, the diffusivity of grain boundaries can be expressed by the diffusivity of dislocations. The diffusivity  $D$  is defined as

$$D = D_0 \cdot e^{\frac{-Q_a}{RT}} \quad (5.1)$$

where  $D_0$  is the diffusivity coefficient independent of temperature( $\text{cm}^2/\text{sec}$ );

$Q_a$  is the activation energy for diffusion(J/mole);

$R$  is gas constant(cal/mole-K);

$T$  is the absolute temperature(K).

The effective diffusivity of a material is given as follows[42,43,44]

$$\bar{D} = D_d + (1 - \bar{f})D_g \quad (5.2)$$

where  $D_g$  is the diffusivity of grain;  $D_d$  is the diffusivity of dislocations.

In this study, it is assumed that the dislocation density is changed due to the pulsed magnetic treatment. The diffusion rate of the magnetized material is then changed. The effective diffusivity after magnetic treatment can be given as

$$\bar{D}' = D_d' + (1 - \bar{f})D_g'$$

Since the magnetic field does not affect the grains of materials, the diffusivity of grains will not be changed. The above equation then becomes

$$\bar{D}' = D_d' + (1 - f)D_g \quad (5.3)$$

From Equation (5.2) and (5.3), we find that the change of effective diffusivity is only from the change of dislocation diffusivity after the magnetic treatment.

Since the diffusion depth is proportional to the  $\sqrt{Dt}$ , the nitrated layer and diffusion zone can be used to verify the change of dislocation density. By using this approach, we can prove the mechanism of pulse magnetic treatment.

## 5.2 Fick's Laws for Diffusion Processes

### 5.2.1 Fick's First Law[45]

In an isotropic material, the rate of diffusion,  $J$ , across a unit area of a section normal to the diffusion direction is proportional to the concentration gradient in the direction of diffusion. It is expressed as

$$J = -D\nabla c \quad (5.4)$$

or, for diffusion in the  $y$  direction

$$J_y = -D \frac{\partial c(y,t)}{\partial y} \quad (5.5)$$

where  $\nabla$  is the gradient vector operator of the form

$$\nabla = \frac{\partial}{\partial x} + \frac{\partial}{\partial y} + \frac{\partial}{\partial z} \quad (5.6)$$

in the rectangular coordinate system;  $c$  is the diffusing concentration (mass per unit volume).

From Equation (5.4), the diffusion flux approaches zero as the concentration become uniform ( $\nabla c \rightarrow 0$ ). The negative sign indicates that diffusing flow occurs in the direction of decreasing diffusant concentration.

### 5.2.2 Fick's Second Law

Fick's first law allows us to calculate the instantaneous mass flow rate past any plane in solids but gives no information about the time dependence of the concentration. By using Fick's first law and considering the material balance across a volume element of the system, Fick's second law can be derived and expressed as

$$\frac{\partial c}{\partial t} = -\nabla J \quad (5.7)$$

If  $D$  is independent of time and position, Equation (5.4) can be put into Equation (5.7) giving

$$\frac{\partial c}{\partial t} = D\nabla^2 c \quad (5.8)$$

where  $\nabla^2$  is the Laplacian operator defined as

$$\nabla^2 = \frac{\partial^2}{\partial x^2} + \frac{\partial^2}{\partial y^2} + \frac{\partial^2}{\partial z^2} \quad (5.9)$$

The analytical solutions to the diffusion Equation (5.8) from Fick's second law can be easily obtained for a variety of initial and boundary conditions. Since the derivation of the equations is described in detail in any standard book[46], only the final form of the solutions are presented here. If we only consider that diffusion occurs in the  $y$  direction only, the diffusion Equation (5.8) is reduced to

$$\frac{\partial c}{\partial t} = D \frac{\partial^2 c}{\partial y^2} \quad (5.10)$$

The solutions of this equation are considered for the case of the two most commonly used diffusion sources.

In the case of diffusion from a instant source at  $y = 0$  into an initially diffusant-free specimen, the solution of Equation (5.10) is given by [46]

$$c(y, t) = \frac{M}{(\pi Dt)^{1/2}} \cdot e^{-\frac{y^2}{4Dt}} \quad (5.11)$$

where  $M$  is the magnitude of the instant source.

In the case of diffusion from a constant source at  $y = 0$  into an initially diffusant-free specimen, the solution of Equation (5.10) is given by

$$c(y, t) = c_0 \operatorname{erfc} \left[ \frac{y}{2\sqrt{Dt}} \right] \quad (5.12)$$

where  $c_0$  is the concentration which remains constant for all  $t \geq 0$ . The complementary error function  $\operatorname{erfc}$  is defined as

$$\operatorname{erfc}(y) = 1 - \frac{2}{\sqrt{\pi}} \int_0^y e^{-u^2} du \quad (5.13)$$

Also, from Equations (5.11), (5.12) we find that the diffusion depth is proportion to  $\sqrt{Dt}$ .

### 5.3 Nail Effect

The diffusion process in solids is normally accomplished by the diffusion through the bulk, grain boundaries and dislocations. Because the diffusivity of dislocations is higher than the diffusivity of bulk, it can be said that the depth of the process in the crystal is dominated by the dislocations. However, the density of dislocations in a crystal is extremely high. An annealed metal can typically have dislocation density on the order of  $10^6$  to  $10^8$  dislocation lines/cm<sup>2</sup>. [47] These dislocations are differently oriented and form a complicated network in the materials. Considering the material flux through the dislocations in the bulk, we can treat this flux as a nail designed to bond the layer developed to the substrate. The adhesive force at the interface can be controlled by the amount of dislocations preferably oriented to the surface.

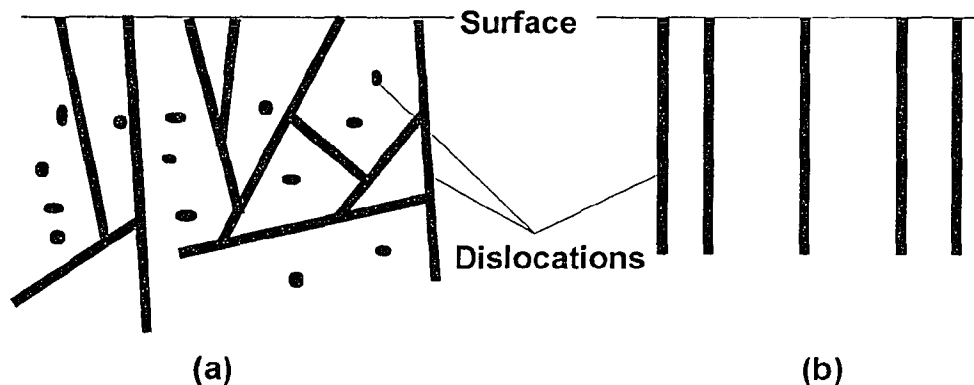


**Figure 5.1** Distribution of dislocations in material : (a) before magnetization; (b) after magnetization.

Experimental study of magnetic treatment [48] show the improvement of wear resistance due to the better quality of applied layers. This can be an indication of the influence of bonding on applicational properties. The shaking effect of the pulsed

magnetic treatment can cause dislocation motion, redistribution, and annihilation. According to the study given by [40], the direction of the dislocation motion must be the same as the applied field. At the end of pulse magnetic treatment, many dislocations are expected to be aligned with the normal direction of the surface as shown in Figure 5.1. The diffusion result of these dislocations is shown in Figure 5.2. The black layer represents the diffusion source which can be the nitrated layer and diffusion zone. The shadow contour around each dislocation is the result of diffusion in dislocations. In this figure, the diffusion source can be recognized as the plate, and dislocations as nails. The plate is nailed to the substrate. The adhesive force is enhanced by these nails. Also, if the diffusion distribution is uniform at the substrate, the bonding between layers is improved. This phenomena is then called by us "Nail Effect" in the magneto-plasma ion nitriding.

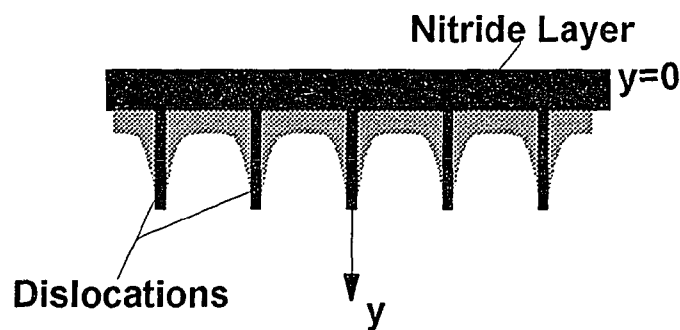
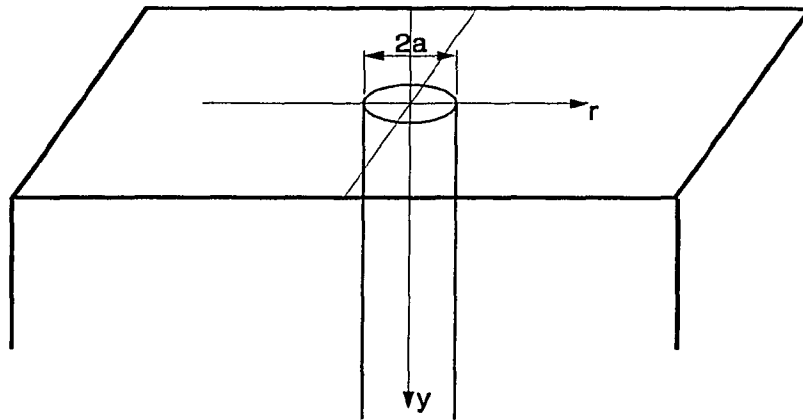


Figure 5.2 Nail Effect.

#### 5.4 Diffusion Through Dislocations

Diffusion through dislocations can be described as mass flow through cylindrical pipes distributed in a crystal perpendicular to the surface plane. The dislocation is treated as a highly diffusive, semi-infinite isotropic pipe with radius  $a$ . It is embedded in a low-diffusivity, semi-infinite perfect crystal normal to the surface that carries the diffusant. Let the  $r$  axis be the radius direction which is normal to the pipe surface and the  $y$ -axis normal to the free surface, as shown in Figure 5.3. In the diffusion process, material transport

takes place along the  $y$ -axis in the volume of the grain as well as along the dislocation. Since the diffusivity within the dislocation is higher than in the crystal,[49] the diffusant penetrates much deeper along the dislocation than anywhere else. Consequently, it starts leaking through the surface of the dislocation pipe into the bulk. The total amount of diffusant in the crystal is the result of two contributions; one directly from the source and the other from the dislocations.



**Figure 5.3** Nail model for "Nail Effect".

Let  $D_g$  be the diffusion coefficient describing diffusion within the grain, and  $D_d$  be the diffusion coefficient describing diffusion in the dislocation pipe. Since  $D_g$  is much smaller than  $D_d$ , the contribution of  $D_g$  will decrease much more rapidly with distance than the dislocation contribution. As a result, the diffusant comes almost entirely from dislocations in the regions far away from the surface.

To derive a diffusion equation for this study, there are some assumptions[50]:

- Fick's law of diffusion is obeyed both in the grain and the dislocation pipe.
- $D_g$  and  $D_d$  are isotropic and independent of concentration, position, and time.



- The diffusant flow is continuous at the dislocations and grain interface. This means that the diffusant concentration and the flux are continuous at  $r = a$ .
- The diameter of the dislocation pipe is so small that the concentration variation in dislocation in the  $r$  direction is negligible.

Applying Fick's second law, Equation (5.8), to diffusion within the dislocation and in the grain, we can get the diffusion equations for dislocation pipe diffusion in cylindrical coordinates.[51] If  $c_g$  and  $c_d$  represent respectively the concentrations of diffusant outside and inside the pipe of dislocation, the equations to be solved are

$$D_g \left[ \frac{1}{r} \cdot \frac{\partial}{\partial r} \left( r \frac{\partial c_g}{\partial r} \right) + \frac{\partial^2 c_g}{\partial y^2} \right] = \frac{\partial c_g}{\partial t} \quad (5.14)$$

for outside the pipe ( $r \geq a$ ) and

$$D_d \left[ \frac{1}{r} \cdot \frac{\partial}{\partial r} \left( r \frac{\partial c_d}{\partial r} \right) + \frac{\partial^2 c_d}{\partial y^2} \right] = \frac{\partial c_d}{\partial t} \quad (5.15)$$

for inside the pipe ( $r < a$ ). Both  $D_g$  and  $D_d$  are assumed to be isotropic and concentration independent.

From the third assumption, the continuity at the grain and dislocation interface gives rise to the following boundary conditions:[52]

$$c_d(a, y, t) = c_g(a, y, t) \quad (5.16)$$

$$D_d \frac{\partial c_d(r, y, t)}{\partial r} \Big|_{r=a} = D_g \frac{\partial c_g(r, y, t)}{\partial r} \Big|_{r=a} \quad (5.17)$$

and

$$\frac{\partial c(r, y, 0)}{\partial y} \Big|_{y=0} = 0 \quad (5.18)$$

Since  $r$  is very small and  $D_d \gg D_g$ , one may combine Equations (5.15) - (5.18) into the following single boundary condition for  $c_g$ . [53]

$$\frac{\partial c_g(a, y, t)}{\partial t} = D_d \cdot \frac{\partial^2 c_g(a, y, t)}{\partial y^2} + \frac{2D_g}{a} \frac{\partial c_g(r, y, t)}{\partial r} \Big|_{r=a} \quad (5.19)$$

This equation is derived assuming  $c_d$  to be radically uniform (independent of  $r$ ). The first term on the right hand side of this equation represents the concentration change due to diffusion within the dislocation pipe. The second term represents the change due to radial leakage of the diffusant from the dislocation pipe into the adjoining crystal.

There are two types of diffusion sources: instant and constant sources. In the case of a constant source, the concentration at the surface is maintained constant at a value for all  $t > 0$ . The instant source is a case which has a very thin layer of diffusant of quantity  $M$  per unit area and is deposited on the surface at  $t = 0$ . The concentration at  $t = 0$  can be expressed as

$$c(t = 0) = 2 \cdot M \cdot \delta(y) \quad (5.20)$$

where 2 here is a normalizing constant, and  $\delta(y)$  is a delta function expressed as

$$\delta(y) = \begin{cases} 1 & y = 0 \\ 0 & y \neq 0 \end{cases} \quad (5.21)$$

Here we use an instant diffusion source to simulate the conditions of the nitriding process. To obtain the solutions, the single-nail and array-nails model are used. Also Fourier-Laplace transform technique are applied to solve the diffusion equations.

### 5.5 Nail Model for Nail Effect

The nail model is based on concentration distribution of the dislocation diffusion process. Figure 5.3 is a simple sketch for the model. It is known that a dislocation is nothing but a pipe in the microstructure. The diffusion rate of dislocation is much higher than other diffusion mechanisms. Through dislocations the diffusant can reach deeper into the materials. If the diffusion process only takes place inside the dislocations, the result of diffusion is just like putting an object into the material. The diffusant just fills out the

dislocations. The bonding force between the substrate and the diffusant is not strong. However, if the diffusion process takes place not only along the dislocations but also from dislocations to the substrate, the bonding force will be enhanced by the result of diffusion from dislocations to the substrate. The concentration distribution along the dislocations can be used to represent the bonding forces and show the model for the "Nail Effect".

In this model the diffusant concentration comes from both grain and dislocations. Let  $c_g(r, y, t)$  represent the concentration from the grain and  $c_d(r, y, t)$  represent the concentration from the dislocations. The diffusion equations are from Equation (5.14) and (5.15). The boundary conditions are from Equation (5.16) to (5.18). The initial conditions are from Equation (5.19) to (5.21). They are collected as follows :

$$D_g \left[ \frac{1}{r} \cdot \frac{\partial}{\partial r} \left( r \frac{\partial c_g(r, y, t)}{\partial r} \right) + \frac{\partial^2 c_g(r, y, t)}{\partial y^2} \right] = \frac{\partial c_g(r, y, t)}{\partial t} \quad r \geq a \quad (5.22)$$

$$D_d \left[ \frac{1}{r} \cdot \frac{\partial}{\partial r} \left( r \frac{\partial c_d(r, y, t)}{\partial r} \right) + \frac{\partial^2 c_d(r, y, t)}{\partial y^2} \right] = \frac{\partial c_d(r, y, t)}{\partial t} \quad r \leq a \quad (5.23)$$

Boundary conditions

$$\left. \frac{\partial c(r, y, t)}{\partial y} \right|_{y=0} = 0 \quad (5.24)$$

$$c_d(a, y, t) = c_g(a, y, t) \quad (5.25)$$

$$D_d \left. \frac{\partial c_d(r, y, t)}{\partial r} \right|_{r=a} = D_g \left. \frac{\partial c_g(r, y, t)}{\partial r} \right|_{r=a} \quad (5.26)$$

$$\left. \frac{\partial c_g(a, y, t)}{\partial t} \right|_{r=a} = D_d \cdot \left. \frac{\partial^2 c_g(a, y, t)}{\partial y^2} + \frac{2D_g}{a} \frac{\partial c_g(r, y, t)}{\partial r} \right|_{r=a} \quad (5.27)$$

Initial conditions

$$c(t = 0) = 2 \cdot M \cdot \delta(y) \quad (5.28)$$

,where 
$$\delta(y) = \begin{cases} 1 & y = 0 \\ 0 & y \neq 0 \end{cases}$$

To solve the diffusion equations, we use Fourier and Laplace transform techniques which were first given by Whipple[54]. The transform of concentration  $c(r, y, t)$  is defined as

$$\psi(r, w, s) = \int_0^{\infty} \int_0^{\infty} c(r, y, t) \cos(wy) \cdot e^{-st} dy dt \quad (5.29)$$

The term,  $\cos(wy)$ , is used for the instant diffusion source. The concentration  $c(r, y, t)$  of the diffusant in the crystal is then obtained through the inverse transform of  $\Psi(r, w, s)$ .

$$c(r, y, t) = \frac{1}{\pi^2 i} \int_0^{\infty} \cos(wy) dw \int_{-i\infty}^{i\infty} \psi(r, w, s) \cdot e^{st} ds \quad (5.30)$$

where the path of the integration over  $s$  is to the right of all the singularities of  $\Psi(r, w, s)$ .

Fourier-Laplace transform of Equation (5.13):

$$\text{Let } F\{c_g(r, y, t)\} = F_g(r, w, t), \text{ and } L\{F_g(r, y, t)\} = \psi_g(r, w, t)$$

After the Fourier cosine-transform, Equation (5.13) becomes

$$D_g \left[ \frac{1}{r} \frac{\partial}{\partial r} \left( r \frac{\partial F_g}{\partial r} \right) - w^2 F_g - \frac{2}{\pi} \frac{\partial c_g}{\partial y} \Big|_{y=0} \right] = \frac{\partial F_g}{\partial t} \quad (5.31)$$

From the boundary condition,  $\frac{\partial c(r, y, t)}{\partial y} \Big|_{y=0} = 0$ , the above equation becomes

$$D_g \left[ \frac{1}{r} \frac{\partial}{\partial r} \left( r \frac{\partial F_g}{\partial r} \right) - w^2 F_g \right] = \frac{\partial F_g}{\partial t} \quad (5.32)$$

The Laplace transform of the above equation is

$$D_g \left[ \frac{1}{r} \frac{\partial}{\partial r} \left( r \frac{\partial \psi_g}{\partial r} \right) - w^2 \psi_g \right] = s \psi_g - F(t=0, w=0) \quad (5.33)$$

$F(t=0, w=0) = 2M$  because of the initial condition. The above equation becomes

$$D_g \left[ \frac{1}{r} \frac{\partial}{\partial r} \left( r \frac{\partial \psi_g}{\partial r} \right) - w^2 \psi_g \right] = s \psi_g - 2M \quad (5.34)$$

This is a modified Bessel differential equation with 0 order. The general solution is

$$\psi_g(r, w, s) = A_1 I_0(kr) + A_2 K_0(kr) + \frac{2M}{k^2 D_g} \quad (5.35)$$

where

$$k^2 = w^2 + \frac{s}{D_g}$$

and  $A_1$  and  $A_2$  are constants;  $I_0$  and  $K_0$  are modified Bessel functions. In this model,

$$\frac{\partial \psi_g}{\partial r} = 0 \text{ when } r \rightarrow \infty. \text{ So the above solution becomes}$$

$$\psi_g(r, w, s) = A K_0(kr) + \frac{2M}{k^2 D_g} \quad (5.36)$$

where  $A$  is a constant.

Fourier-Laplace transform of Equation (5.14):

$$\text{Let } F\{c_d(r, y, t)\} = F_d(r, w, t), \text{ and } L\{F_d(r, y, t)\} = \psi_d(r, w, t)$$

Using the same method as in the previous derivation, we can get the Fourier-Laplace transformed Equation (5.13).

$$D_d \left[ \frac{1}{r} \frac{\partial}{\partial r} \left( r \frac{\partial \psi_d}{\partial r} \right) - w^2 \psi_d \right] = s \psi_d - 2M \quad (5.37)$$

The general solution of the above equation is

$$\psi_d(r, w, s) = B_1 I_0(k'r) + B_2 K_0(k'r) + \frac{2M}{k'^2 D_d} \quad (5.38)$$

$$k'^2 = w^2 + \frac{s}{D_d}$$

where  $B_1$  and  $B_2$  are constants. Since  $\frac{\partial \psi_d}{\partial r} = 0$  when  $r \rightarrow 0$ , the above equation becomes

$$\psi_d(r, w, s) = BI_0(k'r) + \frac{2M}{k'^2 D_d} \quad (5.39)$$

where  $B$  is a constant.

The transformed concentration inside and outside dislocations are expressed as follows :

$$\begin{cases} \psi_g(r, w, s) = AK_0(kr) + \frac{2M}{k^2 D_g} \\ \psi_d(r, w, s) = BI_0(k'r) + \frac{2M}{k'^2 D_d} \end{cases} \quad (5.40)$$

By considering  $a$  very small and  $D_d \gg D_g$ , we can recognize that the concentration inside the dislocation,  $c_d$ , is uniform in the  $r$  direction. This means that  $c_d(r=0) = c_d(r=a) = c_g(r=a)$ . It also indicates that only  $c_g$  has to be determined and Equation (5.16) then can be used. Taking the Fourier-Laplace transformation on Equation (5.16), It becomes

$$\frac{2}{a} \frac{\partial \psi_g(r, w, s)}{\partial r} \Big|_{r=a} - \left( w^2 + \frac{s}{D_d} \right) \Delta \psi_g(a, w, s) = -\frac{2M}{D_g} \quad (5.41)$$

where  $\Delta = \frac{D_d}{D_g}$ .

Applying Equation (5.40) to the above equation, we can get

$$A = \frac{\frac{2M}{D_g} \left[ 1 - \frac{k'^2}{k^2} \Delta \right]}{\frac{2}{a} kK_1(ka) + k'^2 \Delta K_0(ka)} \quad (5.42)$$

Substituting  $A$  into Equation (5.36), we have

$$\begin{aligned} \psi_g(r, w, s) &= \frac{2M}{k^2 D_g} - \frac{2M(\Delta-1)w^2}{k^2 D_g} \frac{K_0(kr)}{\frac{2}{a} kK_1(ka) + k'^2 \Delta K_0(ka)} \\ &= \psi_{g1}(w, s) + \psi_{g2}(r, w, s) \end{aligned} \quad (5.43)$$

The first term,  $\psi_{g1}$ , is the transformed concentration which is contributed from the direct volume diffusion, and the second term,  $\psi_{g2}$ , the radial diffusion from the dislocation pipe.

The inverse transform of the first term,  $\psi_{g1}$ , can be easily derived as follows :

$$\begin{aligned} c_{g1}(r, y, t) &= \frac{1}{\pi} \int_{-\infty}^{\infty} \cos(wy) \frac{1}{2\pi i} \int_{-\infty}^{\infty} \frac{2M}{k^2 D_g} e^{st} dw \\ &= \frac{1}{\pi} \int_{-\infty}^{\infty} e^{-D_g t w^2} \cdot \cos(wy) dw \\ &= \frac{2M}{\sqrt{\pi D_g t}} e^{-\frac{y^2}{4D_g t}} \end{aligned} \quad (5.44)$$

The inverse transform of the second term is shown as follows :

$$c_{g2}(r, y, t) = \frac{1}{\pi} \int_{-\infty}^{\infty} \cos(wy) \frac{1}{2\pi i} \int_{-\infty}^{\infty} \psi_{g2}(r, w, s) e^{st} dw \quad (5.45)$$

Let  $\psi_{g2}(w, s) = \left( \frac{1}{D_g k^2} \right) \cdot Q$ , and regard  $Q$  as the Laplace transform of some function  $q(t, w)$ . So

$$\psi_{g2}(r, w, s) = \frac{1}{D_g k^2} \left( L_{(D_g k^2)} \{q(t, w)\} \right) \quad (5.46)$$

with

$$q(t, w) = \frac{1}{2\pi i} \int_{-\infty i}^{\infty i} Q e^{D_g k^2 t} d(D_g k^2) \quad (5.47)$$

According to a theorem given in Carslaw and Jaeger[55],

$$\frac{1}{D_g k^2} \left( L_{(D_g k^2)} \{q\} \right) = \left( L_{(D_g k^2)} \left\{ \int_0^t q(t', w) dt' \right\} \right) \quad (5.48)$$

So, we can obtain

$$F_{g2}(t, w) \cdot e^{w^2 D_g t} = \int_0^t \left( \frac{1}{2\pi i} \int_{-\infty i}^{\infty i} Q e^{D_g k^2 t'} d(D_g k^2) \right) dt \quad (5.49)$$

Changing the order of the integration and integrating over  $t$  lead to

$$F_{g2}(t, w) \cdot e^{w^2 D_g t} = \frac{1}{2\pi i} \int_{-\infty i}^{\infty i} (e^{D_g k^2 t} - 1) \cdot \psi_{g2}(r, w, s) \cdot d(D_g k^2) \quad (5.50)$$

$$F_{g2}(t, w) = -2M \cdot (\Delta - 1) \cdot w^2 \cdot e^{-w^2 D_g t} \cdot \frac{1}{2\pi i} \int_{-\infty i}^{\infty i} \frac{(e^{D_g k^2 t} - 1) \cdot K_0(kr)}{k^2 D_g \left[ \frac{2}{a} k K_1(ka) + k'^2 \Delta K_0(ka) \right]} \cdot d(D_g k^2) \quad (5.51)$$

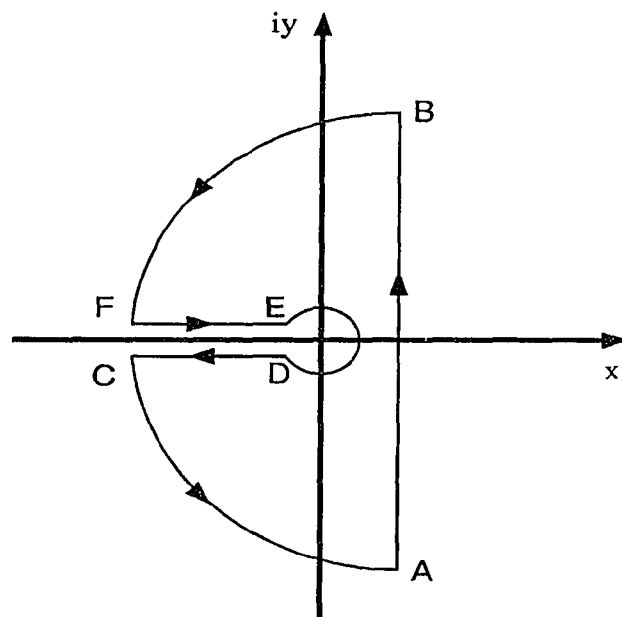


**Figure 5.4** Integral contour.

The integration is now over  $k^2 D_g$  so that the phase of  $k$  itself is in the range  $-\pi/2$  to  $\pi/2$ . It is confined to the right half of the complex plane. It is also found that the integrand of above equation contains no singularities other than a branch point at the origin. The integration will follow Figure 5.4. The line integral can be replaced by the sum of the integrals over CD, EF, and the small circle about the origin.



The integral around the small circle contributes zero because of the exponential term minus one. Let  $k^2 = u^2 e^{i\pi}$  and the integral along EF is expressed as follows :

$$\frac{1}{2\pi i} \int_0^\infty \frac{(e^{-D_g u^2 t} - 1) \cdot K_0\left(rue^{i\pi/2}\right)}{u^2 e^{i\pi} D_g \left[ \frac{2}{\alpha} u e^{i\pi/2} K_1\left(ue^{i\pi/2}\alpha\right) + [u^2 e^{i\pi} + (\Delta - 1)w^2] \Delta K_0\left(ue^{i\pi/2}\alpha\right) \right]} \cdot 2ue^{i\pi} D_g du \quad (5.52)$$

Since  $K_0\left(ze^{i\pi/2}\right) = -\frac{\pi i}{2} [J_0(z) - iY_0(z)]$  and  $K_1\left(ze^{i\pi/2}\right) = -\frac{\pi i}{2} e^{i\pi/2} [J_1(z) - iY_1(z)]$ , [56] the above equation becomes

$$2 \int_0^\infty \frac{[J_0(ru)\theta + Y_0(ru)\varphi] + i[J_0(ru)\varphi' - Y_0(ru)\theta']}{\theta'^2 + \varphi'^2} \cdot \frac{e^{-D_g u^2 t} - 1}{u} du \quad (5.53)$$

where

$$\begin{aligned} \varphi' &= \frac{2}{\alpha} u Y_1(\alpha u) + [(\Delta - 1)w^2 - u^2] Y_0(\alpha u) \\ \theta' &= \frac{2}{\alpha} u J_1(\alpha u) + [(\Delta - 1)w^2 - u^2] J_0(\alpha u) \end{aligned}$$

The integral over CD gives minus the conjugate of above equation

$$-2 \int_0^\infty \frac{[J_0(ru)\theta' + Y_0(ru)\varphi'] - i[J_0(ru)\varphi' - Y_0(ru)\theta']}{\theta'^2 + \varphi'^2} \cdot \frac{e^{-D_g u^2 t} - 1}{u} du \quad (5.54)$$

Combining all these results, we finally have

$$F_{g2}(t, w) = -2M \cdot (\Delta - 1) \cdot w^2 \cdot e^{-w^2 D_g t} \cdot \frac{2}{\pi} \int_0^\infty \frac{J_0(ru)\varphi' - Y_0(ru)\theta'}{\theta'^2 + \varphi'^2} \cdot \frac{e^{D_g u^2 t} - 1}{u} du \quad (5.55)$$

Let  $w^2 = \frac{x^2 \alpha^2}{a^2}$  and  $k^2 = \frac{z^2 \alpha^2}{a^2} e^{i\pi}$ . The above equation becomes

$$F_{g2}(t, w) = 4M \cdot \frac{x^2 \beta}{\pi} \cdot e^{-x^2} \cdot \int_0^\infty \frac{J_0\left(z\alpha \frac{r}{a}\right)\varphi - Y_0\left(z\alpha \frac{r}{a}\right)\theta}{\theta^2 + \varphi^2} \cdot \frac{1 - e^{-z^2}}{z} dz \quad (5.56)$$

where  $\alpha = \frac{a}{\sqrt{D_g t}}$ ,  $\beta = (\Delta - 1)\alpha$ , and

$$\begin{aligned}\varphi &= 2zY_1(\alpha z) + [x^2\beta - z^2\alpha]Y_0(\alpha z) \\ \theta &= 2zJ_1(\alpha z) + [x^2\beta - z^2\alpha]J_0(\alpha z)\end{aligned}$$

Finally  $c_{g2}$  can be derived by Fourier inverse transform of  $F_{g2}$ .

$$\begin{aligned}c_{g2}(r, y, t) &= \frac{2}{\pi} \int_0^{\infty} F_{g2}(t, w) \cdot \cos(wy) dw \\ &= \frac{8}{\pi^2} \frac{\alpha\beta M}{a} \int_0^{\infty} x^2 e^{-x^2} \cos(\eta x) dx \int_0^{\infty} \frac{1 - e^{-z^2}}{z} \frac{J_0\left(z\alpha \frac{r}{a}\right)\varphi - Y_0\left(z\alpha \frac{r}{a}\right)\theta}{\theta^2 + \varphi^2} dz\end{aligned}\quad (5.57)$$

The concentration outside the dislocations,  $r > a$ , is then the sum of  $c_{g1}$  and  $c_{g2}$ . It is expressed as

$$c_g(r, y, t) = c_{g1}(r, y, t) + c_{g2}(r, y, t) \quad (5.58)$$

The concentration inside the dislocations,  $r < a$ , is  $c_d(r, y, t) = c_g(a, y, t)$

Since mean concentration is usually measured in section type experiments, the mean concentration of this model is also derived. From the above result we can see the concentration is the sum of two terms:  $c_{g1}$ , the concentration in the absence of any dislocations, plus the concentration,  $c_{g2}$ , outside a dislocation. Thus the mean concentration,  $\langle c(y, t) \rangle$  can be derived as follows

$$\langle c(y, t) \rangle = c_{g1}(y, t) + d \cdot q(y, t) \quad (5.59)$$

where  $d$  is the dislocation density (number per  $\mu\text{m}$ ) and  $q(y, t)$  is defined as

$$\begin{aligned}q(y, t) &= \int_0^a 2\pi r \cdot c_d(y, t) dr + \int_a^{\infty} 2\pi r \cdot c_{g2}(r, y, t) dr \\ &= q_i + q_e\end{aligned}\quad (5.60)$$

From the assumption,  $c_d(y, t)$  is the function of  $y$  and  $t$ . So  $q_i$  can be derived as

$$q_i = \pi a^2 \cdot c_d(y, t) = \pi a^2 \cdot c_{g2}(a, y, t) \quad (5.61)$$

$q_e$  can be derived as follows

$$\begin{aligned}
 q_e &= \int_a^\infty c_{g2}(r, y, t) \cdot 2\pi r dr \\
 &= \frac{8}{\pi^2} \frac{\alpha\beta M}{a} \int_0^\infty x^2 e^{-x^2} \cos(\eta x) dx \int_0^\infty \frac{1-e^{-z^2}}{z} \frac{\int_a^\infty 2\pi r \left\{ J_0\left(z\alpha\frac{r}{a}\right)\phi - Y_0\left(z\alpha\frac{r}{a}\right)\theta \right\} dr}{\theta^2 + \phi^2} dz \\
 &= \frac{-32Ma}{\pi^2} \frac{\beta}{\alpha} \int_0^\infty x^2 e^{-x^2} \cos(\eta x) dx \int_0^\infty \frac{1-e^{-z^2}}{z^3} \frac{x^2\beta - z^2\alpha}{\theta^2 + \phi^2} dz
 \end{aligned} \tag{5.62}$$

Then

$$\langle c(y, t) \rangle = c_{g1}(y, t) + d \cdot [q_i(y, t) + q_e(y, t)] \tag{5.63}$$

From the above result, we can find the dislocation density plays an important role in the mean concentration. The change of dislocation density will affect the change of mean concentration distribution. Also the mean concentration is a function of  $y$ . The diffusion depth can be represented by the mean concentration distribution.

## CHAPTER 6

### METHODOLOGY

#### 6.1 Material Selection and Specimens Preparation

A list of selected materials and their chemical compositions is shown in Table 6.1. These materials are selected because of their wide usage in industry. The details of the specimens used were as follows:

**Table 6.1** Material Compositions.

Materials	Compositions(wt. %)					
	C	Si	Mn	Cr	Mo	V
AISI D2	1.55	0.3	0.3	12	0.8	0.8
AISI H13	0.38	1.0	0.4	5.3	1.3	0.9
AISI 420	0.38	0.8	0.5	13.6	0.3	

AISI D2 is a high carbon and high chromium tool steel. In this study a cold-worked tool steel is used. It is characterized by high wear resistance, high compressive strength, and good hardening properties. This type of material is always recommended for cutting tools and forming tools which require very high wear resistance and moderate toughness. The nitrided D2 can have a hard diffused surface layer which is very resistant to wear and erosion, and also improves corrosion resistance.

AISI H13 is a chromium-molybdenum-vanadium alloy steel. It is characterized by good resistance to abrasion, high toughness and ductility, good resistance to thermal fatigue, and very limited distortion during hardening. The applications of this material are in tools for extrusion, plastic molding, and punches. The nitriding can enhance the wear and erosion resistance. Also nitriding can result in higher surface hardness.

AISI 420 is a chromium-alloyed stainless steel. It has good corrosion resistance, good wear resistance, and good stability in hardening properties. It is generally used in all

types of moldings, such as injection molds, compression/transfer mold, and extrusion dies. The nitriding can improve its wear resistance and surface hardness.

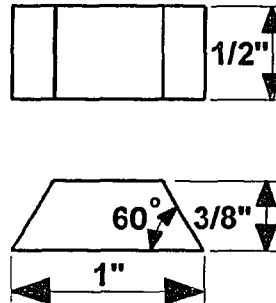


**Figure 6.1** Shoe for wear testing.

All samples for the experiment were cut off from the material bar. One surface of the sample was machine ground. This ground surface was designed for wear testing and metallurgical observation. The wear testing specimen-shoe was prepared as shown in Figure 6.1.

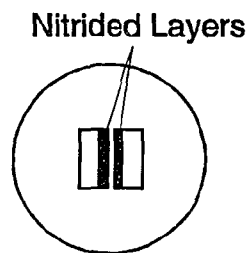


**Figure 6.2** Specimen arrangement for metallurgical analysis.

For metallurgical studies, materials are cut into  $5 \times 5 \times 5 \text{ mm}^3$  pieces by using a Leco CM-20 cut-off machine. The cut-off blade is an aluminum oxide abrasive cutoff wheel. When samples were nitrided, the ground surface was placed face up. The specimens were mounted primarily for easy handling and for protection during preparation. The material for mounting is Lucite. Because the observed surfaces must be flat for microscopic observation and taking photo, a special arrangement for specimen mounting is shown in

Figure 6.2 The ground surfaces from two samples are placed against each other for edge protection and layer observation. The mounted samples were then brought to grind and polish from 180-800 grid siliconcarbide polishing paper. The fine polishing is done by using 5 $\mu$  diamond paste in cloth. The samples were then cleaned by using acetone and methanol in an ultrasonic cleaner. For optical microscopic observation, the following etching solutions were used and are shown in Table 6.2.

**Table 6.2** Etching solutions for tested materials.

Etchant	Compositions	Materials	Sources
1-5% Nital	1-5 ml Nitric Acid 95-100 ml Ethanol or Methanol	Tool Steel	[57]
Ferric Chloride	7 g FeCl <sub>3</sub> 5 ml HCl 100 ml Ethanol	Stainless Steel	[58]
Vilella Reagent	5 ml HCl 1 g Picric Acid 100 ml Ethanol	Tool Steel Stainless Steel	[58]
	5 ml H <sub>2</sub> SO <sub>4</sub> 95 ml H <sub>2</sub> O	Stainless Steel	[59]
Oxalic Acid	10 g Oxalic Acid 100 ml H <sub>2</sub> O	Stainless Steel	[59]
	10 ml HCl 90 ml Methanol	Stainless Steel	[59]

## 6.2. Design of Magneto-Plasma Nitriding Process Parameters

### 6.2.1 The Optimization of PIN Process Parameters

The PIN process can obtain required surface layers for industrial applications. To achieve this requirement, we have to control the process parameters. There are four main process parameters to be controlled. They are gas composition, temperature, time and gas pressure. These four parameters have different influence on the formation of the nitriding layers.

Gas composition can affect the formation of the nitride layer but will have less effect on the formation of the diffusion zone. The dependence of the nitride layers on the gas

composition is shown in Figure 6.3. Temperature can influence the surface structure. In general, case-depth increases with increasing temperature because of the increase of nitrogen diffusivity. Time is an important parameter affecting both the composition and distribution of surface layers. It also plays a key role in the diffusion process. Gas pressure is less important in the formation of surface structure than the rest of the parameters. It is found that the concentration of nitrogen in the surface increases with an increase of pressure in the chamber.

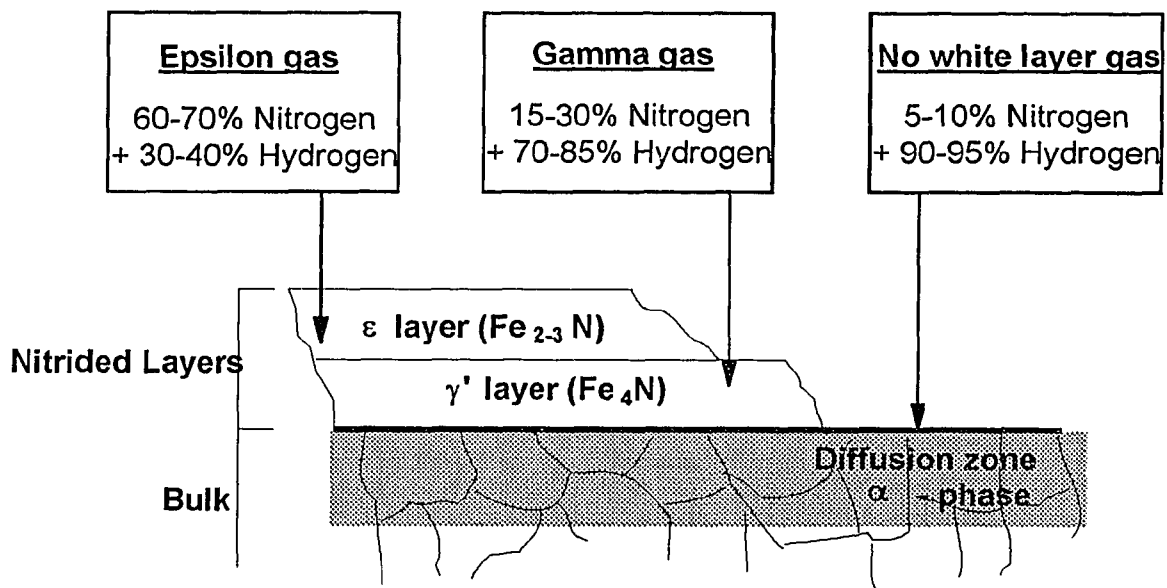


**Figure 6.3** The effect of gas composition on the formation of layers.

Although many reports have discussed the influence of these parameters on nitriding layers separately[60-63], a thorough consideration of all parameters to specific material is still required. However, to accomplish a complete experimental test for one material is tedious and time consuming. It is estimated that around 100 experiments have to be done for one material, if three values of each control parameters are selected.

**Table 6.3** The value of PIN process control parameters.

Parameters	Range
Time	6 - 10 hours
Temperature	550° - 650°C
Gas Composition	50 - 70% N <sub>2</sub>
Pressure	3 - 5 torr

In this study, an orthogonal experimental method is introduced to optimize the PIN control parameters. The orthogonal experimental method is a statistical method for the arrangement and analysis of multi-factor experiments. It is based on the orthogonal theory which is derived from the theory of probability and statistics. According to this theory, if the orthogonal selection and the combination of each parameter in each value are given, the limited number of representative tests can give same information as complete testings can give. By using the method, the number of testing can be minimized without losing the results. Also, the most important thing is that many factors can be considered simultaneously. It can really reflect the relations of all parameters.

**Table 6.4** Parameters for orthogonal testing.

Index Number	Time t(hours)	Temperature T(°C)	Pressure P(torr)	Gas Compositions C(% N <sub>2</sub> )
1	6	550	3	50
2	8	600	4	60
3	10	650	5	70

Testing Number	Time	Temperature	Pressure	Gas Composition
1	t1	T1	P2	C3
2	t2	T1	P1	C1
3	t3	T1	P3	C2
4	t1	T2	P1	C2
5	t2	T2	P2	C3
6	t3	T2	P3	C1
7	t1	T3	P3	C1
8	t2	T3	P2	C2
9	t3	T3	P2	C3



The equal distribution and uniform comparability are two aspects of the orthogonal method. By choosing a range of testing parameters, we can obtain the equal distribution and uniform comparability for both experimental parameters and results. The saving of time, energy, material, and labor are considerable for the multi-factor, multi-value testings. In the optimization experiment, four parameters are chosen and given three representative values. The values of the control parameters for the testing are shown in Table 6.3. The arrangement of these parameters according to orthogonal theory are shown in Table 6.4, where time, temperature, gas composition, and gas pressure are represented by  $t$ ,  $T$ ,  $C$ , and  $P$  respectively. The detailed derivation of the orthogonal factors is shown in the following chapter.

The testing results are carefully analyzed for the influence on hardness, thickness of layers, and weight gain. This work had been described in [64] by Yang. According to the results, it is found that the degree of influence on nitriding results is time, gas, composition, temperature and gas pressure respectively.

**Table 6.5** Magneto-plasma ion nitriding testing parameters and specimen symbols.

Temperature °C	Gas Composition N <sub>2</sub> /H <sub>2</sub>	Magnetic Treatment (20 cycles)		
		None	Before	After
650	65/35	1	2	3
550	65/35	4	5	6
550	25/75	7	8	9
650	25/75	10	11	12
550	5/95	13	14	15
650	5/95	16	17	18

### 6.2.2 The Design of Magneto-Plasma Nitriding Parameters

The design of magneto-plasma ion nitriding process parameters is shown in Table 6.5. In the PIN process, the control parameters of treatment time and gas pressure are fixed and the temperature and gas composition are varied. Although longer treating time can achieve better nitriding results, longer operating time is undesired in industry. The

designed treatment time, 6 hours, is considered for practical applications. One hour preparation, one hour cooling chamber, and 6 hours operating time can fit the standard working time shift of 8-hour days. The gas pressure is fixed because of its smaller influence on nitriding results. The chamber pressure, 3 torr, is chosen because lower pressure can ensure more pure gas inside the chamber. Also, this is the efficient range for our system. In previous studies, small and large nitrogen concentrations were not used. To continue the previous work, different nitrogen concentrations were selected. The nitriding temperature can not be high above the transformation temperature or low to affect the diffusion process. The selected temperature values are discussed in many studies and used for comparison in this study.

The magnetic treatment is applied before and after PIN process. The pre-magnetized nitriding sample is used to study how pulsed magnetic treatment affect the layer formation. The post-magnetized nitriding sample is used to specify the stress relieving in the layer. One cycle of magnetic treatment is designed for applying one period of positive magnetic field and, thereafter, a period of negative magnetic field. Because various magnetic treatment cycles had been tested, 20 cycles are selected in this study.

### **6.2.3. Devices and Procedures**

The PIN process is performed by using Eltec's Aerovac-TM II multipurpose, metallurgical vacuum furnace system[65]. The system includes a vacuum chamber, press frame, pressing ram and bottom stationary ram, hydraulic system, 6" diffusion pumping system, programmable temperature controller, 80 kvA A.C power supply, 50 kvA high Voltage D.C. power supply, and manual gas management system.

The magnetic treatment is done by using the FluxaTron U102 treatment system. This unit applies a series of magnetic pulses separately with periods of zero field. The system generates programmed pulsed magnetic fields up to 450 Oersted at frequencies of 2 to 30Hz[66,67].

### 6.3 Characterization of Nitrided Layers

The nitrided layers and diffusion zone were characterized by optical microscope, Auger electron spectroscopy, and microhardness measurements. The detailed descriptions of these methods are as follows:

#### 6.3.1 Auger Electron Spectroscopy (AES)

**6.3.1.1 Principle :** The principle mechanism involved in AES is that the Auger electrons are produced when the incident radiation (photons, electrons, or neutral atoms) interacts with an atom with an energy exceeding the necessary energy to remove the inner shell electron (K, L, M ... ) from the atom. This interaction leaves the atom in an excited state with a missing inner-shell electron. These excited atoms are unstable. The de-excitation occurs immediately and results in the emission of an Auger electron. As an example, Figure 6.4 illustrates this process with incident x-rays [68]. When the x-ray is absorbed by an inner-shell electron (K electron in Figure 6.4 (a)), the electron is emitted from the atom and is termed a photoelectron. The resulting atom with a K electron missing is unstable, and de-excitation occurs immediately, resulting in emission of an x-ray or Auger electron. Figure 6.4 (b)

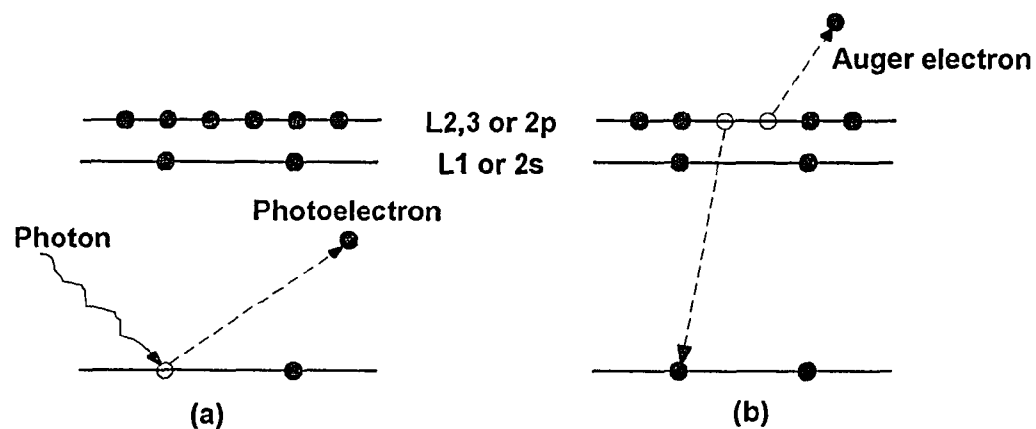


**Figure 6.4** Energy level diagram of (a) photoelectron and (b) Auger electron excitation

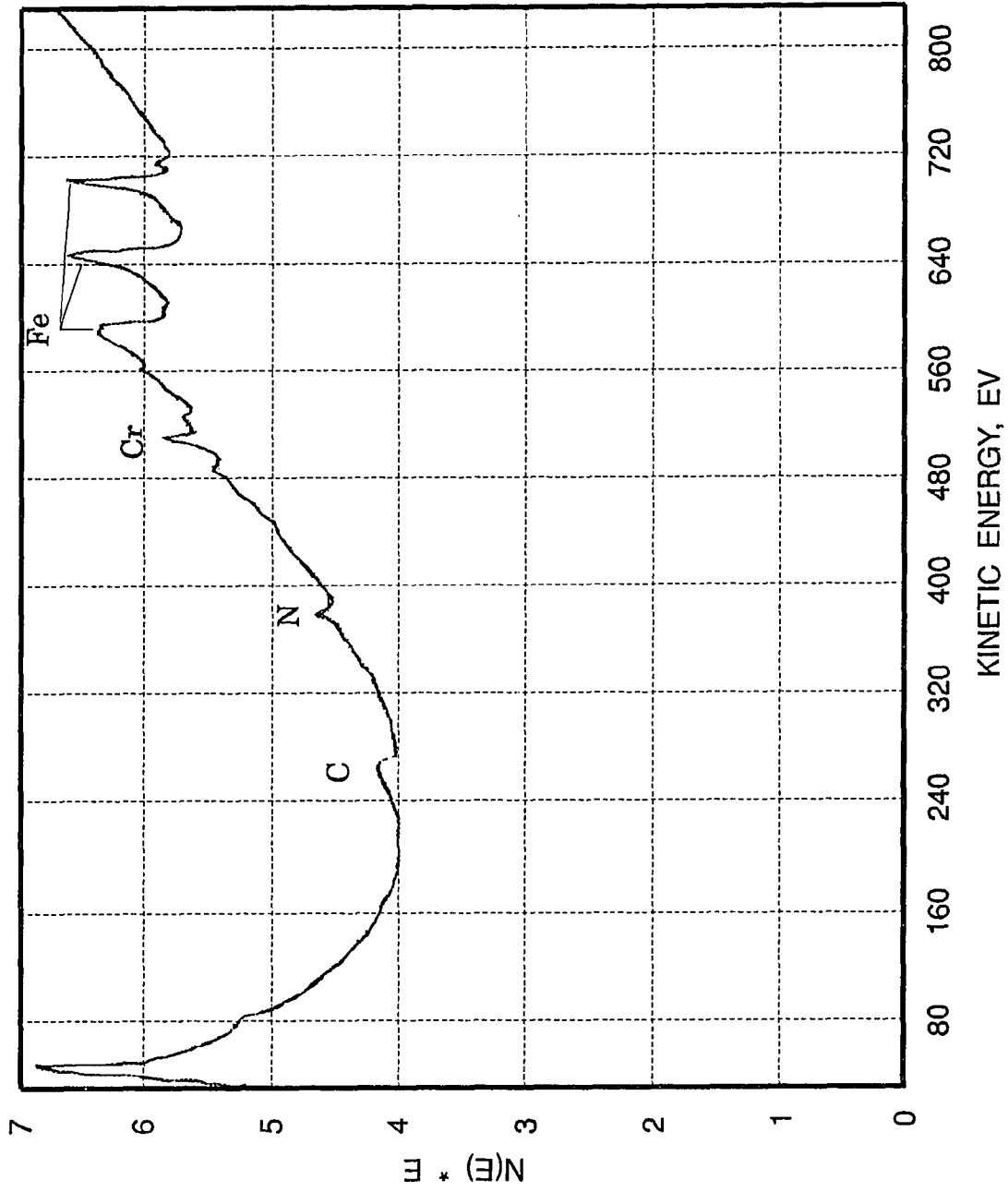


Figure 6.5 Auger electron spectrum for AISI H13 tool steel.

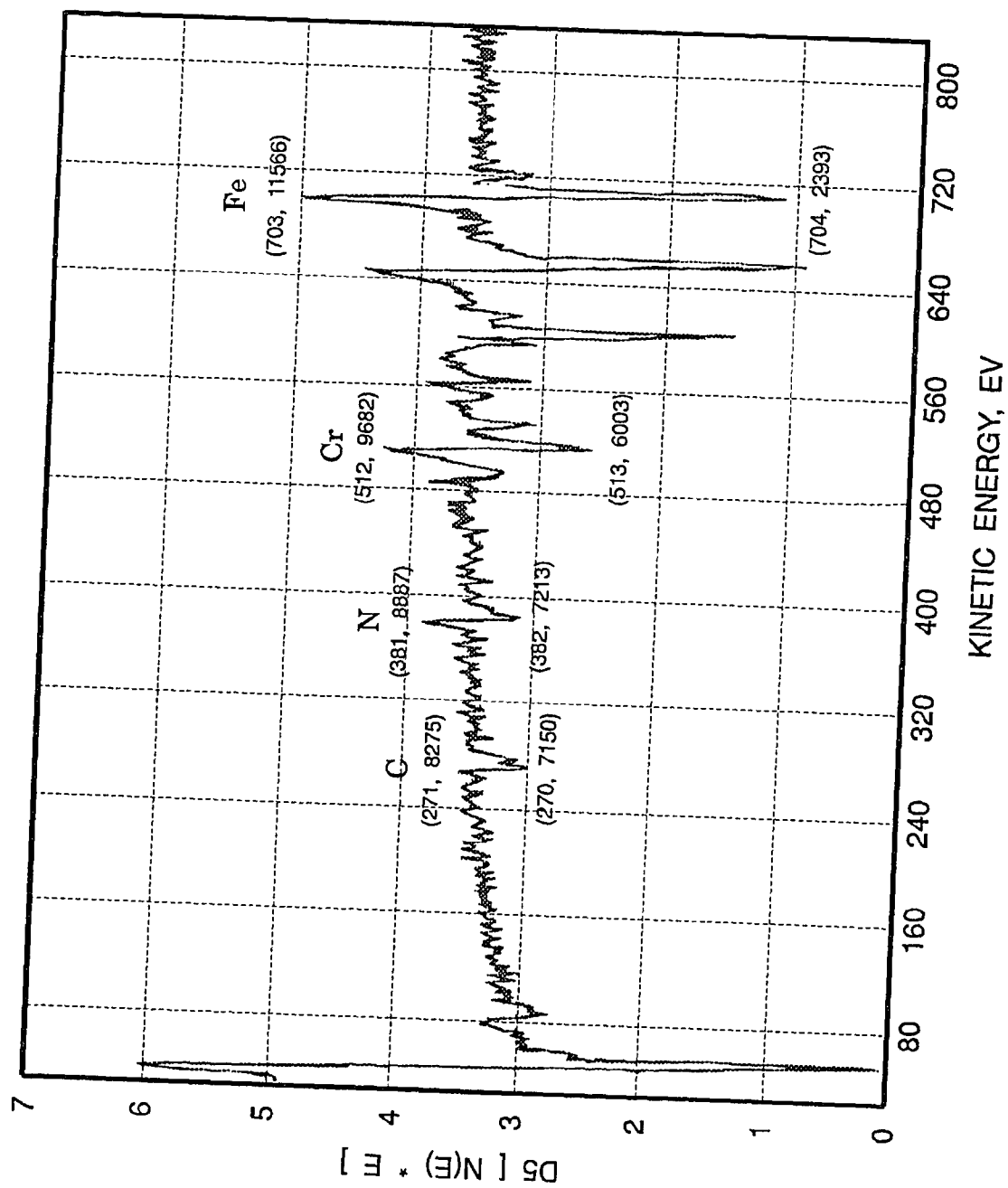
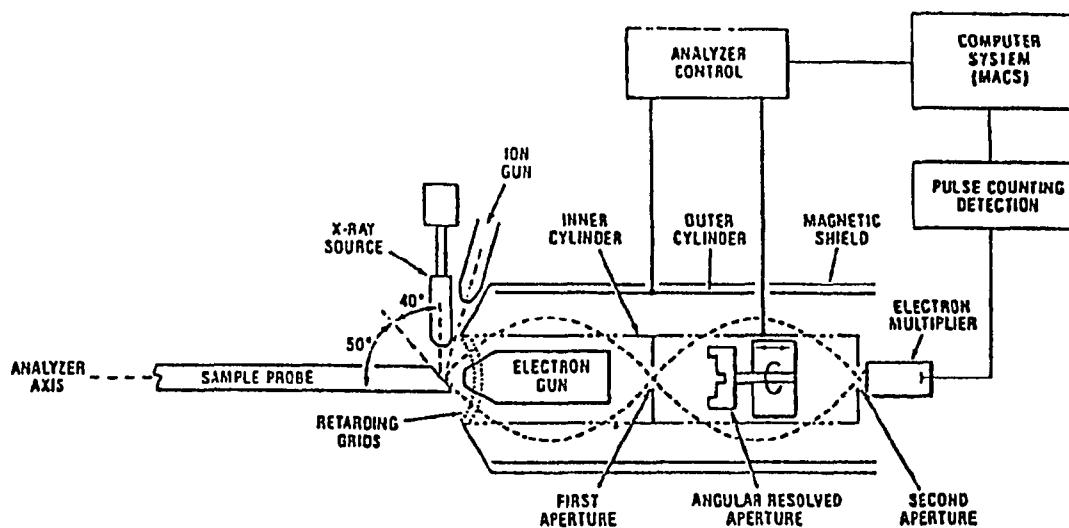


Figure 6.6 Auger electron spectrum for  $d(N(E)/N(E))$  with respect to  $N(E)$ .

The Auger electrons escaping into the vacuum are detected by an electron spectrometer. The Auger electrons are manifest as small peaks in the total energy distribution function  $N(E)$ , such as in Figure 6.5, which is produced from a stainless steel target by a 3keV incident electron beam. The Auger peaks are evident in the  $N(E)$  function, but become more pronounced by electronic differentiation which removes the background disturbances which consist of backscattered primary electrons and inelastic scattered Auger electrons. Figure 6.6 [69]

**6.3.1.2 Equipment and Procedures :** AES instrumentation in its simple form involves a vacuum system, an electron gun for primary electron excitation of the sample, an electron spectrometer for energy analysis of secondary electrons, a secondary electron detector for secondary electron imaging, a stage for sample manipulation, and an ion gun for sputter removal of atoms from the sample surface[70, 71]. Because the AES technique is surface sensitive, an essential requirement is an ultra high vacuum system capable of an ultimate vacuum in the  $10^{-10}$  torr range.



**Figure 6.7** Schematic representation of the PHI Model 550 ESCA/SCM system.

The system used for AES analysis is a Perkin Elmer PHI 560 ESCA(XPS)/SAM/MAC system which is located in the Metallurgy Department of Stevens Institute of Technology(Figure 6.7). The specimen prepared for AES analysis is cleaned in acetone and methanol separately by an ultrasonic cleaner for about 3 minutes. The cleaned specimen is wrapped in aluminum foil for protection and carrying. Before Auger analysis, the specimen is sputtered by using 5 keV electron beam for 10 to 20 minutes in a 2 x 2 mm area to remove the contaminated layers.[72] The AES analysis was performed in two steps. The first step used a survey function in the system to gain the concentration information for N<sub>2</sub>, Cr, and Fe in the layer and bulk materials separately. The next step used a line scan function to get the concentration profile for specific elements from bulk to layer. The way to perform the line scan is shown in Figure 6.8. The exciting beam energy is 3keV, 1mA. Each point scanning time is about 3 minutes. The beam size is 3 to 5 μm. The amplitude of peak from  $dN(E)/dE$  function is collected.[73] The ratio of nitrogen peak to iron peak is calculated. This ratio is then plotted in the ratio vs. depth relation. According to this profile, the position of layer as well as the thickness of layer can be found.

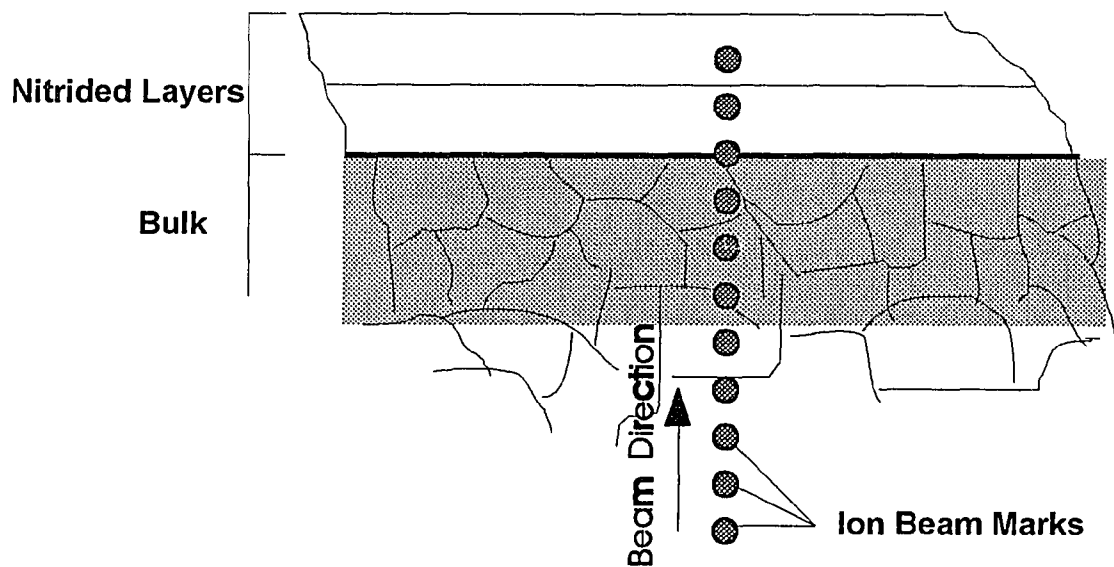


**Figure 6.8** The process of Auger indentation.

However, the technique has a limitation. The atomic ratio of elements in the material must be over 10 to 15%. An atomic ratio less than 10 to 15% can not be detected. According to Figure 2.5, only the compound layers ( $\epsilon, \gamma'$ ) can be detected. It is difficult to show the diffusion zone.

### **6.3.2 Microscope Analysis**

The microscopic observation of the specimen was performed with the LECO 2001 Microanalysis Image Analysis System. The system includes a multipurpose metallographic microscope, 386 computer system, image analysis processor and peripheral devices. This system is a combination of microscope, computer, image processing and artificial intelligence technology.

The prepared specimens are examined under the microscope. The image is received from the microscope and bulk materials. The microscopic examination gives us the most direct result of surface structure. A well prepared specimen, proper etching, and adequate interpretation are keys to obtain a proper microscopic analysis.

### **6.3.3 Microhardness Measurement**

Microhardness measurement is the most common tool used to characterize the nitride layers. It is used to get impressions of point hardness variations along the coated layer to the bulk materials.

The microhardness measurement was performed by using a LECO Microhardness Tester System. The system is composed of a M-400 microhardness tester, a DME digital micrometer microscope, a monitor and a TR6193 digital printer. The Vickers Knoop hardness measurement was chosen for this study. The applied load was 25g and time duration was 15 to 20 seconds. The selected load and duration can make the indentation size small enough to measure microhardness in the material and large enough to have precise measurement. The error of each measurement is about  $\pm 5-10\%$ . The way to



indents is shown in Figure 6.9. The hardness gradients can be determined by these point to point hardness indentations. The approximate thickness of the developed surface layer can be determined through microhardness distribution from the surface to the bulk material.

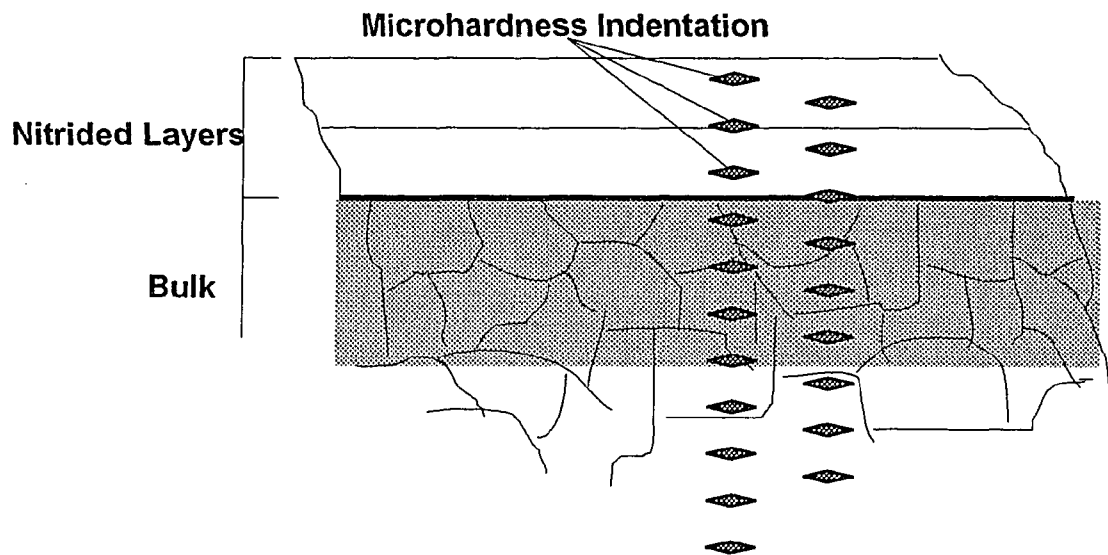


**Figure 6.9** The method to perform microhardness indentation.

A software package, Grapher, was used to make a regression analysis of the hardness profile. A cubic spline, second order, was chosen for the curve fitting.

## 6.4 Wear Testing Process

The computer controlled wear testing approach described in [74] was developed and implemented in the Surface Engineering Laboratory of the ME department of NJIT during the period 1984-1989.

### 6.4.1 Wear Testing Methodology

The wear testing machine is designed on a power loss principle. The power loss information is produced by the stator of the suspended motor. If the shaft with a roller

fixed on it is made to rotate, any resistance to shaft rotation will cause the stator of the motor to rotate in a direction opposite to the rotor or shaft rotation. By recording this reaction, the losses caused by friction in the area of load and slide contact between the engaged roller and shoe can be found after eliminating the total losses in the standard units of the designed system. This can be expressed as

$$e = \frac{P_f}{P_t} \quad (6.1)$$

where  $P_f$  is power generated by friction force at the load and slide contact area;  $P_t$  is total power spend to compensate the losses in the system;  $e$  is efficiency of the total system.

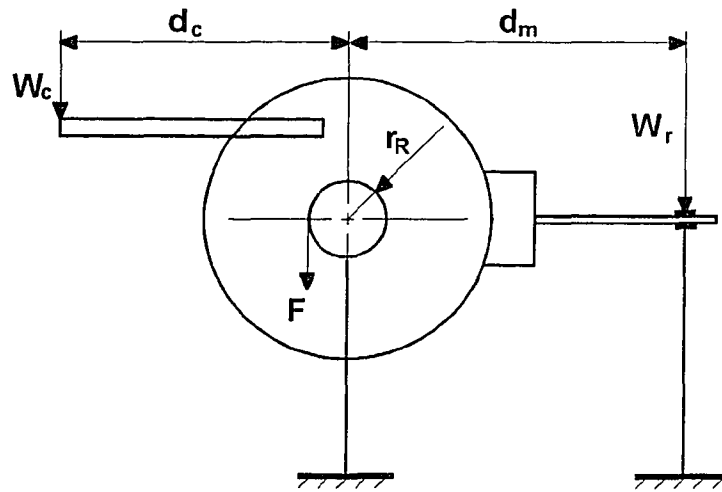


Figure 6.10 Schematic of the suspended motor.

The balanced motor is fixed in the bearings as shown in Figure 6.10.  $P_f$  and  $P_t$  can be computed if appropriate reactive moment on motor's stator- $M_m$  and friction moment on the roller- $M_f$  are defined

$$M_m = W_r \times d_m = F \times r_R \quad (6.2)$$

$$M_f = F_f \times r_r \quad (6.3)$$

where  $W_r$  is the reaction of interaction between rod and stator's bar;  $d_m$  is the distance of  $W_r$  from the rotor axis;  $F_f$  is the friction force on the shoe;  $r_r$  is the radius of the roller;  $F$  is the reactive force generated at the rotor;  $r_R$  is the radius of the rotor.

After substituting Equation (6.2) and (6.3) into (6.1) and assuming that  $N$  and  $N_r$  are speed of the rotor and roller, consequently we can obtain

$$e = \frac{F_f \times r_r \times N_r}{F \times r \times N} = \frac{F_f \times r_r \times N_r}{W_r \times d_m \times N} \quad (6.4)$$

The total efficiency  $e$  of standard units of the system can be assumed as a constant value during the test period. Then Equation (6.4) can be rewritten as

$$F_f = W_r \times \frac{d_m}{r_r} \times \frac{N}{N_r} \times e \quad (6.5)$$

Since

$$F_f = W \times f \quad (6.6)$$

where  $W$  is the applied normal load on the roller and  $f$  is the friction coefficient.

So Equation (6.5) can be expressed as

$$f = \frac{W_r}{W} \times \frac{d_m}{r_r} \times \frac{N}{N_r} \times e \quad (6.7)$$

According to the Equation (6.5) and (6.7), the friction force  $F_f$  and friction coefficient  $f$  are a function of  $W_r$  and  $W_r/W$  consequently.

$$F_f = g(kW_r) \quad (6.8)$$

$$f = h(kW_r/W) \quad (6.9)$$

The requested  $W_r$  and  $W_r/W$  values can be obtained from strain gages which are attached to the stator's bar by preliminary calibration of the designed system. Calibration is done by steadily applying known weights in steps on the side of the motor opposite to the stator's bar as shown in Figure 6.10. In this case

$$M_m = W_r d_m = W_c d_c \quad (6.10)$$

with  $W_c$  as the calibration weight, and  $d_c$  as the distance of the placed weight to the motor's axis. The varying strains developed by calibration will result in different signals given by the strain recorder to the computer. As the result of this calibration a calibration chart can be developed. Using the calibration chart, a simple computer program can be developed to define and analyze the friction force and friction coefficient. This program is capable of providing the researcher with requested test data at any moment and can pick up the moment when the friction coefficient, friction force, and power losses are catastrophically increased; this represents the beginning of catastrophic wear in the area of load and slide contact.

#### **6.4.2 Wear Testing Machine**

The overall design of the wear testing apparatus is shown in Figure 6.11. The apparatus was designed to measure wear, friction force, friction coefficient and surface finish. It consists of a motor, reducer, load mechanism, output mechanism and a roller-on-shoe friction couple.

The roller-on-shoe friction couple was selected to simulate operational conditions. The rotor's shaft of the motor-(1) is redesigned and suspended between two pillow block bearings. One end of this shaft is coupled to a parallel shaft of gear reducer-(2). The other end is connected to a counter-(3) which is capable of recording test runs. The other end of the reducer is coupled to the shaft-(4) to which the roller-(5) is fixed. A shoe-(6) clamped by a shoe holder is designed to perfectly engage with the roller while the load is applied. The load mechanism-(7) consists of a lever system and a linear sliding-pusher. The lever system is arranged to have higher output load while a small input load is added. The precise linear slider-pusher is used to load the contact area of the tested specimens. The output mechanism includes a bending bar-(8), a set of strain gages-(9) attached to the bar, a strain recorder-(10), and a computer-(11). One end of the bending bar is fixed to the stator and another is fastened to the stopper. The strain gages attached to the bending

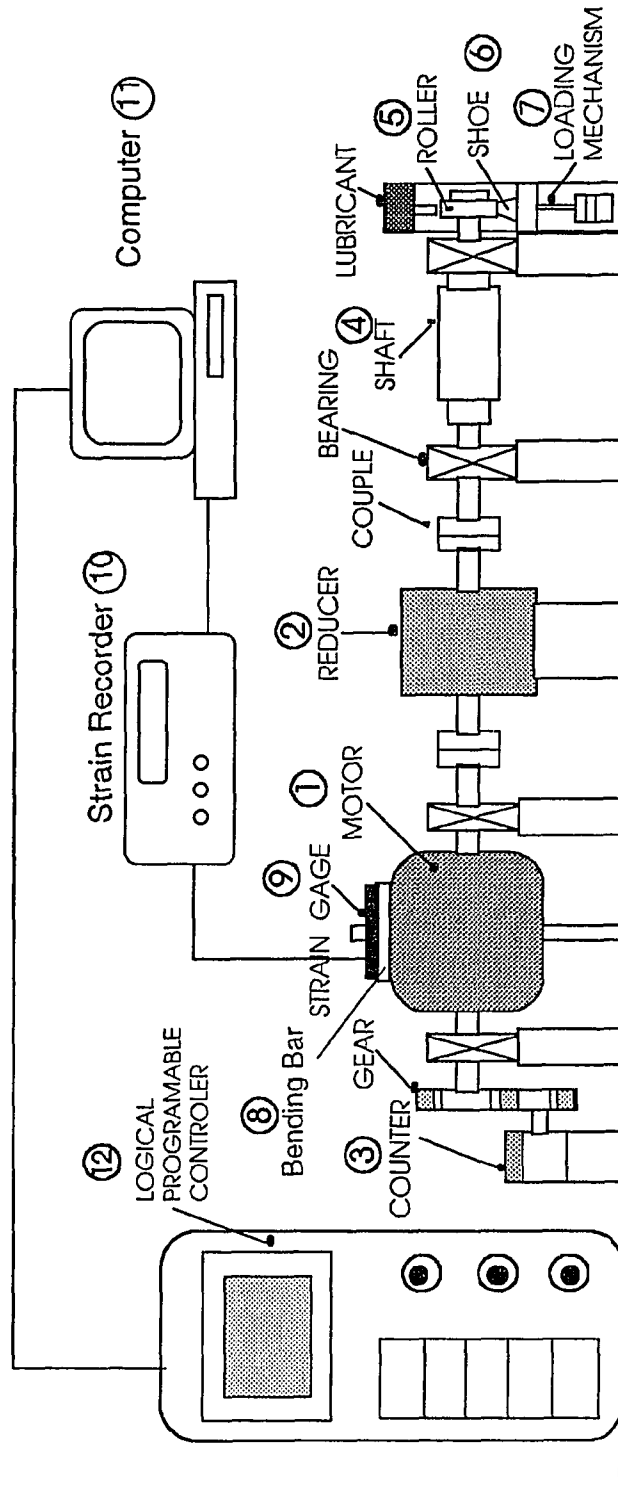


Figure 6.11 Wear testing machine and system.

bar and connected to the strain recorder are used to monitor the varying torque of the suspended motor. The strain recorder is used to collect the varying signals from the strain gages and feed these signals into the computer which is furnished with a program that can automatically analyze and evaluate the power losses, the friction force, and the friction coefficient, and print the obtained results.

The programable logic controller-(12)(PLC) was installed on the wear testing machine by Yao.[75] The PLC was used to control and monitor the testing procedures. It can perform precisely in time, turning on and off the motor for the sliding test, switching lubrication on and off, loading and unloading applied weights, and starting the program in the computer to record the data. Once the PLC is initialized, the wear testing can be automatically done by executing the step program in PLC. Man-is not requested to monitor testing.

#### **6.4.3 Process Control and Procedure**

The wear experiments were conducted at ambient temperature and one atmosphere. The specimens were tested under boundary lubrication condition by using SAE 10 oil. The circumferential velocity of the rotating roller was 0.74 m/sec. The test was run for 30 minute intervals or a sliding distance of 1580 m until catastrophic wear occurred. The applied nominal load was 95 kg. The efficiency of the driving system,  $e$ , was set to 0.8. In each test interval, the roller and shoe were dismantled for the measurement of wear rate and the surface analysis. Before and after examination, specimens were cleaned with acetone, weighed with an electron balance (accuracy of 0.00001 mg) and inspected with an optical microscope.

The computer was used to control the process and analyze wear, friction, and power losses. Once the above parameters were set and the calibration chart was prepared, the whole wear testing process was monitored by the computer and the output data were

recorded in the disk. As soon as the data were collected, the relationships of friction force and friction coefficient vs. sliding distance were established.

#### **6.4.4 Surface Measurement**

The surface measurements were made with a FEDERAL Surfanalyzer System 4000 tracer type instrument. Surface measuring takes place before and after the wear testing interval. Three traces were taken on each shoe and roller. The places to be measured in each shoe and roller were marked for the comparison. Each trace was recorded in the computer. A Basic program was used to analyze the recorded data. The results from the running the program can give different roughness parameters, such as  $R_a$ ,  $R_y$ ,  $T_p$ .

## CHAPTER 7

### RESULTS AND DISCUSSION

#### 7.1 Selection of Control Parameters for PIN Process

As described in previous section, the orthogonal experimental method is used to optimize the PIN process parameters. These parameters are shown in Table 6.4. The procedures to obtain the orthogonal values for the testing are presented by using the analysis of the maximum hardness for AISI D2 tool steel as an example. All the procedures are concluded in the following steps:

1. Calculation of the range percentage  $R_p$  for the max. hardness data (Table 7.1).

$$R_p = \frac{100}{H_{max} - H_{min}} = \frac{100}{1880 - 1250} = 0.159$$

2. Computation of the range value  $H'_i$  for each max. hardness data .

$$H'_1 = R_p \cdot H_1 = 0.159 \times 1800 = 286.2$$

⋮

$$H'_9 = R_p \cdot H_9 = 0.159 \times 1250 = 198.8$$

3. Definition of the scale value I, II, III for parameters.

$$I(t = t_1) = \frac{1}{3}(H'_1 + H'_4 + H'_7) = \frac{1}{3}(286.2 + 278.3 + 298.9) = 287.8$$

$$II(t = t_2) = \frac{1}{3}(H'_2 + H'_5 + H'_8) = \frac{1}{3}(262.4 + 214.7 + 238.5) = 238.5$$

$$III(t = t_3) = \frac{1}{3}(H'_3 + H'_6 + H'_9) = \frac{1}{3}(238.5 + 230.6 + 198.9) = 222.7$$

$$I(T = T_1) = \frac{1}{3}(H'_1 + H'_2 + H'_3) = \frac{1}{3}(286.2 + 262.4 + 238.5) = 262.4$$

$$II(T = T_2) = \frac{1}{3}(H'_4 + H'_5 + H'_6) = \frac{1}{3}(278.3 + 214.7 + 230.6) = 241.2$$

$$III(T = T_3) = \frac{1}{3}(H'_7 + H'_8 + H'_9) = \frac{1}{3}(298.9 + 238.5 + 198.9) = 245.4$$



$$I(P = P_1) = \frac{1}{3}(H'_2 + H'_4 + H'_9) = \frac{1}{3}(262.4 + 278.3 + 198.8) = 246.5$$

$$II(P = P_2) = \frac{1}{3}(H'_1 + H'_5 + H'_8) = \frac{1}{3}(286.2 + 214.7 + 238.5) = 246.5$$

$$III(P = P_3) = \frac{1}{3}(H'_3 + H'_6 + H'_7) = \frac{1}{3}(238.5 + 230.6 + 298.9) = 256$$

$$I(C = C_1) = \frac{1}{3}(H'_2 + H'_6 + H'_7) = \frac{1}{3}(262.4 + 230.6 + 298.9) = 264.0$$

$$II(C = C_2) = \frac{1}{3}(H'_3 + H'_4 + H'_8) = \frac{1}{3}(238.5 + 278.3 + 238.5) = 251.8$$

$$III(C = C_3) = \frac{1}{3}(H'_1 + H'_5 + H'_9) = \frac{1}{3}(286.2 + 214.7 + 198.9) = 233.2$$

4. Rate(R) calculation of each parameter by subtracting the minimum scale value from maximum scale value.

$$R(t) = I(t) - III(t) = 287.8 - 222.6 = 65.2$$

$$R(T) = I(T) - II(T) = 262.4 - 241.2 = 21.2$$

$$R(P) = III(P) - I(P) = 256.0 - 246.5 = 9.5$$

$$R(C) = I(C) - III(C) = 264.0 - 233.2 = 30.8$$

**Table 7.1** Orthogonal analysis of maximum hardness for AISI D2 tool steel.

	H <sub>1</sub>	H <sub>2</sub>	H <sub>3</sub>	H <sub>4</sub>	H <sub>5</sub>	H <sub>6</sub>	H <sub>7</sub>	H <sub>8</sub>	H <sub>9</sub>
Max. Hardness	1800	1650	1500	1750	1350	1450	1880	1500	1250
Range Value	286.2	262.4	238.5	278.3	214.7	230.6	298.9	238.5	198.9
	Time		Temperature		Pressure		Composition		
I	287.8		262.4		246.5		264.0		
II	238.5		241.2		246.5		251.8		
III	222.6		245.4		256.0		233.2		
R	65.2		21.2		9.5		30.8		
Optimized Value	6 hour		550°C		5 torr		50% N <sub>2</sub>		

5. The optimized value of each parameter (time, temperature, pressure, gas composition) for the searching conditions are the largest scale values from I, II, or III. The highest influence is defined by the rate calculation R. For example, the optimized value of time is 6 hours because I(t=t<sub>1</sub>) has the largest scale value

among I( $t=t_1$ ), II( $t=t_2$ ), and III( $t=t_3$ ), where  $t_1$ ,  $t_2$  and  $t_3$  are defined in Table 6.4. It also can be seen that the highest influence parameter is time because it has the largest rate value R (= 65.2). From the calculation we can conclude that the process parameters for obtaining maximum hardness are 6 hours, 550°C, 5 torr and 50% N<sub>2</sub>.

The analysis for the selected testing values are conducted by following the above steps. Each parameter is carefully analyzed by its influence on hardness, thickness of case and weight gain. Tables 7.1 to 7.3 show the result of orthogonal analysis for hardness, thickness of case hardened, and weight gained respectively.

**Table 7.2** Orthogonal analysis of case depth for AISI D2 tool steel.

	L <sub>1</sub>	L <sub>2</sub>	L <sub>3</sub>	L <sub>4</sub>	L <sub>5</sub>	L <sub>6</sub>	L <sub>7</sub>	L <sub>8</sub>	L <sub>9</sub>
Case Depth(μm)	120	170	350	110	150	300	190	250	300
Range Value	52.2	73.9	152.2	47.8	65.2	130.4	82.6	108.7	130.4
	Time		Temperature		Pressure		Composition		
I	60.9		92.8		84		95.6		
II	82.6		81.1		97.1		102.9		
III	137.7		107.2		100		82.6		
R	76.8		26.1		16		20.3		
Optimized Value	10 hour		650°C		5 torr		60% N <sub>2</sub>		

**Table 7.3** Orthogonal analysis of weight gain for AISI D2 tool steel.

	W <sub>1</sub>	W <sub>2</sub>	W <sub>3</sub>	W <sub>4</sub>	W <sub>5</sub>	W <sub>6</sub>	W <sub>7</sub>	W <sub>8</sub>	W <sub>9</sub>
Weight Gain(%)	.101	.160	.137	.163	.159	.199	.152	.148	.262
Range Value	62.5	98.8	84.4	100.4	98.3	122.9	93.6	91.3	162.6
	Time		Temperature		Pressure		Composition		
I	85.49		81.9		120.6		105.1		
II	96.1		107.19		92.2		92.02		
III	123.3		115.8		62.1		107.8		
R	37.81		33.9		28.5		15.78		
Optimized Value	10 hour		650°C		3 torr		70% N <sub>2</sub>		

If we only consider the hardness in nitriding, we should chose lower temperature, short time, less nitrogen percentage and higher pressure. Also time is the parameter which

causes the biggest change in microhardness. The pressure parameter has less influence on the microhardness.

However, the microhardness is not the only surface property with which we are concerned, we should also consider the contribution from other process parameters and their interrelation to these properties. Table 7.2 and 7.3 give us a general idea if we only consider, for example, deeper case thickness, we must choose 10 hour, 650°C, 5 torr, 60% N<sub>2</sub>; if we want to obtain better weight gain, we can select 10 hour, 650°C, 3 torr, 70% N<sub>2</sub>. In both cases, time is a very important factor to influence the obtained results.

Table 7.4 collects all final optimized process parameters for three different materials.

**Table 7.4** The results of orthogonal analysis.

Materials	Characterizations	Optimized Control Parameters			
		Time (hours)	Temperature (°C)	Pressure (torr)	Composition (% N <sub>2</sub> )
AISI D2	Microhardness	6	550	5	50
	Case Thickness	10	650	5	60
	Weight Gain	10	650	3	70
AISI H13	Microhardness	6	550	5	50
	Case Thickness	10	650	3	70
	Weight Gain	10	650	3	70
AISI 420	Microhardness	6	550	5	50
	Case Thickness	10	650	3	70
	Weight Gain	10	650	3	70

## 7.2 Nitrided Layer Characterization

The case of the nitrided material can be distinguished into three layers,  $\epsilon$ ,  $\gamma'$ , and diffusion zone. These layers are very difficult to verify because of its diffusion nature. In this study, the optical microscopy, Auger Electron Spectrum analysis, and microhardness measurement are used to characterize the nitrided layers and diffusion zone.

Microhardness measurement is the most common tool used to characterize the nitrided layers. The microhardness indentations are marked along the case depth.

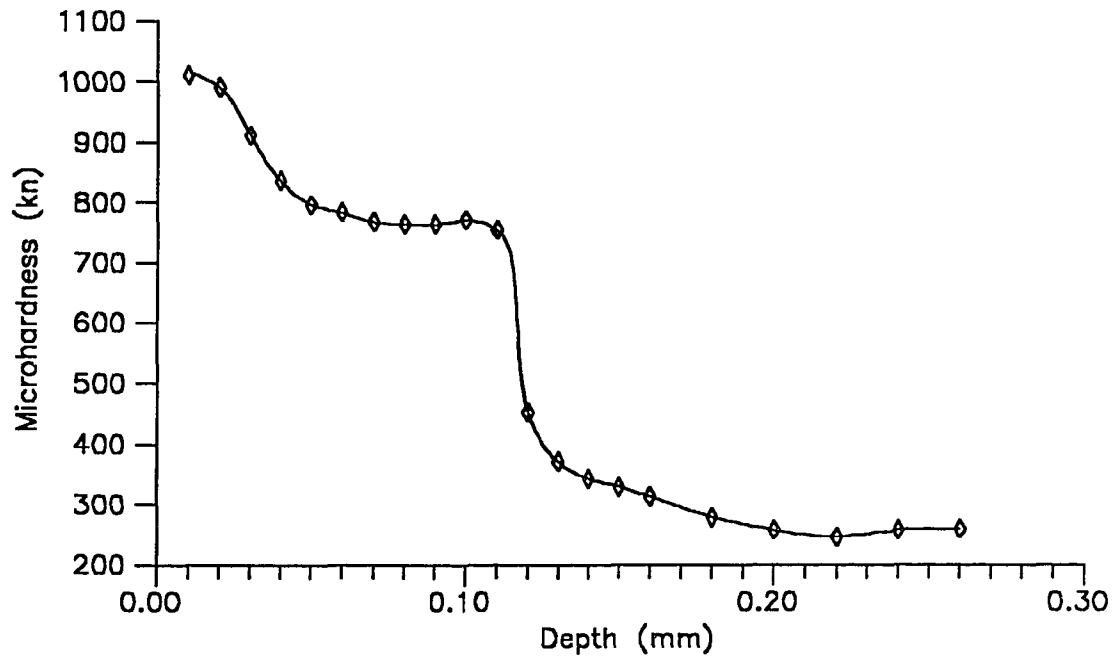


**Figure 7.1** Microhardness profile along the hardened case.(AISI H13 tool steel; 6 hours, 600°C, 4 torr, 55 % N<sub>2</sub> PIN process parameters)

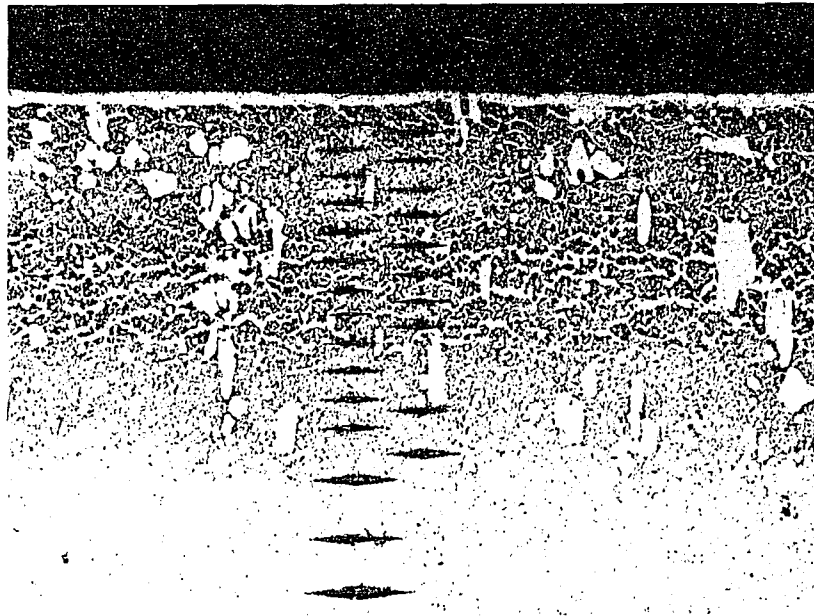


**Figure 7.2** Nitrided layer microstructure of AISI D2 tool steel.

Microhardness data is then collected. The second order cubic spline interpolation is applied to these data to plot the microhardness profile along the case depth. According to the profile in Figure 7.1, the layers can be specified.

However, there are a few disadvantages of this method. The precision of the measurements is affected by the size of the indenter. Since the dimension with which we are concerned is about one micrometer, the indenter can not be very large. Also the distance between two indentation marks can not be too close. If two indentions are too close, this will affect obtaining hardness data. Another disadvantage is the difficulty in measuring a near-edge microhardness. Due to the applied load from indentation, cracks may be initiated at the range close to the edge and result in low microhardness . Sometimes we can find the near-edge microhardness has much smaller hardness than the interior zone. It contradicts what we expect. The homogeneity of grain size in the material can also influence the measurement of microhardness. As can be noticed from the microstructure of the AISI D2 , Figure 7.2, the grains with white color can effect the results of indentation. The microhardness can be different if the indentation is made on those grains. The last problem is the specimen preparation. If the observed surface is not flat, the indentation mark will be difficult to focus. This will affect the measurement. To define the thickness of layers, these concerns must be taken into account. Nevertheless, the microhardness measurements can give the main information of the layer condition. we still need to use other methods to double check and prove the existence of nitrided layers.

Figure 7.3 and 7.4 show the microstructure of nitrided AISI H13 and AISI 420 steels. By using the proper etching process, we can easily find different microstructures for the nitrided layer. For AISI H13 , the white layers indicate layers with the highest hardness. Inside this layer, we also can find the coarse and fine microstructures. Between these layers and bulk material, a layer with the darkness fading away and the feather formation can be found. From all the layers we find, we can define these layers as  $\epsilon$  layers,  $\epsilon+\gamma'$  layers,  $\gamma'$  layers, and diffusion zone, respectively. The  $\epsilon$  layers are always white under

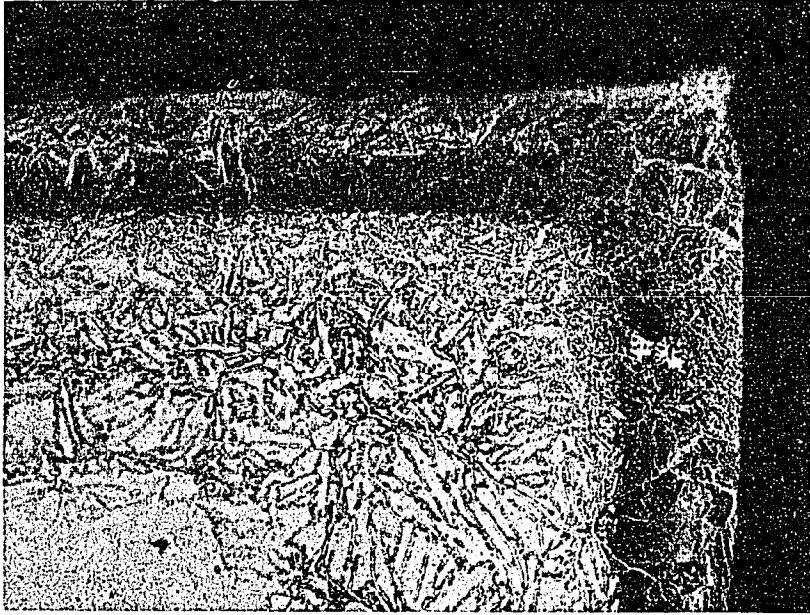


**Figure 7.3** Nitrided layer microstructure of AISI H2 tool steel.

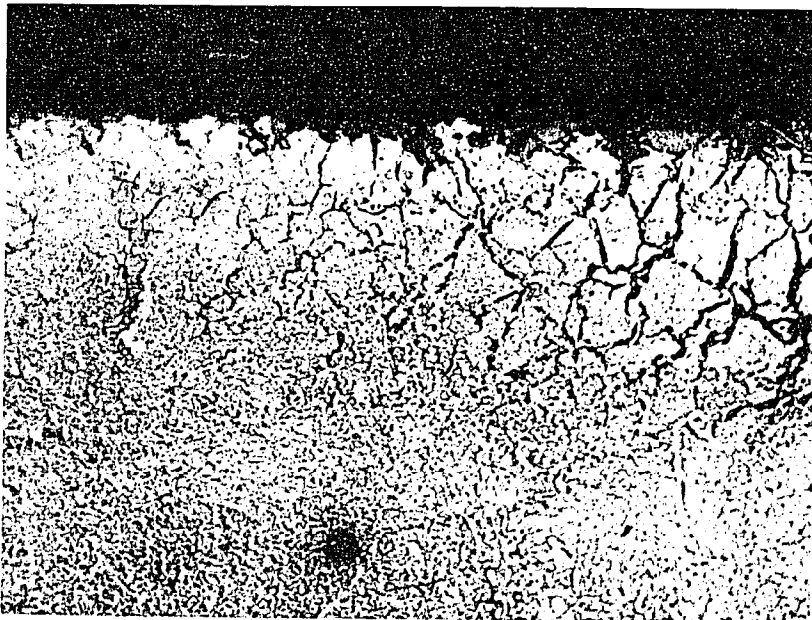


**Figure 7.4** Nitrided layer microstructure of AISI 420 stainless steel.

1  
 t  
 e  
 c  
 st  
 di  
 the  
 7.3  
 etc  
 The  
 etch  
 etch  
 incre  
 can n  
 obtain  
 beam  
 eleme  
 as AE  
 atomic  
 and ird  
 Figure  
 measur

ling... Because of  
 these... phases is also  
 ows... the nitrogen  
 etched... ructure is  
 an... different using  
 the... ructure of  
 shown in... 7.2 and  
 ... al. The  
 elements in the metals.  
 ... Under-  
 the... but over-  
 etching... h may  
 layer... and  
 ... to  
 at... electron  
 fingerprint... for the  
 me energy... plots  
 include... the  
 ... of nitrogen  
 tively... shown in  
 ... and both... and  
 ... and a

the optical microscope. It is also the hardest structure in the nitriding process. Because of the diffusion process, between the  $\epsilon$  and  $\gamma'$  layers, the mix of these two phases is also expected. The fading darkness under the microscope shows that the nitrogen concentration decreased along the case depth.

However, the way we define layers depending on the etched microstructure is strongly related to experience and luck. The microstructure can be different using different etching solutions. Even using the same etching solution, the microstructure of the same nitride layer can be different under the microscope, as shown in Figures 7.2 and 7.3.

The image of the microstructure is related to the elements in the material. The etching solutions have different chemical reactions with different elements in the metals. These can increase the difficulty in defining the layers.

Another important factor in defining layer thickness is the etching time. Under-etching will not give etching solution enough time to react with the material, but over-etching may lose the details of the layers microstructure. The etching approach may increase one layer's thickness at the expense of decreasing another layer's thickness and can mislead the observer in layer thickness measurement.

The method of Auger Electron Spectroscopy(AES) is a very precise technique to obtain information about kinds of elements in the microstructure. At specific electron beam energy, we can only find a specific element. It is just like a fingerprint for the element. The AES collects the number of atoms which release the same energy and plots as AES peaks shown in Figure 6.5. The ratio of these peak amplitudes can give the atomic percentage of the element in material. For example, the auger peaks of nitrogen and iron can be found at electron energies 379 keV and 703 keV respectively, as shown in Figure 6.5. Taking the differential of the curve in Figure 6.5, we can find both peak and measure the amplitude of these peaks as shown in Figure 6.6. For example, we can find a



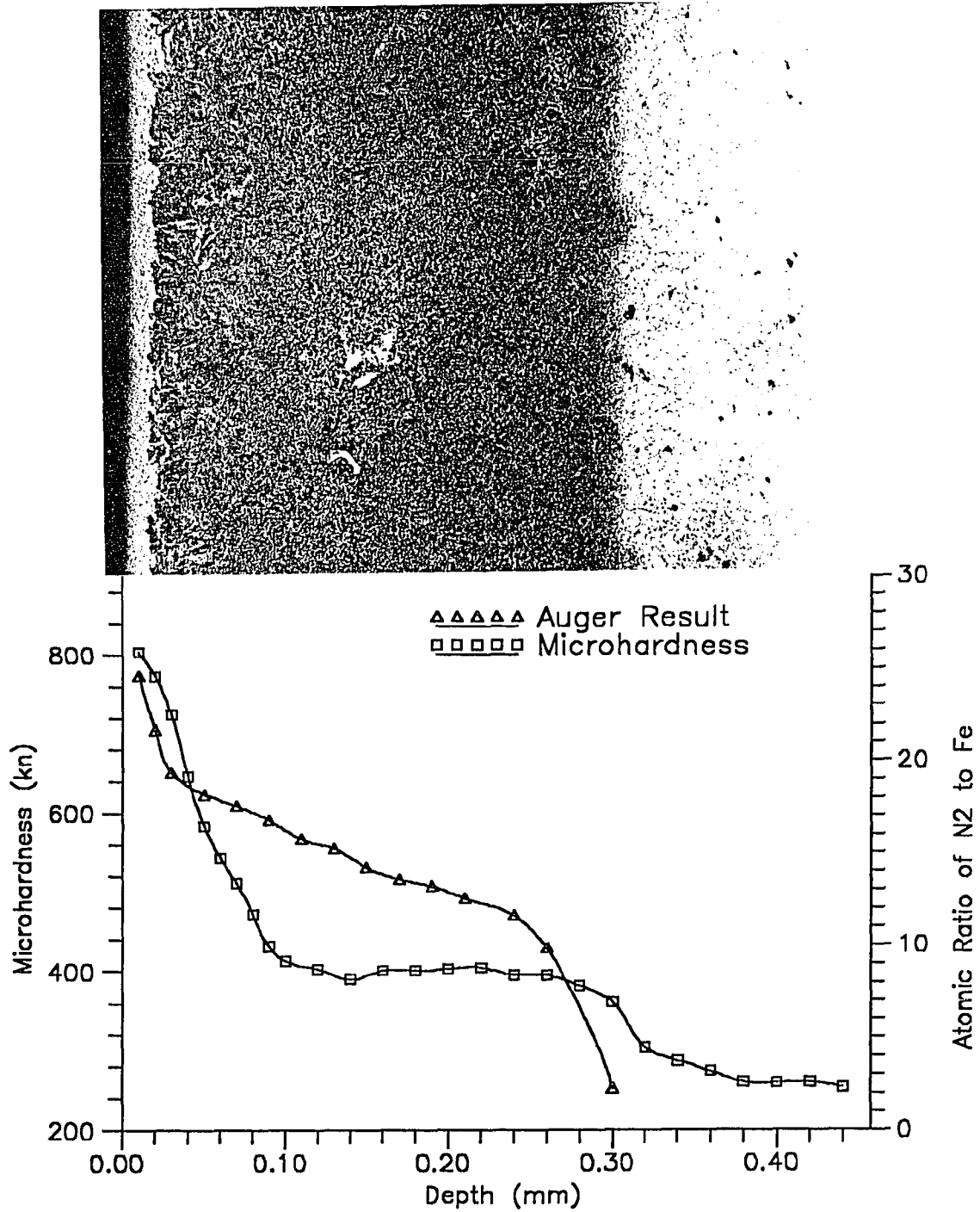


**Figure 7.5** Layers characterization by microstructure, microhardness distribution, and AES analysis for AISI H13 tool steel.

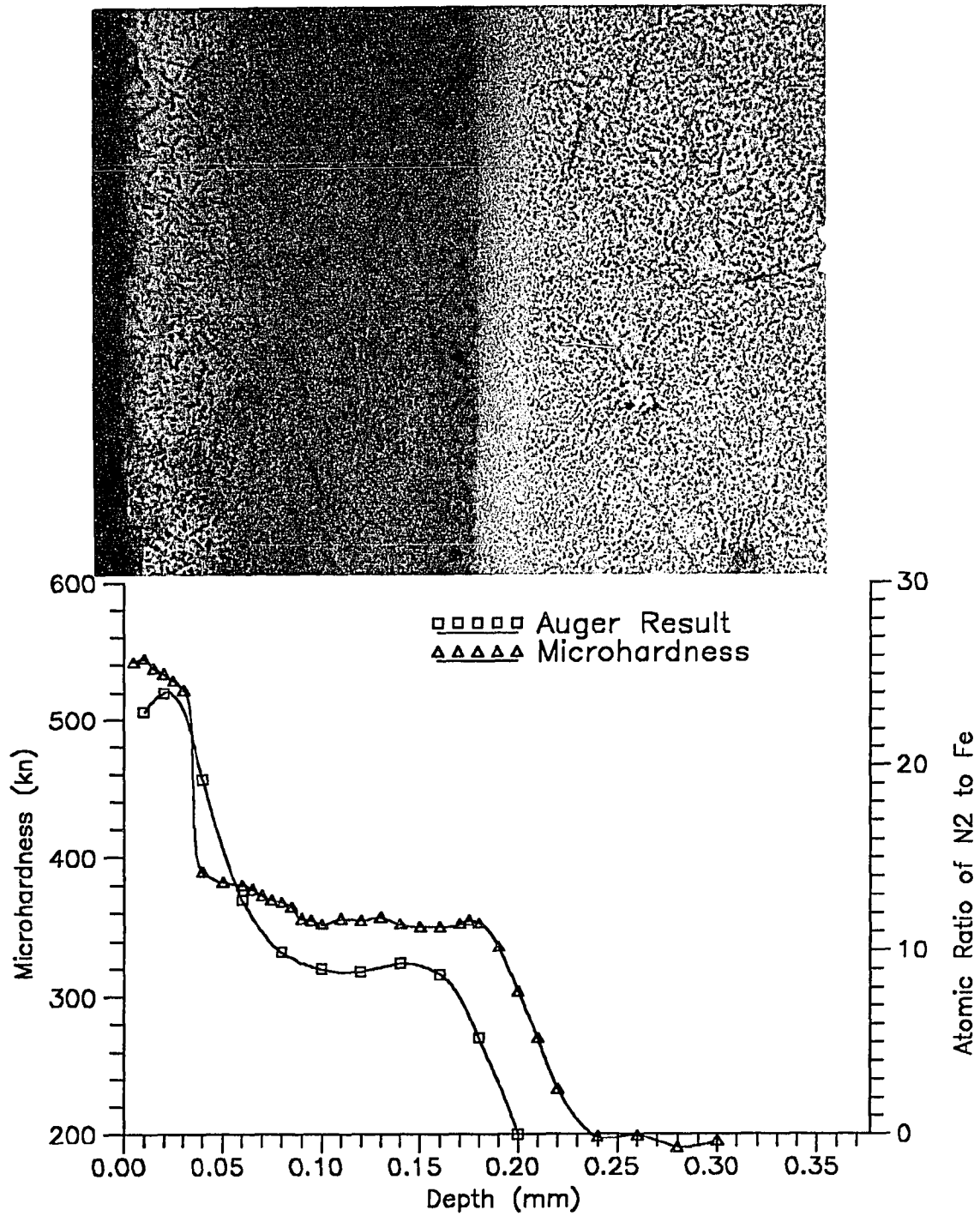


**Figure 7.6** Layers characterization by microstructure, microhardness distribution, and AES analysis for AISI 420 stainless steel.

peak ratio of nitrogen to iron is 18.1. Going to the atomic percentage scale of Fe-N equilibrium diagram, we can define that for such peak ratio 18.1 we have  $\gamma'$  phase.

Although AES can precisely define the element's weight ratio in the material, it can not define an element whose weight ratio is less than 5%. Unfortunately, the diffusion zone of the nitride layer is in this range. The nitrogen in the diffusion zone can not be detected by this method.

All mentioned methods are used to describe and to confirm obtained layers. The microhardness measurements can generally show layer distribution, but the AES method can clearly define and confirm the type of compound layers. The microstructure of the nitrated layers can define the  $\epsilon+\gamma'$  layers, and the diffusion zone distribution, but the microhardness measurement can confirm the diffusion zone obtained by using the above three methods as shown in Figure 7.5 and 7.6.

### **7.3 The Effect of Gas Composition and Temperature on PIN Process**

#### **7.3.1 Temperature**

Because of the practical considerations, the time and gas pressure of the PIN process are fixed in the following experiment. The temperature and gas composition are then left for further study. Both parameters are studied for the effect on the structure and properties of diffusion layers.

According to the result from the optimization experiment, temperature is the next most important parameter in PIN process. Figures 7.7 to 7.9 show the microstructure, and microhardness-depth curves relationship for different obtained testing materials. (See also Appendix A)

In general, the case depth is increased with the increasing of temperature over a fixed time. This is due to the increase of nitrogen diffusivity. The diffusion of nitrogen becomes more rapid and the hardened case tends to get deeper but not so hard on the surface. In Figure 7.8, as an example, we can find that at 650°C the nitride layers and

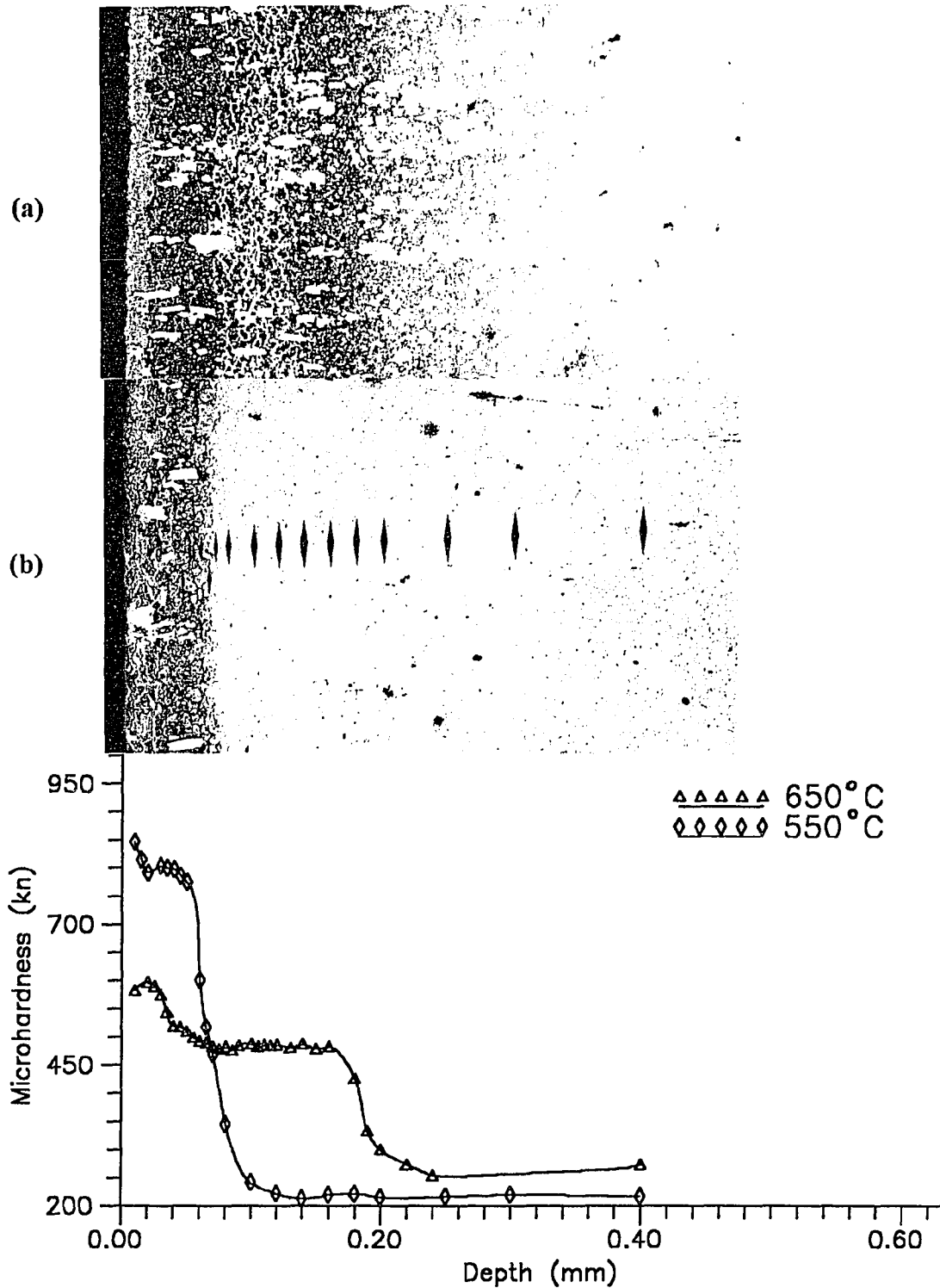


**Figure 7.7** Variation in the microstructure and microhardness of the nitrided layer at different temperature for AISI D2 tool steel (65% N<sub>2</sub>, 6 hours, 3 torr): (a) 650°C; (b) 550°C.

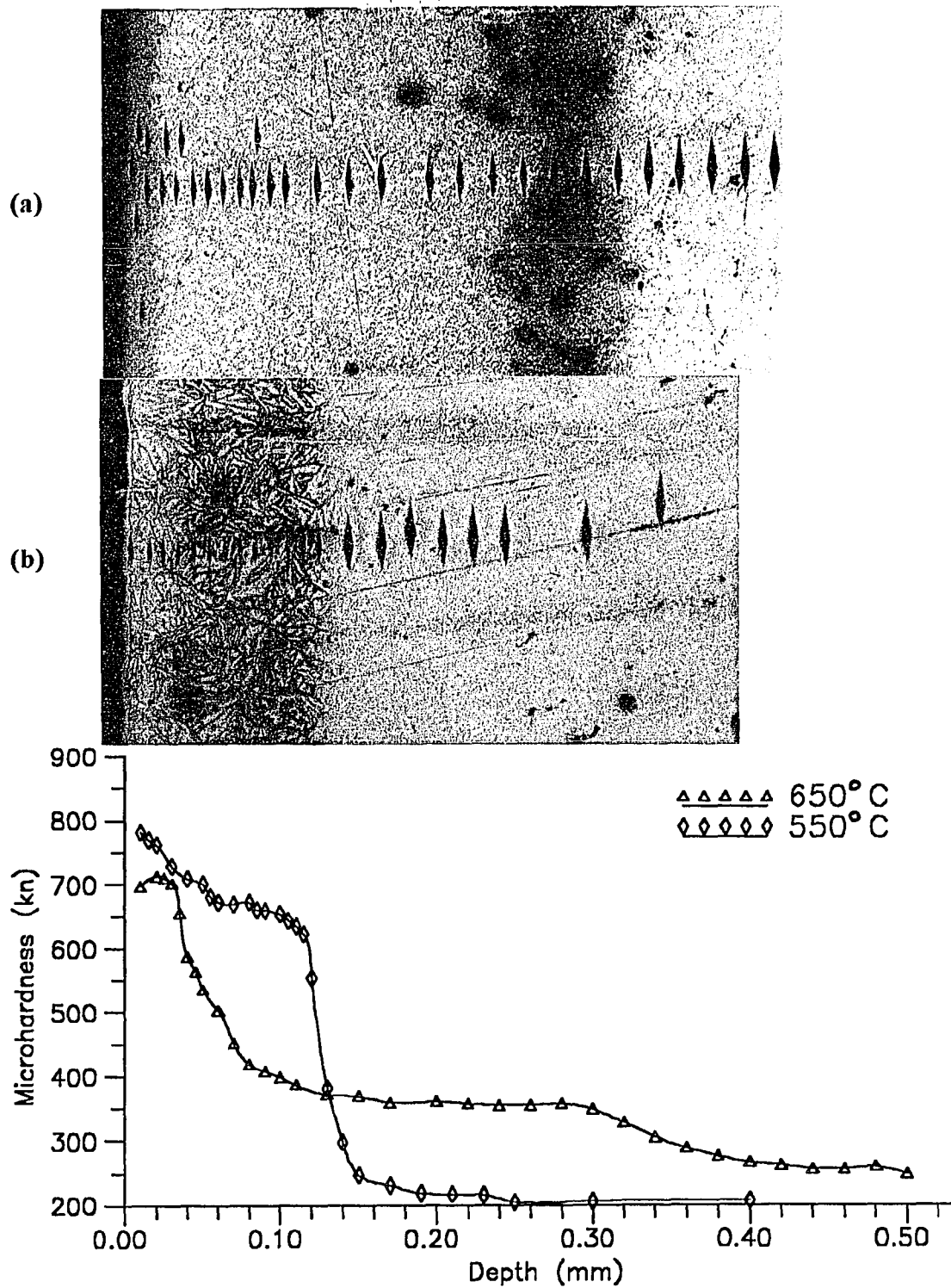


**Figure 7.8** Variation in the microstructure and microhardness of the nitrided layer at different temperature for AISI H13 tool steel (65% N<sub>2</sub>, 6 hours, 3 torr): (a) 650°C; (b) 550°C.

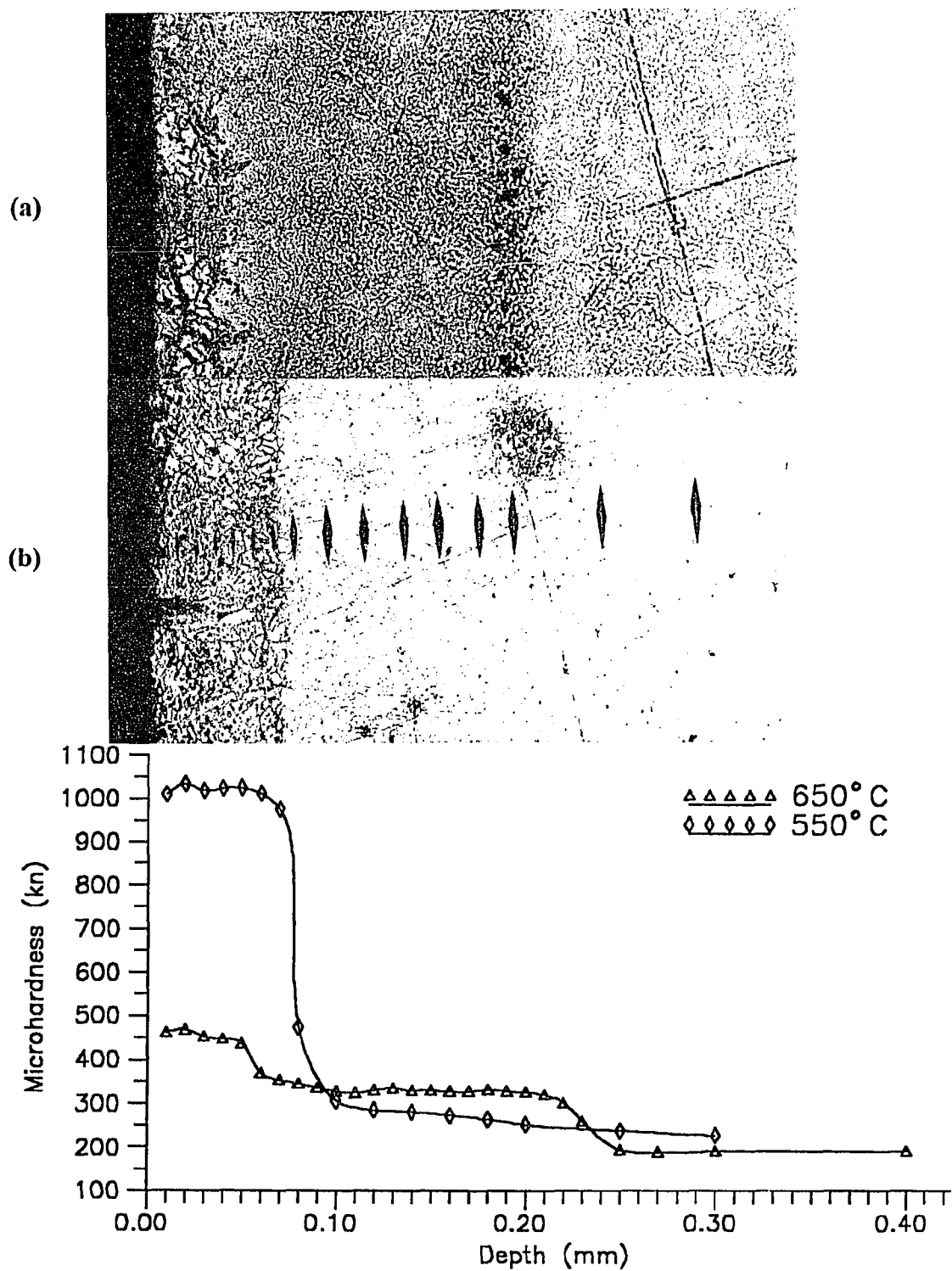


**Figure 7.9** Variation in the microstructure and microhardness of the nitrided layer at different temperature for AISI 420 stainless steel (65% N<sub>2</sub>, 6 hours, 3 torr): (a) 650°C; (b) 550°C.

diffusion zone are thicker than at 550°C, but the overall microhardness is less than at 550°C.

For tool steels, AISI D2 and H13, we find that the compound layers,  $\epsilon$  and  $\gamma'$  layers, at 650°C, are thicker than at 550°C. From the microstructure of specimens treated at 650°C, the compound layers can be easily observed. At the same time, from the microstructure of specimens treated at 550°C, the compound layers are not so easily defined. We also can see that the  $\epsilon$  layers (white layers) do not exist in some specimens at 550°C temperature. This can be explained by the different diffusivity rate at both temperatures. At high temperature, the diffusion of nitrogen into the iron is easy and fast. More nitrogen can diffuse into the iron and support the formation of the nitride layers. At low temperature,  $\epsilon$  layer is also formed at the beginning, but it can not grow and exist constantly throughout the process. Because the  $\epsilon$  layer is an unstable phase, it always tries to transform into the  $\gamma'$  layer. However the nitrogen supply is not quick enough to maintain the nucleation and growth of the  $\epsilon$  phase. This results in the thin or no  $\epsilon$  layers found on the surface. Only  $\epsilon + \gamma'$  and  $\gamma'$  layers can be found at low temperature. This kind of result also can be found at 650°C and the low gas composition situation.

The lower hardness at 650°C is due to the tempering and softening of material. The hardness can be reduced at higher temperature due to further tempering of the matrix and precipitation process.

For AISI 420 stainless steel, the case depth obtained at 650°C is thicker than at 550°C, but the compound layers at 550°C are deeper than at 650°C. Also there are only  $\epsilon$  or  $\epsilon + \gamma'$  layers, and diffusion zone that can be observed at 550°C. At low temperature, because the diffusivity is low, nitrogen is reacting with chromium and is forming a hard chromium nitride. Because of the formation of hard chromium nitride, the surface formed at 550°C has higher microhardness than other surfaces.

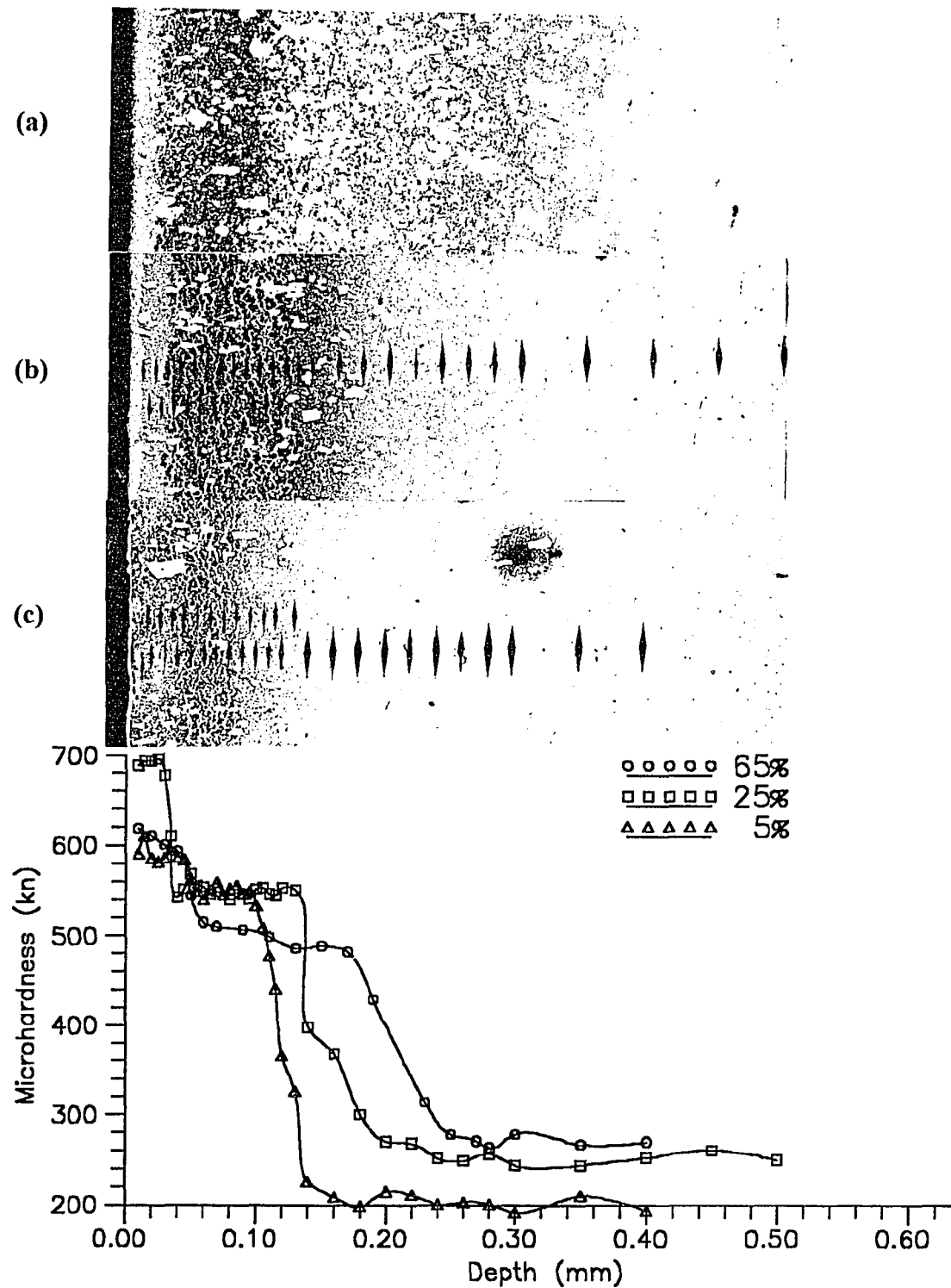


**Figure 7.10** Variation in the microhardness and microstructure of the nitrated layer at different nitrogen concentration for AISI D2 steel : (a) 65% N<sub>2</sub>; (b) 25% N<sub>2</sub>; (c) 5% N<sub>2</sub>.



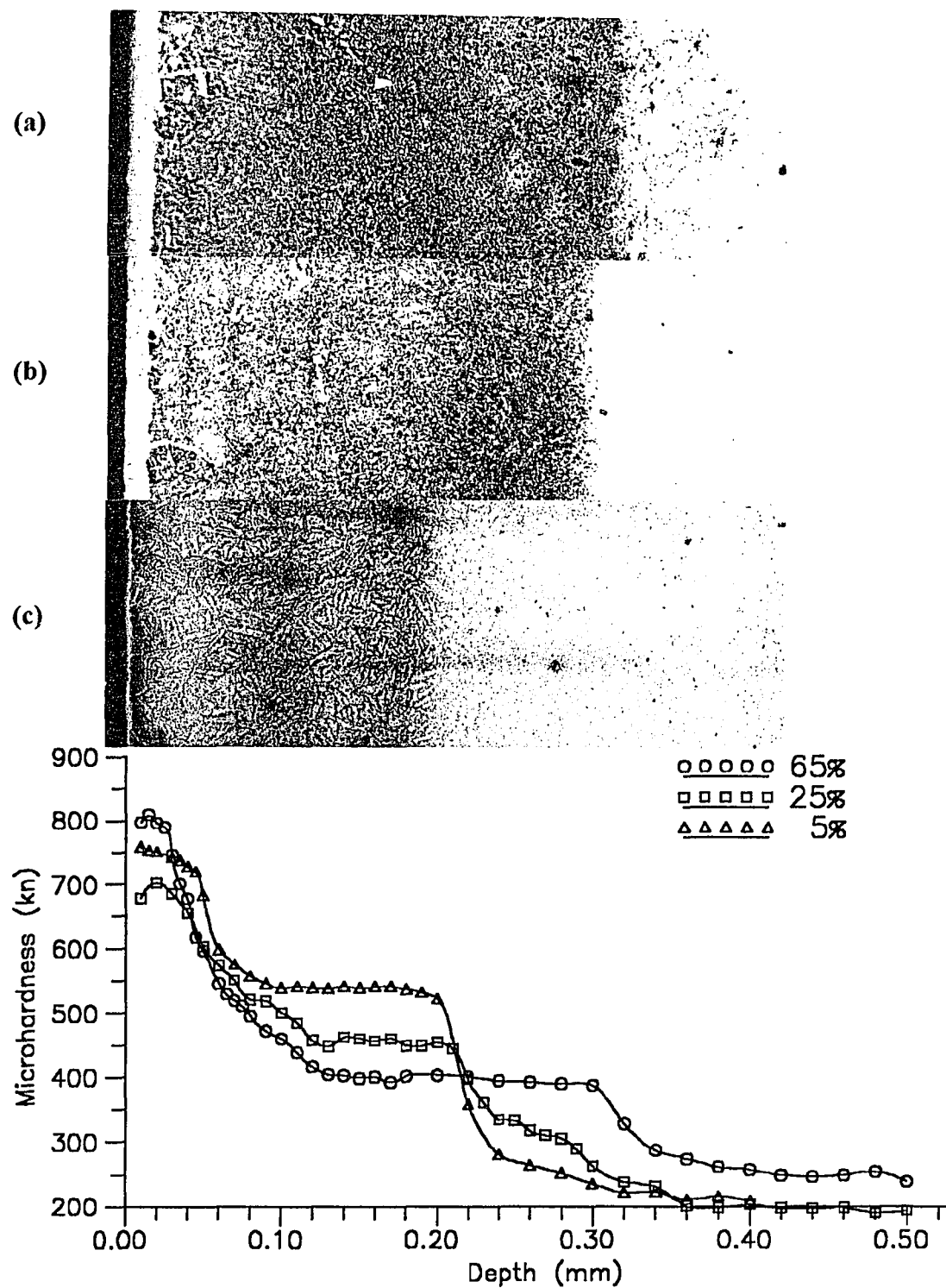


**Figure 7.11** Variation in the microhardness and microstructure of the nitrided layer at different nitrogen concentration for AISI H13 tool steel (650°C, 6 hours, 3torr): (a) 65% N<sub>2</sub>; (b) 25% N<sub>2</sub>; (c) 5% N<sub>2</sub>.

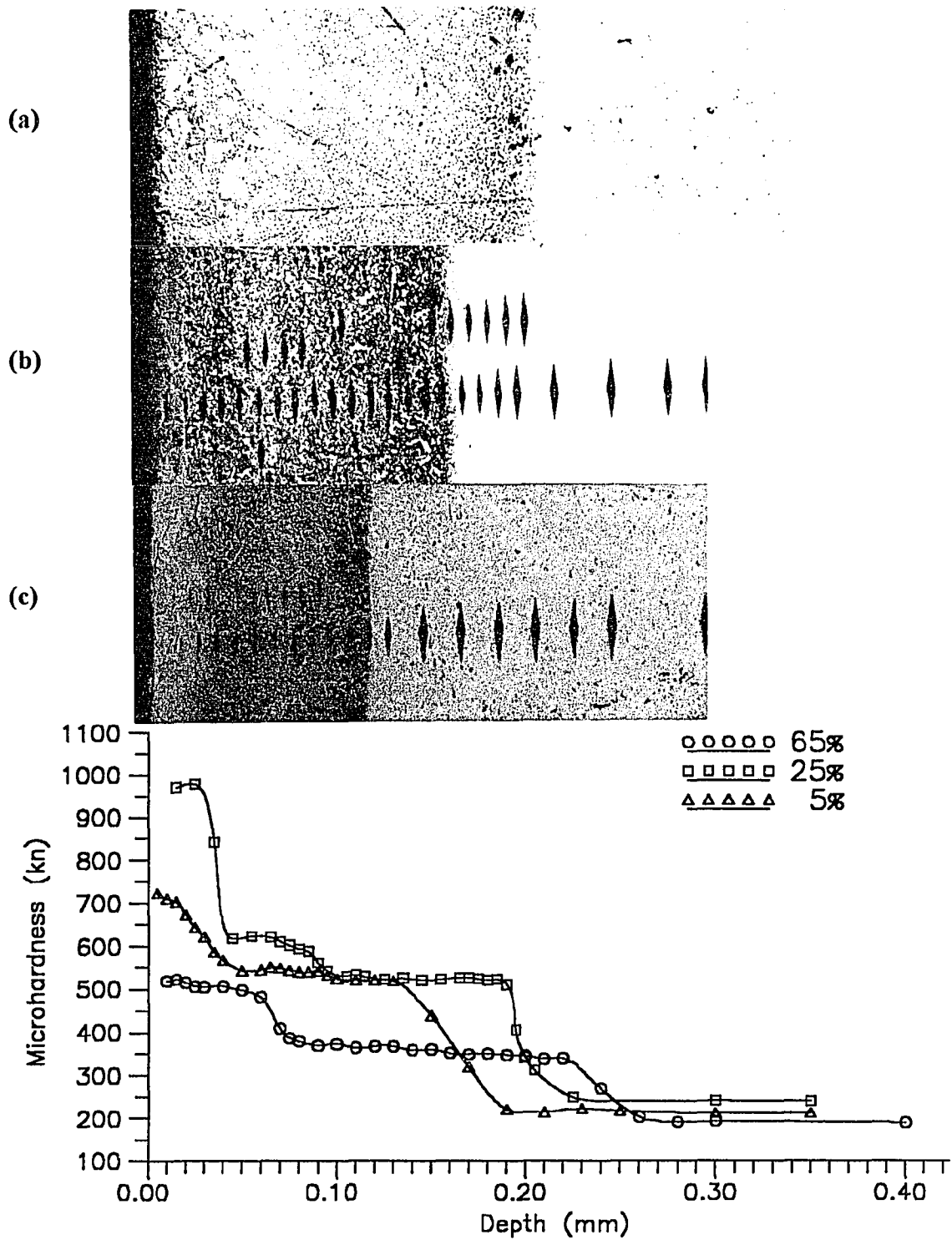


**Figure 7.12** Variation in the microhardness and microstructure of the nitrided layer at different nitrogen concentration for AISI 420 stainless steel (650°C, 6 hours, 3torr): (a) 65% N<sub>2</sub>; (b) 25% N<sub>2</sub>; (c) 5% N<sub>2</sub>.

### 7.3.2 Gas Composition

The dependence of case depth and microstructure from gas composition is shown in Figures 7.10-7.12. (See also Appendix B) It is found that the gas composition has strong influence on the formation of nitride layers, but it has indirect influence on the nitride layer hardness.

The gas used in the PIN process is composed of  $N_2$  and  $H_2$ . Nitrogen is used as the active diffusant for the PIN process and hydrogen is used to control nitrogen density during treatment and to act as a catalyst for the process. The volume percentage of the nitrogen used in the process are 65, 25, and 5%.

The testing results in Table 7.8 show that the case depth increases with the increase of nitrogen composition. The  $\epsilon$  and  $\gamma'$  layers in 65%  $N_2$  are thicker than in the 25%  $N_2$ . With higher nitrogen concentration, the possibility of nitrogen diffusion into the material is increased. At 5%  $N_2$  gas composition, the  $\epsilon$  layer is seldom found for all three materials. According to the N-Fe phase diagram, to develop a normal nitriding surface, which has the  $\epsilon$ ,  $\gamma'$  phases and diffusion zone, the nitrogen weight percentage must be over 6%. Supplying insufficient nitrogen mixed gas will result in difficulty in forming the compound layers. From the test results it is found that the specimen treated in low nitrogen concentration has thinner compound layers than the one in higher nitrogen concentration.

## 7.4 Role of Magnetic Field in Magneto-Plasma Ion Nitriding

### 7.4.1 Cycle Effect of Applied Magnetic Field

Table 7.5 shows the case depth and maximum microhardness for different magnetization treatments. The magnetization number of cycles used in this study were 20, 40, and 60. Also, the magnetization was applied to the specimen before, after, and before-after the plasma nitriding treatment. The parameters for the PIN process were chosen from the optimization approach shown in Table 6.5. These parameters were purposely selected to have better case depth and hardness.

Table 7.5 Influence of pre-post magnetization on surface treatment.

AISI D2 Tool Steel									
Characterizations (mm)	Pre-magnetization			Post-magnetization			Pre- & Post-magnetization		
	20 cycles	40 cycles	60 cycles	20 cycles	40 cycles	60 cycles	20 cycles	40 cycles	60 cycles
Compound Layer	0.14	0.13	0.13	0.145	0.13	0.14	0.11	0.1	0.09
Diffusion Zone	0.1	0.08	0.07	0.13	0.13	0.12	0.1	0.09	0.06
Case Depth	0.24	0.22	0.195	0.275	0.26	0.26	0.21	0.19	0.15
Max. Hardness	800	740	720	770	740	640	820	770	720

AISI H13 Tool Steel									
Characterizations (mm)	Pre-magnetization			Post-magnetization			Pre- & Post-magnetization		
	20 cycles	40 cycles	60 cycles	20 cycles	40 cycles	60 cycles	20 cycles	40 cycles	60 cycles
Compound Layer	0.165	0.15	0.14	0.15	0.16	0.16	0.14	0.13	0.12
Diffusion Zone	0.065	0.06	0.05	0.09	0.08	0.075	0.075	0.07	0.07
Case Depth	0.23	0.21	0.19	0.24	0.24	0.235	0.215	0.2	0.19
Max. Hardness	1180	1100	1100	1120	1020	950	1080	1020	950

AISI 420 Stainless Steel									
Characterizations (mm)	Pre-magnetization			Post-magnetization			Pre- & Post-magnetization		
	20 cycles	40 cycles	60 cycles	20 cycles	40 cycles	60 cycles	20 cycles	40 cycles	60 cycles
Compound Layer	0.11	0.1	0.09	0.115	0.105	0.11	0.11	0.09	0.085
Diffusion Zone	0.06	0.05	0.05	0.075	.055	0.065	0.07	0.06	0.06
Case Depth	0.17	0.15	0.14	0.19	0.16	0.175	0.18	0.15	0.145
Max. Hardness	1200	1200	1150	1000	960	800	1000	920	880

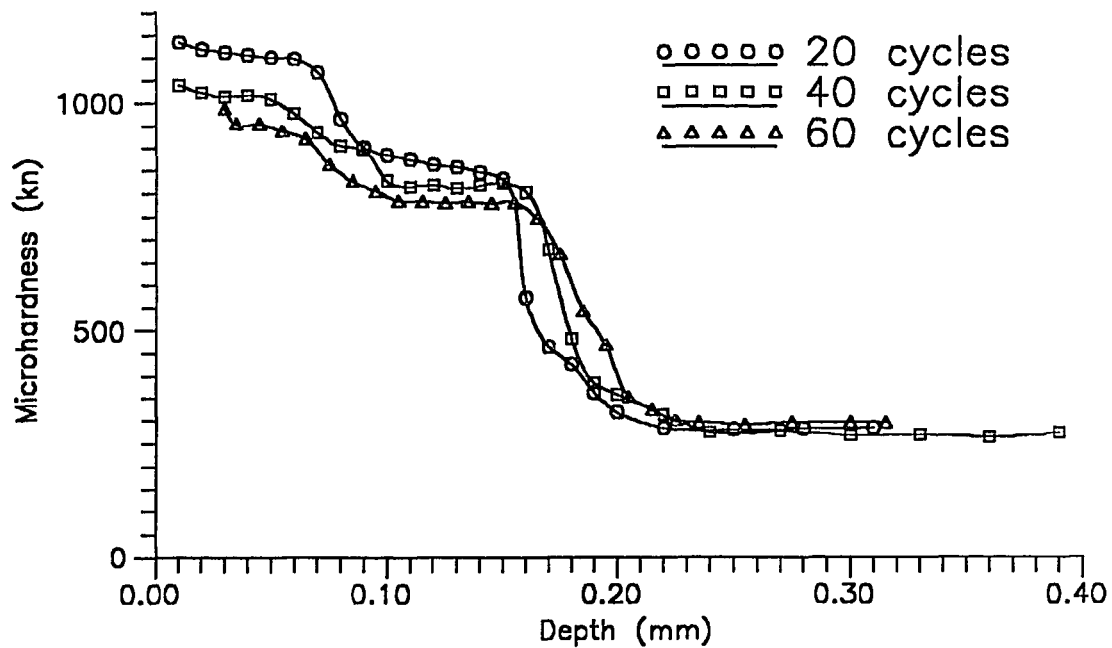


Figure 7.13 Microhardness profile for post-magnetized AISI H13 tool steel.

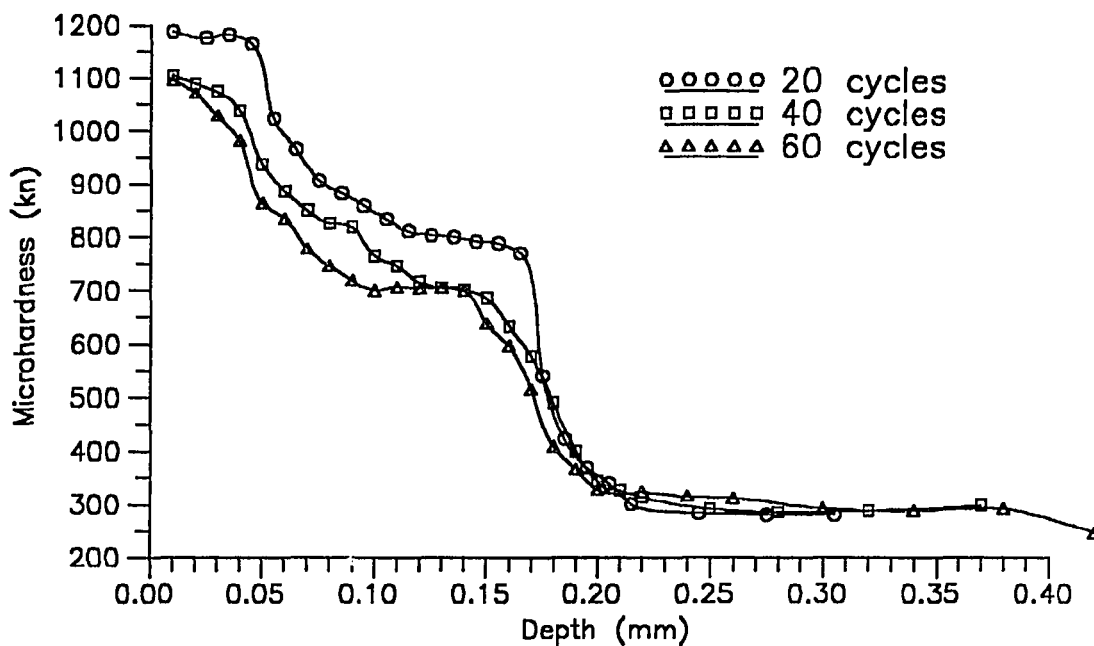
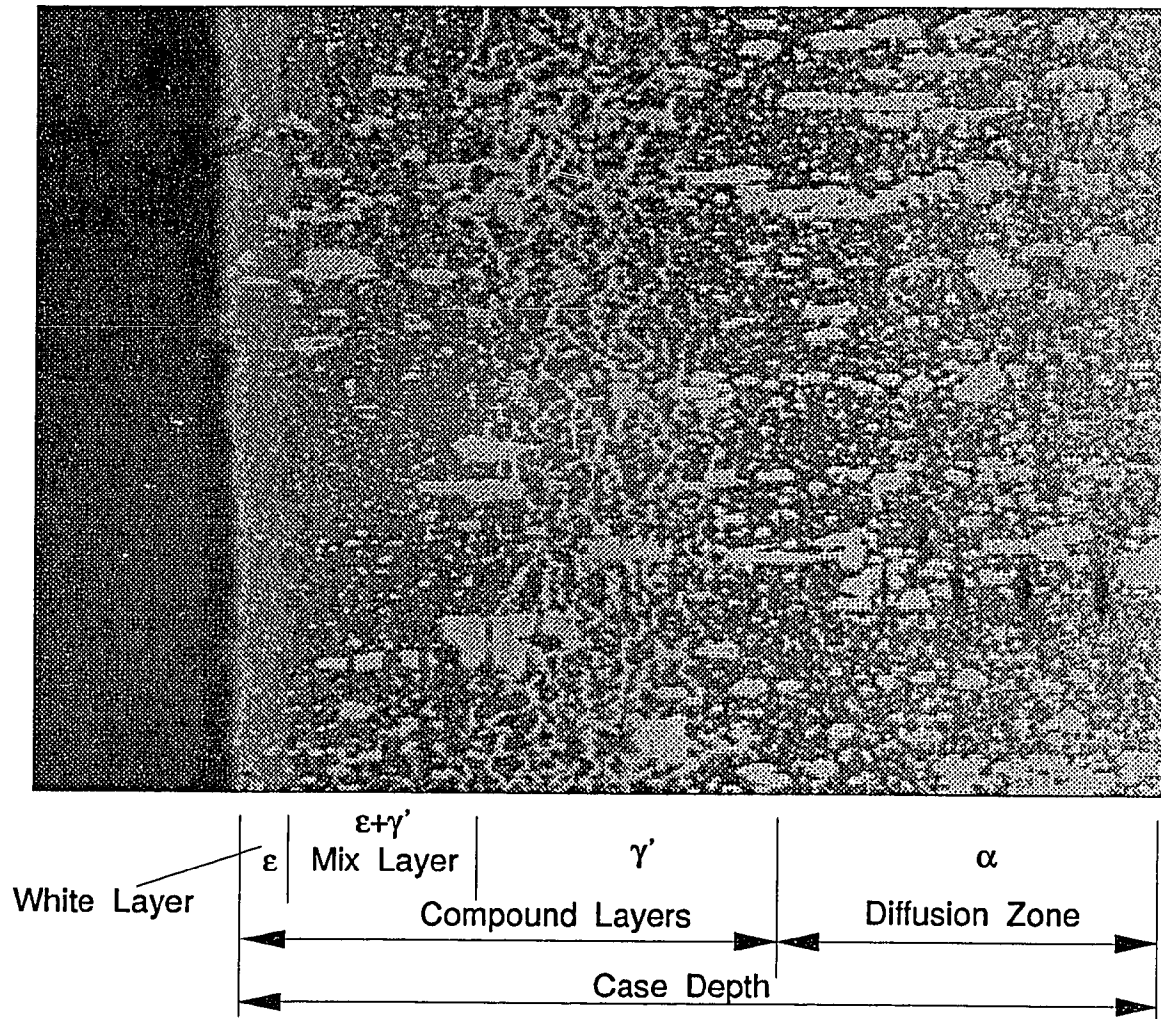


Figure 7.14 Microhardness profile for pre-magnetized AISI H13 tool steel.

From the testing results, we can find that the increase of magnetization number of cycles decreases the maximum microhardness for the post-magnetized specimen and decreases the case depth for the pre-magnetized specimen. A plot of microhardness versus depth for the AISI H13 stainless steel magnetized by 20, 40, 60 cycles after nitriding is given in Figure 7.13. If we only consider the overall microhardness, this figure shows that the specimen magnetized by 60 cycles has the smallest overall microhardness and the specimen magnetized by 20 cycles has the largest overall microhardness. The decrease of layer overall microhardness is due to the "Nail Effect". It is known that the residual stresses can be generated during the nitriding. The residual stresses are the result of microstructure disorder. In microstructure, the disordering comes mainly from the high density of dislocations. The material with high density dislocation exhibits higher microhardness. Due to the shaking effect coming from the magnetization and demagnetization, the microstructure of the material can be rearranged. The dislocations are forced to shift by magnetization shaking. As the result of shaking, the density of dislocations is reduced. The larger amount of magnetization cycles has a longer shaking effect on material. The materials experience better relaxation. This should result in reducing the amount of dislocations and then lower the microhardness in microstructure.

Figure 7.14 is a plot of microhardness versus depth for the AISI H13 tool steel magnetized by 20, 40, and 60 cycles before the nitriding. From this figure and Table 7.5, we can find that the case depths for 20, 40, and 60 magnetization cycles are 230  $\mu\text{m}$ , 210  $\mu\text{m}$ , and 190  $\mu\text{m}$  respectively. Since the magnetization was applied before the nitriding process, the structure of the specimen had experienced the relaxation. The density of dislocations is reduced. As the result of this reduction the rate of diffusion process which is controlled by the amount of dislocations will be reduced. If the microstructure has a higher density of dislocations, the diffusion process can take place more easily and quickly. In PIN, the growth of layer is related to the nitrogen diffusion into the material. The decrease of the amount of dislocations will decrease the diffusion rate. In general,



**Figure 7.15** The definition of case depth and layer distribution.

applying the magnetization process with higher magnetization cycles before nitriding should decrease the case depth.

#### **7.4.2 Pre-magnetized and Post-magnetized PIN Approach**

From previous section, we know that applying the magnetization process before and after the nitriding process will affect case depth and overall microhardness of the nitrided layers respectively. The case depth is used as a term for total depth of formed layers. Figure 7.15 includes the thickness of  $\epsilon$ ,  $\epsilon+\gamma'$ ,  $\gamma'$  layers and diffusion zone. The thickness of each defined layer and the effect of magnetization on layer formation are shown in Tables 7.6 to 7.8.

As can be seen from Tables 7.6 - 7.8, the case depth formation, white layer( $\epsilon$ ), mix layer( $\epsilon+\gamma'$ ), second layer( $\gamma'$ ), diffusion zone, and microhardness depend on different PIN process parameters. At high temperature, all layers can be clearly defined for all testing materials. The pre-magnetized materials have smaller compound layers than non-magnetized and post-magnetized materials. But the diffusion zone in the pre-magnetized materials is larger than under other treatments. At low temperature, the layers are not so easily defined. The  $\epsilon$  phase has disappeared in most of the tests. The mixing zone( $\epsilon+\gamma'$ ) and  $\gamma'$  layers are blended. The microhardness profiles of the tests show that the change of overall microhardness only takes place in the range of compound layers. The microhardness of the diffusion zone has an exponential relationship and depends on nitrogen concentration.

The reasons for smaller compound layers and larger diffusion zone for pre-magnetized specimens are related to the "Skin Effect" of the magnetization process. As mentioned in chapter 4, the induced magnetic field is a function of the depth. It is the surface which first reaches the saturation magnetization. The saturation magnetization gradually moves into the material. The shaking or the "Nail Effect" has the same influence on the material. The longer magnetization takes place, the deeper the surface layers are



Table 7.6 Influence of PIN treatment on surface properties of AISI D2 tool steel.

	Thickness of Layers ( $\mu\text{m}$ )			Hardness Range for Layers
	A1	A2	A3	
	Hardness (Photo)	Hardness (Photo)	Hardness (Photo)	
White Layer	40 (25)	20	30	>600
Mix Layer	40 (75)	40	45	500---600
Wave Layer	90 (80)	60	85	~ 500
Diffusion Zone	70	100	75	<500
Case Depth	240	220	235	
Max. Hardness (kn)	620	620	595	

	Thickness of Layers ( $\mu\text{m}$ )			Hardness Range for Layers
	A10	A11	A12	
	Hardness (Photo)	Hardness (Photo)	Hardness (Photo)	
White Layer	(10)	(5)	(10)	>700
Mix Layer	35 (25)	20 (20)	30 (20)	>600
Wave Layer	100 (100)	95 (95)	100 (105)	500---600
Diffusion Zone	100	110	100	<500
Case Thickness	235	225	230	
Max. Hardness (kn)	700	740	660	

	Thickness of Layers ( $\mu\text{m}$ )			Hardness Range for Layers
	A16	A17	A18	
	Hardness (Photo)	Hardness (Photo)	Hardness (Photo)	
White Layer	(2.5)	(2.5)	(5)	
Mix Layer	45 (35)	35 (32.5)	45 (40)	>600
Wave Layer	50 (40)	45 (50)	65 (50)	~ 600
Diffusion Zone	75	80	70	<600
Case Thickness	170	160	180	
Max. Hardness (kn)	610	620	540	

Table 7.6(continued) Influence of PIN treatment on surface properties of AISI D2 tool steel.

	Thickness of Layers ( $\mu\text{m}$ )			Hardness Range for Layers
	A4	A5	A6	
	Hardness (Photo) (2.5)	Hardness (Photo)	Hardness (Photo)	
White Layer				
Mix Layer	55 (75)	30 (65)	50 (40)	>800
Wave Layer				
Diffusion Zone	75	80	70	<800
Case Thickness	130	110	120	
Max. Hardness (kn)	880	910	850	

	Thickness of Layers ( $\mu\text{m}$ )			Hardness Range for Layers
	A7	A8	A9	
	Hardness (Photo) (5)	Hardness (Photo) (5)	Hardness (Photo) (5)	
White Layer				
Mix Layer	55 (50)	50 (60)	60 (60)	>800
Wave Layer				
Diffusion Zone	75	70	75	<800
Case Thickness	130	120	135	
Max. Hardness (kn)	1010	1000	930	

	Thickness of Layers ( $\mu\text{m}$ )			Hardness Range for Layers
	A13	A14	A15	
	Hardness (Photo)	Hardness (Photo)	Hardness (Photo)	
White Layer				
Mix Layer	55 (20)	45 (17.5)	50 (35)	>800
Wave Layer				
Diffusion Zone	95	75	110	<800
Case Thickness	150	120	160	
Max. Hardness (kn)	915	965	840	

**Table 7.7 Influence of PIN treatment on surface properties of AISI H13 tool steel.**

	Thickness of Layers (µm)			Hardness Range for Layers
	B1	B2	B3	
	Hardness (Photo)	Hardness (Photo)	Hardness (Photo)	
White Layer	35 (20)	15 (15)	30 (20)	> 700
Mix(Net) Layer	95 (88)	85 (85)	100	400---700
Fine Layer	180 (195)	170 (170)	180	~400
Diffusion Zone	90	110	80	< 400
Case Thickness	400	380	390	
Max. Hardness (kn)	810	800	715	

	Thickness of Layers (µm)			Hardness Range for Layers
	B10	B11	B12	
	Hardness (Photo)	Hardness (Photo)	Hardness (Photo)	
White Layer	30 (17)	15	20	~ 700
Mix(Net) Layer	100 (50)	55	100	400---700
Fine Layer	80 (237.5)	90	85	~ 400
Diffusion Zone	150	180	150	< 400
Case Thickness	360	340	355	
Max. Hardness (kn)	700	700	690	

	Thickness of Layers (µm)			Hardness Range for Layers
	B16	B17	B18	
	Hardness (Photo)	Hardness (Photo)	Hardness (Photo)	
White Layer	(6)		(4)	
Mix(Net) Layer	100 (200)	75 (200)	95 (200)	> 450
Fine Layer	100	100	105	~ 450
Diffusion Zone	115	135	115	< 450
Case Thickness	315	310	310	
Max. Hardness (kn)	760	740	720	

**Table 7.7(continued) Influence of PIN treatment on surface properties of AISI H13 tool steel.**

	Thickness of Layers (µm)			Hardness Range for Layers
	B4	B5	B6	
	Hardness (Photo)	Hardness (Photo)	Hardness (Photo)	
White Layer	(8.3)	(4.1)	(4.1)	
Mix(Net) Layer	120 (117)	100 (130)	110 (133)	>700
Fine Layer				
Diffusion Zone	70	80	75	<700
Case Thickness	190	180	185	
Max. Hardness (kn)	800	840	780	

	Thickness of Layers (µm)			Hardness Range for Layers
	B7	B8	B9	
	Hardness (Photo)	Hardness (Photo)	Hardness (Photo)	
White Layer	(6.2)	(4.1)	(4.1)	
Mix(Net) Layer	60 (133)	100 (117)	45 (33)	>700
Fine Layer	60		75 (88)	
Diffusion Zone	40	50	35	<700
Case Thickness	160	150	155	
Max. Hardness (kn)	835	840	765	

	Thickness of Layers (µm)			Hardness Range for Layers
	B13	B14	B15	
	Hardness (Photo)	Hardness (Photo)	Hardness (Photo)	
White Layer				
Mix(Net) Layer	30 (33)	20 (29)	20 (33)	>700
Fine Layer	70 (75)	70 (67)	70 (71)	
Diffusion Zone	60	60	60	<700
Case Thickness	160	150	150	
Max. Hardness (kn)	840	850	805	

**Table 7.8 Influence of PIN treatment on surface properties of AISI 420 stainless steel.**

	Thickness of Layers (µm)			Hardness Range for Layers
	C1	C2	C3	
	Hardness (Photo)	Hardness (Photo)	Hardness (Photo)	
White Layer				> 900
Mix Layer	60 (50)	35 (30)	50 (50)	500---800
2nd Layer	165 (156.5)	150 (155)	160 (155)	~ 500
Diffusion Zone	40	50	40	< 500
Case Thickness	265	235	250	
Max. Hardness (kn)				

	Thickness of Layers (µm)			Hardness Range for Layers
	C10	C11	C12	
	Hardness (Photo)	Hardness (Photo)	Hardness (Photo)	
White Layer	25 (20)	20	30 (21)	> 900
Mix Layer	80 (50)	80	75 (16)	600---900
2nd Layer	90 (163)	70	90 (136)	500---600
Diffusion Zone	30	45	30	< 500
Case Thickness	225	215	225	
Max. Hardness (kn)	700	700	690	

	Thickness of Layers (µm)			Hardness Range for Layers
	C16	C17	C18	
	Hardness (Photo)	Hardness (Photo)	Hardness (Photo)	
White Layer				> 600
Mix Layer	50 (30)	40 (30)	45 (24)	500---600
2nd Layer	90 (89)	70 (98)	90	< 500
Diffusion Zone	50	70	50	
Case Thickness	190	180	185	
Max. Hardness (kn)	720	720	680	

**Table 7.8 (continued)** Influence of PVD treatment on surface properties of AISI 420 stainless steel.

	Thickness of Layers ( $\mu\text{m}$ )			Hardness Range for Layers
	C4	C5	C6	
	Hardness (Photo)	Hardness (Photo)	Hardness (Photo)	
White Layer	75 (68)	65 (68)	75 (71)	> 900
Mix Layer				
2nd Layer				
Diffusion Zone	50	55	55	< 900
Case Thickness	125	120	130	
Max. Hardness (kn)	1110	1085	1100	

	Thickness of Layers ( $\mu\text{m}$ )			Hardness Range for Layers
	C7	C8	C9	
	Hardness (Photo)	Hardness (Photo)	Hardness (Photo)	
White Layer	65 (65)	60 (75)	70 (65)	> 900
Mix Layer				
2nd Layer				
Diffusion Zone	55	60	50	< 900
Case Thickness	120	120	120	
Max. Hardness (kn)	1100	1040	1020	

	Thickness of Layers ( $\mu\text{m}$ )			Hardness Range for Layers
	C13	C14	C15	
	Hardness (Photo)	Hardness (Photo)	Hardness (Photo)	
White Layer				
Mix Layer	60 (10)	55 (6)	55 (12)	> 600
2nd Layer	(44)	(45)	(42)	< 600
Diffusion Zone	50	25	40	
Case Thickness	110	80	100	
Max. Hardness (kn)	820	820	815	

relaxing. However, in this experiment, the chosen magnetization cycles may only influence the depth of compound layer formation. Although it should be noticed that the case depth controlled by the PIN process parameters is always deeper than the layer depth affected by magnetization. The depth of saturation magnetization is in the range of compound layer thickness. Considering the complexity of the dislocations in the non-magnetized material and the reordered dislocations arrangement in magnetized material, we can conclude that inside the skin depth the diffusion process is slow. The formation of the compound layer is then lagged. However the diffusion process beyond the skin depth could be performed in a manner similar to that in the non-magnetized material. During the same nitriding time, the compound layers in pre-magnetized material are not as deep as the non-magnetized material, but the diffusion zone in the pre-magnetized material may be thicker than for non-magnetized material.

However, the compound layer formation and diffusion zone have little differences at low nitrogen composition and low temperature treatment. At low temperature, because of reduced diffusion rate, the difference of layer thickness and diffusion zone is very small. Similar result also can be observed in the case of low nitrogen concentration.

From the plots of microhardness versus depth, we can also realize the influence of the "Skin Effect". The microhardness of the compound layer is reduced for the pre-magnetized specimen, but the microhardness of the diffusion zone and bulk material for the pre-magnetized specimen has the same microhardness as the non-magnetized specimen. If we want to have a deeper shaking effect of the magnetization, we have to increase the number of magnetization cycles.

### **7.5 Nail Model for Magneto-Plasma Ion Nitriding**

In section 5.5, we mathematically derived a nail model for the "Nail Effect". In this model, a diffusant concentration in material is composed from concentration distribution of inside and outside nails or dislocations. However the diffusion rate inside the nails is

much higher than outside the nails. It is assumed that the concentration is the same in  $r$  direction, Figure 5.5,  $c_d(y, 0, t) = c_d(y, a, t)$ , and then  $c_d(y, a, t) = c_g(y, a, t)$ . So the outside concentration distribution is what we are concerned with. The outside concentration distribution is not only the complicated problem and should be solved, but also it influences the treatment results, such as the properties of coating and wear resistance.

The concentration outside nails,  $c_g(y, r, t)$ , is derived in Equation (5.58) and is shown as follows

$$\begin{aligned}
 c_g(r, y, t) &= c_{g1}(r, y, t) + c_{g2}(r, y, t) \\
 &= \frac{2M}{\sqrt{\pi D_g t}} e^{-\frac{y^2}{4D_g t}} + \frac{8}{\pi^2} \frac{\alpha \beta M}{a} \int_0^\infty x^2 e^{-x^2} \cos(\eta x) dx \int_0^\infty \frac{1 - e^{-z^2}}{z} \frac{J_0\left(z\alpha \frac{r}{a}\right)\varphi - Y_0\left(z\alpha \frac{r}{a}\right)\theta}{\theta^2 + \varphi^2} dz \\
 &= \frac{2M}{\sqrt{\pi D_g t}} \left( e^{-\frac{\eta}{4}} + \frac{4}{\pi^{3/2}} \beta \int_0^\infty x^2 e^{-x^2} \cos(\eta x) dx \int_0^\infty \frac{1 - e^{-z^2}}{z} \frac{J_0(\rho)\varphi - Y_0(\rho)\theta}{\theta^2 + \varphi^2} dz \right) \quad (7.1)
 \end{aligned}$$

where  $\rho = z\alpha \frac{r}{a}$ . The first term  $c_{g1}(\eta, t)$  gives the contribution to  $c_g(y, r, t)$  from direct volume diffusion and the second term  $c_{g2}(\eta, \rho, t)$  is from diffusion through dislocations. Since in this study time  $t$  is a constant, in fact  $c_{g1}(\eta, t)$  is a function of  $\eta$  only and  $c_{g2}(\eta, \rho, t)$  is the function of  $\eta$  and  $\rho$ . In here,  $\eta$  and  $\rho$  represent the depth and radial length respectively.

To analyze the distribution of the concentration, a numerical program (see Appendix D) is developed according to above equation. The constants in the equation are given as follows,  $\alpha = 0.001$ ,  $\beta = 100$ ,  $\Delta = 10^5$ ,  $D_g = 1$ ,  $t = 21600$  sec.[76] It has to be noted that all constants are dimensionless in the equation. Also, from the constants given above, the derived radius of dislocations is about  $10^{-1}$   $\mu\text{m}$ .

From the iteration result, it is found that when  $\eta < 4$ , the concentration is mostly from  $c_{g1}$ . When  $\eta > 4$ ,  $c_{g2}$  gradually increases. As  $\eta$  keep increasing, the concentration



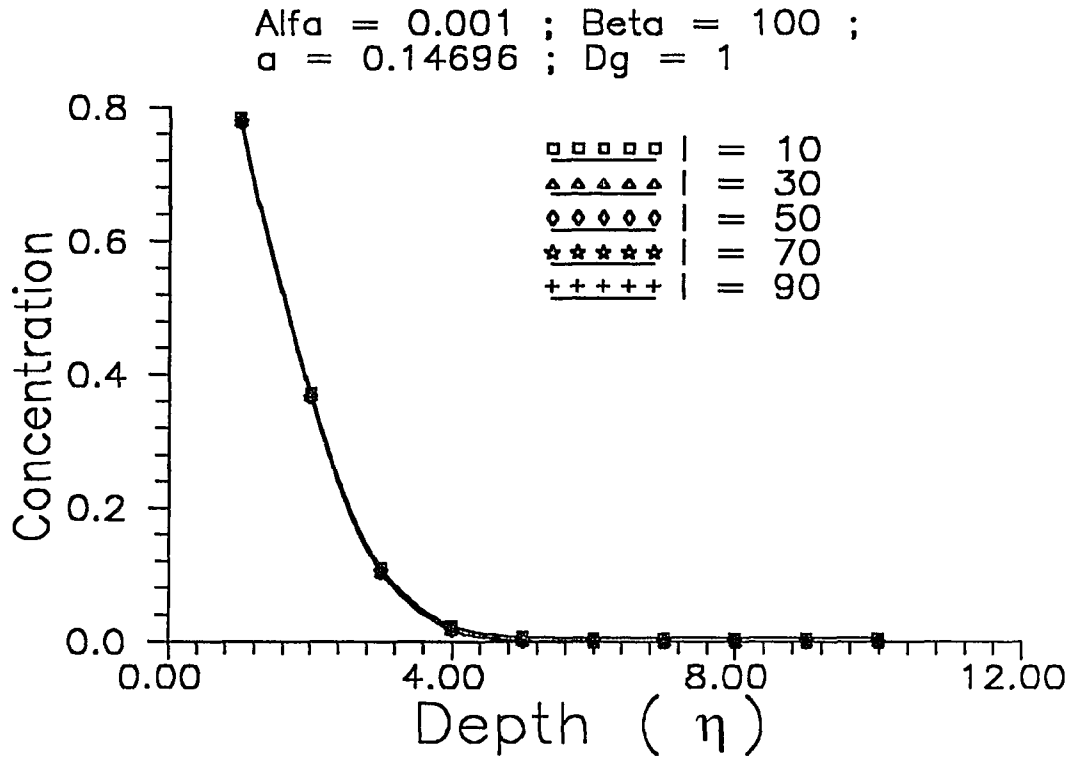


Figure 7.16 The variation of concentration along depth( $\eta$ ).

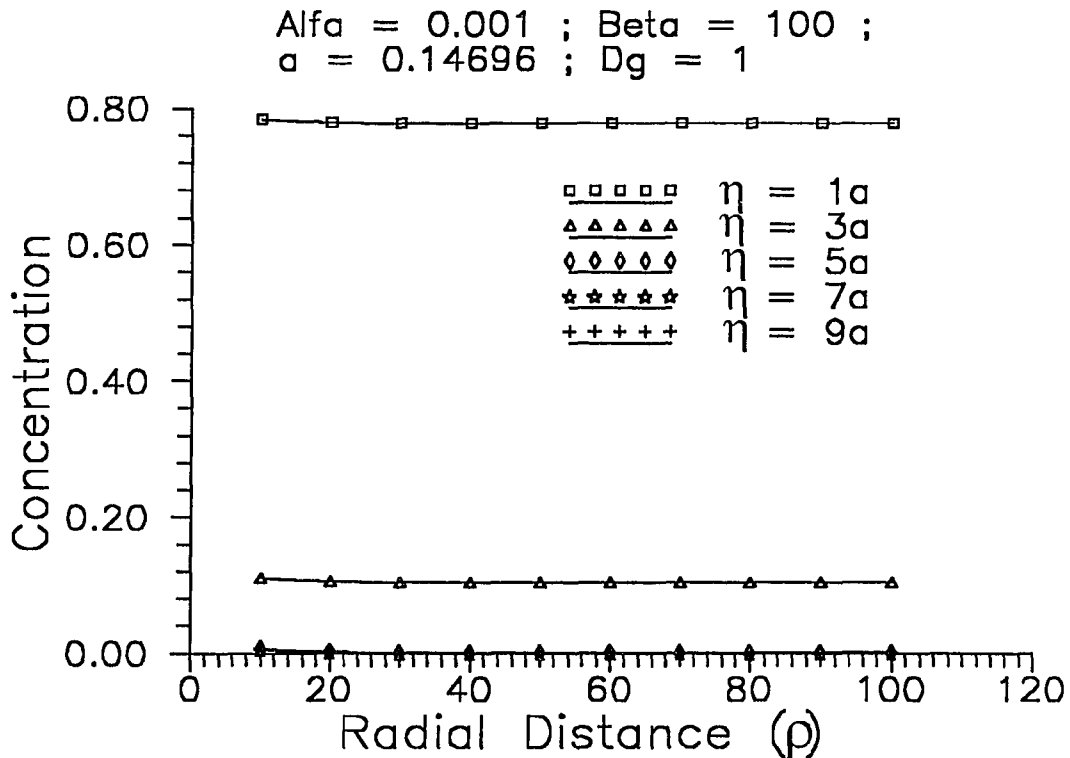
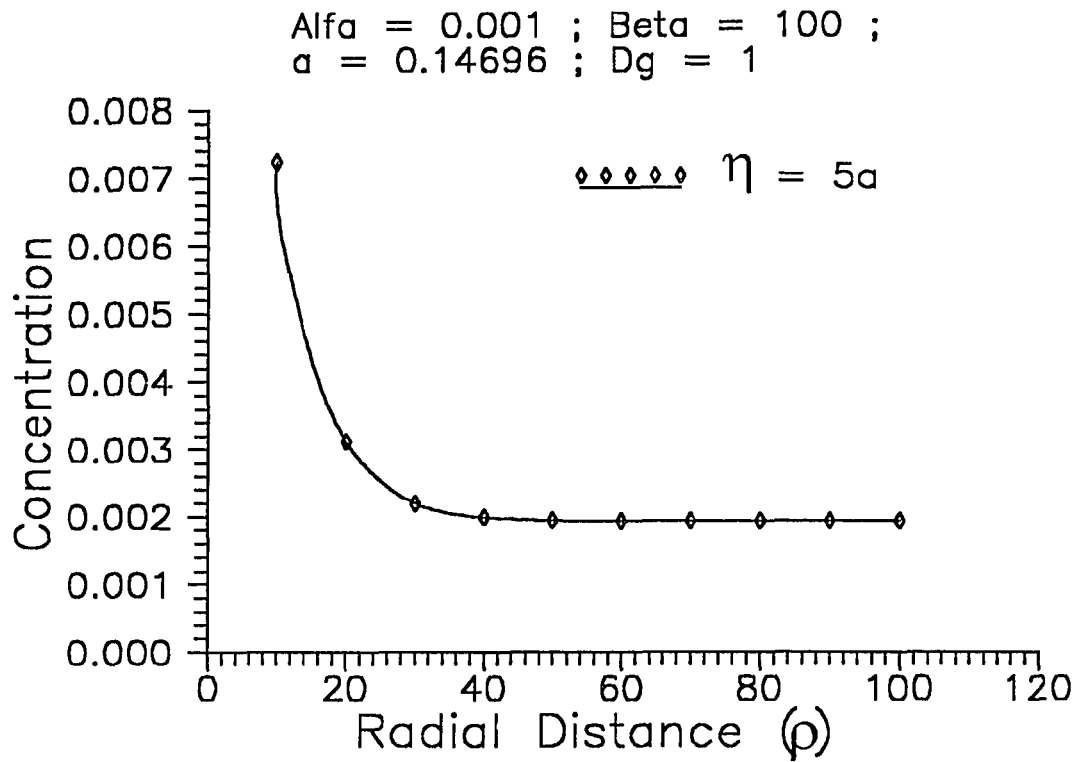
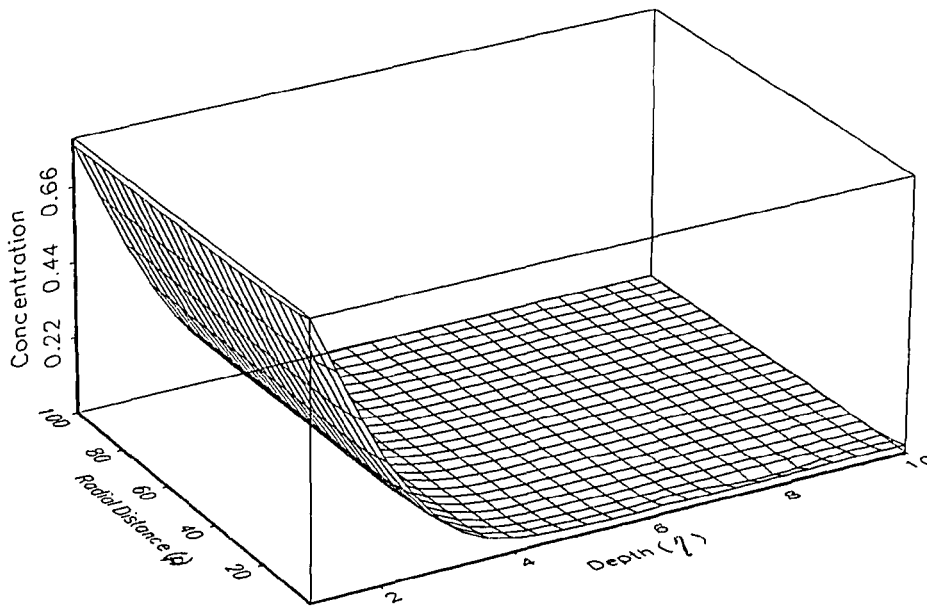


Figure 7.17 The variation of concentration along radial distance( $\rho$ ).



**Figure 7.18** The concentration distribution along the radial distance when depth  $\eta = 5a$ .



**Figure 7.19** Three dimensional concentration distribution along depth and radial distance.

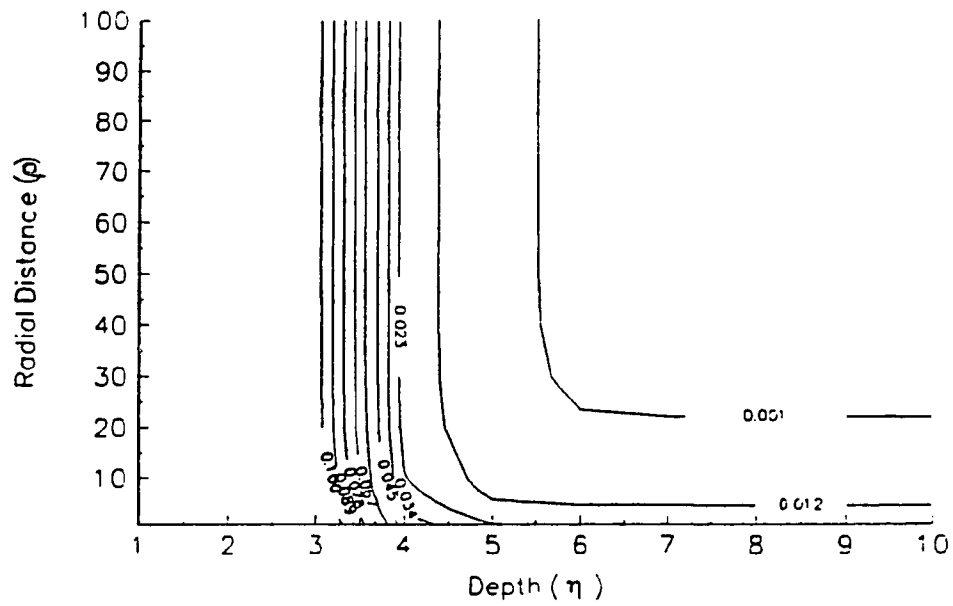


Figure 7.20 Isoconcentration line in depth and radial directions.

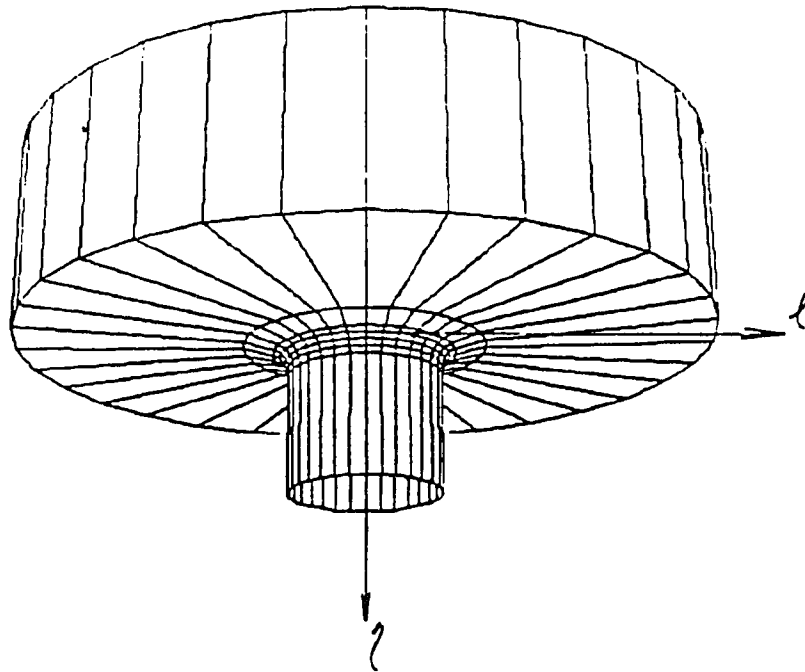
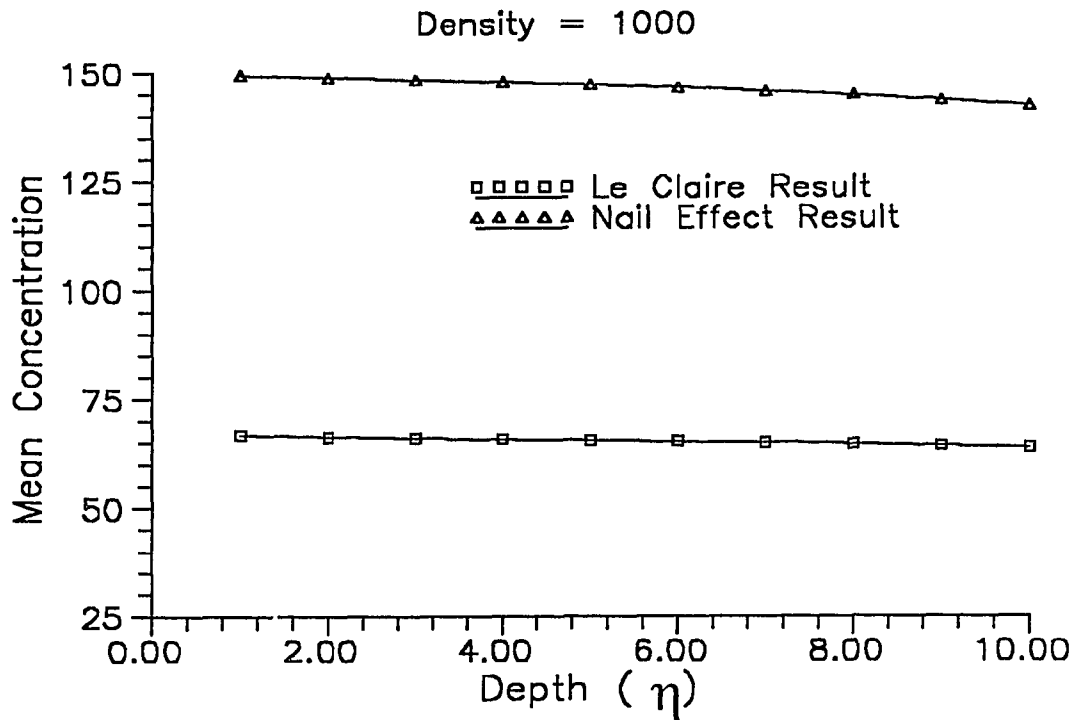


Figure 7.21 A profile for "nail" in 3 dimensional view for mean concentration  $\langle c \rangle = 0.001$

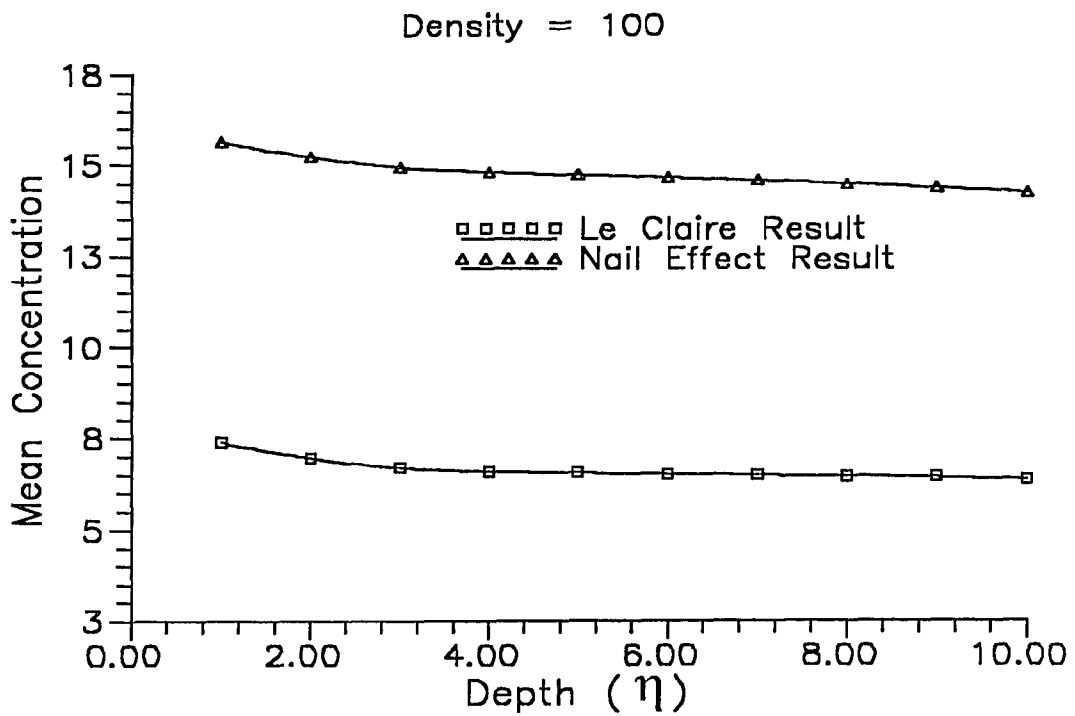
contributed from  $c_{g1}$  becomes less and almost disappears. This indicates that the concentration near the surface is influenced by volume diffusion. The concentration at the points which are away from the surface is related to the diffusion from dislocations.

Figure 7.16 and 7.17 show the change of concentration along  $\eta$  and  $\rho$ . From both figures the exponential relationship for concentration to depth and radial distance can be found. Although lines in Figure 7.17 look like straight lines, in fact they have an exponential character. If we reduce the scale in the  $y$  direction, the exponential line as shown in Figure 7.18 can be obtained. This is due to a very small change of concentration along the radial direction. The range of these changes is between  $10^{-3}$  to  $10^{-7}$ . This also can be observed in Figure 7.16 in which all the lines are stacked. Figure 7.19 is a 3-dimensional representation of concentration distribution from the surface. From this figure we can see how concentration is distributed along the nails. Figure 7.20 shows the iso-concentration line along the depth( $\eta$ ) and radial distance( $\rho$ ). According to this figure, a 3-dimensional surface, Figure 7.21, can be constructed by sweeping the profile of Figure 7.20 over  $360^\circ$ . From the constructed picture, we can see that the concentration distribution along the nail has a conical shape with an exponential profile. We are calling this profile "nail".

Figures 7.22 to 28 show the comparison of mean concentration  $\langle c \rangle$  from the nail equation and Le Claire result.[77] It is found that when the dislocation density is less than 0.01, both mean concentrations are almost the same. We can conclude that when the dislocation density is less than 0.01, the nail model perfectly fits the Claire model. From the above figures, the mean concentration for high dislocation density is higher than mean concentration for low dislocation density at the same depth. This indicates that the diffusion depth for high dislocation density is larger than for low dislocation density. Also from the curve of Figures 7.22 and 28, the mean concentration distribution for high dislocation density is linearly decreased with an increase of depth. But the mean concentration distribution for low dislocation density is exponentially decreased with an



**Figure 7.22** Mean concentration distribution along depth( $\eta$ ) for Nail model and Le Claire model at dislocation density  $d = 1000$ .



**Figure 7.23** Mean concentration distribution along depth( $\eta$ ) for Nail model and Le Claire model at dislocation density  $d = 100$ .

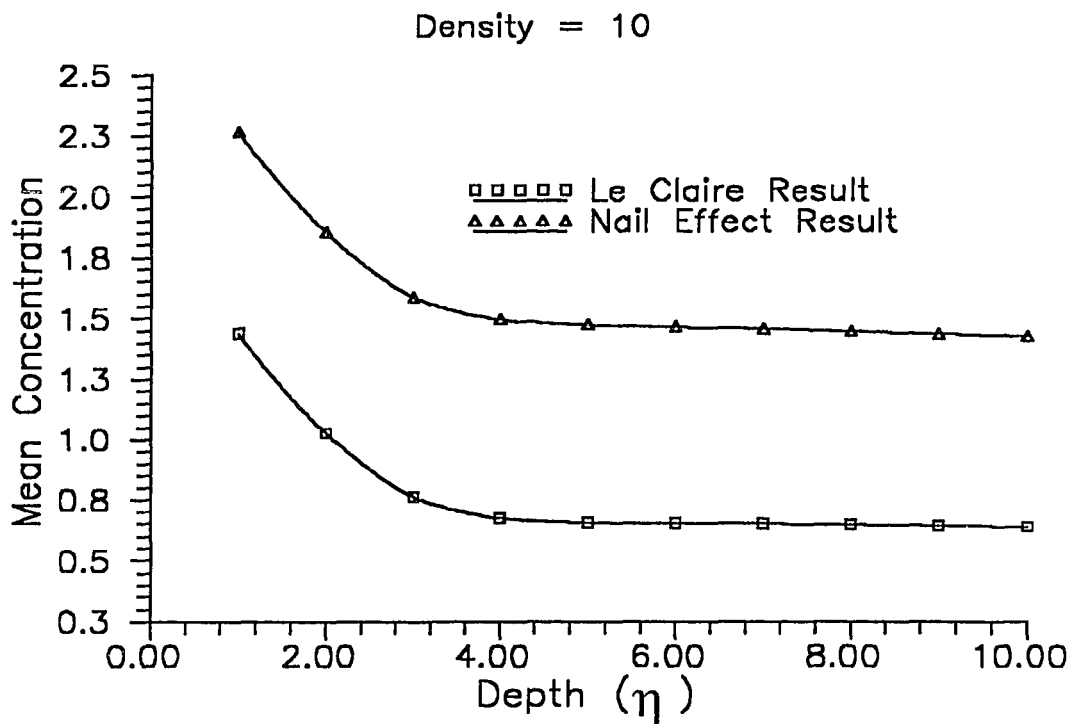


**Figure 7.24** Mean concentration distribution along depth( $\eta$ ) for Nail model and Le Claire model at dislocation density  $d = 10$ .

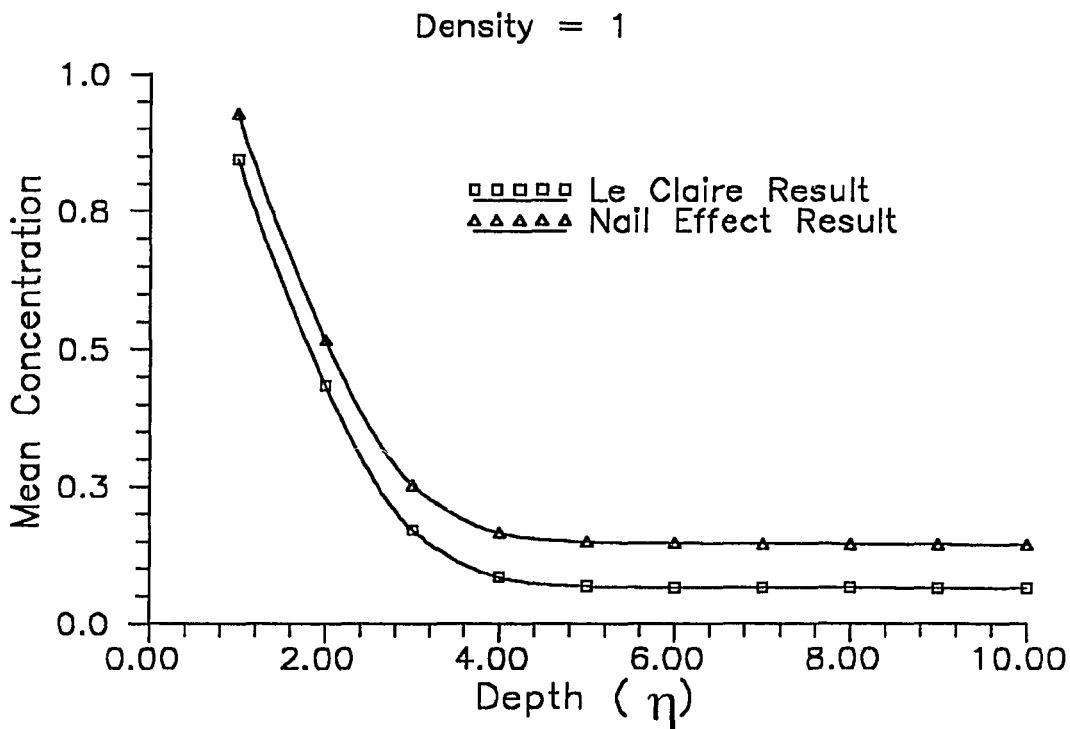


**Figure 7.25** Mean concentration distribution along depth( $\eta$ ) for Nail model and Le Claire model at dislocation density  $d = 1$ .

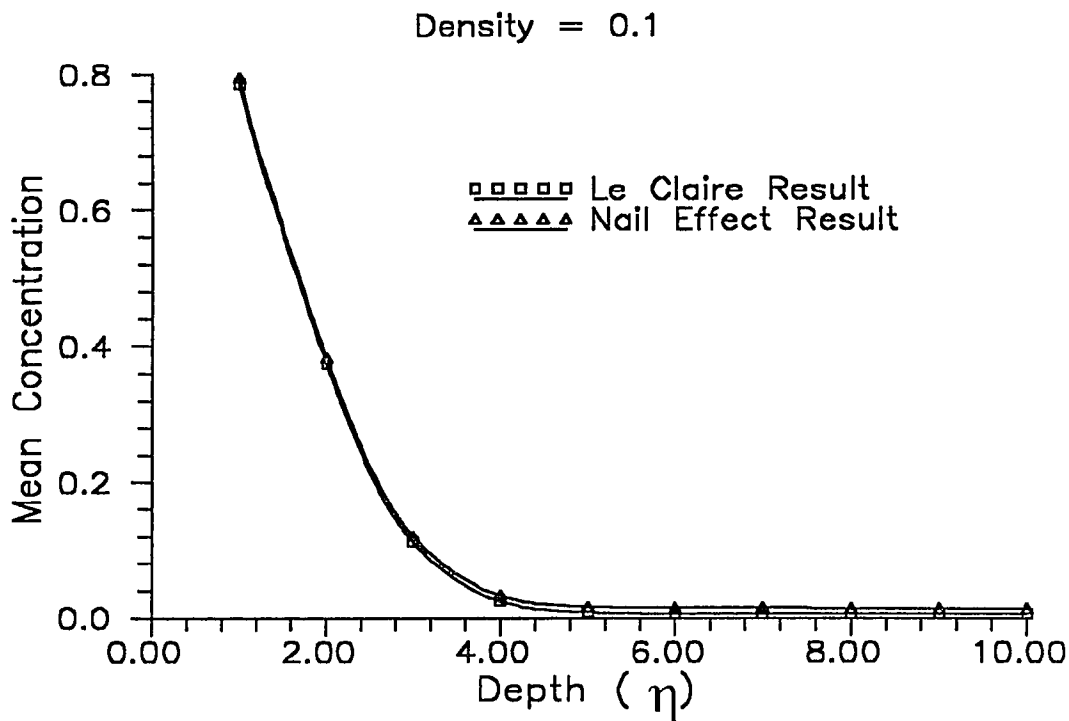


**Figure 7.26** Mean concentration distribution along depth( $\eta$ ) for Nail model and Le Claire model at dislocation density  $d = 0.1$ .

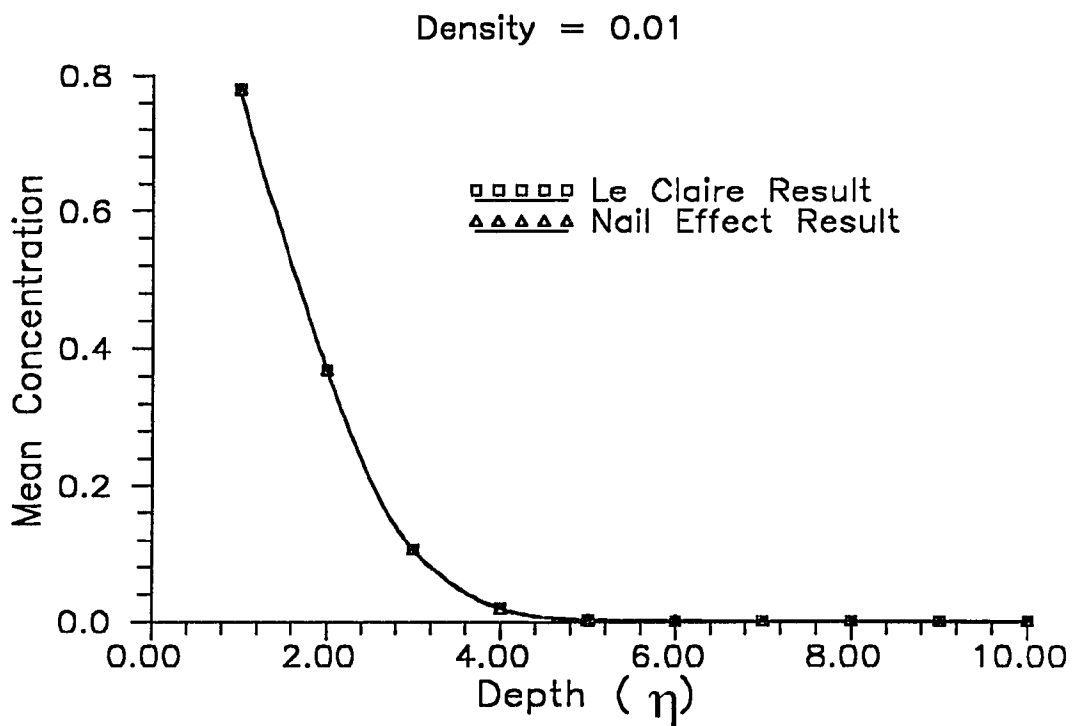


**Figure 7.27** Mean concentration distribution along depth( $\eta$ ) for Nail model and Le Claire model at dislocation density  $d = 0.01$ .

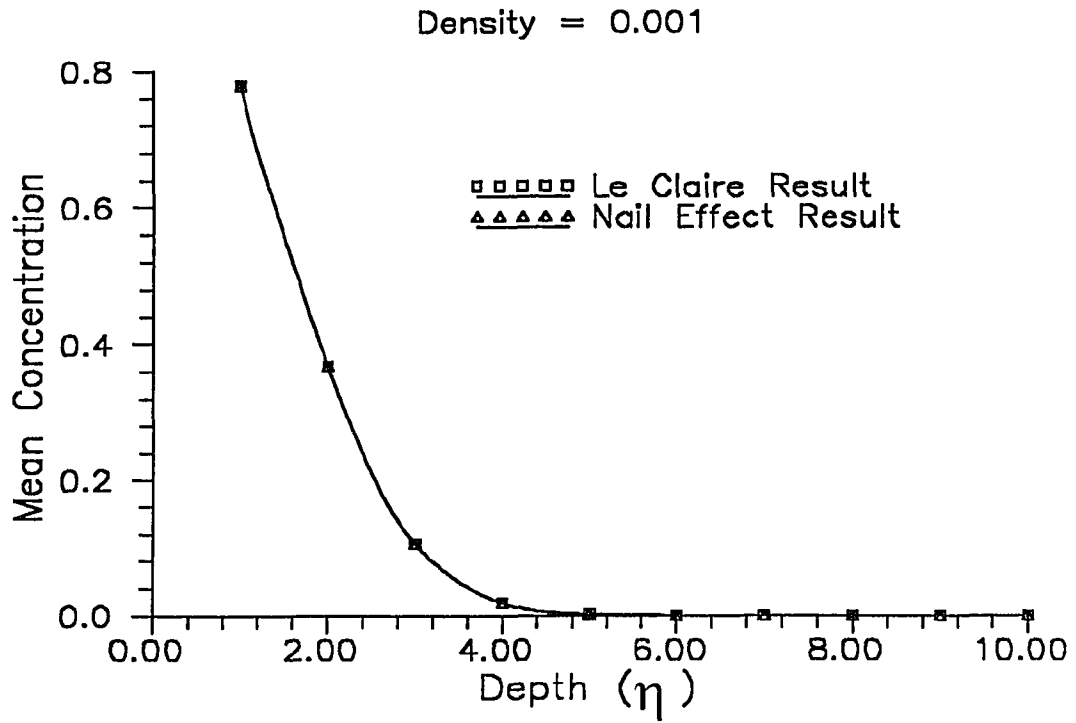


**Figure 7.28** Mean concentration distribution along depth( $\eta$ ) for Nail model and Le Claire model at dislocation density  $d = 0.0001$ .

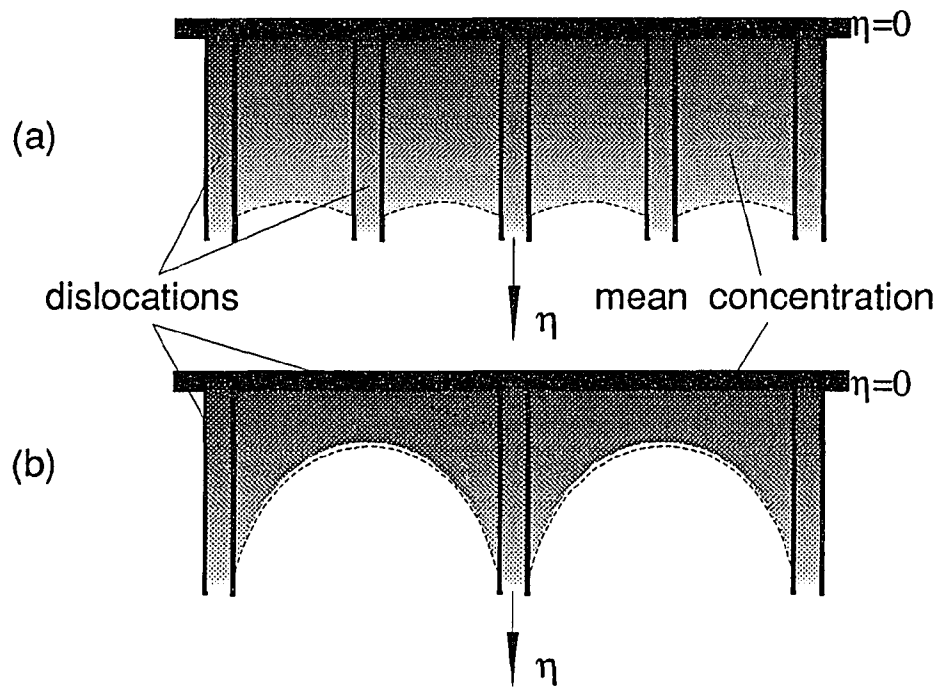


**Figure 7.29** Mean concentration distribution for (a) high dislocation density, (b) low dislocation density.



increase of depth. The mean concentration distribution for high dislocation density and low dislocation density could be constructed as shown in Figure 7.29. We can find that the diffusion process in a high dislocation density is strongly affected by the interaction of dislocations. A deep and homogeneous diffusion zone can be found. At low dislocation density the diffusion process along dislocations can not be affected by other dislocations. Although the diffusion zone is smaller than in high dislocation density, the nail character of the diffusion looks more significant.

## 7.6 Wear Evaluation

### 7.6.1 Friction Coefficient for Wear Testing Process

As we discussed earlier, the developed computer controlled wear testing machine and methodology are able to pick up and to record the friction moment, friction coefficient, wear, and wear rate during the friction test. The detail calibration work is described in [25]. The calibration has to be performed before the tests in order to obtain the constant  $K$  in Equation (6.8) and (6.9). The calibration charts represent the dependence of friction coefficient and friction force versus strain gage readings shown in Figures 7.30 and 7.31. From these charts, equations of these relations can be derived and then put into the program. Once the strain gage readings are picked up, the computer can directly obtain the friction information by running the program.

Figure 7.32 (a)-(d) shows the variation of friction coefficient during the wear testing for AISI H13 tool steel. The testing conditions are as follows:

Load : 216 lb.

Sliding speed : 277.8 rpm.

Time : 150 mins.

Distance :  $2 \times 10^5$  in

As can be noticed from friction force - sliding distance relationship shown in the above figures, we can observe three zones : running-in, steady-state, and catastrophic

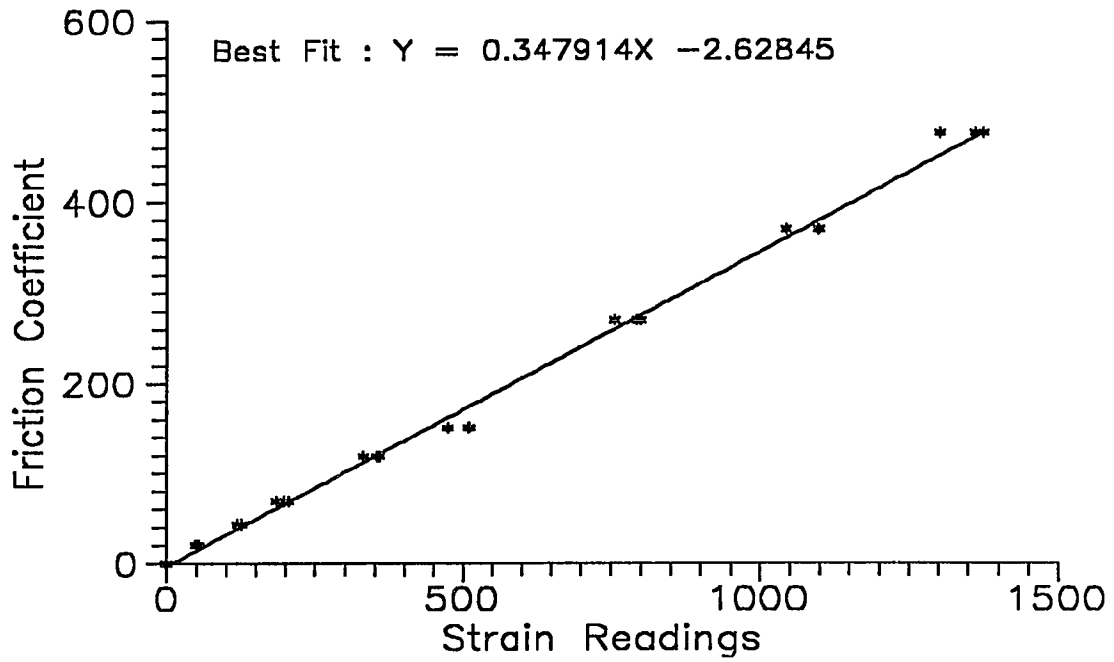


Figure 7.30 Calibration chart for friction coefficient versus strain readings.

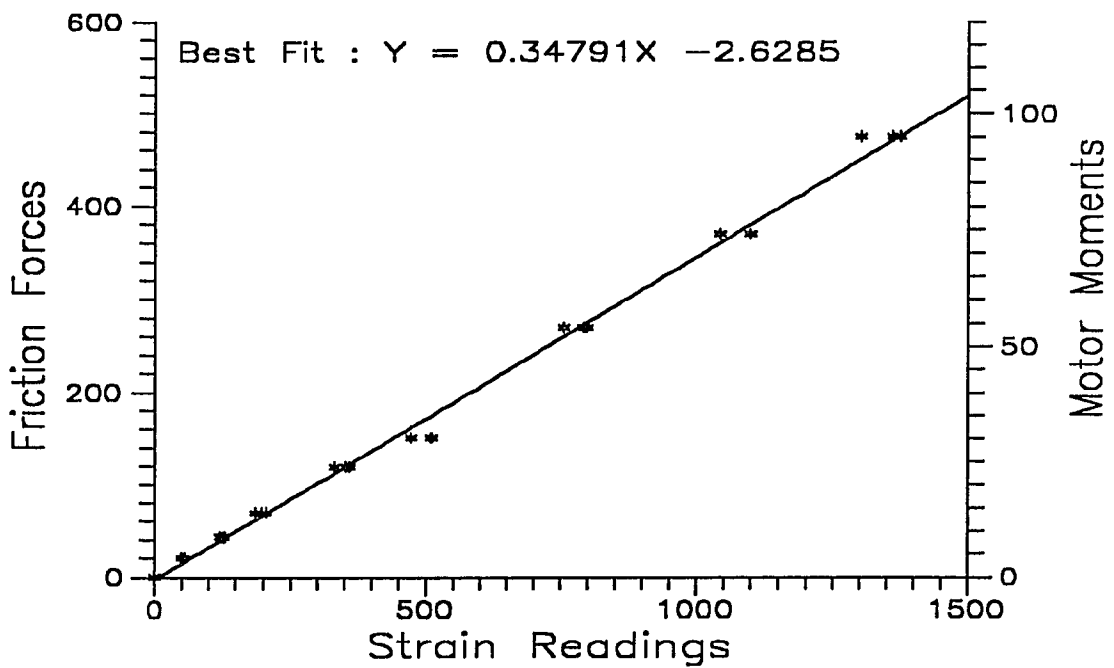


Figure 7.31 Calibration chart for friction force and motor moments versus strain readings.

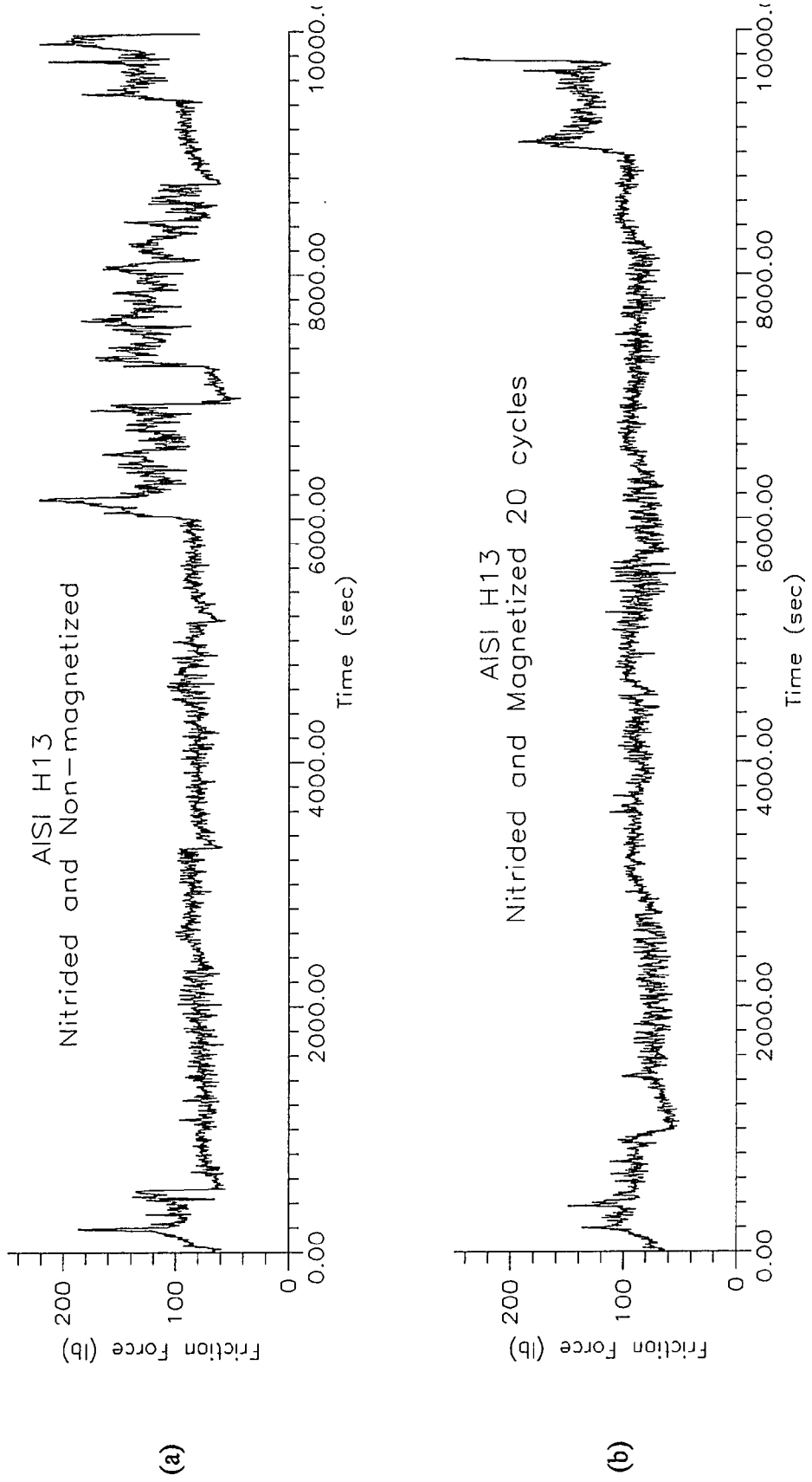
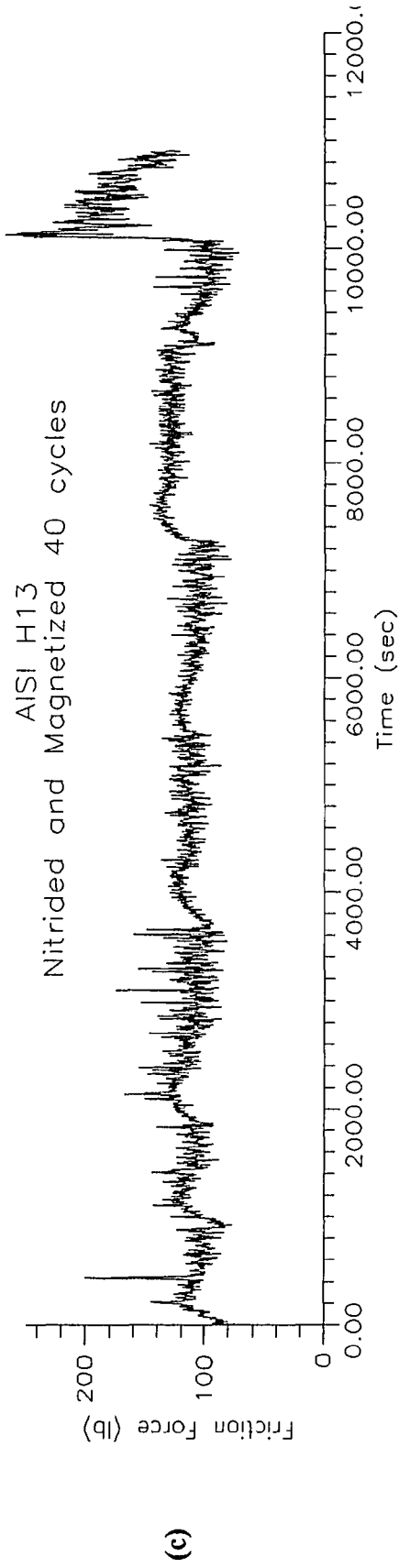
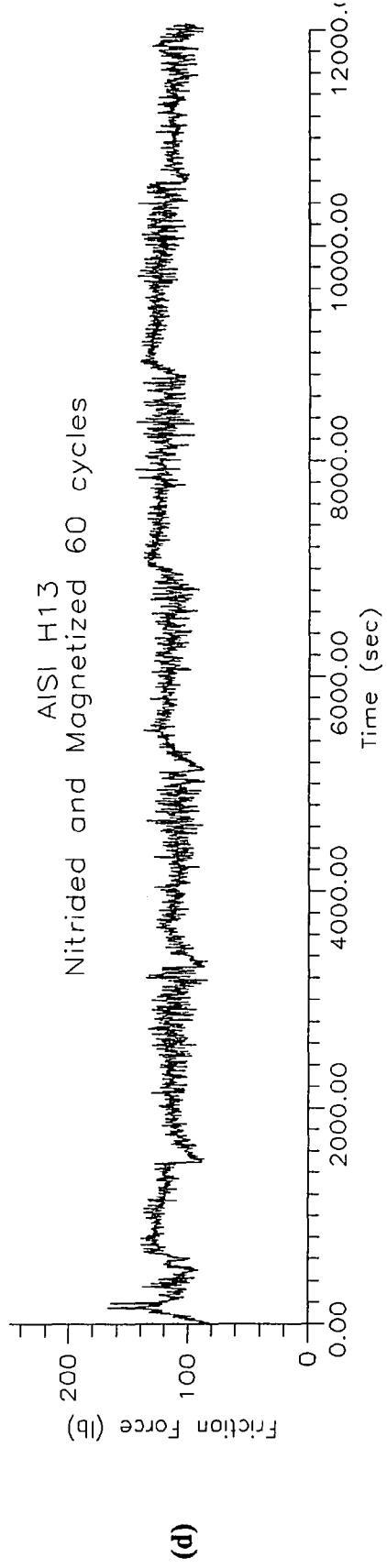


Figure 7.32 Friction forces versus sliding time for differently treated AISI H13 tool steel : (a). nitrided; (b). nitrided + 20 cycles pre-magnetization; (c). nitrided + 40 cycles; (d). nitrided + 60 cycles pre-magnetization.



(c)



(d)

**Figure 7.32(continued)** Friction forces versus sliding time for differently treated AISI H13 tool steel : (a). nitrided; (b). nitrided + 20 cycles pre-magnetization; (c). nitrided + 40 cycles; (d). nitrided + 60 cycles pre-magnetization.

stages during the wear test. In the running-in stage, we can see the dramatic increase of the friction force. This is due to the two unmatched surfaces being brought together. A larger shear force is required to remove the irregularities on the surface. The second stage, steady-state stage, has a steady increase of friction force. The curve in this range is smooth. This is due to the perfect match of surface condition of the wear couple. Finally, we can see a rapid increase of the friction forces in the last stage. This indicates the approach of the catastrophic stage of wear. The surfaces of two engaged wear components are destroyed in this stage. So we call this stage catastrophic wear.

From Figure 7.32 (a)-(d), we also can find the wear resistance of the tested specimens with AISI H13 tool steel and PIN treated at different magnetization conditions. By observing the time to reach catastrophic stage, we can see that the magnetized specimens have better wear resistance than non-magnetized specimens. Also, the specimens treated by higher number magnetization cycles have better wear resistance.

**Table 7.9** Testing parameters and specimen symbols for group 1.

Materials	Nitriding Parameters			
	Time (Hours)	Temperature (°C)	Pressure (torr)	Gas Composition (N <sub>2</sub> /H <sub>2</sub> )
4	6	650	3	55/45
6	8	600	3	70/30
8	6	600	4	55/45

Material 4, 6, 8 Magnetized	Magnetic Treatment Parameters		
	20 cycles	40 cycles	60 cycles
Before	MB1	MB2	MB3
After	MA1	MA2	MA3
Both	MC1	MC2	MC3

### 7.6.2 Wear Rate

Since wear testing was conducted to study the wear behavior of differently treated materials, two different groups of wear testing specimens were prepared. The first group

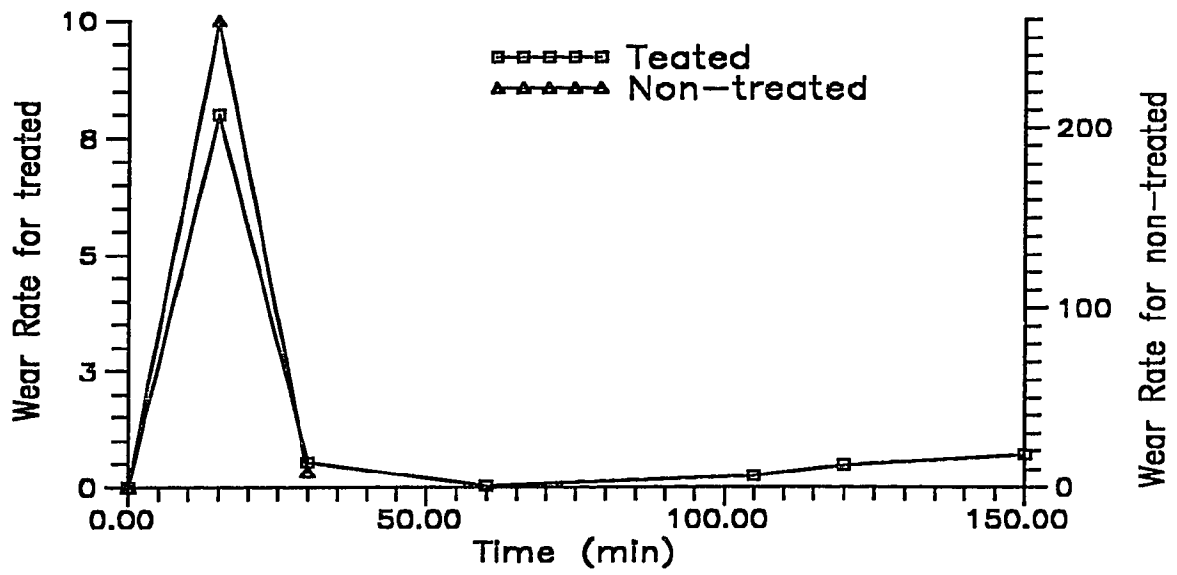


Figure 7.33 Wear rate of nitrided and non-nitrided AISI D2 tool steel.

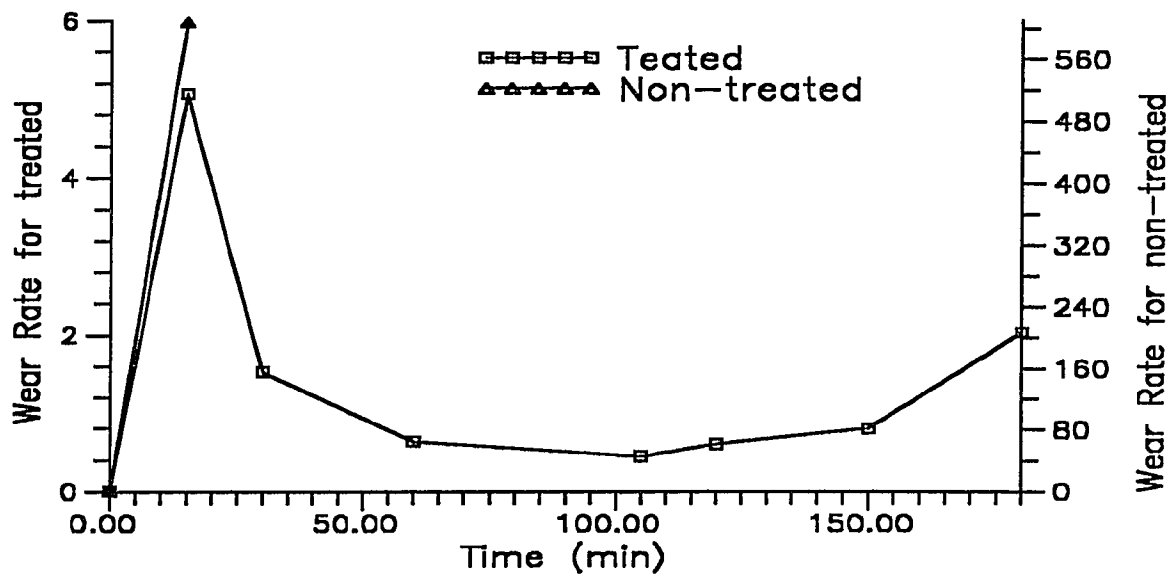


Figure 7.34 Wear rate of nitrided and non-nitrided AISI H13 tool steel.

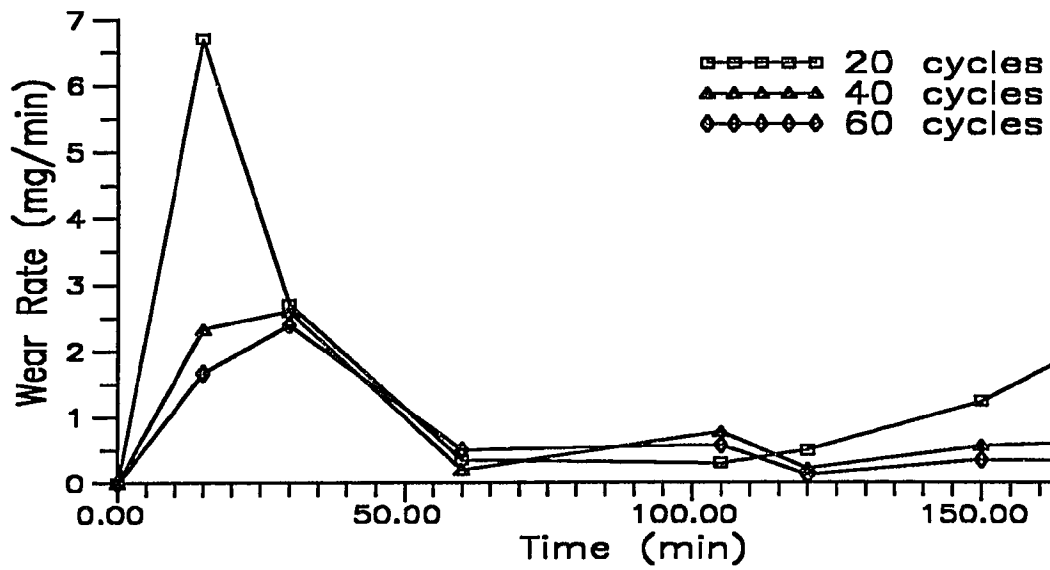


Figure 7.35 Wear rate for pre-magnetized and nitrated AISI H13 tool steel.

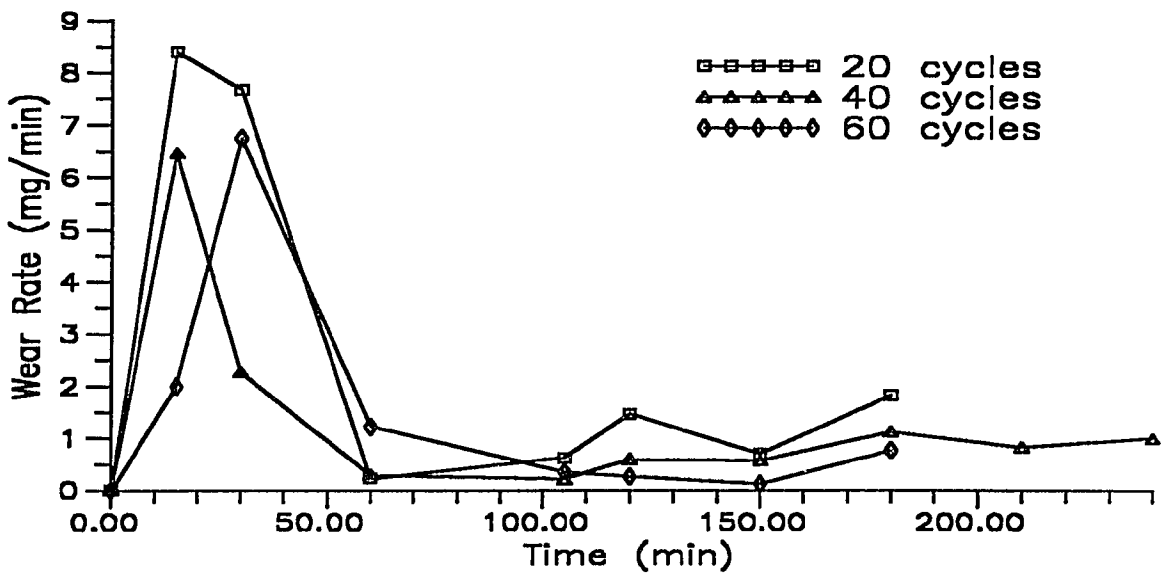


Figure 7.36 Wear rate for post-magnetized and nitrated AISI H13 tool steel.

of specimens was prepared for studying the effect of magnetization treatment. The parameters of the treatment and symbols for the specimens are shown in Table 7.9. The second group of specimens was prepared to study the influence of gas composition on wear resistance. The symbols and parameters for the specimens are shown in Table 7.10. This group of tests also can give the information about wear behavior of the pre-magnetized and post-magnetized specimens. The material used for wear testing are AISI D2 and H13 tool steels for group 1 and AISI H13 tool steel for group 2. For the wear testing couple, rollers are made from AISI 4320 alloy steel and shoes are made from AISI D2 and H13 tool steels.

Figures 7.33 and 7.34 show the wear rate of the nitrided and un-nitrided specimens done from D2 and H13 tool steel. All untreated specimens were quickly worn out or destroyed in the first 15 minutes. But the nitrided specimens provided wear resistance for more than 3 hours. Comparison of wear rate for these specimens shows that during the first 15 minutes of the test the wear resistance of PIN treated D2 steels is improved about 25 times and for PIN treated H13 specimens about 70 times.

Figures 7.35 and 7.36 show the wear rate for pre-magnetized and post-magnetized H13 respectively. From Figure 7.35, we can find that the running-in period extended from 15 minutes for 20 cycles to 1 hour for 60 cycles. This is thought to be the result of the "Nail Effect" from the magnetization process. The "Nail Effect" is stronger and deeper for the higher magnetization cycles. During the magnetization process, dislocations are shifted and eliminated. The rearranged dislocations are distributed in the structure. The possibility of the interaction between dislocations is reduced. With higher magnetization cycles, the rearrangement is deeper and the interaction is less. Once nitrogen diffuses into the structure, the arranged dislocations act like nails: the layer is closely attached to the next layer or bulk material. So the pre-magnetized specimens with higher magnetized cycles have better wear resistance.



Also from the total weight loss during the running-in stage, we can observe that the nitrided case is thicker in low magnetization cycles. This confirms the result of layer formation mentioned in the previous section. In post-magnetization cases, the total weight loss in the running-in stage are the same for all specimens. This is due to the same case depth formed under the same nitriding process. Residual stresses are diminished by the magnetization process. From the test results obtained from the post-magnetized specimen, we find that the specimen with less residual stresses has better wear resistance. Figure 7.36, as an example, shows that the specimen treated by higher magnetization cycles has less weight loss in the first 15 minutes than the others. Due to the nail effect, the density of dislocations is reduced and the interaction between dislocations is also decreased. The microstructure has less defects in the material. The shear force generated from friction forces can not so easily initiate the defects to tear the material away. So it has less weight loss than the other.

The dependence of wear resistance from layer properties obtained at different gas composition of PIN process are shown in Figure 7.37. The 65 % N<sub>2</sub> nitrided specimen has better wear resistance than the 25% N<sub>2</sub> nitrided specimen. As can be seen from microstructures obtained in the previous section, the higher nitrogen concentration gas forms a thicker  $\epsilon$  layer and  $\gamma'$  layers than lower nitrogen concentration treatment. Because the  $\epsilon$  layer has higher microhardness, the wear resistance of this layer is better than the other layers. The thicker  $\epsilon$  layer can prolong the weigh loss at the beginning. For the 5% nitrogen nitrided specimen, there is no  $\epsilon$  layer on the surface, so the weigh loss at the beginning is the highest.

Figures 7.38-40 are wear results for pre-magnetized and post-magnetized specimens. In general, we find that the wear rate of the pre-magnetized specimen is less than the post-magnetized specimen in the first 15 minutes. Also the magnetized specimens have a lower wear rate than non-magnetized specimens. This result also is true for the specimens of group 1. The nail effects enhance the bonding between the layers for the pre-magnetized

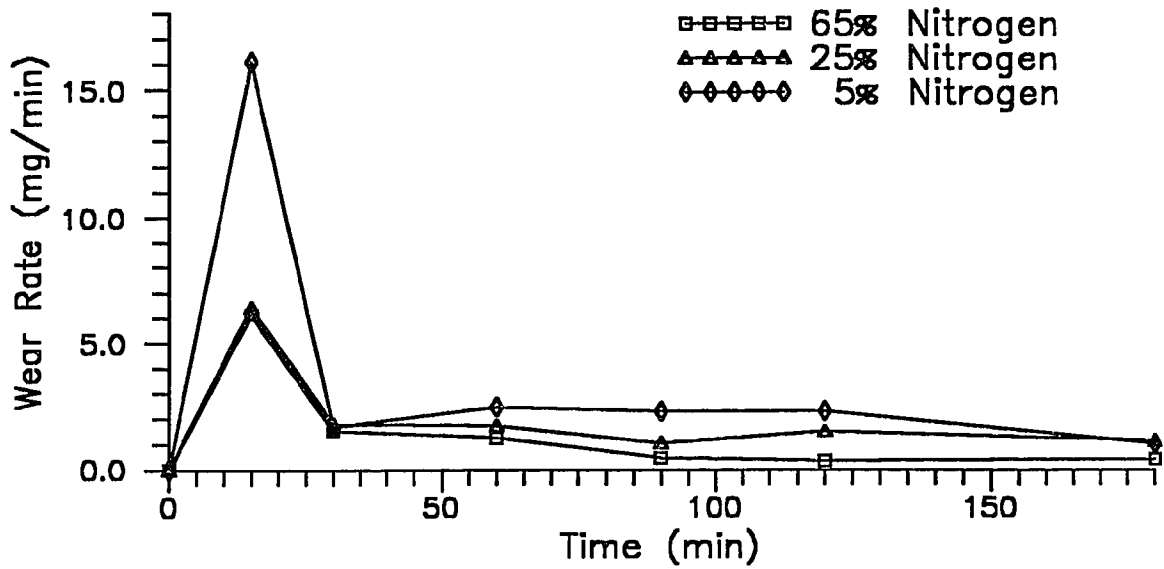


Figure 7.37 Wear rate for different nitrogen concentration of AISI H13 tool steel.

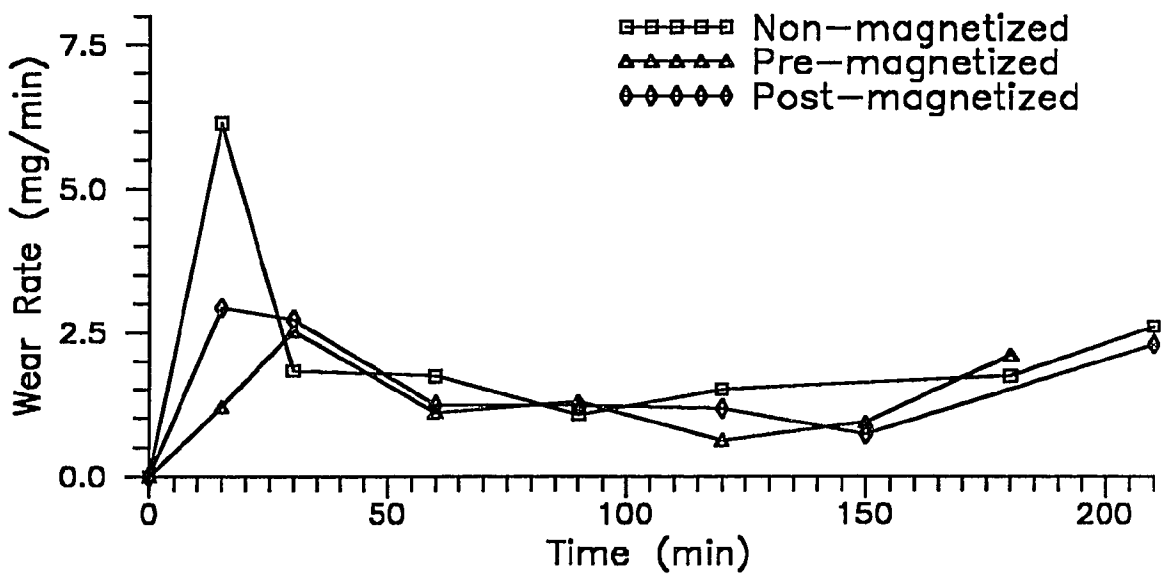


Figure 7.38 Wear rate for 65% nitrogen concentration of AISI H13 tool steel.

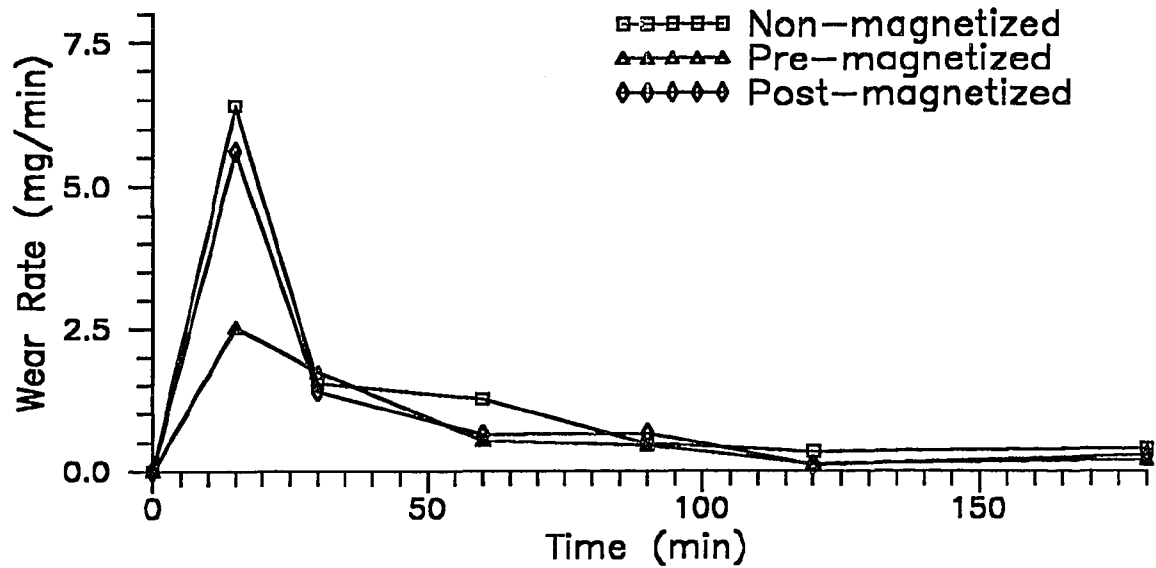


Figure 7.39 Wear rate for 25% nitrogen concentration of AISI H13 tool steel.

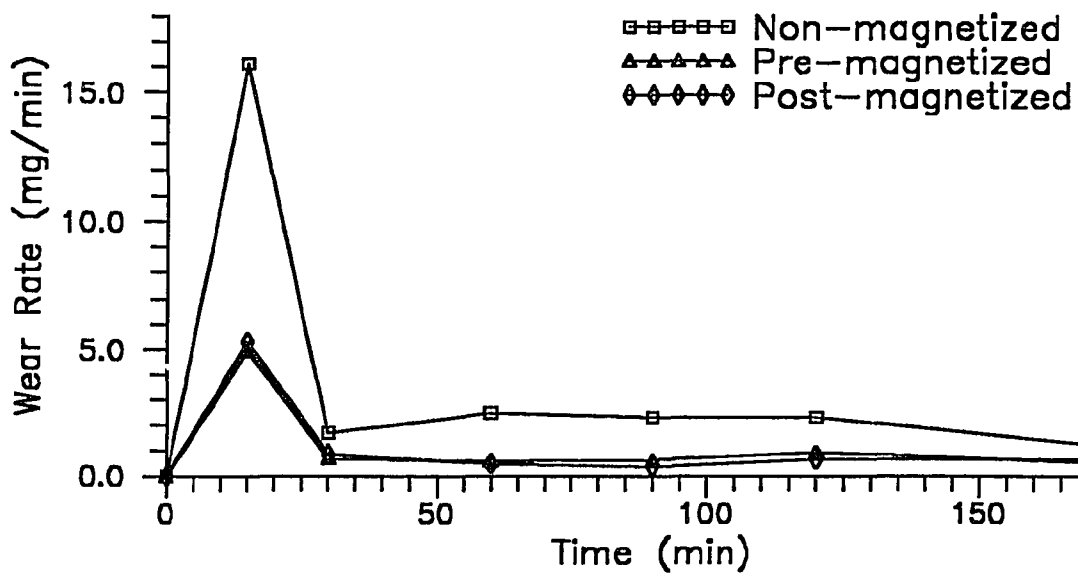


Figure 7.40 Wear rate for 5% nitrogen concentration of AISI H13 tool steel.

specimen, and release the residual stresses for the post-magnetized specimen. From these results, they show that the magnetization process applied before nitriding has better effects on wear than after nitriding. But the magnetized specimen has better wear resistance than non-magnetized specimen.

## CHAPTER 8

### CONCLUSIONS

In this work a new surface treatment process, magneto-plasma ion nitriding, was developed and studied. This process was developed to increase durability and wear resistance of working surfaces of different machine components.

To perform this study the following methods were used : image analyzing approach for microstructure study, scanning electron and Auger microscopy; computer-controlled microhardness study; surface finishing measurement with the program for evaluation of coating surfaces; orthogonal method for optimization of process parameters and layers development, and wear resistance methodology.

During this work, plasma ion nitriding and magnetic treatment equipment were set up. The process parameters were developed, optimized and selected. Surface layers were characterized and studied. The influences of different process treatment parameters, such as temperature, gas composition, magnetization treatment, on layers properties were studied. Wear testing methodology was designed and developed. The computer-controlled wear testing machine was designed, manufactured, assembled, and implemented. The wear resistance of machine components was tested by using the designed machine.

The following results were obtained during this study :

Selected orthogonal experimental method helped us to chose the process parameters, such as time, temperature, pressure, and gas concentration, for obtaining the desired nitriding results. As an example the result of orthogonal analysis for treated AISI D2 tool steel to obtain better weight gain during the nitriding process, the selected process parameters are 10 hours, 650°C, 3 torr, and 50% nitrogen concentration. Also we defined which process parameters are needed to obtain desired properties of deposited layers.

Image analysis provided the microstructure of all deposited layers obtained at the selected process parameters. These layers are shown in the Appendix A to C. Each layer represents a specific phase in the microstructure, such as  $\epsilon$ ,  $\gamma'$ , and the diffusion zone. All microstructures were analyzed and the microhardness distribution profiles were obtained. Auger and scanning electron microscopy analysis clearly defines the type of deposited compound layers, such as  $\epsilon$ ,  $\gamma'$ , or  $\epsilon+\gamma'$  layers. The optical microscopy analysis distinguishes the compound layers and diffusion zone.

The developed case-depth increases with the increase in temperature for nitriding treatment. However the overall microhardness inside the case-depth decreases with increase in temperature. Increasing nitrogen concentration has a beneficial effect on forming compound layers. To form  $\epsilon$  and  $\gamma'$  compound layers, the nitrogen concentration should be at least 25%. At low nitrogen concentration the  $\epsilon$  layer does not form even at high temperature.

The specimens treated with longer magnetization duration experience deeper and longer structure relaxation. Because of the stress relaxation, the microhardness of the long-treated structure is smaller than the short-treated specimens. The case-depth of specimens decreases with the increasing duration of magnetic treatment.

It is found that the pre-magnetized process influences formation of compound layers and nitrided case depth but does not affect the residual stresses on the surface. At the same time, the post-magnetized process does not influence compound layers formation but reduces the residual stresses in the case.

As a result of this work, the "Nail Effect" was discovered and the mechanism of magneto-plasma ion nitriding process was developed. Because of the relocation and elimination of dislocations after magnetization and demagnetization, dislocations are reoriented with respect to the treated surface. Most probably, dislocations are oriented in a direction normal to the surface. These dislocations look like pipes and can serve for mass transfer during diffusion. As a result of the diffusion process, the diffusant forms a

strong bond of obtained compound layers with the bulk materials. The concentration distribution along these dislocations works as the nails which bond the developed layers to the substrate. Observed improvement in mechanical bonding of developed layers on the surface to the substrate because of magneto-plasma ion nitriding is explained as the "Nail Effect". This name has been introduced by us during establishment of the mechanism of the magneto-plasma ion nitriding process.

The conical shape of concentration distribution around the dislocation in this model, as shown in Figure 7.21, is an example of a nail-like diffusion picture in the "Nail Effect".. On the basis of the "Nail Effect", we can conclude that the bonding force between compound layers and the substrate can be explained by two mechanisms. When the case depth is less than  $4\eta$ (see Equation (7.1)), the bonding force depends on bulk diffusion from the surface into the substrate. As the case-depth becomes larger than  $4\eta$ , the bonding force is a function of diffusion through dislocations into the substrate. In both cases the bonding forces are enhanced by the diffusion process. It is very important to underline the relationship between dislocation density and mean concentration. As shown in Figure 7.22 for high dislocations density, we have higher value of mean concentration and this results in a deeper and smoother diffusion zone. For low dislocation density, the mean concentration distribution has a shallow character and the diffusion front looks nail-like around the dislocation. This approach confirms the obtained experimental results that pre-magnetized specimens have thinner case depth than non-magnetized specimens. It should be noticed that the magnetization treatment reorients the dislocations by reducing their density. From our research, the "Nail Effect" can explain the mechanism of layer formation, layer bonding and diffusion zone character as well as the improvement of wear resistance of deposited compound layers.

The wear testing results show that the developed wear testing methodology and the designed computer controlled wear testing machine are capable of performing wear

resistance testing. This machine is able to monitor and record the wear testing process and to prevent any operational errors during wear testing experiments.

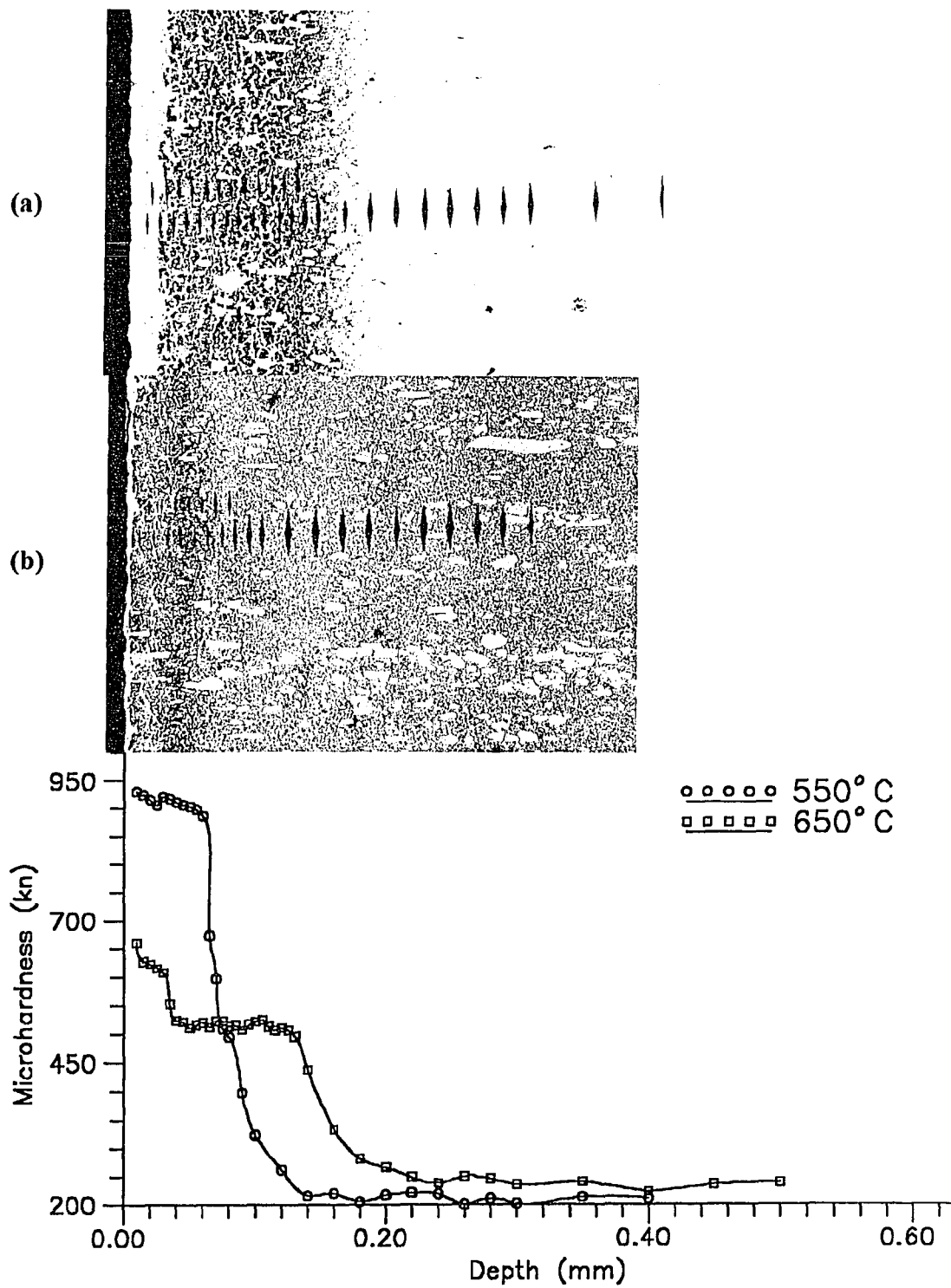
The friction force versus sliding time relationship indicates the existence of three stages of wear: running-in stage, steady state stage, and catastrophic wear. The wear testing experiments show that wear rate is improved about 70 times for nitrided specimens in comparison to non-nitrided specimens. The specimens treated in a high nitrogen concentration atmosphere have better wear resistance than specimens treated in a low nitrogen concentration atmosphere. This is due to the  $\epsilon$  and  $\gamma'$  layer formation. From the friction force - sliding time relationship, we can conclude that the specimens magnetized by a higher number of cycles have better wear resistance than the specimens treated by a low number of cycles. Specimens treated with a higher number of magnetic cycles have thinner compound layers but a deeper diffusion zone. At the same time, specimens treated by a smaller number of magnetic cycles should have thicker compound layers and a thinner diffusion zone. As found from the wear tests, specimens treated by a higher number of magnetic cycles have higher wear resistance, which is due to the "Nail Effect". Pre-magnetized specimens have smaller case-depth than post-magnetized specimens, but better wear resistance. This is due to the better bonding force between compound layers and the substrate enhanced by the "Nail Effect".

Although the objectives of this study have been accomplished and numerous results have been obtained, there are further studies still to be carried out. For example, applying the magneto-plasma ion nitriding process to different materials; further study of the roles of each nitride layer and their combinations during wear testing; additional microstructural investigation of developed nitride layers and their role in wear, corrosion, and fatigue resistance should be examined..

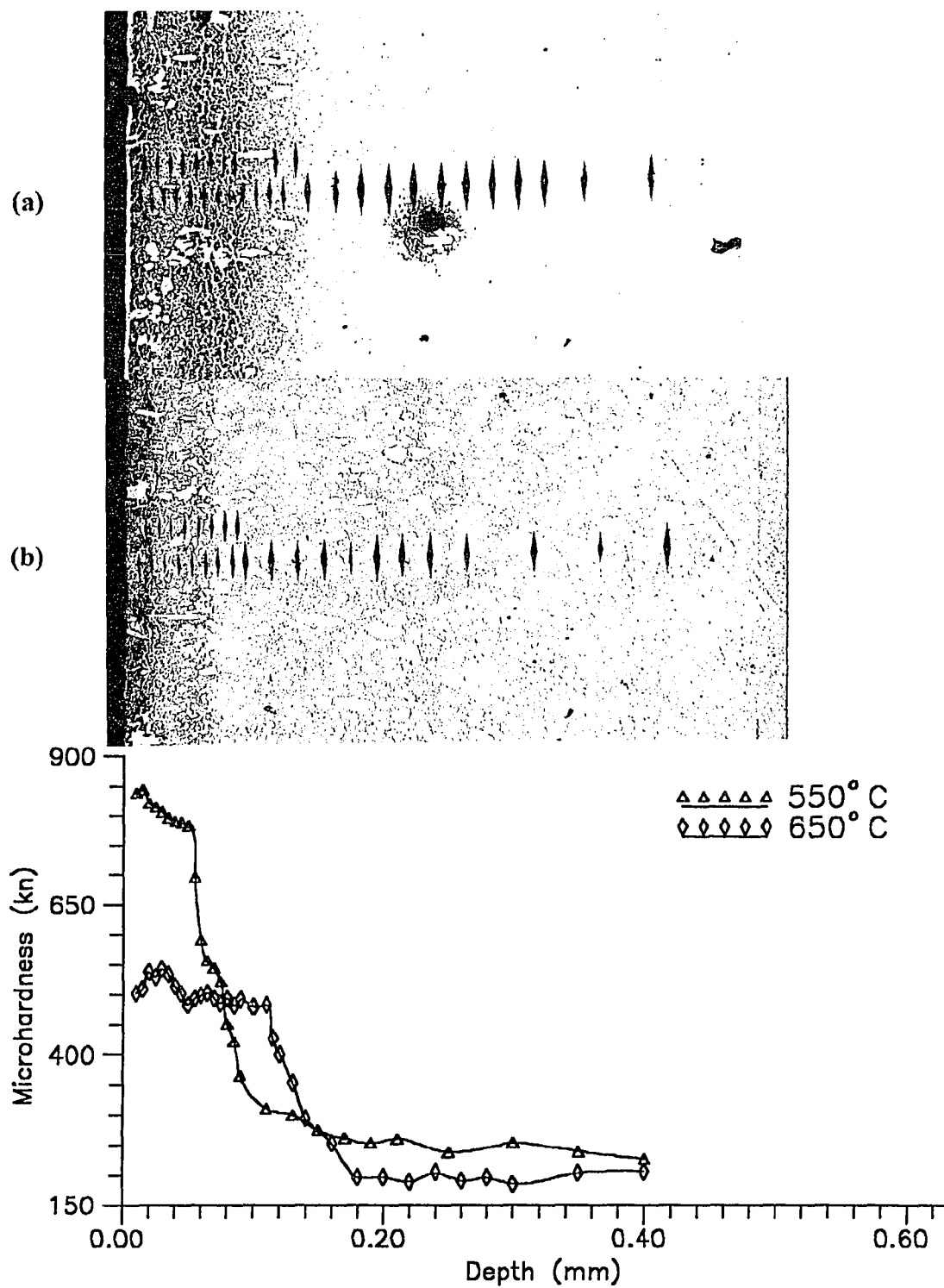


## **APPENDIX A**

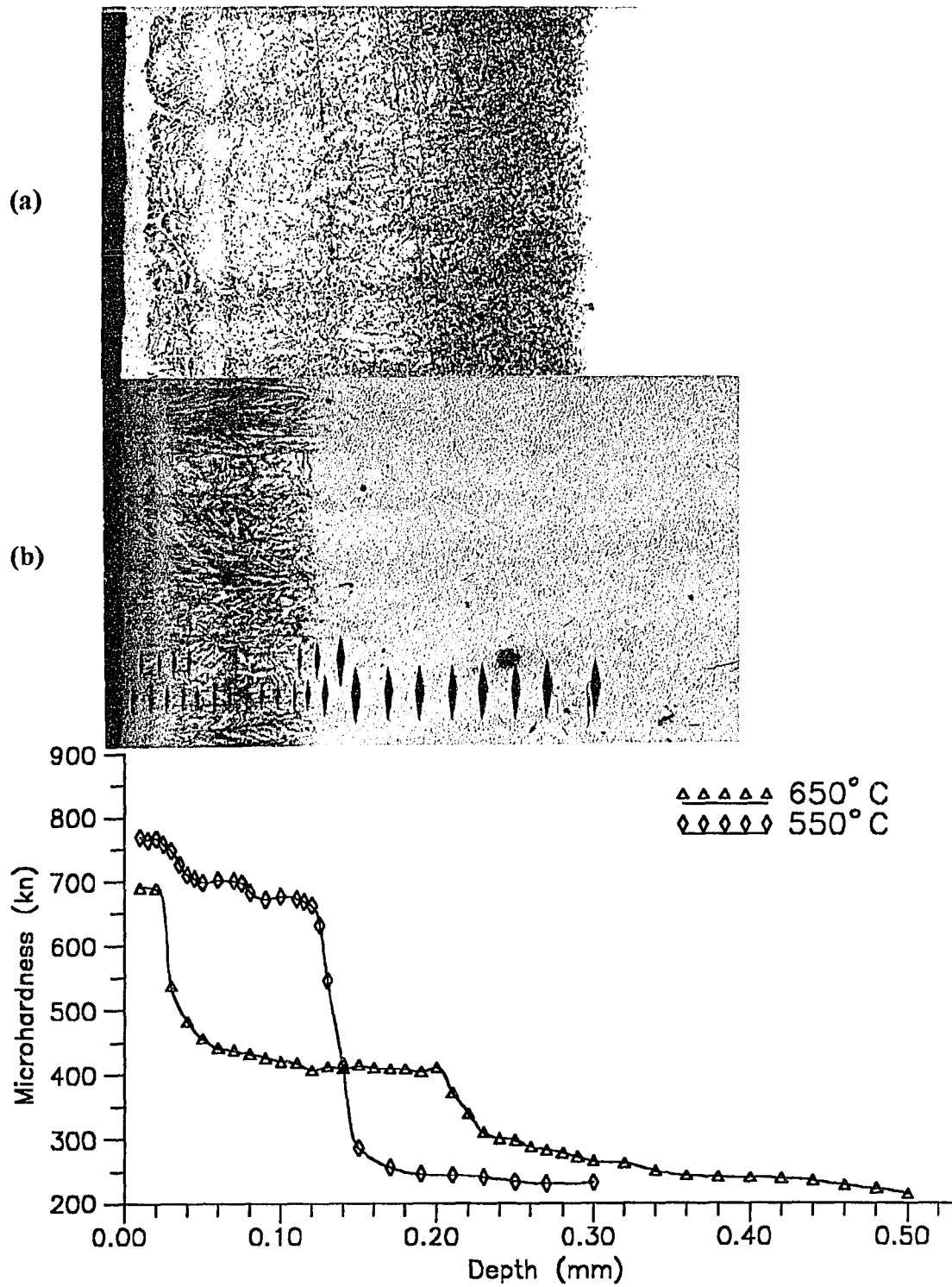
### **Layer Formation at Different Temperature**



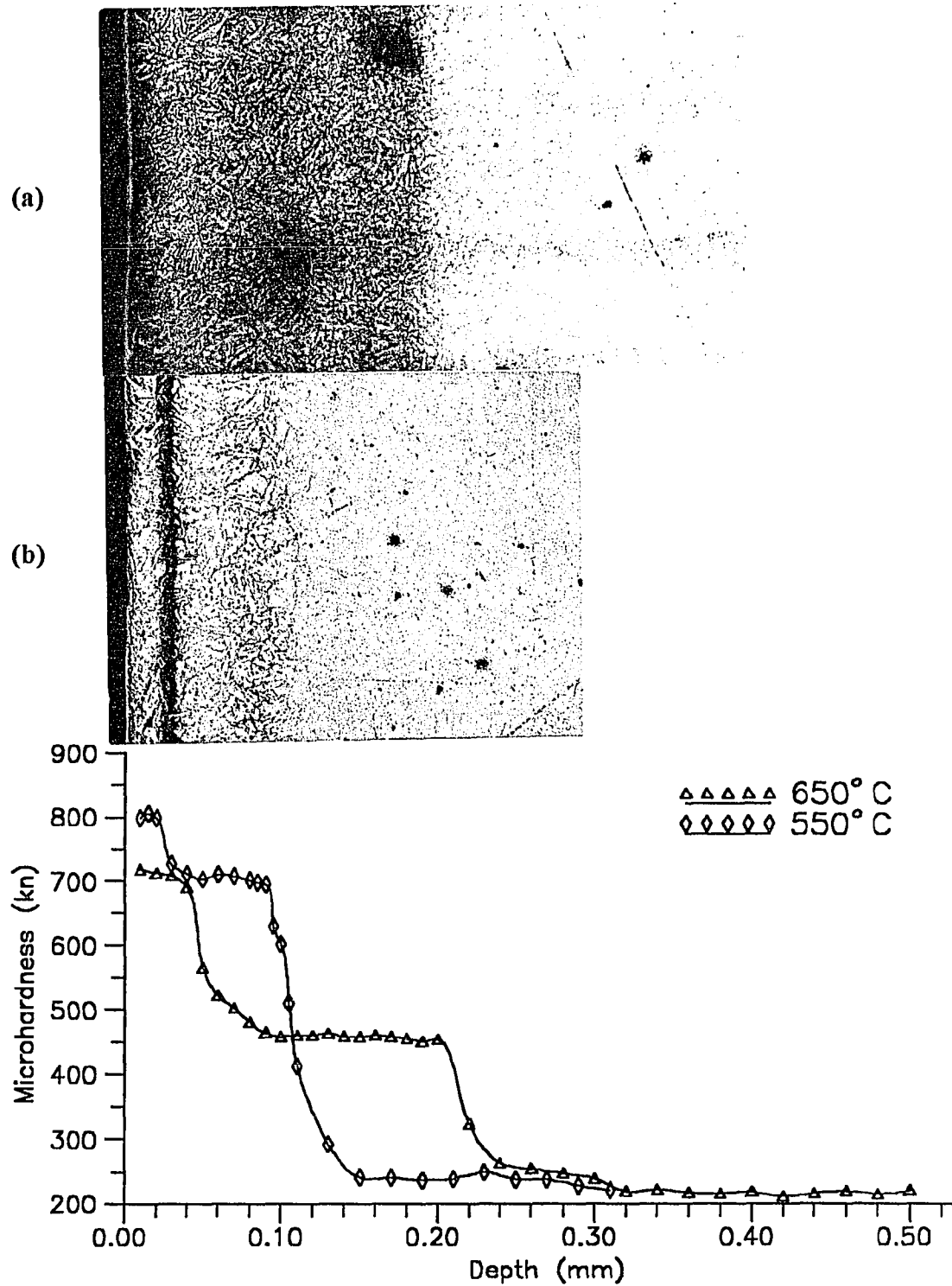
**Appendix A1** Variation in the microstructure and microhardness of the nitrided layer at different temperature for AISI D2 tool steel (25% N<sub>2</sub>, 6 hours, 3 torr): (a) 650°C; (b) 550°C.



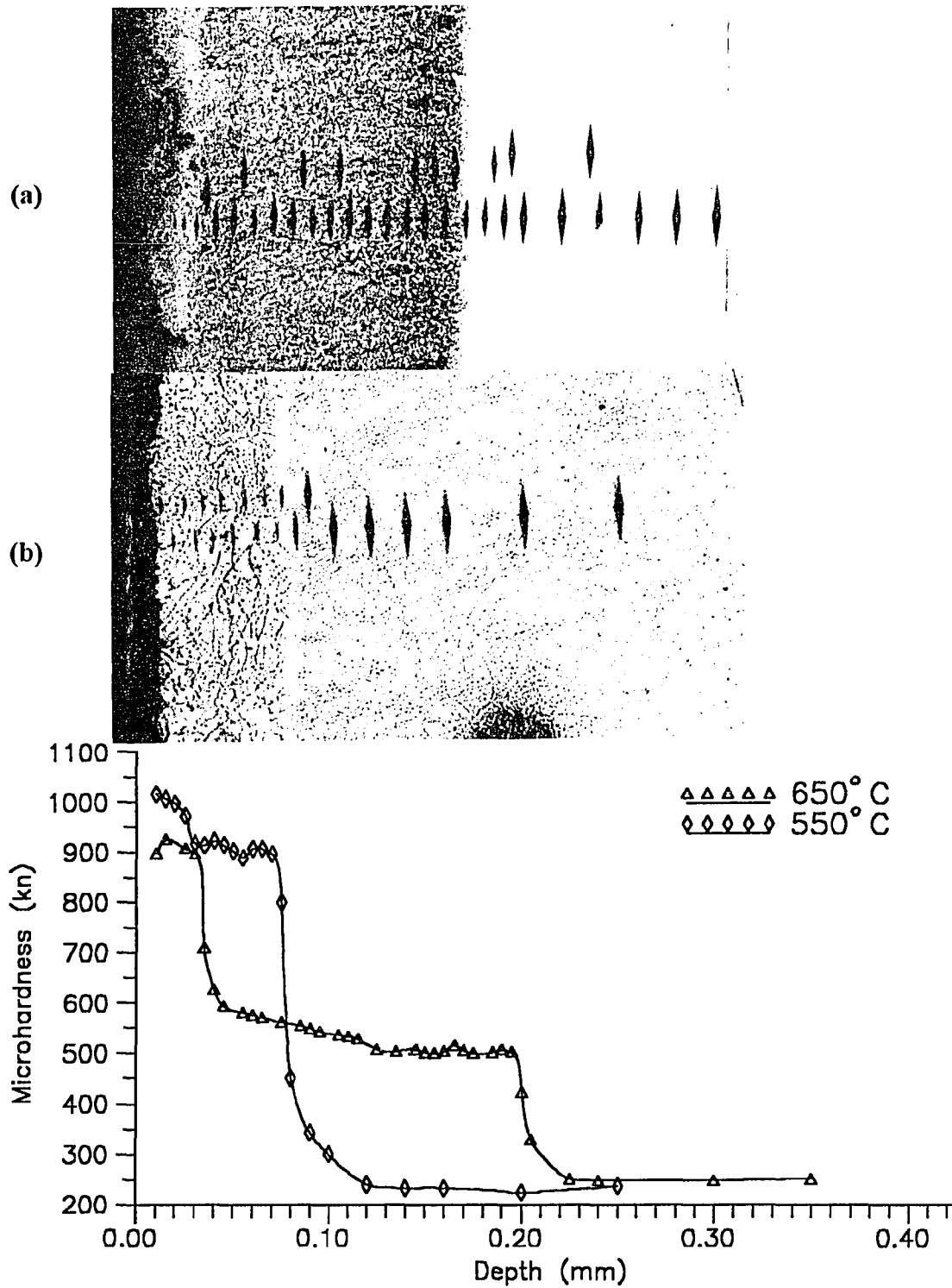
**Appendix A2** Variation in the microstructure and microhardness of the nitrided layer at different temperature for AISI D2 tool steel (5% N<sub>2</sub>, 6 hours, 3 torr): (a) 650°C; (b) 550°C.



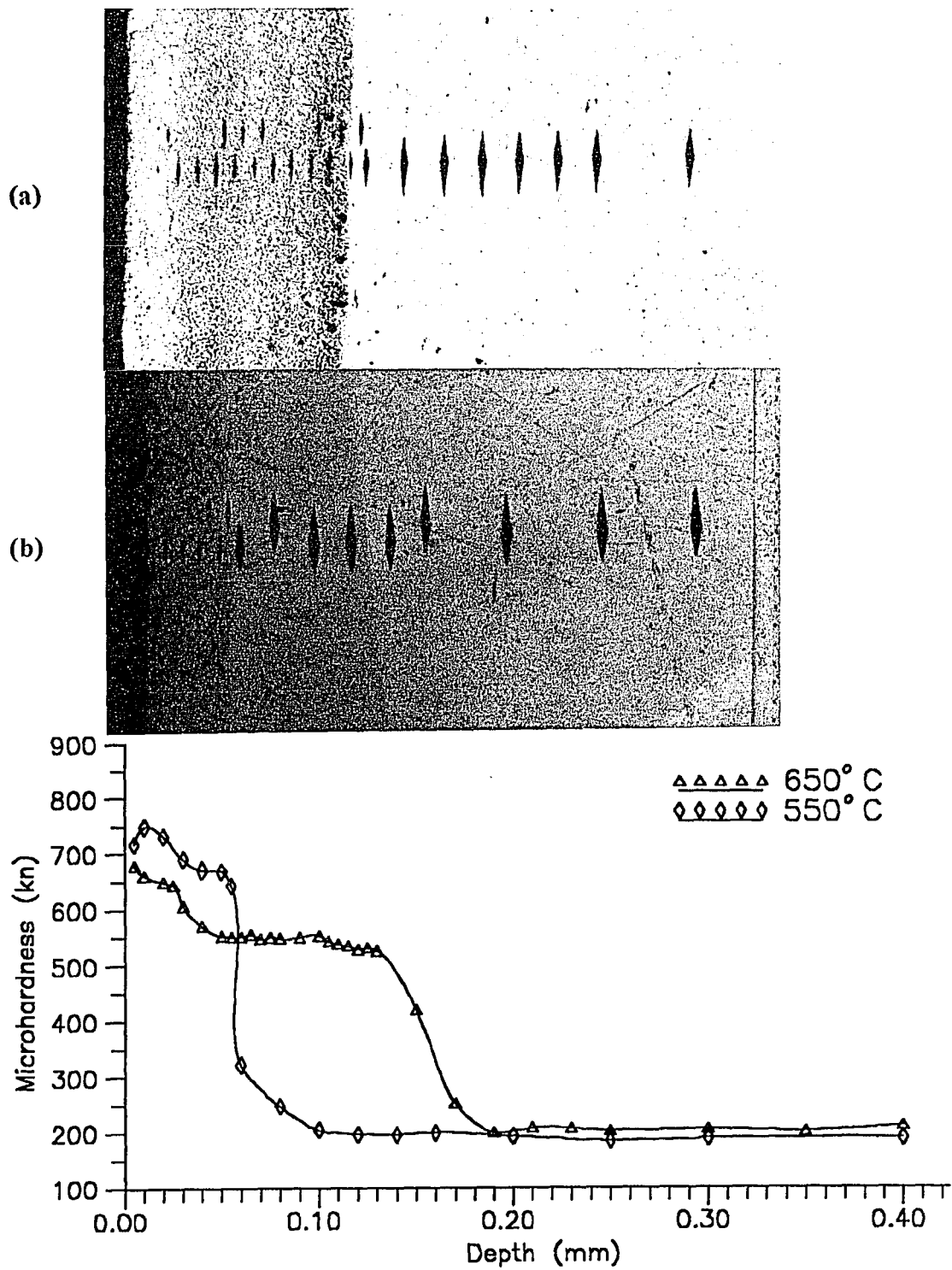
**Appendix A3** Variation in the microstructure and microhardness of the nitrided layer at different temperature for AISI H13 tool steel (25% N<sub>2</sub>, 6 hours, 3 torr): (a) 650°C; (b) 550°C.



**Appendix A4** Variation in the microstructure and microhardness of the nitrided layer at different temperature for AISI H13 tool steel (5% N<sub>2</sub>, 6 hours, 3 torr): (a) 650°C; (b) 550°C.



**Appendix A5** Variation in the microstructure and microhardness of the nitrided layer at different temperature for AISI 420 stainless steel (25% N<sub>2</sub>, 6 hours, 3 torr): (a) 650°C; (b) 550°C.

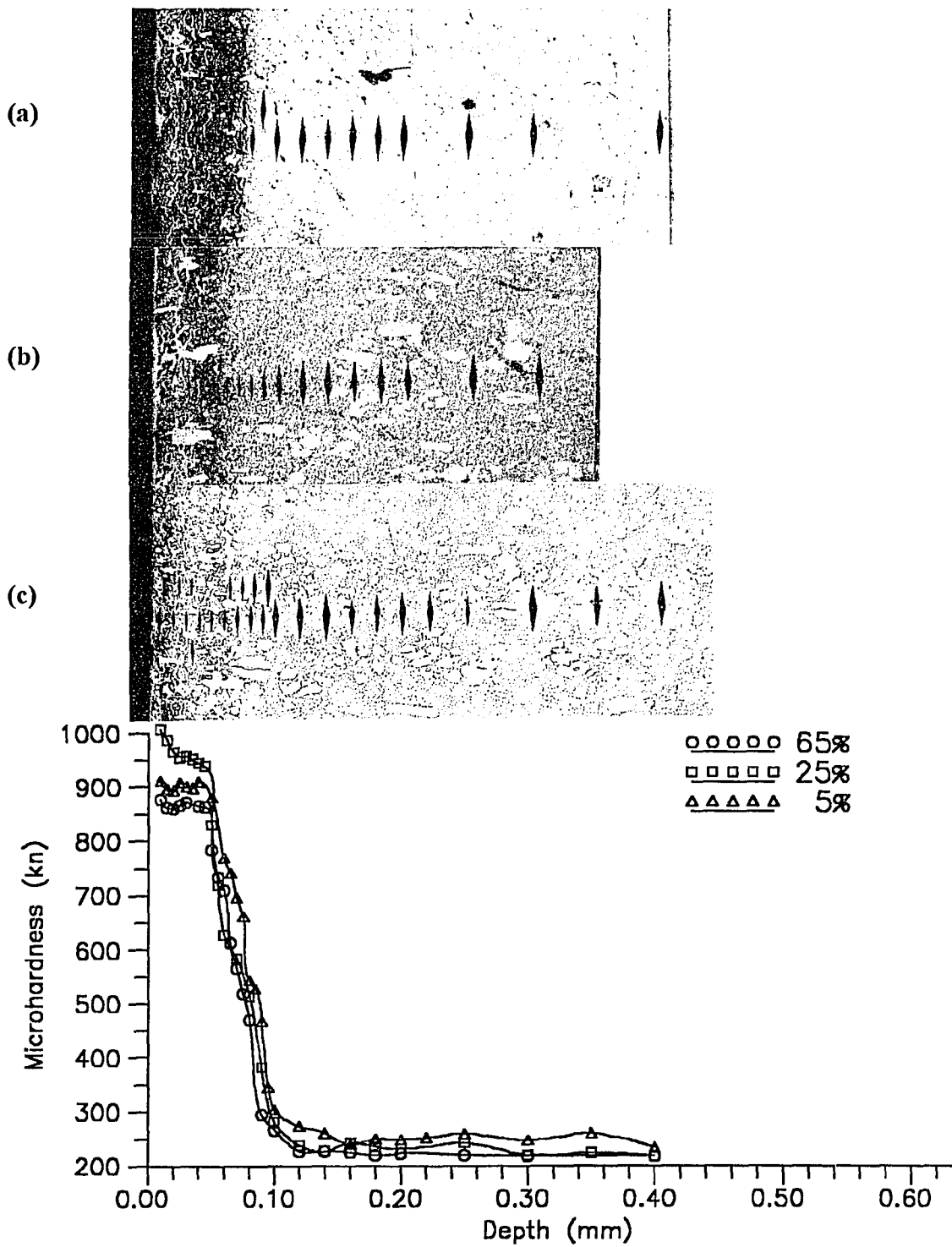


**Appendix A6** Variation in the microstructure and microhardness of the nitrided layer at different temperature for AISI 420 stainless steel (5% N<sub>2</sub>, 6 hours, 3 torr): (a) 650°C; (b) 550°C.

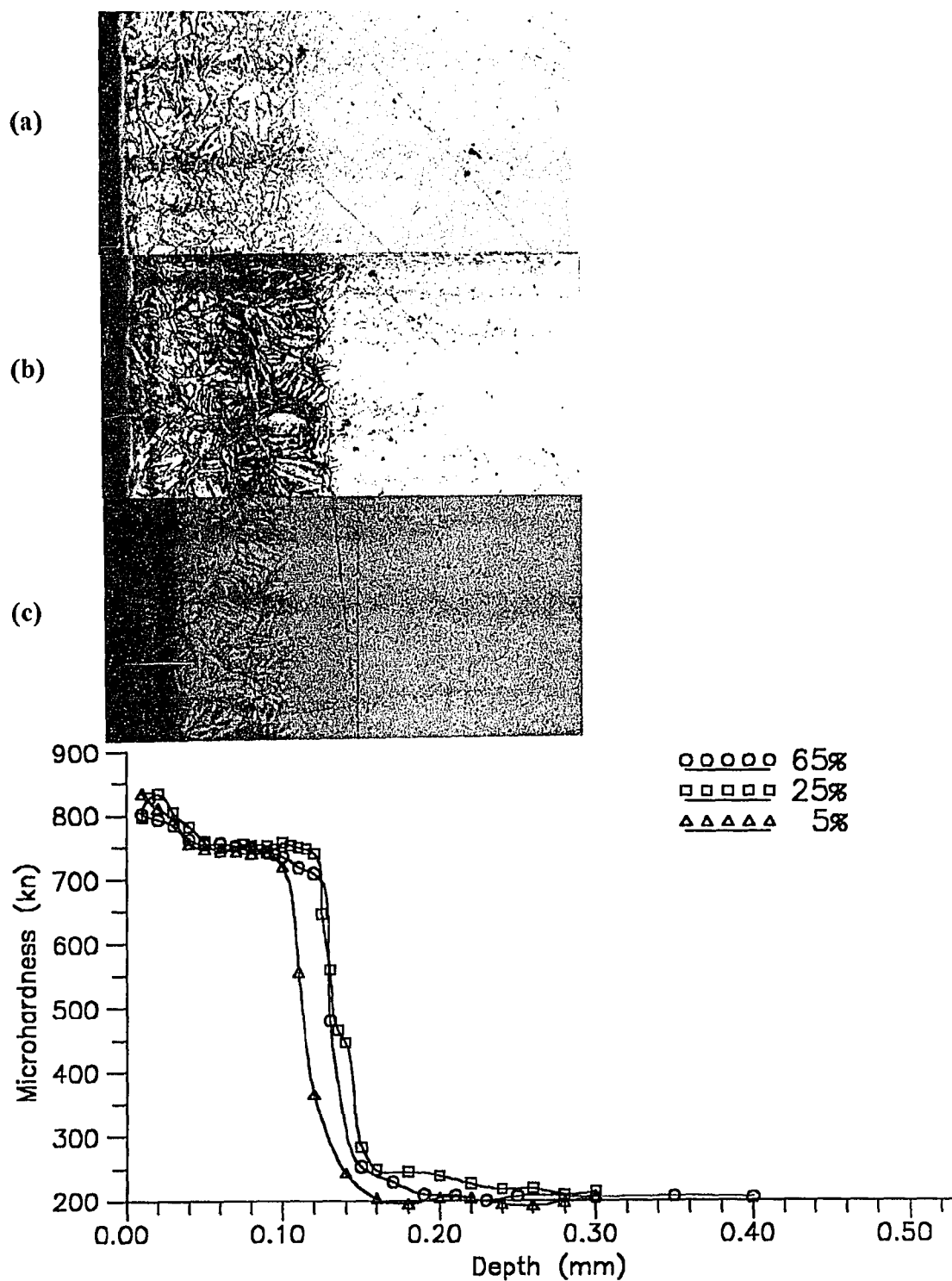
## **APPENDIX B**

### **Layer Formation at Different Nitrogen Concentration**

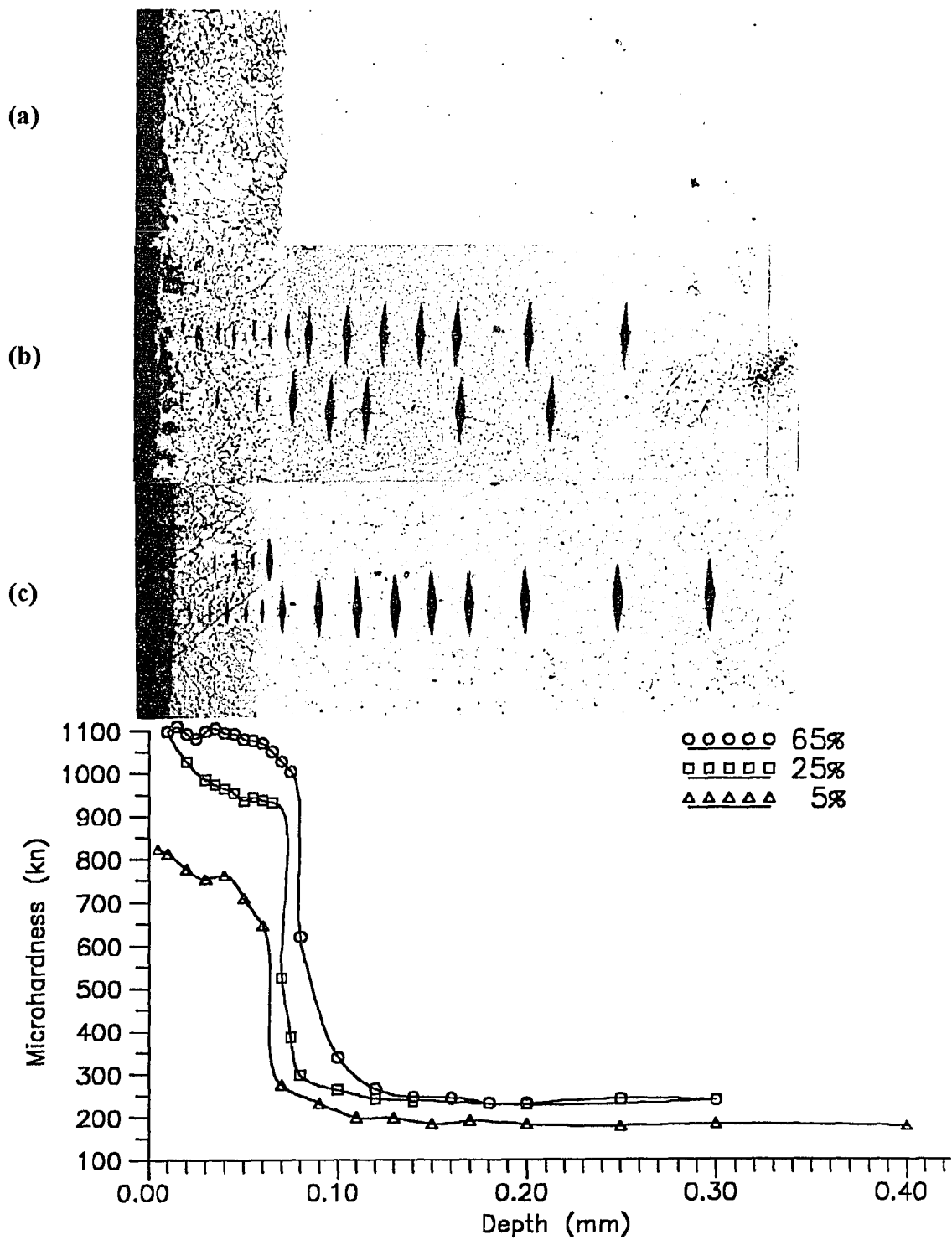




**Appendix B1** Variation in the microhardness and microstructure of the nitrided layer at different nitrogen concentration for AISI D2 steel (550°C, 6 hours, 3torr): (a) 65% N<sub>2</sub>; (b) 25% N<sub>2</sub>; (c) 5% N<sub>2</sub>.



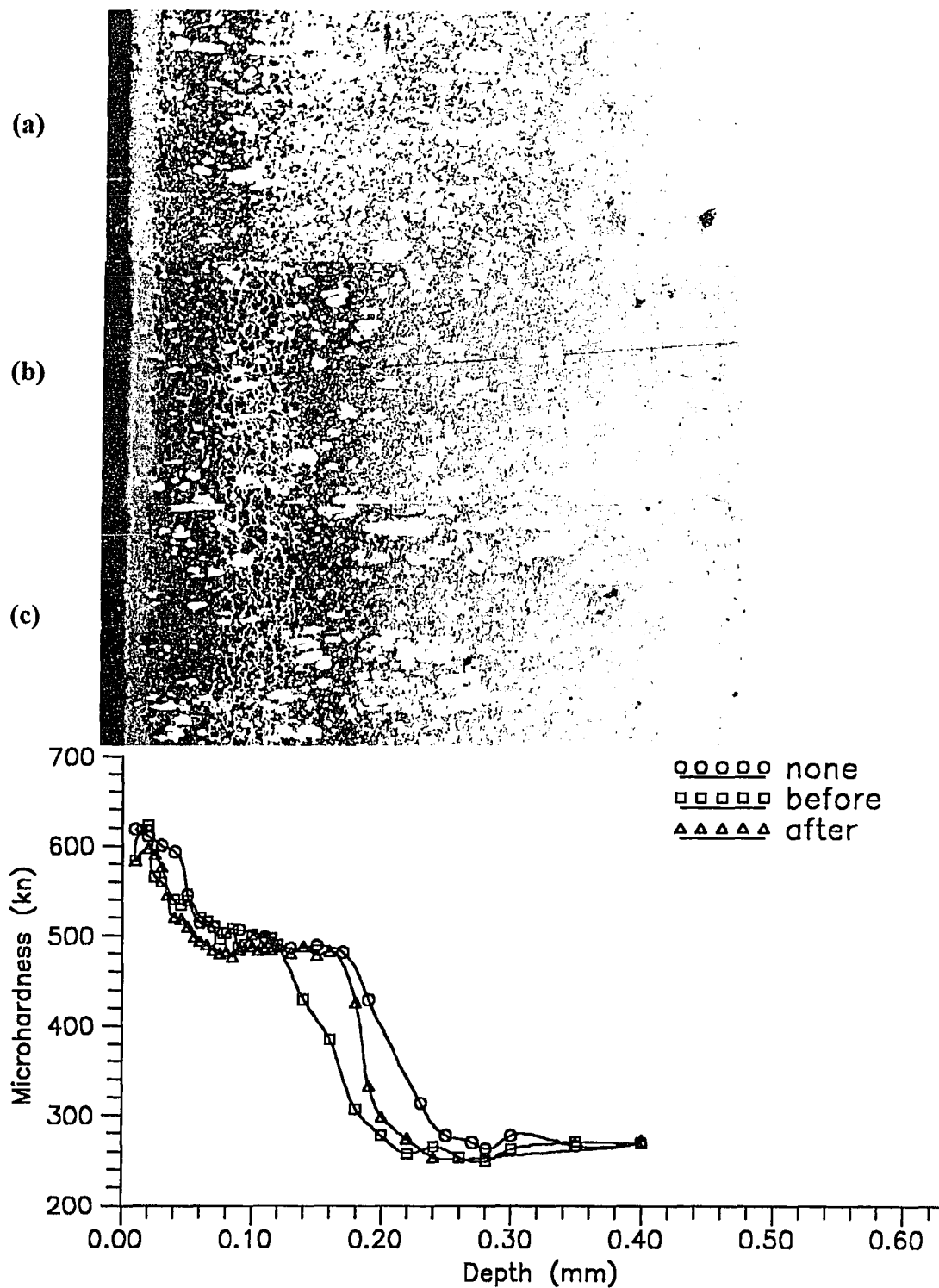
**Appendix B2** Variation in the microhardness and microstructure of the nitrided layer at different nitrogen concentration for AISI H13 tool steel (550°C, 6 hours, 3torr): (a) 65% N<sub>2</sub>; (b) 25% N<sub>2</sub>; (c) 5% N<sub>2</sub>.



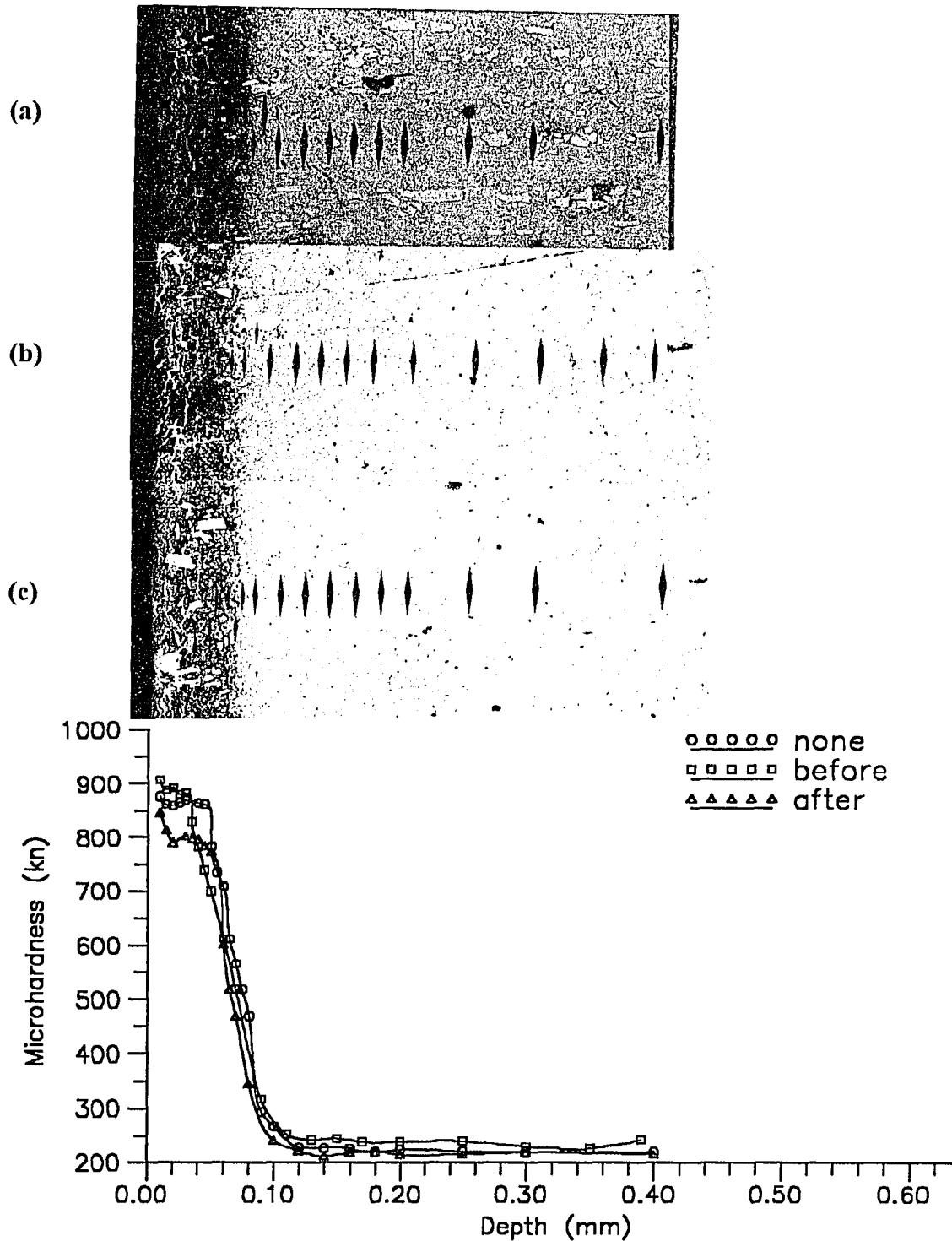
**Appendix B3** Variation in the microhardness and microstructure of the nitrided layer at different nitrogen concentration for AISI 420 stainless steel (550°C, 6 hours, 3torr): (a) 65% N<sub>2</sub>; (b) 25% N<sub>2</sub>; (c) 5% N<sub>2</sub>.

## **APPENDIX C**

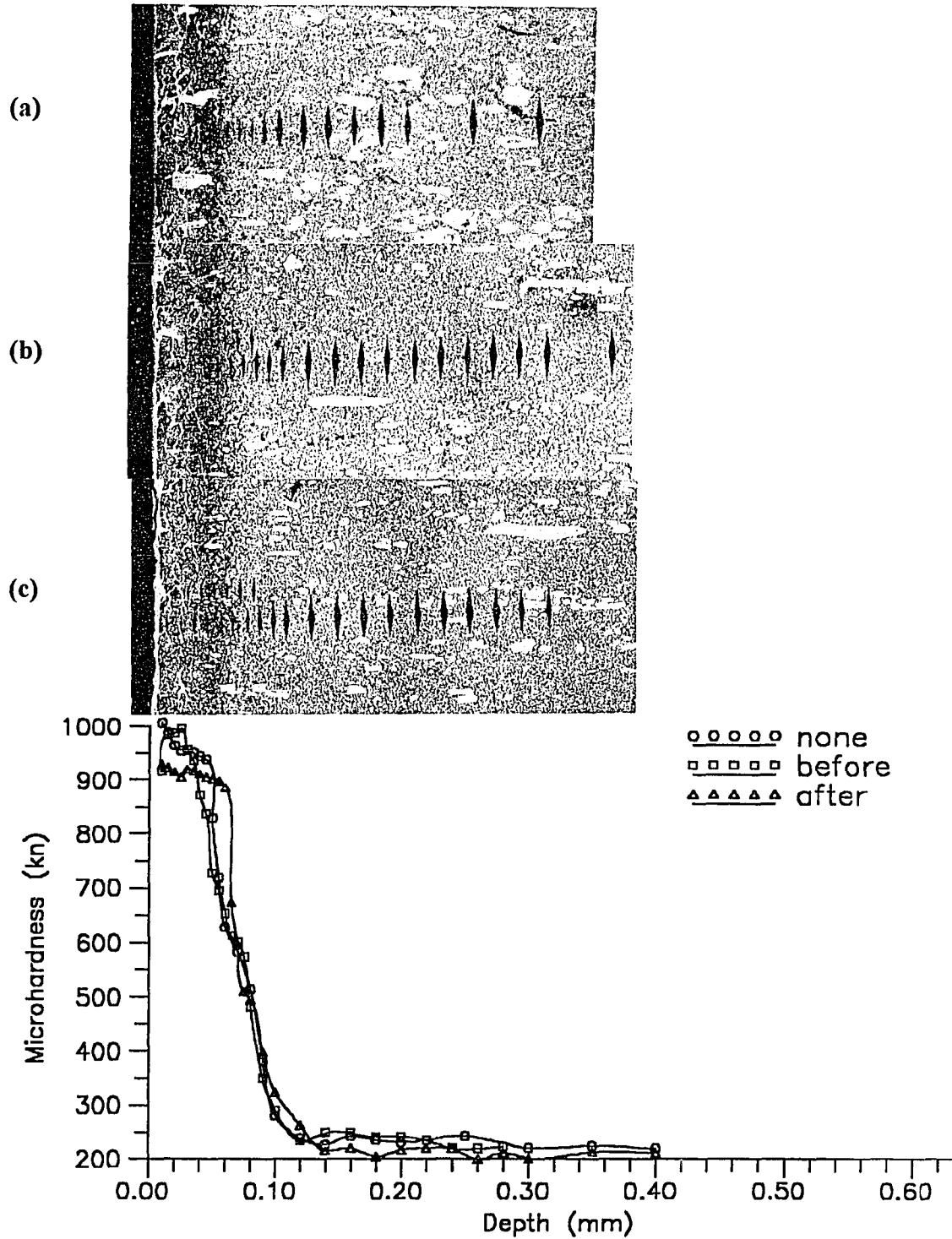
### **Properties of Pre-magnetized and Post-magnetized Specimens**



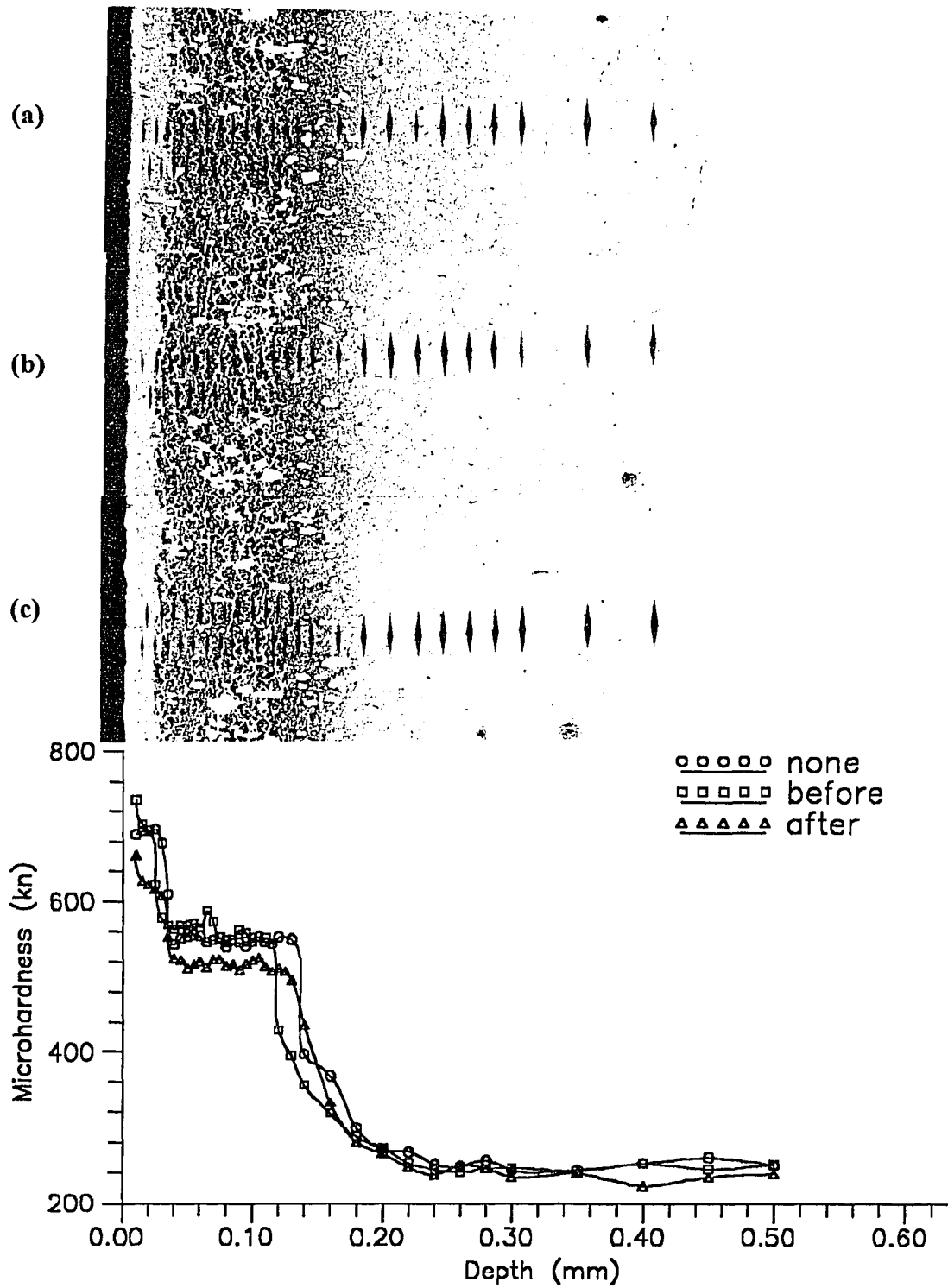
**Appendix C1** Variation in the microstructure and microhardness of the nitrided layer at different magnetization treatment for AISI D2 tool steel (65% N<sub>2</sub>, 650°C, 6 hours): (a) none; (b) 20 cycles before; (c) 20 cycles after.



**Appendix C2** Variation in the microstructure and microhardness of the nitrided layer at different magnetization treatment for AISI D2 tool steel (65%  $N_2$ , 550°C, 6 hours): (a) none; (b) 20 cycles before; (c) 20 cycles after.

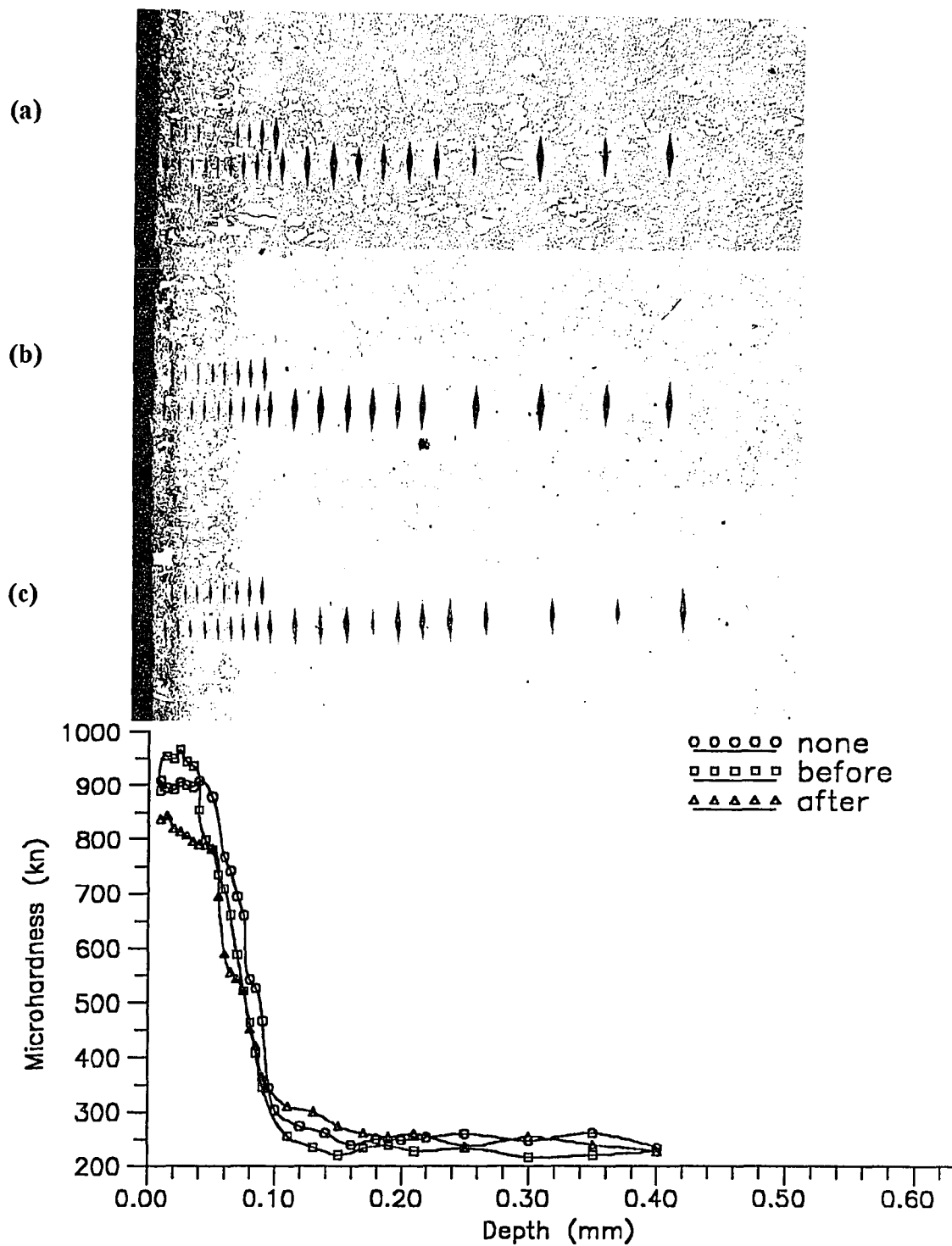


**Appendix C3** Variation in the microstructure and microhardness of the nitrided layer at different magnetization treatment for AISI D2 tool steel (25% N<sub>2</sub>, 550°C, 6 hours): (a) none; (b) 20 cycles before; (c) 20 cycles after.

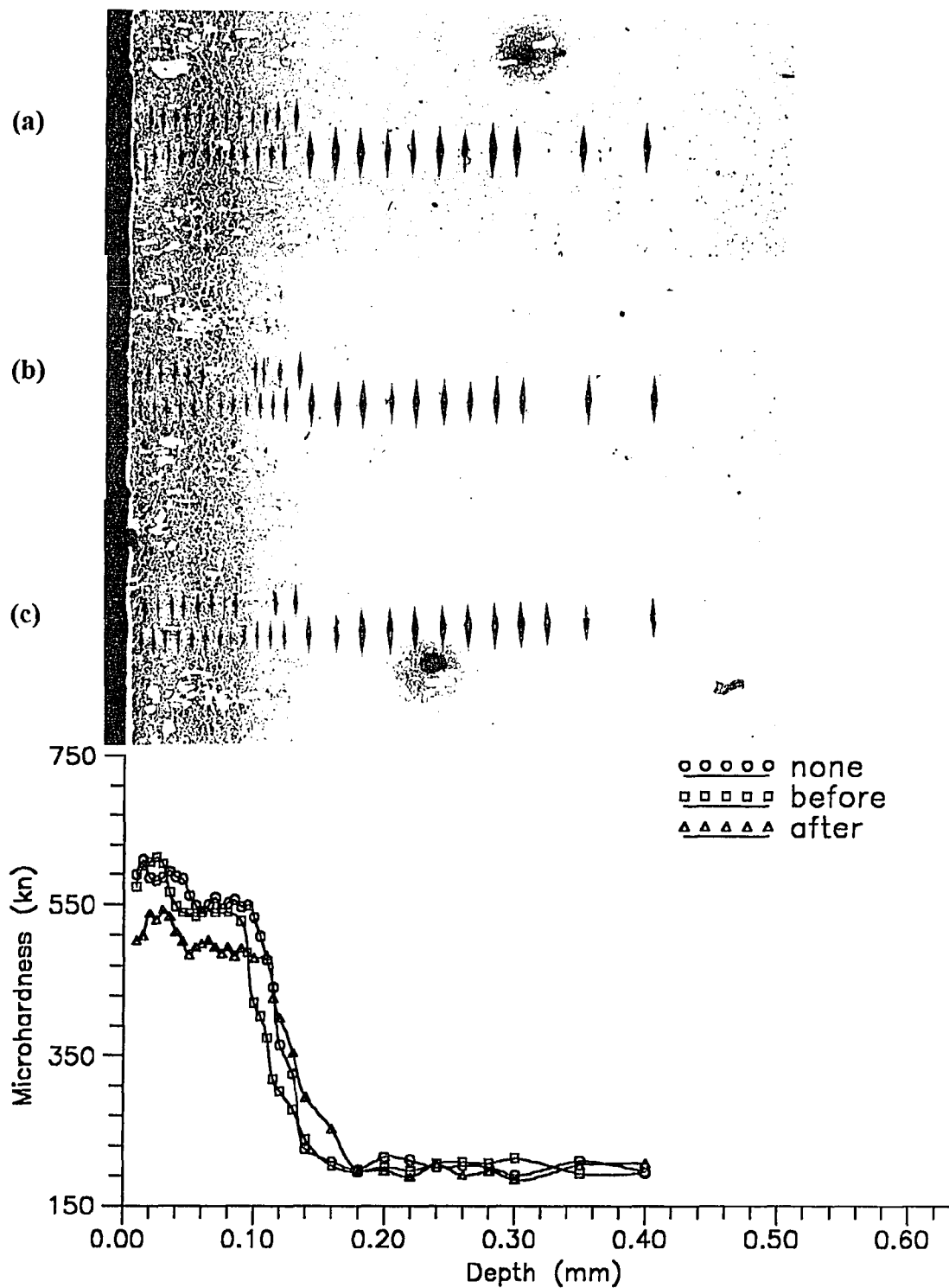


**Appendix C4** Variation in the microstructure and microhardness of the nitrided layer at different magnetization treatment for AISI D2 tool steel (25% N<sub>2</sub>, 650°C, 6 hours): (a) none; (b) 20 cycles before; (c) 20 cycles after.

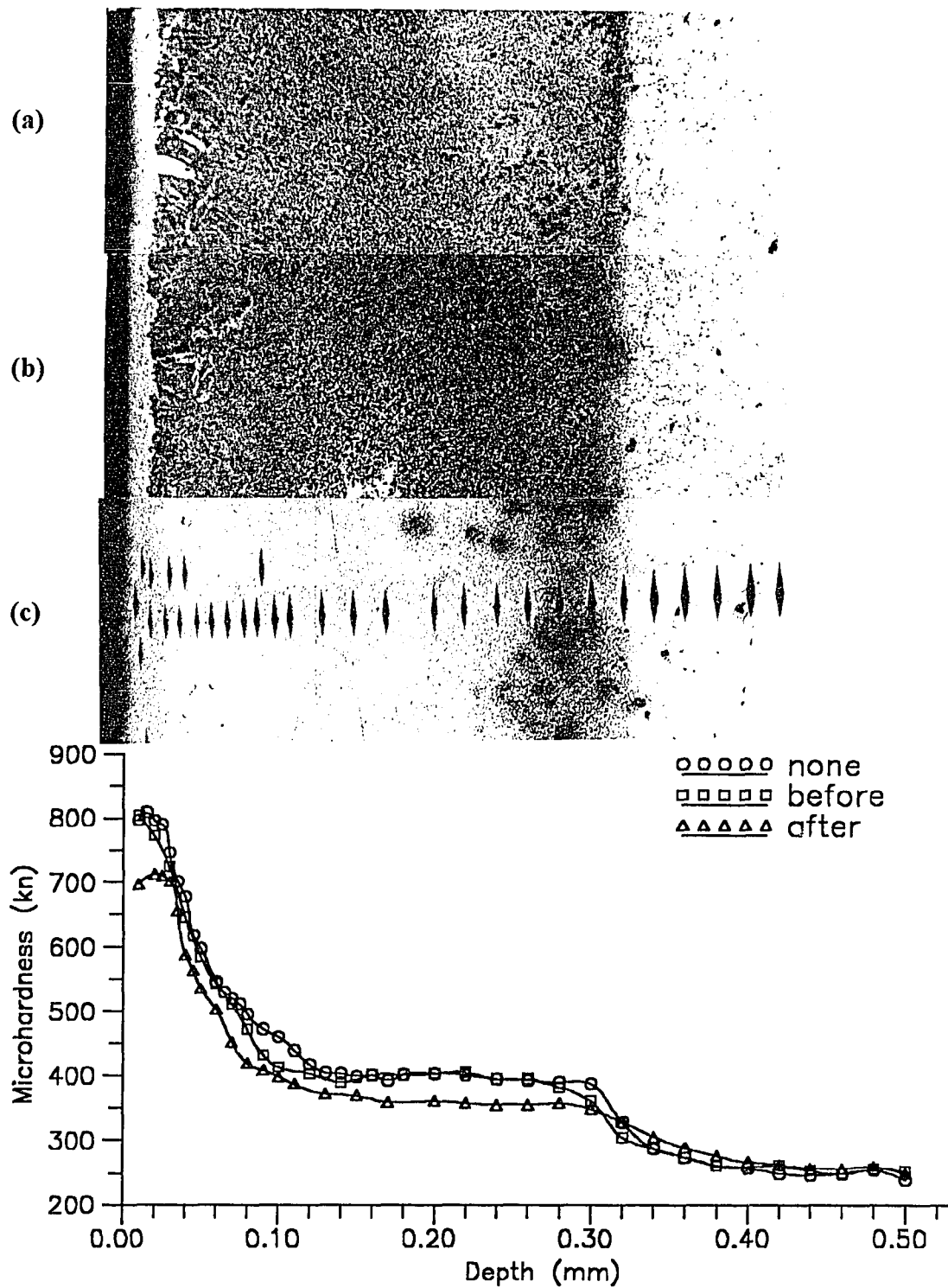




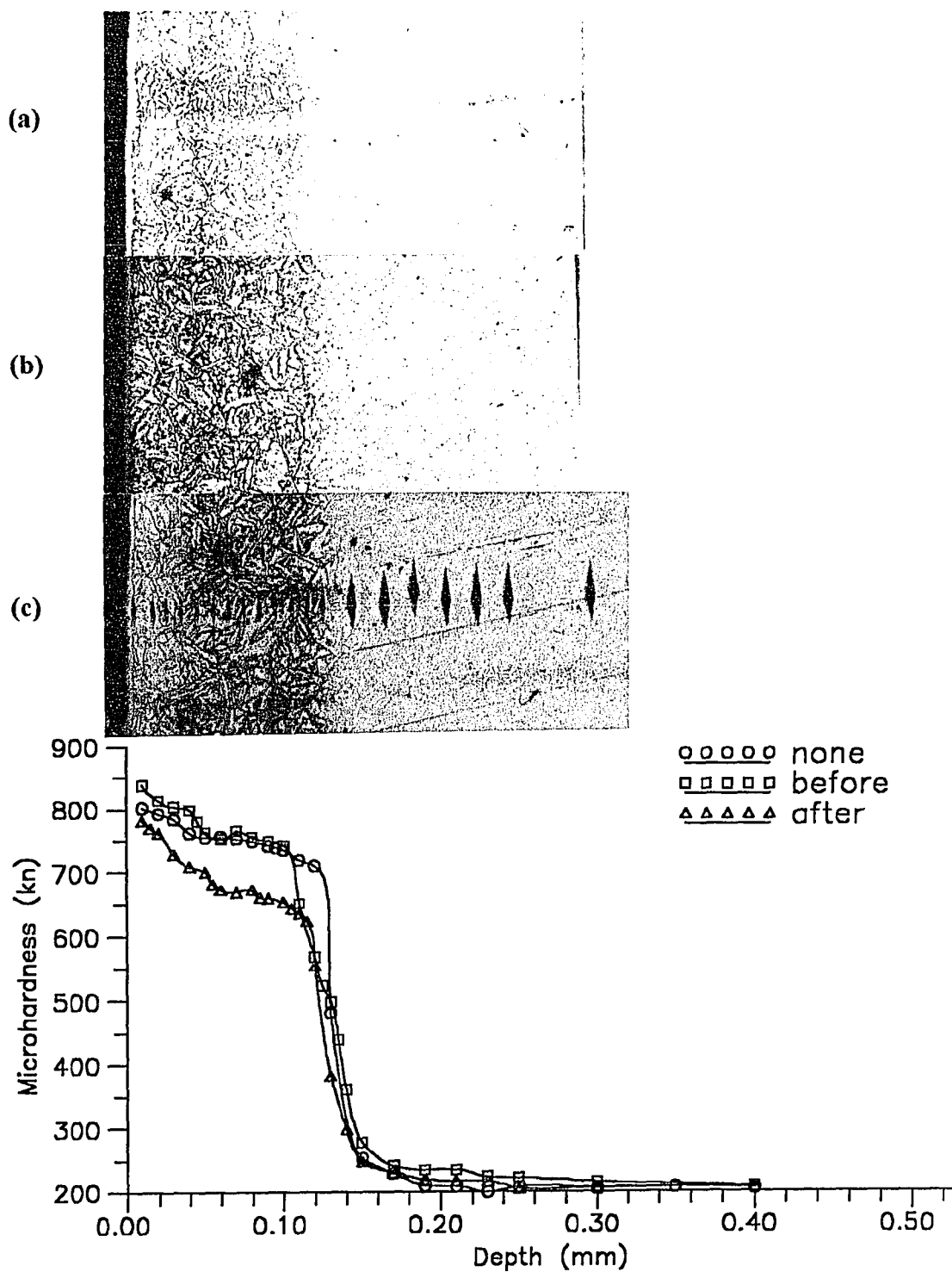
**Appendix C5** Variation in the microstructure and microhardness of the nitrided layer at different magnetization treatment for AISI D2 tool steel (5% N<sub>2</sub>, 550°C, 6 hours): (a) none; (b) 20 cycles before; (c) 20 cycles after.



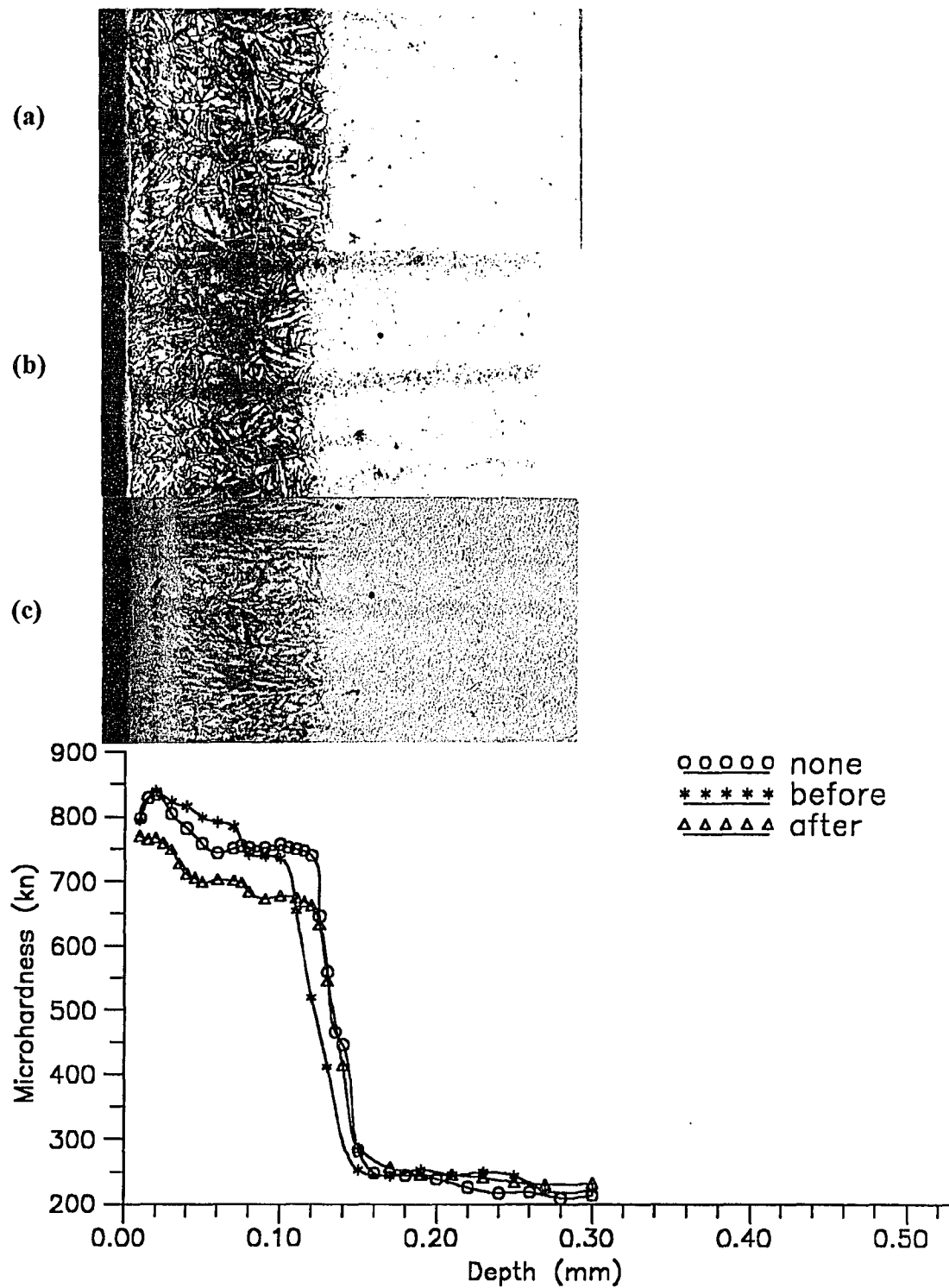
**Appendix C6** Variation in the microstructure and microhardness of the nitrided layer at different magnetization treatment for AISI D2 tool steel (5% N<sub>2</sub>, 650°C, 6 hours): (a) none; (b) 20 cycles before; (c) 20 cycles after.



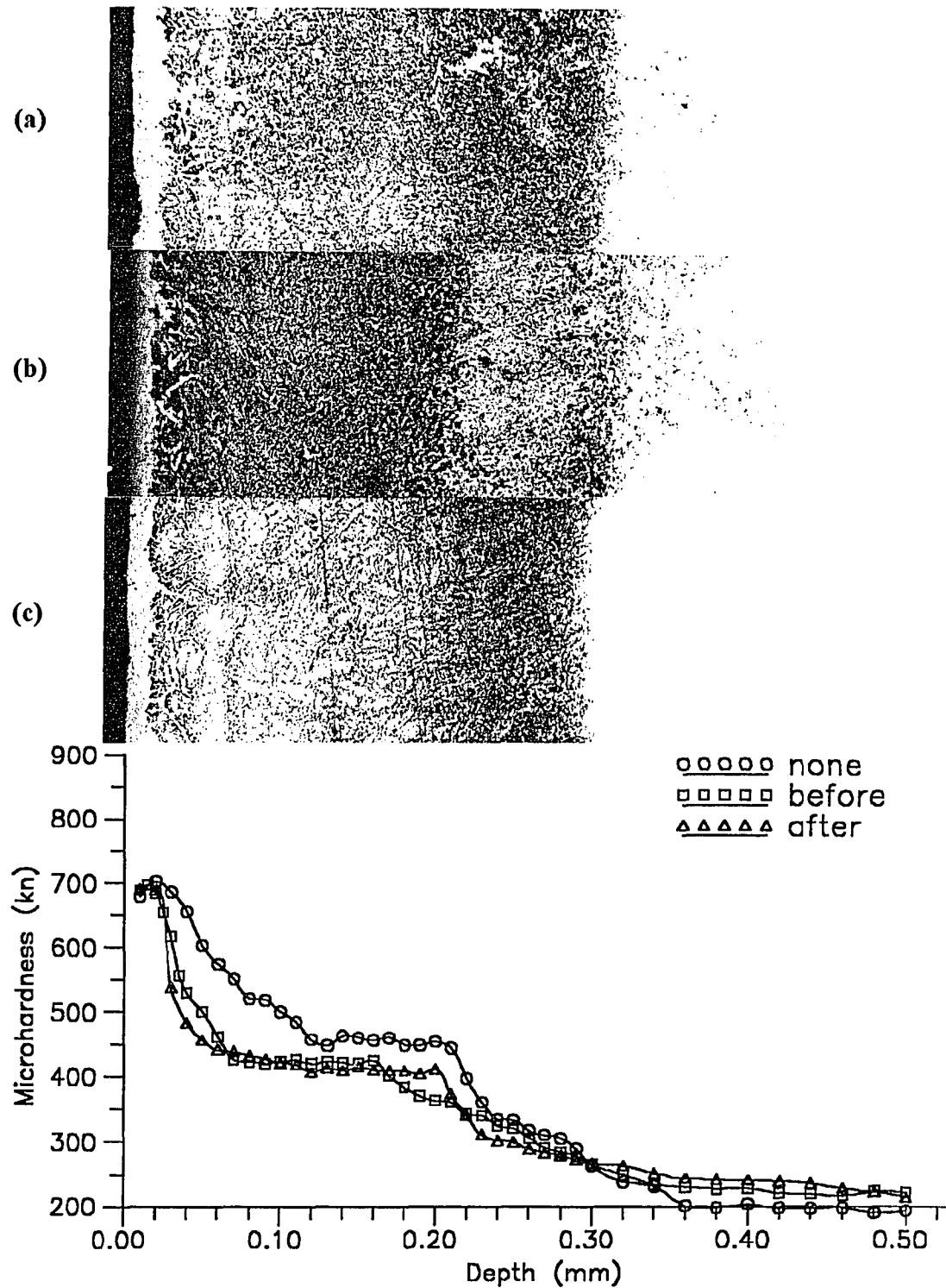
**Appendix C7** Variation in the microstructure and microhardness of the nitrided layer at different magnetization treatment for AISI H13 tool steel (65% N<sub>2</sub>, 650°C, 6 hours): (a) none; (b) 20 cycles before; (c) 20 cycles after.



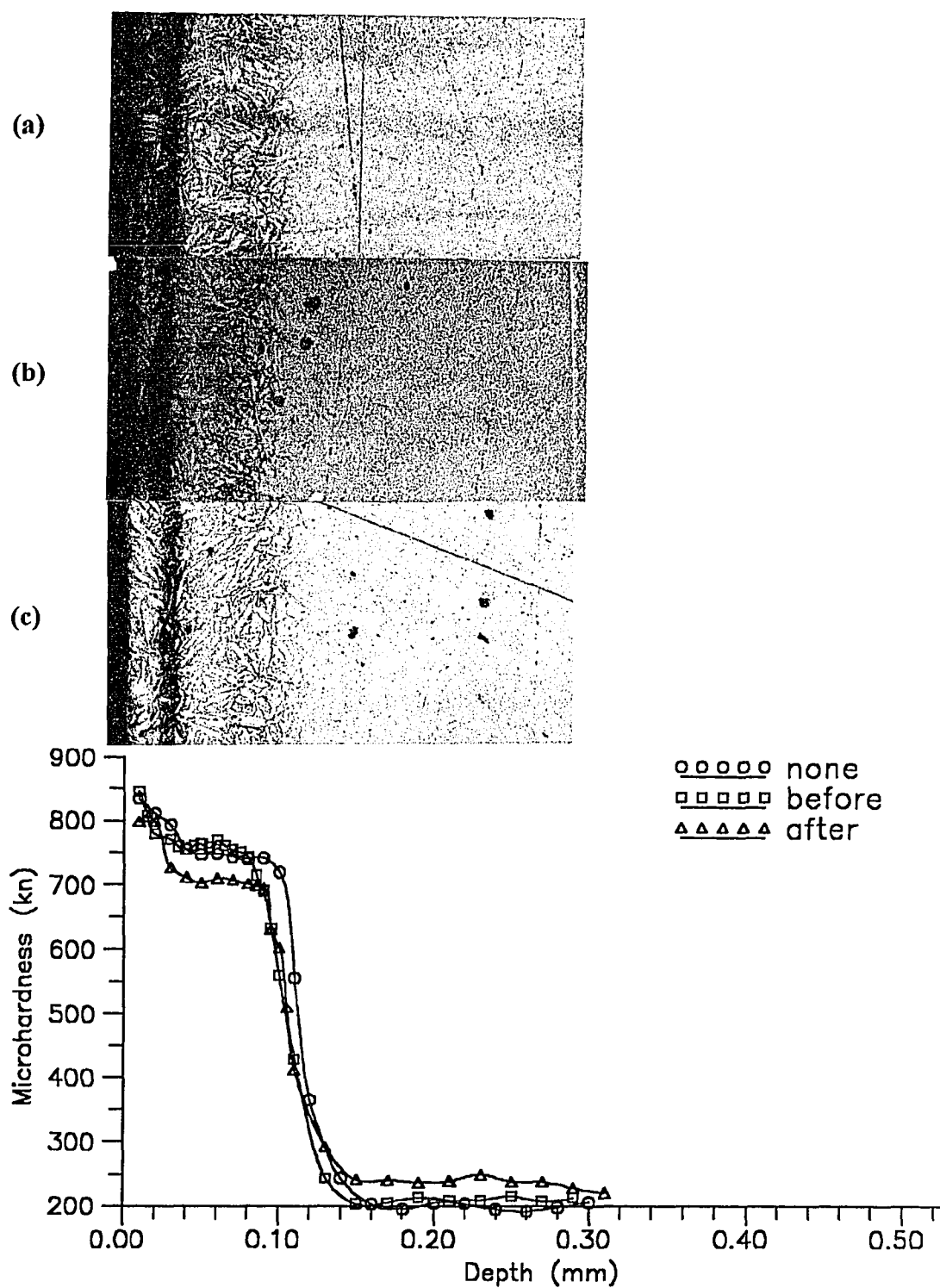
**Appendix C8** Variation in the microstructure and microhardness of the nitrided layer at different magnetization treatment for AISI H13 tool steel (65% N<sub>2</sub>, 550°C, 6 hours): (a) none; (b) 20 cycles before; (c) 20 cycles after.



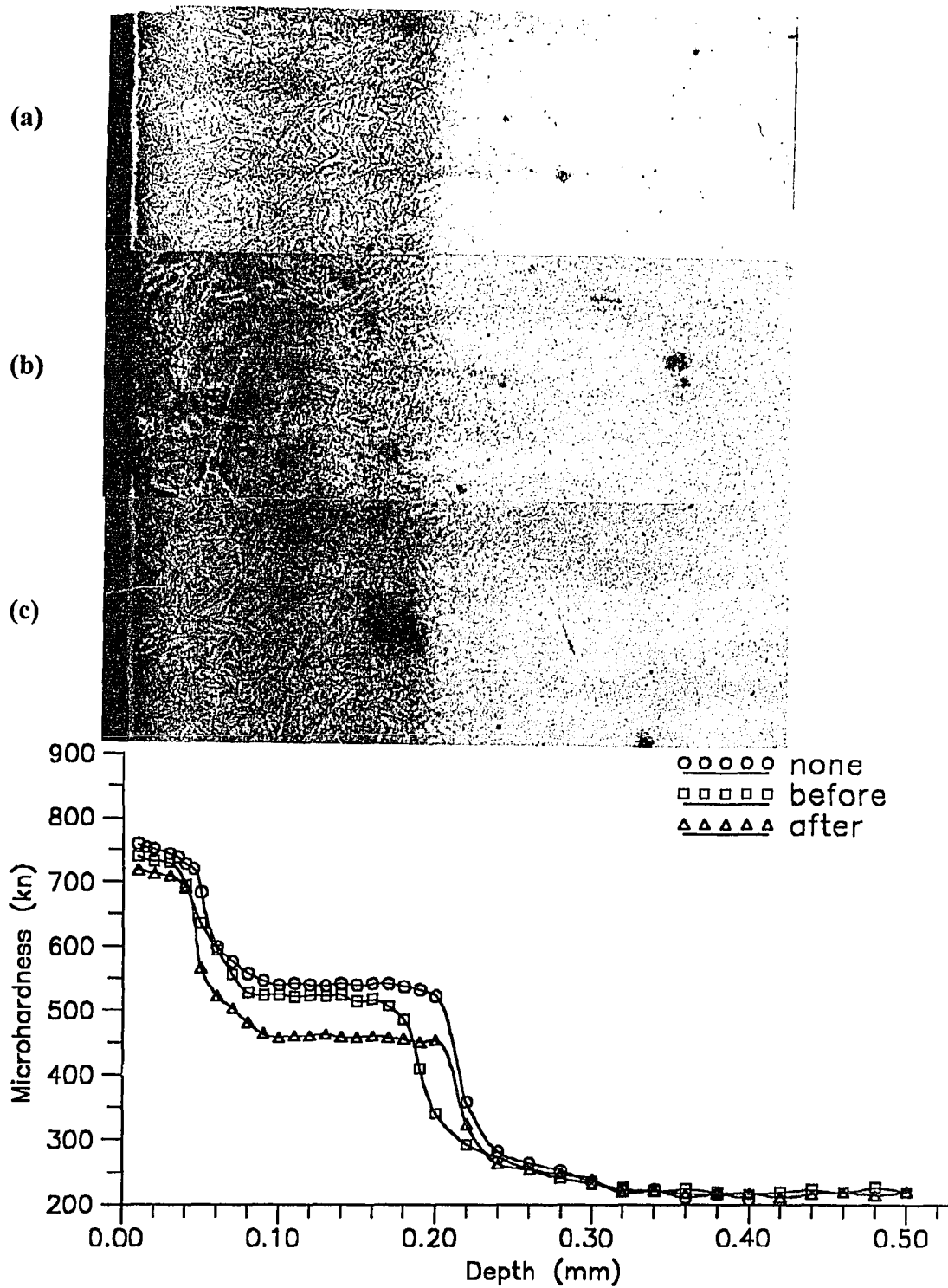
**Appendix C9** Variation in the microstructure and microhardness of the nitrided layer at different magnetization treatment for AISI H13 tool steel (25% N<sub>2</sub>, 550°C, 6 hours): (a) none; (b) 20 cycles before; (c) 20 cycles after.



**Appendix C10** Variation in the microstructure and microhardness of the nitrided layer at different magnetization treatment for AISI H13 tool steel (25% N<sub>2</sub>, 650°C, 6 hours): (a) none; (b) 20 cycles before; (c) 20 cycles after.

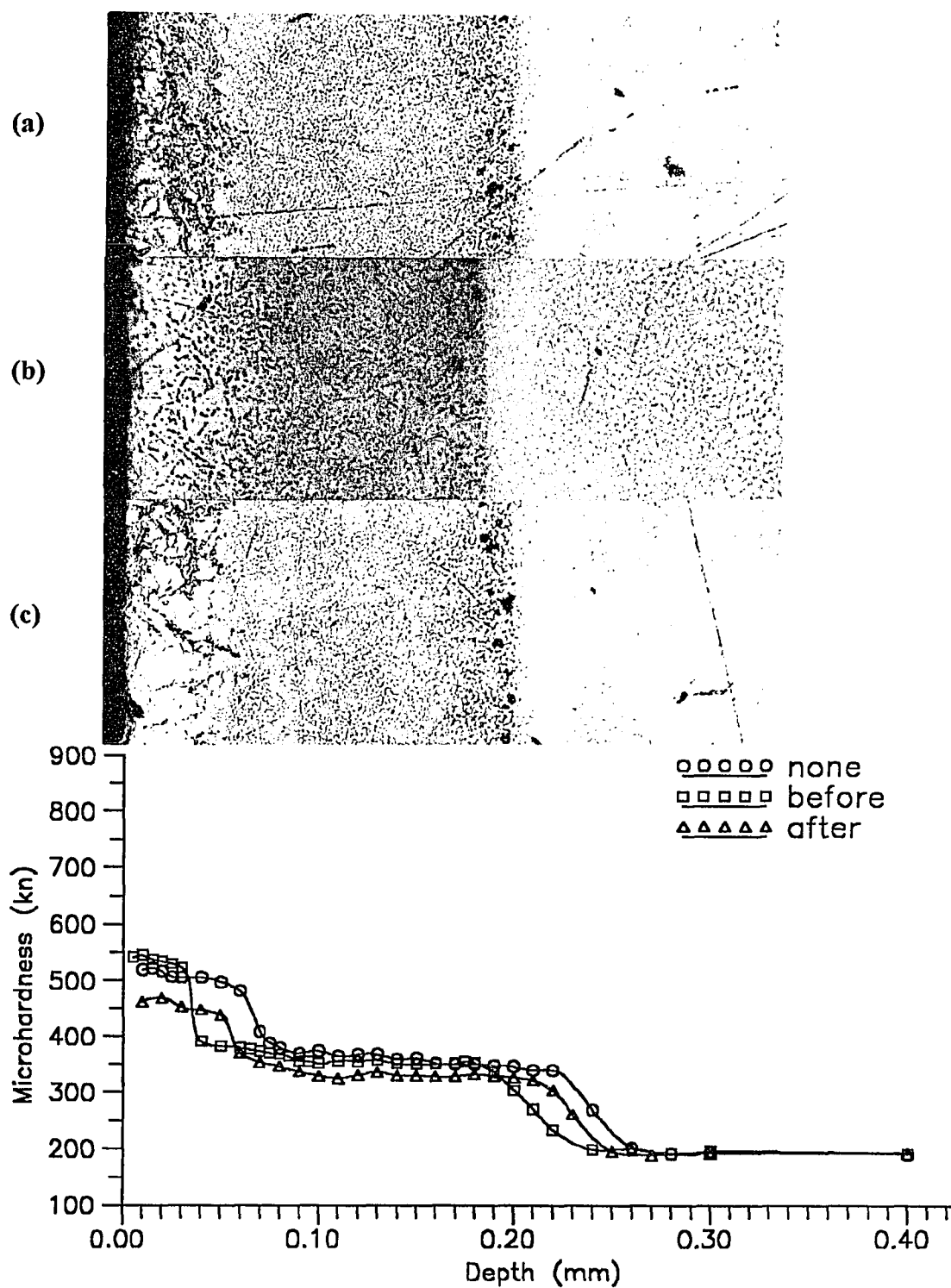


**Appendix C11** Variation in the microstructure and microhardness of the nitrided layer at different magnetization treatment for AISI H13 tool steel (5% N<sub>2</sub>, 550°C, 6 hours): (a) none; (b) 20 cycles before; (c) 20 cycles after.

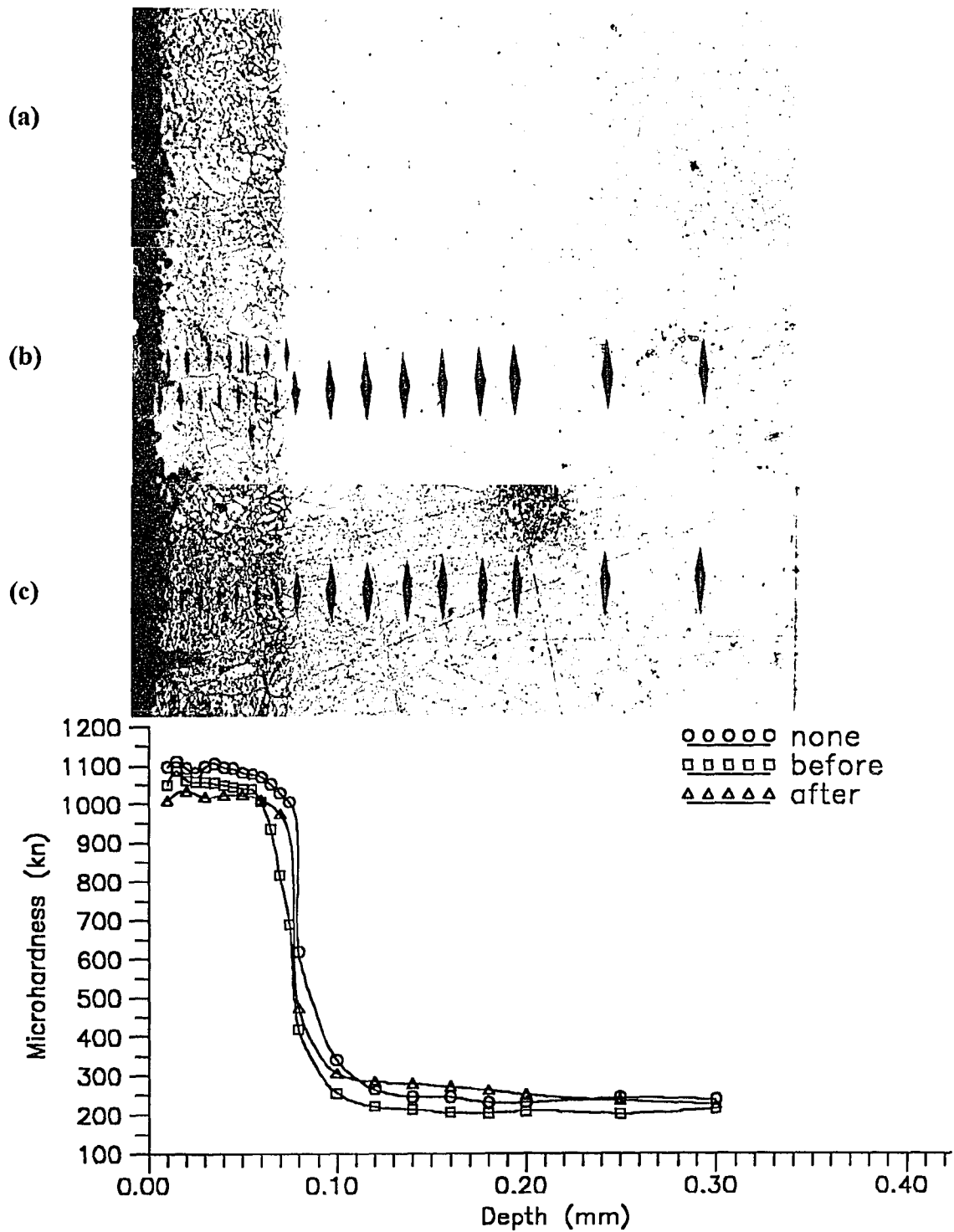


**Appendix C12** Variation in the microstructure and microhardness of the nitrided layer at different magnetization treatment for AISI H13 tool steel (5% N<sub>2</sub>, 650°C, 6 hours): (a) none; (b) 20 cycles before; (c) 20 cycles after.

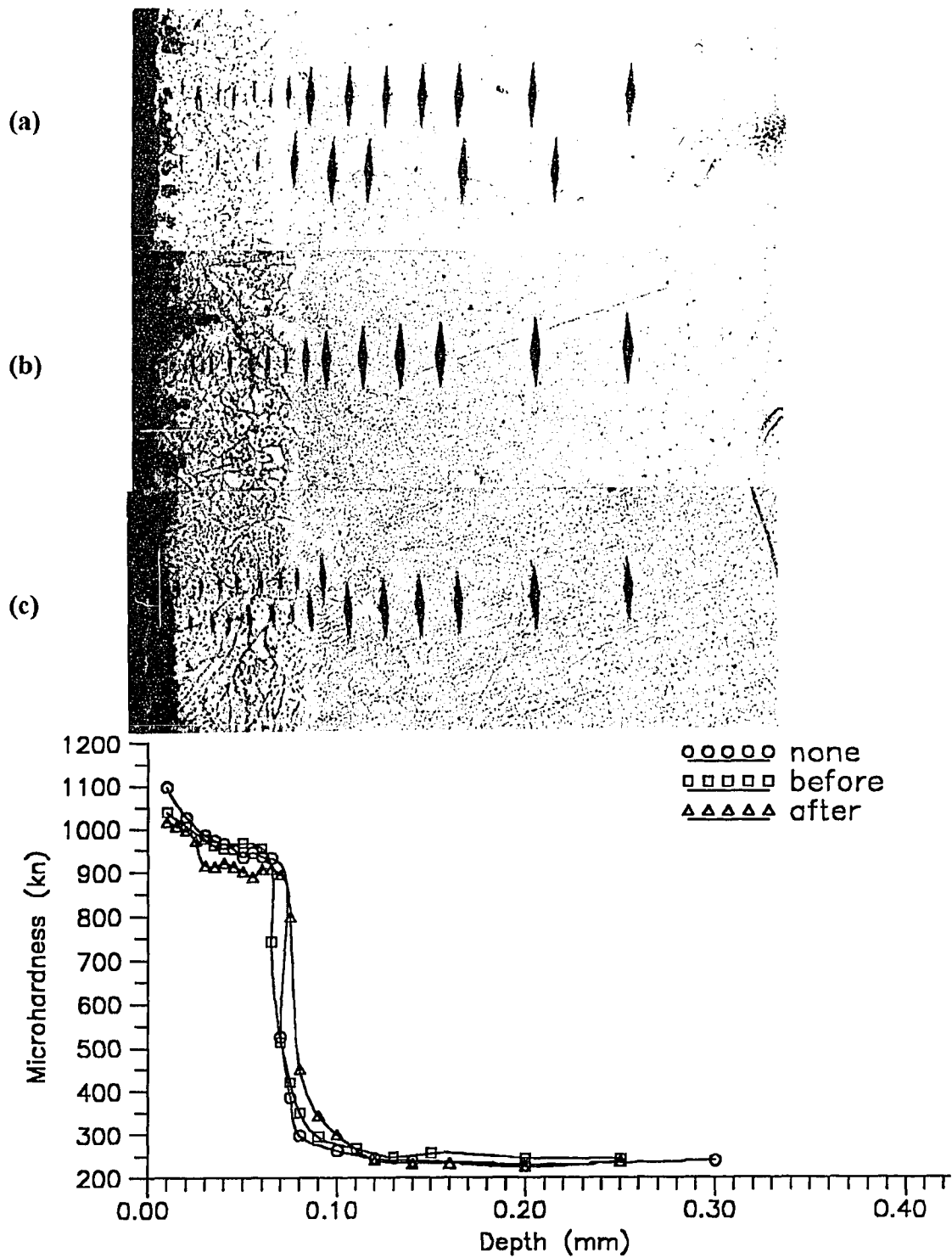




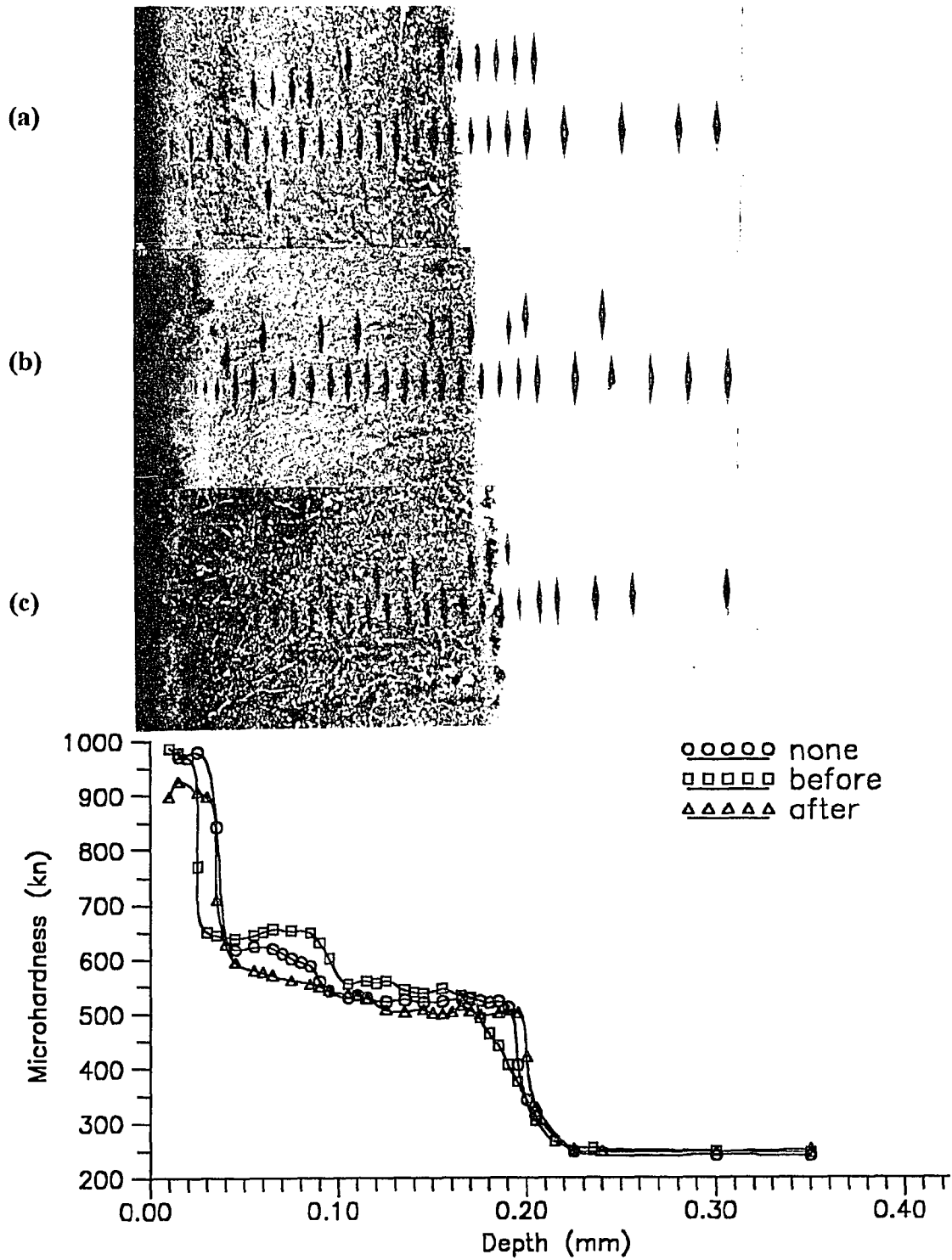
**Appendix C13** Variation in the microstructure and microhardness of the nitrided layer at different magnetization treatment for AISI 420 stainless steel (65% N<sub>2</sub>, 650°C, 6 hours): (a) none; (b) 20 cycles before; (c) 20 cycles after.



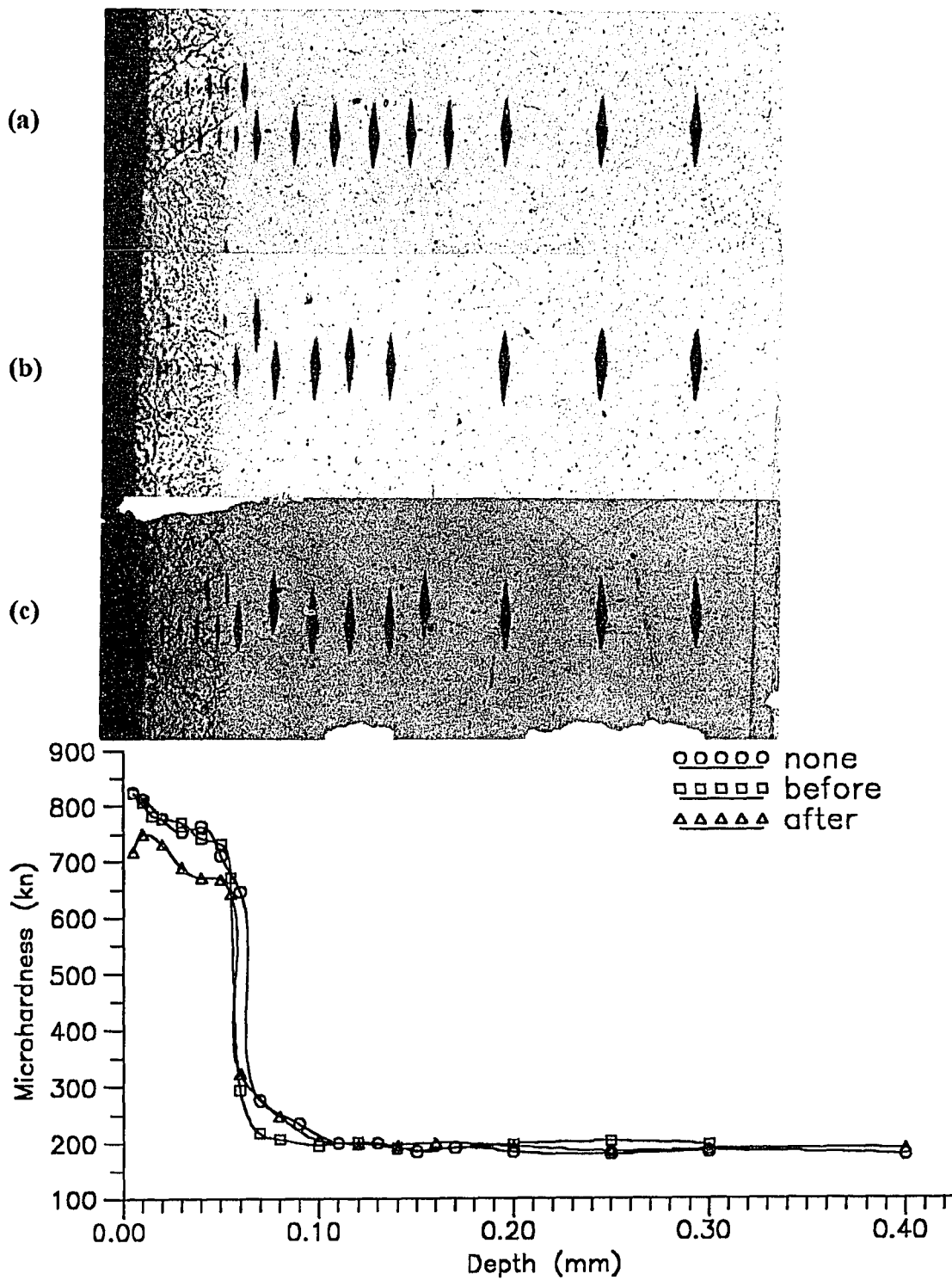
**Appendix C14** Variation in the microstructure and microhardness of the nitrided layer at different magnetization treatment for AISI 420 stainless steel (65% N<sub>2</sub>, 550°C, 6 hours): (a) none; (b) 20 cycles before; (c) 20 cycles after.



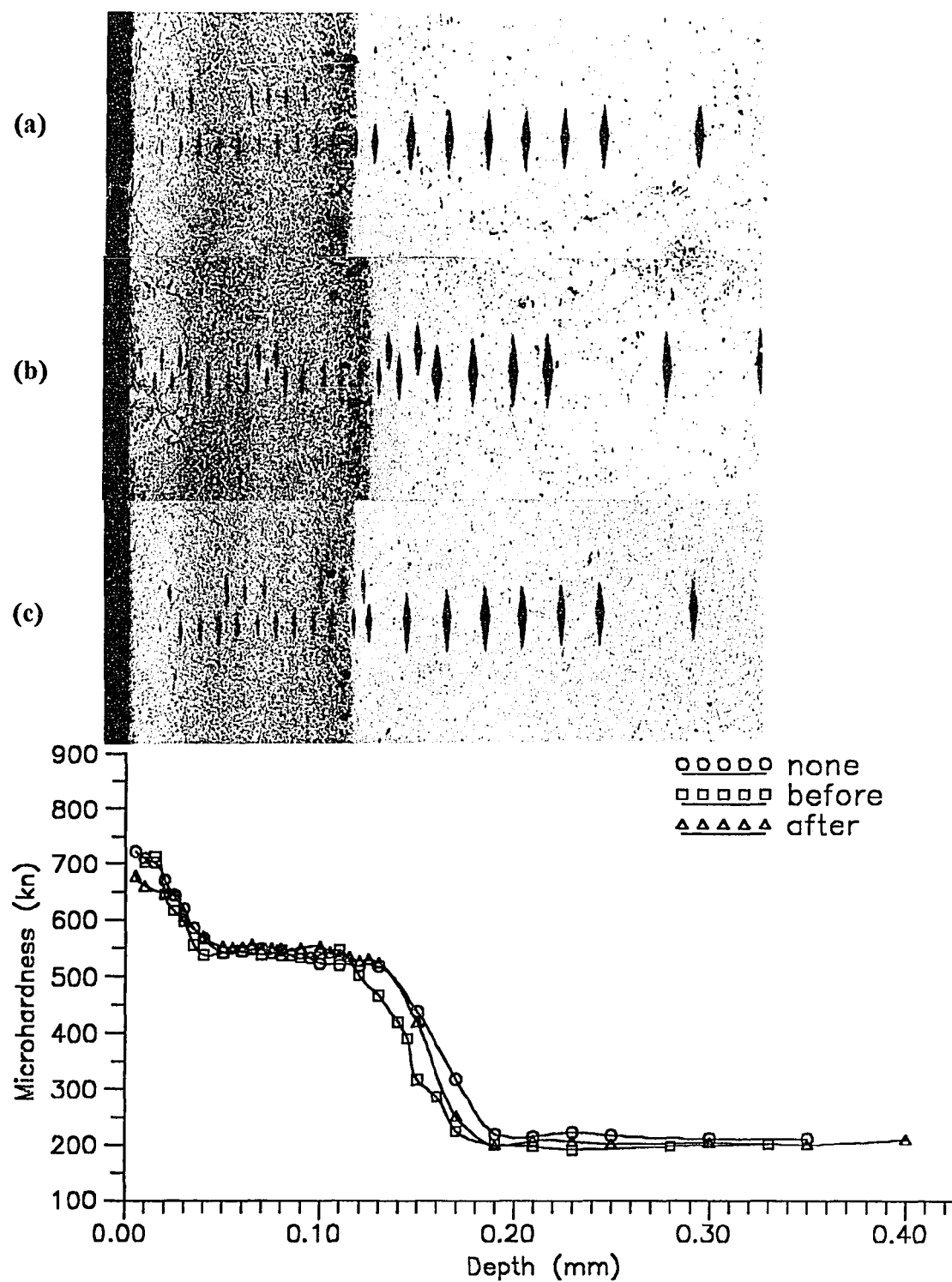
**Appendix C15** Variation in the microstructure and microhardness of the nitrided layer at different magnetization treatment for AISI 420 stainless steel (25% N<sub>2</sub>, 550°C, 6 hours): (a) none; (b) 20 cycles before; (c) 20 cycles after.



**Appendix C16** Variation in the microstructure and microhardness of the nitrided layer at different magnetization treatment for AISI 420 stainless steel (25% N<sub>2</sub>, 650°C, 6 hours): (a) none; (b) 20 cycles before; (c) 20 cycles after.



**Appendix C17** Variation in the microstructure and microhardness of the nitrided layer at different magnetization treatment for AISI 420 stainless steel (5% N<sub>2</sub>, 550°C, 6 hours): (a) none; (b) 20 cycles before; (c) 20 cycles after.



**Appendix C18** Variation in the microstructure and microhardness of the nitrided layer at different magnetization treatment for AISI 420 stainless steel (5% N<sub>2</sub>, 650°C, 6 hours): (a) none; (b) 20 cycles before; (c) 20 cycles after.

**APPENDIX D**

**Program for Nail Model**

```

PROGRAM NAILMODE;
{N+}
USES PRINTER;

VAR
  outfile      : text;
  alfa, beta, delta, nu, uplimit, lowlimit      : double;
  dummy, dummy1 ,dummy2 ,dummy3, dummy6 ,dummy5  : double;
  a, aa, c, d, r, y, Dg, s, const1, xxx, yy, zzz : double;
  n, i, ii, j, kk, ri, yi, t, midinflt, midinflt1 : integer;
CONST
  nmax = 4 ;

FUNCTION bessj0(x: double):double;
VAR
  ax, xx, p: double;
  q, ans, ans1, ans2: double;
BEGIN
  IF abs(x) < 8.0 THEN BEGIN
    q := sqr(x);
    ans1 := x*(72362614232.0+q*(-7895059235.0+q*(242396853.1
      +q*(-2972611.439+q*(15704.48260+q*(-30.16036606)))));
    ans2 := 144725228442.0+q*(2300535178.0+q*(18583304.74
      +q*(99447.43394+q*(376.9991397+q*1.0)))));
    bessj0 := ans1/ans2
  END
  ELSE BEGIN
    ax := abs(x);
    p := 8.0/ax;
    q := sqr(p);
    xx := ax-2.356194491;
    ans1 := 1.0+q*(0.183105e-2+q*(-0.3516396496e-4
      +q*(0.2457520174e-5+q*(-0.240337019e-6)));
    ans2 := 0.04687499995+q*(-0.2002690873e-3
      +q*(0.8449199096e-5+q*(-0.88228987e-6+q*0.105787412e-6)));
    ans := sqrt(0.636619772/ax)*(cos(xx)*ans1-p*sin(xx)*ans2);
    IF x < 0.0 THEN ans := -ans;
    bessj1 := ans
  END
END;

FUNCTION bessy0(x: double): double;
VAR
  xx, p: double;
  q, ans, ans1, ans2: double;
  ans := sqrt(0.636619772/ax)*(cos(xx)*ans1-p*sin(xx)*ans2);
7));

```



```

BEGIN
  IF x < 8.0 THEN BEGIN
    q := sqrt(x);
    ans1 := -2957821389.0+q*(7062834056.0+q*(-512359803.6
      +q*(10879881.29+q*(-86327.9257+q*228.4622733)))));
    ans2 := 40076544269.0+q*(745249964.8+q*(7189466.438
      +q*(47447.26470+q*(226.1030244+q*1.0)))));
    ans := (ans1/ans2)+0.636619772*bessj0(x)*ln(x)
  END
  ELSE BEGIN
    p := 8.0/x;
    q := sqrt(p);
    xx := x-0.785398164;

    ans1 := 1.0+q*(-0.1098628627e-2+q*(0.2734510407e-4
      +q*(-0.2073370639e-5+q*0.2093887211e-6)));
    ans2 := -0.1562499995e-1+q*(0.1430488765e-3+q*(-
      0.6911147651e-5
      +q*(0.7621095161e-6+q*(-0.934945152e-7)));
    ans := sin(xx)*ans1+p*cos(xx)*ans2*sqrt(0.636619772/x)
  END;

  bessy0 := ans
  END;

  FUNCTION bessy1(x: double): double;
  VAR
    xx, p: double;
    q, ans, ans1, ans2: double;
  BEGIN
    IF x < 8.0 THEN BEGIN
      q := sqrt(x);
      ans1 := x*(-0.4900604943e13+q*(0.1275274390e13+q*(-
        0.5153438139e11
        +q*(0.7349264551e9+q*(-
        0.4237922726e7+q*0.8511937935e4)))));
    ans2 :=
      0.2499580570e14+q*(0.4244419664e12+q*(0.3733650367e10
      +q*(0.2245904002e8+q*(0.1020426050e6+q*(0.3549632885e3+q*1.0)))));
    ans := (ans1/ans2)+0.636619772*(bessj1(x)*ln(x)-1.0/x)
  END
  ELSE BEGIN
    p := 8.0/x;
    q := sqrt(p);
    xx := x-2.356194491;

    ans1 := 1.0+q*(0.183105e-2+q*(-0.3516396496e-4
      +q*(0.2457520174e-5+q*(-0.240337019e-6)));
    ans2 := 0.04687499995+q*(-0.2002690873e-3+q*(0.8449199096e-5
      +q*(-0.88228987e-6+q*0.105787412e-6)));
    ans := sqrt(0.636619772/x)*(sin(xx)*ans1+p*cos(xx)*ans2)
  END;
  bessy1 := ans
  END;

  FUNCTION theta(g,h : double): double;
  VAR
    a1, a2 : double;
  BEGIN
    a1 := h * alfa;
    a2 := g * beta - sqrt(h) * alfa;
    theta := 2 * h * bessj1(a1) + a2 * bessj0(a1)
  END;

  FUNCTION varphi(g,h : double): double;
  VAR
    a1, a2 : double;
  BEGIN
    a1 := h * alfa;

```

```

a2 := g * beta - sqrt(h) * alfa;
varphi := 2 * h * bessY1(a1) + a2 * bessY0(a1)
END;

FUNCTION equation2(u, v : double): double;
VAR
  m1, m2, m3, m4, m5, m6, e1, e2, e3 :double;
BEGIN
  m1 := sqrt(v);
  m2 := v * alfa * r / a;
  m3 := varphi(u, v);
  m4 := theta(u, v);
  e1 := (1-Exp(-m1)) / v;
  m5 := bessJ0(m2) * m3;
  m6 := bessY0(m2) * m4;
  e2 := -m5 - m6;
  dummy5:=m5;
  dummy6:=m6;
  dummy2 := e2;
  dummy1:= e1;
  e3 := sqrt(m4) + sqrt(m3);
  dummy3:= e3;
  equation2 := exp(-r) * e2 * e1 / e3
END;

PROCEDURE midexpinf1(top, base, w : double;
  VAR s1 : double;
  n : integer);
VAR
  k : integer;
  x1, tnm1, sum1, del1, ddell1, up1, low1 :double;
FUNCTION equationk1(xf2, zf1 : double) : double;
VAR aaa : double;
  BEGIN
    if zf1<>0 then begin
      aaa := sqrt(ln(1/zf1));
      equationk1 := equation2(xf2,aaa)*0.5/zf1/aaa
    end
    else begin
      writeln('equk1 out of range!');
      exit
    end
  END;
  BEGIN {midexpinf1}
  low1 := base;
  up1 := top;
  IF n=1 THEN BEGIN
    s1 := (up1-low1)*equationk1(w, 0.5*(up1+low1));
    midinf1 := 1
  END
  ELSE BEGIN
    tnm1 := midinf1;
    del1 := (up1-low1)/(3.0*tnm1);
    ddell1 := del1 + del1;
    x1 := low1 + 0.5*del1;
    sum1 := 0.0;
    FOR k := 1 TO midinf1 DO BEGIN
      sum1 := sum1 + equationk1(w, x1);
      x1 := x1 + ddell1;
      sum1 := sum1 + equationk1(w, x1);
      x1 := x1 + del1
    END;
    s1 := (s1+(up1-low1)*sum1/tnm1)/3.0;
    midinf1 := 3*midinf1
  END;

```

```

END;
{ writeln('s1=',s1:15)}
END;
FUNCTION equ1(f: double): double;
VAR
  dump, dump1, s1 : double;
BEGIN
  dump1 := sqr(f);
  FOR ii := 1 TO nmax DO BEGIN
    midexpinf1(uplimit, lowlimit, dump1, s1, ii);
  END;
  dummy := COS(nu*f/180*pi);
  equ1 := dump1 * Exp(-dump1) * dummy * s1;
END;
PROCEDURE midexpinf(top, base : double;
  VAR s : double;
  n : integer);
VAR
  j : integer;
  x, tnm, sum, del, ddell, up, low :double;
FUNCTION equk(xf1 : double) : double;
VAR aa :double;
BEGIN
  if x<>0 then begin
    aa := sqrt(ln(1/xf1));
    equk := equ1(aa)*0.5/xf1/aa
  end
  else begin
    writeln('equk out of range!');
    exit;
  end
end
END;
{ midexpinf }
low := base;
up := top;
IF n = 1 THEN BEGIN
  s := (up-low)*equk(0.5*(up+low));
  midinf1 := 1
END
ELSE BEGIN
  tnm := Midinf1;
  del := (up-low)/(3.0*tnm);
  ddell := del + del;
  x := low + 0.5*del;
  sum := 0.0;
  FOR j := 1 TO midinf1 DO BEGIN
    sum := sum + equk(x);
    x := x + ddell;
    sum := sum + equk(x);
    x := x + del
  END;
  s := (s+(up-low)*sum/tnm)/3.0;
  Midinf1 := 3*Midinf1
END
END; { midexpinf }
FUNCTION equationk1(xf2, zf1 : double) : double;
VAR aaa : double;
BEGIN
  if zf1<>0 then begin
    aaa := sqrt(ln(1/zf1));
    equationk1 := equation2(xf2,aaa)*0.5/zf1/aaa
  end
end

```

```

else begin
  writeln('equk1 out of range!');
  exit
end
END;

BEGIN
  { MAIN }
  assign (outfile,'b:\naily1.dat');
  rewrite(outfile);
  a := 1.4696e-1;
  t := 21600;
  Dg := 1;
  delta := 1e5;
  alfa := 1e-3;
  beta := 1e2;
  lowlimit := 0;
  uplimit := 1;
  const1 := 4*beta/pi/sqrt(pi);
  writeln('alfa=',alfa:6,'beta=',beta:6,'delta=',delta:8,'a=',a:10);
  writeln('-----');
  nu := 1;
  FOR yi := 1 TO 10 DO BEGIN
    FOR ri := 1 TO 10 DO BEGIN
      aa := ri * 10;
      r := aa * a;
      FOR i := 1 TO nmax DO BEGIN
        midexpintf(uplimit, lowlimit, s, i)
      END;
      xxx := SQR(nu);
      zzz := 1/EXP(xxx/4);
    END;
  END;

  yyy := const1*s;
  c := zzz + yyy;
  writeln('=',aa:5:2,'x a', 'nu=',nu:5:2, 'ct=',zzz:15:12,
  ',c2=',yyy:15:12, 'c=',c:15:12);
  writeln(outfile,aa:5,'nu:5',c:20);
  writeln;
  END;
  nu := nu + 1;
  END;

  END. { MAIN }
  □

```

## REFERENCES

1. Dubrovsky, R., and V. Drits. "Surface Engineering by Magnetic Treatment and Glow Discharge." *Symposium on Advanced Manufacturing*, NJ (1990): 33-37.
2. Rigsbee, J. M. "Physical Vapor Deposition." in *Surface Modification Engineering*, Kossowsky, R. ed., CRC Press, New York (1989): 231-256.
3. Bunshah, R. F. *Deposition Technologies for Films and Coatings*. Noyes Pub., NJ (1982).
4. Ahmed, N. A. *Ion Plating Technology*. John Wiley & Sons, New York (1987).
5. Blackish, R. "Electron Beam Melting, Refining, and Heat Treatment." *Industrial Heating*. (1985): 26-30.
6. Booth, M. "Plasma Thermochemical Treatment." *Metallurgia*. (1985): 492-496.
7. *Source Book on Nitriding*, ASM, OH (1977): 107-143.
8. Grube, W. L., and S. Verhoff. "Plasma (Ion) Processes for Case Hardening of Metals." in *Surface Modification Engineering II*, Kossowsky, R. ed., CRC Press, New York (1989): 107-149.
9. Tibbetts, G. G. "Role of Nitrogen Atoms in Ion-nitriding." *J. of Appl. Phys.* 45 (1974): 5072-5073.
10. Keller, K. "Schichtaufbau Glimmnitrierter Eisenwerkstoffe." *HTM*. 26 (1971): 120-130.
11. Bell, T., and Dearnley, P. A. "Plasma Surface Engineering." *Proc. Intern. Seminar on Plasma Heat Treatment*, Senlis (1987): 13-53.
12. Hudis, M. "Study of Ion Nitriding." *J. Appl. Phys.* 44 (1973): 71-77.
13. Xu, B., and Y. Zhang. "Collision Dissociation Model in Ion Nitriding." *Proc. 5th Intern. Cong. Heat Treatment*, Budapest (1986): 1086-1093.
14. John, C. K., D. J. Sturges, and S.W. Martin. "Glow Discharge Nitriding in Production." in *Source Book on Nitriding*, ASM, OH (1977): 186-187.
15. Metin, E., and T. Inal. "Formation and Growth of Iron Nitrides during Ion-Nitriding." *J. of Material Science*. 22 (1987): 2783-2788.
16. Lightfoot, B. J., and D. H. Jack. "Kinetics of Nitriding with and without White-Layer Formation." *Heat Treatment '73*. (1973): 59-65.

17. Martovitskaya, N. N., and T. S. Tonchev. "Effect of Nitriding Temperature in a Glow Discharge on the Thickness and Composition of the Nitride Zone." *Metallurgical Science of Heat Treatment*. 27 (1985): 825-829.
18. Eltoukhy, A. H., and J. E. Greene. "Diffusion Enhancement Due to Low-Energy Ion Bombardment during Sputter Etching and Deposition." *J. Appl. Phys.* 51 (1980): 4444-4452.
19. Thornton, P. A., and V. J. Colangelo. *Fundamentals of Engineering Materials*. Prentice-Hall Inc., NJ (1985): 369-371.
20. Cullity, B. D. *Introduction to Magnetic Materials*. Addison-Wesley Publishing Co., MA (1972).
21. Kittel, C. "Physical Theory of Ferromagnetic Domains." *Reviews of Modern Physics*. 21 (1949): 541-583.
22. Weiss, P. "L'Hypothese du Champ Moleculaire et de la Propriete Ferromagnetique." *J. De Physique*. 6 (1907): 661-690.
23. Bloch, F. "Theory of the Exchange Problem and of Residual Ferromagnetism." *Zeit. fur Phys.* 74 (1932): 295.
24. Joseph, J. "Pulsed Magnetism Boosts Tool Life." *American Machinist & Automated Manufacturing*. (1987): 80-82.
25. Dubrovsky, R., Y. Kin, and I-Tsung Shih. "Development of the Computer Controlled Wear Testing Methodology." *Proc. IAMSDC-1*, TN (1989): p57.1-p57.4
26. Shih, I-Tsung. *Seizure and Wear Testing Methodology*. Master Thesis, NJIT (1988).
27. Chikazumi, S. *Physics of Magnetism*. John Wiley & Sons, New York (1964): 245-248.
28. Craik, D. J., and R. S. Tebble. *Ferromagnetism and Ferromagnetic Domains*. John Wiley & Sons, New York (1965).
29. Carey, R., and , E. D. Isaac. *Magnetic Domains and Techniques for Their Observation*. John Wiley & Sons, New York (1966): 32-33.
30. Neel, L., J. Pauleve, R. Pauthenet, J. Laughier, and D. Dautreppe. "Magnetic Properties of an Iron-Nickel Single Crystal Ordered by Neutron Bombardment." *J. Appl. Phys.* 35 (1964): 873-876.
31. Williams, H. J. "Direction of Domain Magnetization in Powder Patterns." *Phys. Rev.* 71 (1947): 646-647.
32. Hull, D. *Introduction to Dislocations*. Pergamon Press, New York (1965).

33. Polcarova, M., and A. R. Lang. "X-Ray Topographic Studies of Magnetic Domain Configurations and Movements." *Appl. Phys. Letters*. 1 (1962): 13-15.
34. Becker, R., and W. Doring. *Ferromagnetisms*. Springer-Verlag, New York (1938).
35. Vicena, F. "The Effect of Dislocations on the Coercive Force of Ferromagnetics." *Czech, J. Phys.* 5 (1955): 480-499.
36. Peach, M., and J. S. Koehler. *Phys. Rev.* 80 (1950): 436.
37. Berkowitz, A. E., and E. Kneller. *Magnetism and Metallurgy*. Academic Press, New York 2 (1969): 628-633.
38. Hogan, B. J. "Magnetostriction Relieves Residual Stresses in Tools, Fasteners." *Design News*. (1987): 94-95.
39. Miller, P. C. "A Look at Magnetic Treatment of Tools and Wear Surfaces." *Tooling and Production*. (1990): 100-103.
40. Pavlov, V. A., I. A. Pereturina, and N. L. Pecherkina. "The Effect of Constant Magnetic Field on Mechanical Properties and Dislocation Structure of Niobium and Molybdenum." *Phys. Stat. Sol., (a)*. 57 (1980): 449-456.
41. Peierls, R. "The Size of Dislocation." *Proc. Phys. Soc.* 59 (1940): 34-37.
42. Hart, E. W. "On the Role of Dislocations in Bulk Diffusion." *Acta Metallurgica*. 5 (1957): 597.
43. Morrison, H. M. "Dislocation Enhanced Impurity Diffusion." *Phil. Mag.* 12 (1965): 985-995.
44. Gupta, D. "Self-Diffusion Along Dislocations in Single-Crystal Au Films." *Phys. Rev.* 7 (1975): 586-594.
45. Fick, A., *J. Pogg. Ann.* 94 (1855): 59.
46. Shewmon, P. G. *Diffusion in Solid*. McGraw-Hill, New York (1963).
47. Hertzberg, R. W. *Deformation and Fracture Mechanics of Engineering Materials*. John Wiley & Sons, New York (1989): 49-80.
48. Terry, L. V., R. Dubrovsky, and V. Drits. "Surface Modification by Magnetic Treatment." *Surface Modification Technologies III*. (1990): 393-402.
49. Turnbull, D., and R. E. Hoffmann. "Effect of Relative Crystal and Boundary Orientations on Grain Boundary Diffusion Rate." *Acta Metallurgica*. 2 (1954): 419.

50. Fisher, J. C. "Calculations of Diffusion Penetration Curves for Surface and Grain Boundary Diffusion." *J. Appl. Phys.* 22 (1951): 74-77.
51. Pavlov, P. A., V. A. Panteleev, and A. V. Maiorov. "Diffusion of Antimony Along Dislocations in Silicon." *Sov. Phy. Sol. Stat.* 6 (1964): 305-310.
52. Suzuoko, T. "Lattice and Grain Boundary Diffusion in Polycrystals." *Tran. Japan Insti. of Metals.* 2 (1961): 25-34.
53. Kaur, I., and W. Gust. *Fundamentals of Grain and Interphase Boundary Diffusion.* Ziegler Press. (1989): 31-32.
54. Whipple, R. T. P. "Concentration Countours in Grain Boundary Diffusion." *Phil. Mag.* 45 (1954): 1225-1236.
55. Carslaw, H. S., and J. C. Jaeger. *Operational Methods in Applied Mathematics.* Oxford University Press, Clarendon (1941): 71-87.
56. McLachlan, N. W. *Bessel Functions for Engineers.* Oxford University Press, Clarendon (1955).
57. Petzow, G. *Metallographic Etching.* ASM, OH (1976).
58. *CRC Handbook of Metal Etchants.* CRC Press, FL (1990).
59. Colijn, P. F., E. J. Mittemeijer, and H. C. F. Rozendaal. "Light Microscopical Analysis of Nitrided or Nitrocarburized Iron and Steels." *Zeitschrift Fur Metallkunde.* 74 (1983): 620-627.
60. Avin, R., and T. Spalvins. "Nitriding Mechanisms in Ar-N<sub>2</sub>, Ar-N<sub>2</sub>-H<sub>2</sub> and Ar-NH<sub>3</sub> Mixtures in D.C. Glow Discharges at Low Pressures (Less than 10 Torr)." *Material Science and Engineering.* 95 (1987): 237-246.
61. Priestner, R., and J. Aghazadeh-Mohandesi. "Effects of Nitriding at Low Nitrogen Partial Pressure on Yield and Fatigue in Some Stainless Steels." *Heat Treatment '81.* (1983): 207-214.
62. Dixon, G. J., S. A. Plumb, and H. C. Child. "Processing Aspects of Plasma Nitriding." *Heat Treatment '81.* (1983): 137-146.
63. Kurny, A. S., R. M. Mallya, and M. M. Rao. "A Study on the Nature of the Compound Layer Formed During the Ion Nitriding of En40B Steel." *Material Science and Engineering.* 78 (1986): 95-100.
64. Yang, Wnge. *Development of Plasma Ion Nitriding Process Parameters to Increase Durability of Machine Components.* Master Thesis, New Jersey Institute of Technology (1991).



65. Elatec Inc. Document. "Instruction Manual for Aerovace-TM II Multipurpose Vacuum Furnace." Woburn, MA, Elatec Inc. (1987).
66. Jablonowski, J. "Pulsed Magnetism Boosts Tool Life." *American Machinist & Automated Manufacturing*. (1987): 80-82.
67. Milton, R. "Relaxing Stresses to Better Tool Life." *Modern Machine Shop*. (1988): 64-69.
68. "Materials Characterization," in *Metals Handbook vol. 10*. ASM, OH (1986): 549-567.
69. Feldman, L. C., and J. W. Mayer. *Fundamentals of Surface and Thin Film Analysis*. North-Holland Pub., New York (1986): 257-281.
70. Wolf, G. J., and B. L. Daris. "Microanalysis of Hard Coatings." in *Surface Modification Technologies*. Sudarshan, T. S., and Bhat, D. G., ed. The Metallurgical Society (1988): 97-120.
71. Joshi, A, L. E. Davis, and P. W. Palmberg. "Auger Electron Spectroscopy." in *Methods of Surface Analysis vol. II*, Czanderna, A. W.,ed. Elsevier Scientific Publishing Co., New York (1975): 159-218.
72. Palmberg, P. W. "Use of Auger Electron Spectroscopy and Inert Gas Sputtering for Obtaining Chemical Profile." *The Journal of Vacuum Science and Technology*. 9 (1971): 160-163.
73. Harris, L. A. "Analysis of Materials by Electron-Excited Auger Electrons." *J. of Appl. Phys.* 39 (1968): 1419-1427.
74. Dubrovsky, R., and Itsung Shih. "Development of The Computer Controlled Seizure Testing Methodology." *MRS*. 140s(1988).
75. Yao, wen-Long. *Wear Testing with Programmable Logic Controller and Automated Data Acquisition System*. Master Thesis, NJIT (1988).
76. Knesl, Z., J. Jinoch, and Z. Bilek. *Czech. J. Phys.* B24 (1974): 343.
77. Le Claire, A. D., and A. Rabinovitch. "A Mathematical Analysis of Diffusion in Dislocations: I. Application to Concentration 'Tails'." *J. Phys. C: Solid State Physics*. 14 (1981): 3863-3879.